Yu-Shiba-Rusinov states in superconductor-quantum dot transistors made by electromigration

Alvaro Garcia Corral

Université Grenoble Alpes

THÈSE

Pour obtenir le grade de

DOCTEUR DE L'UNIVERSITE GRENOBLE ALPES

Spécialité : **Nanophysique**

Arrêté ministériel : 25 mai 2016

Présentée par

Alvaro GARCIA CORRAL

Thèse dirigée par **Clemens Winkelmann**
et codirigée par **Hervé Courtois**

préparée au sein du **Laboratoire Institut Néel, CNRS**
dans **l'École Doctorale de Physique**

Yu-Shiba-Rusinov states in superconductor-quantum dot transistors made by electromigration

Thèse soutenue publiquement le **16 Octobre 2020**
devant le jury composé de :

Franck Balestro
Directeur de recherche, CNRS Délégation Alpes, President
Richard Deblock
Directeur de recherche, University Paris-Sud, Rapporteur
Marcelo Goffman
Directeur de recherche, SPEC-CEA Saclay, Rapporteur
Pascal Simon
Professeur des Universités, University Paris-Sud, Examinateur
Romain Maurand
Cadre scientifique des EPIC, IRIG-CEA Grenoble, Examinateur
Hervé Courtois
Professeur, Université Grenoble-Alpes, Co-directeur de thèse
Clemens Winkelmann
Maître de Conférences, Grenoble INP, Directeur de thèse

Abstract

A magnetic impurity embedded in a superconductor (SC) can have a disruptive effect on superconductivity, locally reducing the pairing energy of Cooper pairs and leading to the generation of Yu-Shiba-Rusinov (YSR) sub-gap states around it. The antiferromagnetic exchange interaction between the spin at the impurity and the electrons at the medium favors a many-body configuration consisting on a Kondo-screening singlet, while superconducting correlations oppose to the formation of such screening cloud, leaving the impurity unscreened in a doublet state. The local ground state of the system (GS) is then determined by the complex interplay between both phenomena, giving rise to intriguing properties that have been subject of great interest over the last couple of decades.

Hybrid devices contacting individual quantum-dot (QD) structures to superconducting leads offer an ideal platform for the study of such competition, as QDs display a magnetic character for odd fermionic occupancies, conferred by the spin of the unpaired electron. In this thesis, we investigate the transport properties of metallic nanoparticles individually contacted to bare aluminum leads through tunnel barriers made by electromigration, backgated following a transistor structure. The combination of a strongly discretized density of states in the nanoparticles with the sharp gap present in superconducting aluminum allows to measure the YSR spectra, appearing in SC-QD-SC junctions displaying a large asymmetry in the tunnel coupling, with an unprecedented resolution. The response of these systems against gate voltage, external magnetic field and temperature has been characterized, identifying the transition point (QPT) from the singlet-GS phase to the doublet-GS phase. A striking upturn of the QPT gate position is revealed at low magnetic fields, stemming from the combined effect of the superconducting gap reduction and the Zeeman-splitting of the doublet state.

Resumé

Une impureté magnétique intégrée dans un supraconducteur (SC) peut avoir un effet perturbateur sur la supraconductivité, réduisant localement l'énergie d'appariement des paires de Cooper et conduisant à la génération d'états sous-gap Yu-Shiba-Rusinov (YSR) autour d'elle. L'interaction d'échange antiferromagnétique entre le spin à l'impureté et les électrons au milieu favorise une configuration de singulet d'écrantage Kondo, tandis que les corrélations supraconductrices s'opposent à la formation d'un nuage d'écrantage, laissant l'impureté non-écrantée à l'état de doublet. L'état fondamental local du système (GS) est ensuite déterminé par l'interaction complexe entre les deux phénomènes, donnant lieu à des propriétés intrigantes qui ont fait l'objet d'un grand intérêt au cours des deux dernières décennies.

Les dispositifs hybrides mettant en contact des structures à boîte quantique (QD) avec des bornes supraconductrices offrent une plateforme idéale pour l'étude d'une telle concurrence, car les QD également montre un caractère magnétique pour les occupations impaires, conférée par le spin de l'électron non apparié. Dans cette thèse, nous étudions les propriétés de transport des nanoparticules métalliques mis en contact individuellement avec des bornes d'aluminium nu à travers des barrières tunnel faites par électromigration, backgated en suivant une structure de transistor. La combinaison d'une densité d'états fortement discrétisée dans des nanoparticules avec le gap abrupte présent dans l'aluminium supraconducteur permet de mesurer les spectres YSR, apparaissant dans des jonctions SC-QD-SC affichant une grande asymétrie dans le couplage tunnel, avec une résolution sans précédent. La réponse de ces systèmes versus la tension de grille, le champ magnétique externe et la température a été caractérisée, identifiant le point de transition (QPT) dès la phase singulet-GS à la phase doublet-GS. Une reprise frappante de la position du QPT est révélée à des faibles champs magnétiques, résultant de l'effet combiné de la réduction du gap supraconducteur et de la séparation Zeeman de l'état du doublet.

Acknowledgments

When I first arrived to Grenoble to pursue my Master studies more than five years ago I had a single objective in mind: to carry out a PhD project. Why? Because I firmly believe that technological progress is the best chance and only way for humanity to thrive, because along my entire bachelor I always had the feeling of studying subjects fast and superficially or in-depth and lacking time for understanding them properly so a PhD would be the perfect opportunity to focus on a single and clear objective for the first time in my life. I wanted to see how far I could go and what is my full potential. In that sense, making new friends, visit new places or going through new experiences, have been secondary for me. The word is not ambition, but rather a self-experiment to test my limits in the working life, as it was my first contact with the real academic world and with a living-abroad experience. I wanted to see how far I could push myself and oh, boy! I figured it out pretty well. However, as the old saying goes, "extreme sides have never been good" and exploiting yourself up to the very edge of your energies and motivation can be rewarding in terms of productivity, but it can also become a double-edged sword that damages your personal life. Not following the usual format I want to shortly discuss such effect in this acknowledgment letter and express my gratitude to all of my friends and family who have remained there for me over these difficult years of my life. But before that, I want to thank the people directly involved in the progression and culmination of this work.

To begin with, I would like to start by acknowledging my advisors, Clemens Winkelmann and Hervé Courtois for choosing me as a PhD candidate four years ago, and for their guidance and advice ever after. Bountiful times, Clemens have come to my office to check the experimental data and analysis together with me. I still remember the day when he said "Alvaro, can you come back to the previous graph? Why is there a slight energy shift in that conductance resonance? Hmmmm, that is very strange". Or the day he suggested "What about considering a bias lever arm in the simulations?". Not only his large experience on the field but also his exceptional clinical eye were absolutely decisive for the success of our project. Clemens, while we have different personalities and diverging points of view in several aspects, that has not impeded me to admired your ability for understanding experimental data and give qualitative, or even quantitative, diagnoses rapidly, how fast you can change from one scientific topic to another and manage different projects simultaneously, and your ability for synthesizing information (which I totally lack). I also remembered that, numerous times, Hervé was coming into the lab in the afternoon to check on the other students and me, help us with our cryostats, measurements, and delineating the next step in the action plan, always with careful, polite and wise advices. Some of his phrases, like "Alvaro, life is a choice", will stay in my mind for the rest of my life. Clemens and Hervé, I know I have not been the easiest student to work with, and I can hardly imagine how much of your patience I required from the very first moment to the very last, but I believe that thanks to our reciprocal good intentions, hard work, and mutual understanding we manage to bring this thesis to fruition. I also appreciate a lot how much effort you put in helping me to give nice presentations and develop my speech, as well as introducing me to most of our visitors, despite my lack of political skills or touch when discussing about experiments (and despite having mistaken the University of Columbia by some University in Colombia, as awful as that can get). The barbecues and Christmas dinners at your places were great but, specially, I want to thank you for letting me attend to the summer school in "Les Houches" and for allowing me to participate in conferences at Grenoble, Ravello and, in particular, that conference in Lisbon I asked you for.

The accomplishment of our project would not have been possible without the exchange with our collaborator, Serge Florens. Besides having a profound knowledge both on the theory and experiments that surround this subject, his kind character makes extremely easy to talk with him. On several

occasions, I arrived to his door with list of articles I could not understand, and he always found a moment for replying my questions in detail. Furthermore, Serge was part of my thesis follow-up committee, which is an institution that require PhD students to make reports and presentations every year, taking away a non-negligible amount of time and being considered by many colleagues not particularly useful. In my case, however, those meetings turned out to be fundamental, as they stimulated discussions between Serge, my advisors and me, key for realizing the physical effects behind my main experimental results, and key for me to comprehend the bibliography and write this manuscript. Serge, at the end of my second year I had many doubts whether to continue or quit and, partly, it was you who gave me the motivation and courage necessary to endure and stay. Words fall short to express how grateful I am.

At this point, I would like to thank the jury members of my defense; Frank Balestro, Richard Deblock, Marcelo Goffman, Pascal Simon and Romain Maurand, for the care with which they read my manuscript and the fruitful dialogue we had after the presentation, which developed perfectly well in spite of the virtual format. I am also thankful to Katharina Franke and Denis Basko for all the helpful conversations we have been having along the last years, also of great help for understanding our experimental results.

At a more personal level, I want to thank all the permanent members of the QuNES group for their general support, specially Benjamin Sacépé for his advices ranging from experiments and scientific writing to maintaining in good shape the heater of his old house (in which I have been living during these years) and Hendrika Borsje-Hekking for bringing up non-science-related subjects during lunch that felt like a flush of fresh air.

In general, carrying out the novel experiments that appear in the PhD proposals is very challenging for recently graduated students, not only due to the intrinsic difficulty that exploring the unexplored carries along, but also because they involve handling equipments and applying techniques that are not teach or shown in bachelor's and master's programs at all. Before I came to Néel Institute, I had never stepped into a cleanroom and had only manipulated a cryogenic set-up once, let alone soldering wires and connectors or configuring measuring instruments. It was not easy, but it would have been much harder without all the hands I have been given by the technical departments of the laboratory. First of all, I need to state how much I appreciated the warm treat and administrative help that Florence Pois gives to all the students. Then, I want to thank Christophe Hoarau for showing me how to solder components so tiny that you can easily inhale them if you are not careful enough when looking at them in the palm of your hand, Christophe Guttin for spending two entire weeks with me setting a cryostat controller that accidentally broke, Guillaume Donnier-Valentin and Thibaut Gandit for advising me on how to use a thermometer as a molecule evaporator and providing us with the required materials. I am also grateful to Henri Rodenas for all the indium and the homemade Génépi, Guillaume Bres, Kévin Herbe and Johan Guilhot for the large quantities of helium I demanded and for installing a level meter in my cryostat, which saved me lots of nights waking up every two hours to check the cryostat status and rushes to the lab after midnight and on weekends and both. I am also thankful to Laurent del Rey, Julien Jarreau and Grigor Kapoujyan for showing me how to use safely metal drillers and cutters, design and create custom metal pieces and terminate them properly, Julien Michel and Patrick Belmain for all the help they provided me with computers, using the NAS, discussing the best way for synchronizing data, scripts and files among the different computers and for extending once and again my email account always with a smile, and the Nanofab team: Bruno Fernández, Latifa Abbassi, Gwénaëlle Julie, Simon Le-Denmat, Jean-François Motte and Thierry Crozes, for their hard work to make the cleanroom operational and for their closeness to the students, despite all the adversities. Finally, I want to point out that it will be forever stuck in my memory how Wolfgang Wernsdorfer stopped his work and come out of his office to help this PhD student on his first year stabilizing the cryostat with a working sample inside a cold Saturday evening in winter, and agreed on exchanging with us one of his last-generation Dewar vessels to reduce the helium consumption.

From my sight, I have always believed that the most efficient way for progress does not lie in the competition between people, but rather in the collaboration. On top of the intrinsic and extrinsic

difficulties signaled above being generally present for PhD students, laboratories are mysterious environments where there often are certain non-written rules and non-documented knowledge that is only through crashing on the wall (sometimes literally) that you end up obtaining, unless you are told by someone who has crashed on the wall before you. It is impossible to know beforehand things like the precise turning of a needle valve for a stable cryogenic operation, the presence of ground loops disturbing the measurements, the behavior of certain old instruments that only start working five minutes after turning them on or to which you need to plug the power supply cable at an specific angle, the characteristic pressures of a cryostat under operation and how different problems affect them,... Moreover, when fabricating micrometric/nanometric samples, that kind of unpleasant surprises show up continuously, and sometimes it is extremely difficult to diagnose a problem or identify a detrimental step as we are unable to see what is going on during the processes and we rely on characterization tools that only provide limited information. It is very frustrating to see that two samples you prepared in, what you think, is the same way behave differently. As we like to call them among my teammates, those evil "Lab-ghosts" show up continuously, becoming totally necessary that students working with similar samples or setups cover each others' back by exposing it to the others every time they come across one of them. That is the reason why I became part and then leaded the organization committee of the Non-permanent seminars, to promote communication between students and fight against those destructive ghosts! That is also the reason for all the effort I put into organizing a common data base in our group where both the standard information like manuals, scripts, data, logbooks, as well as such crashing-into-a-wall knowledge can be stored and is easy to find for new students, so that they can progress faster. In my personal fight for my project to prosper, I am totally grateful towards David van Zanten, who not only taught me everything I know about nanofabrication, but whose devotion for work and science has been a great source of inspiration since I arrived, and whose advices on how to dodge specific lab-ghosts have kept me away from a lot of struggle. I also want to thank other previous students in my group, Alessandro de Cecco and Bivas Dutta for assisting me when I asked them and for letting me help them when I could. In addition, I appreciate deeply all the wonderful students that have joined our group after me. On one hand, I am thankful to Louis Veyrat and Corentin Deprez for all the pause-cafés, soirées and apéros, for sharing all their scientific experience with me, and for being always ready to give a hand out of the lab. Particularly, I want to thank Corentin for taking over the Non-Permanent seminars organization after I left, for keeping it up and doing such a great job! On the other hand, I am thankful towards Danial Majidi, Efe Gumus, David Wander and Rini Ganguly, who always listened patiently to my endless list of advices, helping me to reaffirm concepts in my mind. In fact, I have also learned a lot from them, for example, Danial taught me how powerful the ability of staying calm and remaining polite can be, Efe has taught me how important it is to start the day with a smile and saying good morning first, no matter what, Rini has taught me that if you cannot reach what you need, you look for a ladder, and David has taught me that I put way too much chorizo whenever I cook traditional Spanish dishes. I wish you the best of the lucks buddies, and thanks for all the cake!

However, the good companies did not stop within my group! Two key people were responsible in the first place that I choose Grenoble to pursue my studies: my fellow traveler, Roberto Riesco, who was studying physics with me at Madrid and embarked with me in the adventure of coming to Grenoble to follow the nanoscience master and hunt a PhD, and our counselor, Jorge Nacenta, who was also studying with us in Madrid but came here a few years earlier and guided us through the labyrinthine French administration, the fancy laboratories and the sweetest spots of the city. I can remember Roberto shouting at me in the middle of the supermarket because I was obsessed with putting into the cart all sorts of French items, while we did not even have a bottle of water in our cheap rooms. Thanks to Roberto, I managed to survive over the first year. I also wish just the best for him, as he moved away to pursue the PhD dream after the master course. Nevertheless Jorge, or as I like to call him, "El Patrón" (because whenever we go skiing he is not flexible or complaisant at all with noobies) remained in the city. All the problems Jorge and I have gone through supporting each other, all the amazing plans we have arranged together, and all the mutual trust and respect we

have develop for each other have turned him into one of the five fingers of my right hand and I am deeply grateful towards him, to the very bottom. And whereas he wanted to abandon me in Zaragoza during a road trip back to Madrid, quarantines cannot stop him from bringing a cake to his friends on their birthday.

I can say I have got lucky for all the beautiful flatmates that already were or have come to 25 Rue de Turenne and shared such amusing livings with this huge mess I am. Johanna, being one of the loveliest people I have ever met, have opened up my mind in so many ways, from cooking to painting, from having a more respectful life with the environment to making honey-wine and apfelmus, from drinking boxes and boxes of Bavarian beer to growing strawberries and fixing bikes, that I thought I was loosing grab. Against every chance, you managed to turn the tiger into a human being again and I cannot contain enough thankyous inside to be evens with you for that. Differently, basic but indispensable cleaning lessons were provided to me by Ana and Dani, as well as dinner ready on the table waiting for me on so many of those nights I stayed late at the lab. They cared for me so much that I still get receiving food from them even though we no longer live together, and also a cake on my birthday during quarantine! While most of the people just take, they have always been giving to me to the point that feels like I have family in Grenoble. Thank you. Now talking about Julien, together with him we transform the concept of bothering our annoying neighbors to its maximum expression. While most of the times I could not make it to our early breakfast meetings at the balcony, the moments and conversations with you while feeling the cold breeze of the grenoblaise morning while watching the sun coming up in between the mountains of Belledone are priceless. Thanks for all the respect you have always shown and inculcated on me. And last but not at all least, Jun Liang (or Ángel for friends), is one of the few people that have made my ethical foundations and scientific knowledge to tremble when discussing, as well as my knees when trying to dance at his speed in bars. Lots of friendships go to trash after living together for a few months, specially over pandemic confinements, but with you that is only growing up. How is it possible that we have gone through collapsing dishwashers, wildfires in the balcony, moth infestations, mosquitoes infestations, génépis infestations, colocataires crisis, parties that have almost destroyed our house, and I cannot find a single complain in my head about you?! I am starting to understand why you have the Spanish name you have... My thanks have been skyrocketing to the sky ever since you came in, and still you supported me so much over the quarantine period that I truly believe I would not have been able to hand in the thesis manuscript on time without you. What else can I say but thank you and that I hope you know you have me here for anything you need.

And yet the good companies did not end up there! In Grenoble, I have had the chance to meet magnificent people from many different countries that have enriched me at a personal level. I want to start by thanking the friends I did in the master's year, Juliette, Marianne, Tonatiuh, Laura and Maria for those all the messy meals we had together at the dirty kitchens of our student residences. That is what I call an ideal way of starting living abroad! Now coming back to the lab, I am completely grateful to all the respectful members of "Los Pastiseros": Joachim, Simone, Maria, Francesco, Thanasis, Stefano, Hugo, Saint Roberto and Kimon, who always had a fresh glass of pastis waiting for me at Shakesbeer on Friday night, even those Fridays I never arrived because I stayed at the lab until late. Chili-thai flavored tacos never tasted better than they did with you guys! Together, we have adventured into the darkest and wildest corners of the city and come out of there alive, holding all our belongings and having enjoyed as only the best enfants de la patrie know! Some other extraordinary people I met at Néel Institute answer by the name of Inna, Everton, Javier, Luca, Michael, Martin, Alessandro F., David N. and Katee, some of them having become experts in Spanish food at my place, some others the soul of our parties either by winning the best costume price with a full-body pijama, preparing a ton of caipiroskas or dancing even while policemen were at the door! Turning to people I meet outside the lab and even if I do not like it, while my parties were awesome those ones launched by Tomás at his apartment (where Jorge also happened to live in) always surpassed them, lightened up by the Spanish crew: Jaione, Xenia, Marila, Raquel, Ana, Maddi, Javi, Isa, Rob, Arianna, Andrea, Jorge, Vanni and Tomás. I am very thankful to all of you for accepting me so fast

and without a single prejudice, for inviting me to your gatherings and for taking me out in your trips as one more, from skiing to pirate rural houses, from kayaking to chilling in the beach of the lake. Unfortunately, such an amazing group has being dissolving soon after I arrived, as people finished their PhD and left Grenoble. But at least I got the chance of drawing ugly puppets and writing down stupid rap songs in all your congratulating picture books. I largely thank you for that, but I know you also thank me largely for this! Now the Spanish band is still alive, as new potential members have been arriving to Grenoble and asking for a place. I am talking about Bea, who, for everyone's surprise, always have more things to complain about even than me and I thank you because you always made me feel better, Jesús, who displays very similar mental "properties" as me and I thank him because it feels like having a brother in Grenoble, Gonzalo and Miren, who are always up for anything, as their company is great, and I am thankful that they count on me, and finally Sara, who was the only person worried about my bleeding right hand a night just before my writing period and healed it, keeping me away from failure at first, and same at second, by pushing me out of my house when my head needed a break. These last years would not have been the same without all of you, and I want to say thanks for being there over such difficult covid times. To finish with, many other people from different laboratories and places I have met during the five years I have spent in Grenoble, but among them I want to mention the delightful guys that inhabit LiPhy, specially my trainers, Laila and Georges, together with Luiza, Saranath, Nilankur and Eric, because there are people that c'est pas la peine but them, they very much do. And I cannot forget about, Paco and Beñat, who I met in the summer school, and their extremely atypical and critical points of view makes them pop out of standards into the weirdest but healthiest side of life. I want to thank them for accepting me as a limited experimentalist mind, for the surrealistic trips we have done so far, and for the many others yet to come!

In sight of such a long acknowledgment letter and opposite to what I wrote at the very beginning, it may look as if social life was my first priority but, sadly enough, that is far from being true. While every single little piece of free time I had I tried to use it for socializing, I have been continuously canceling plans and meetings with all of the friends above. It is just because they are such great people that they have had patience, and kept on insisting, and did not give up on me. As you can see, I do have a lot to say thanks for. The actual truth is that, as it often happens over the course of a PhD project, almost everyday new "challenges" arose, some of them easy to resolve, some others taking a lot more of time than expected to get solved, and some other simply unsolvable. At some point, the amount of goals and setbacks one has to reach and fix can grow to a completely absurd volume, and one can easily fall in the trap of just following certain tracks because they are working correctly or constitute problems easily solvable, and let aside other ones which involve an unknown amount of side research and effort. My approach was to create a list of priorities that finds the balance between the important things and the urgent ones, allowing to draw a relevant schedule, that I put under revision every time I came across a new difficulty or a solution did not work out. From my opinion, all options should be tested, so that the problem's origin is understood and proved under control, but it is a risky approach, since you generally ignore even the order of magnitude of the time it will take you when you start working on the solution of a particular obstacle. From my opinion, all options should be tested, so that the problem's origin is understood and proved under control, which, for me, was only achievable by adopting an ant-like sight of the world, detaching from the big picture, fragmenting the obstacle into multiple small tasks and, little by little, carrying out every single one of them. This process can be very hard to carry out at a personal level, as it requires a total devotion (including the consequent isolation for focusing properly) with zero guarantees of success and can lead to a feeling of stagnancy. Furthermore, it can lead to completely stopping all leisure activities, neglecting the concept of free-time. I started following up this approach after the first year, and only when I was feeling completely unable to work, I was using my time to hang out with my friends. The issue here is that you stop having time to spend alone with yourself (for reading, drawing, playing music, doing sports, watching TV or simply sleeping) and I discovered by the end of my third year that, at least for me, such self-time is absolutely necessary to settle concepts, consolidate ideas, and,

in general, get a clear mind that allows you to advance more efficiently whenever you get your hands back to work. I completely underestimated the value of those activities, besides work and friends, which you do alone and which many people call "lazy activities". After some time my body and mind slowed down, I was not able to think clearly anymore, I was like a zombie, both at the lab and with my friends. A floor lamp would have contributed more to conversations going on around me than I did. The only thing my head was able to think about was the small fragment of the particular problem I was trying to solve that week. In such state, one can easily loose the direction, the right path to follow is not evident anymore and doubts start arising, but you don't have time to answer them because you are busy solving fragments of problems, and the little resting time you have, you spend it with friends. At such point, it usually happens that those doubts start keeping you from sleeping over night. Then, life becomes a spiral that unavoidably brings you, sooner or later, to one of those famous breakdowns, where you cannot get up from bed anymore. I got a couple of those during my fourth year, one after finishing my article, and the other after finishing this manuscript, but over the entire second and third year I manage to stay put and keep up with the work. Partly, this was thanks to the small kitchen-garden I planted in the balcony of my house and the compost bit I set at the basement of my house. The insatiable thirst of all those tomatoes, peppers, zucchinis, potatoes, strawberries, roses and different kinds of spice plants gave me the only reason I could find to get up when I woke up (for watering them), and from that, I could start the day. Soon after springs, the kitchen-gardens turned into an outlandish forest, providing me a spot where I could relax my mind in the summer nights. It was at such critical moment that I started conversing with a magical beautiful "kat" of great mystery, who continuously reminded me that life can be a wonderland and the future is just there waiting, giving me reasons to go to sleep irresponsibly fearless. I saved a very special space in this acknowledgment letter to thank both of them, as I know very well that, without them, I would not have been able to maintain my obstinacy and pigheadedness writing scripts for data analysis and interfacing instruments, testing measurement routines and reading related-articles until the waking-up alarm of my flatmate started ringing in the other room, and ultimately allowing me to hand this manuscript right under the wire.

During those two central years of my PhD I gradually disappeared from my social life, completely vanishing during the fourth one. Over that time, I received very often text messages from my family and friends, both in Spain and France, which I was not able to reply before one or two or more weeks, if ever, and my replies where often short and insubstantial, as my mind was a total chaos. On top of that, most of my people in Spain I was only seeing once or twice per year, when coming back home for holidays, and still, I was canceling plans because I needed to work. There have been opportunities that I missed and will never come back. I know it has not been easy and I want to apologize for not having been smart enough to find time for you, and I want to let you know that, whatever comes up next in my life, I am going to make sure that it gives me enough free time for you, and for myself, so that I never arrive to that extenuation point again. This is my priority now. And despite the facts, most of my family and friends have remained there for me all these years, answering me immediately when I called them, and seeing me when I could, and for that I deeply thank you.

First of all, I want to thank the boys and girls I grew up with, my brothers and sisters, Adri, Alex, Isma, Andrea F., Andrea R., Jorge, Juan, Anabel, David, Eduardo P., Eduardo F. Carlos R., Ezekiel and Pablo Q. While there are things I will never understand about you, there are others that I understand very well, and one of those is that you are responsible of me having a place that I call home. People appreciate conversations discussing different opinions on international and national news, history, politics, science,... but I believe whoever says so, does it because have never experienced the extraordinary and unusual ability of joking forever, which we acquire every time we get together. You have shaped my core and have always been the first people to call me and force me out of my house whenever I came back for holidays.

Among all the people I met in my school, two bright and brilliant souls have stayed with me all the way long: Cristian and Carlos S. There are friendships that last the whole life and you two are the living proof of that. All that mocking around in school, those microcar adventures, crazy macroparties

either on top of a mountain, in Beverly-Hills-like chalets or in a disco-boat, all-payed dinners at some of the fanciest restaurants of the country in San Sebastián then running under the rain the morning after from one pharmacy to another, magic tricks in Madrid's underground, all that stuff speak on its own. Elisa and Jennifer are also in this pack as they always find new ways of surprising me and keeping it wild. I am talking about trips to the mountains where we surf the snow the whole day and party the whole night. I am talking about so many unique experiences, from flooded clubs to epic mañaneos that lasted for the entire day. Party has evolved but it has never stopped! And while time has past, and there has been long periods without seeing you, every time we meet it feels like nothing has ever changed between us. That is why you are the people I want to keep for the rest of my life.

They say that hard times bring people together, and I have never felt as close to anyone as to the fine people I met during the Physics bachelor at the Autonomous University of Madrid: Gonzalo, Borja, Juan, Alberto C. and Alvaro (who managed to escape from that horrible place after the first year). Together, we fight like warriors, we supported each other as brothers in arms, we went through the bad times together, and we celebrated together the good ones as if it was the last day of the world. First with Juan, I learned how to cook love tortillas for señoritas and how to survive by myself and without getting eaten alive by the fluffs under my bed. And then with all of you, plus Alberto J., Jaime and Gabriel, I learned how to drink more than 20 shots in a single night, that the legendary Yeti lives in the science faculty and that to sacrificing our last water bottle to use it for capturing grasshoppers cannot be more worth it. I learned that taxi drivers in Barcelona drive better than plane pilots, that Japanese people die for a well-cooked gin tonic and that you can also find after-hours in the farthest village of Castilla y León. I learned to make water vortex in a pot, to run "encierros" without being caught by the bulls and that leaving the plastic on the meat increase the flavor of barbecues. But more important than anything else, I learned that I can be less clever than I could ever possibly imagined, and that it is not a big deal. And all these many things I learned the best way: not by talking about it but by living through it! Those years I spent in the campus changed me forever and made me who I am today, thanks to all this knowledge, I have managed to keep my determination during the PhD. And I have still been learning over the few times we met, for example, that Extremoduro don't like we record their concerts with a cell phone or that wearing cowboy hats tune people into precisely the same vibe. It is a pleasure to meet you now and see how we have evolved and how far we have arrived. Thanks for all that and, specially, thanks to Gonzalo for assisting me during so many days with Kondo physics when I was writing this manuscript and Borja for always organizing such amazing plans and booking trendy restaurants much before I took the plane back. Each day of my life I have very present that I literally own you my life (or, at least, my right arm).

The last paragraph goes for my family, starting with my aunts and uncles, Maria, Pedro, Pepe, Rosa, Justina and Piedad, because they keep on sending me food by ordinary mail without ever asking for anything in return. I want to name here my little cousins, Cristian, Sara, Félix, Alba and Alejandro, who make me to irredeemably smile every time I meet them, and my great cousin Pilar, who cares for her family so hard that hurts and who is the only person of my family that is able to hang out with my friends. The last and most special comment is for thanking my parents, Esperanza and Pedro. I have no clue how you do what you do, how you have gone through all you have gone through and still having such impeccable mindset, pure feelings, being such good people, and yet, being able to bear with me. Your combination is and have always been the model that I aspire to be like. All my thesis is dedicated to you, for your livelong support and your wiseful advices that I never listen.

Contents

Introduction

Superconductivity is a long-studied, yet fascinating phenomenon in which electrons of opposite momenta and spin experience an attractive interaction that couples them by pairs, called Cooper pairs (CPs), forming a bosonic condensate that embodies a collective quantum state of macroscopic extension. In a superconductor (SC), CPs generate dissipationless currents, known as supercurrents, which can transport electrical charges across the entire superconducting (SC) object without energy losses, regardless of its size. Leaving aside the practical interests that the avoidance of power losses induced by Joule heating arise, extremely interesting behaviors emerge in mesoscopic circuits that combine superconductivity with other quantum effects, like energy discretization, spin degeneracy, etc. Moreover, it is possible to take advantage of superconductivity to improve the operation of specific non-SC devices, and even to obtain unique comportments that would not be achievable without it. In this sense, we can make up a classification of such hybrid devices, depending on the particular role that superconductivity plays in them and its link to the actual research objective:

- **Electronic transport in presence of superconductivity**: Consisting of devices made of SC materials that are used to study the fundamental effect that the pairing interaction exerts on their conduction properties, as opposed to those observed for the normal (N) metallic state.
- **Employment of superconducting elements**: Certain devices include SC structures devoted to accomplish specific functionalities that benefit from particular aspects of superconductivity, using it as a tool for investigating a different physical phenomenon. For example, SC resonators of an increased quality factor, Josephson junctions used for thermometry/heating,...

In our work, we investigate the evolution of the transport features of tunnel junctions formed by contacting a quantum dot (QD) to bulk SC leads (typically displaying phenomena as Coulomb blockade and Kondo effect), as pairing correlations gain strength when the temperature is lowered or an external magnetic field is diminished. In particular, we focus on the study of junctions presenting large coupling asymmetries that enable for performing spectroscopies of emerging Yu-Shiba-Rusinov (YSR) bounded states. Additionally, SC-QD-SC junctions can behave as a single-electron pump if a fast oscillation is induced in the QD's chemical potential (μ_{QD}), taking advantage of the gapped density of states (DOS) in the SC leads. The transistor-like configuration of our SC-QD-SC devices also allowed us to observe and investigate such non-conventional mode of operation, altogether conferring to this project a hybrid character between the above categories, as elucidated in the following.

FROM ANDREEV BOUND STATES TO YU-SHIBA-RUSINOV STATES

The macroscopic model of superconductivity considers SCs as systems with an arbitrarily large number of electrons and a well-defined quantum phase φ. All CPs in a SC are described by a single wave function of the form $\Psi = \Psi_0\, e^{i\varphi}$, which does not collapse to zero at its physical boundary but displays an exponential decay that allows the CPs to penetrate into the surrounding non-SC medium over a certain length. This behavior, known as Holm-Meissner or proximity effect, is generic as it takes place regardless of the particular material of the non-SC medium (X), although its extension presents large differences that range from atomic distances in insulators, to several hundreds of microns in certain metals. In fact, proximity effect enables the exchange of CPs between separated SC objects, hence making possible to convey a supercurrent across the X material in between them, as described by Josephson equations for SC-X-SC junctions. The charge transport at each SC-X interface is microscopically described by Andreev reflections (ARs) that binds together electrons at the boundary, forming a CP that travels into the SC and scattering back a hole-like excitation into X. The AR

processes, responsible of the supercurrents established in Josephson junctions, entangle electron and hole states at the SC boundaries (for an insulating barrier) or at the separating medium (for a N-state metallic barrier), constituting the so-called Andreev bound states (ABS).

Conventionally, ABS are formally described as the constructive interferences of the SC wave functions of both SCs at the medium separating them. The SC-X-SC Josephson junction can be regarded as a Fabry-Pérot interferometer of CPs, resulting in the formation of a discrete set of ABS, their number and intensity depending on the thickness of X and the transparency of the interfaces. In contrast to standard Josephson junctions, where the separating material is an insulator or a metal, radically different behaviors appear when X is replaced by a nanometric structure, like a quantum dot (QD). On one hand, electrostatic effects, arising in such structures due to their small size, result in the discretization of electrical charge, fixing the number of electrons in them. As electrical charge and quantum phase are conjugate variables, this behavior constitutes the opposite quantum limit than that one taken to describe superconductivity. On the other hand, the development of ABS relies on the electron-hole symmetry present both in the DOS of the SCs and X, a condition that is not necessarily fulfilled by nanostructures small enough to display a non-negligible energy discretization, caused by quantum confinement. Then, how does proximity effect develop in these hybrid systems where a different kind of electronic correlations (stemming from Coulomb interactions) is already present? Under which conditions do the ABS form under the rupture of particle-hole symmetry? The answer lays in the relative magnitudes of the energy scales that characterize the system, namely, the charging energy, E_U, the level spacing, E_δ, the SC gap, Δ, and the tunnel couplings between the QD and each SC electrode, γ_L and γ_R. An extremely rich phenomenology arises from the combination and interplay of such diverse effects, which has been studied over the past 40 years in distinct experimental conceptions of SC-QD-SC junctions. Although these characteristic energies may change greatly from one sample to another (as several kinds of QD structures, SC materials and contacting techniques can be employed), the nature of the interactions giving rise to electronic correlations remains universal. Like this, the characterization of electronic transport in SC-QD-SC systems fabricated employing distinct materials or following different sample configurations has allowed to gradually map the evolution of conduction features and properties at various energy-scale hierarchies, unveiling how electrostatic and proximity effects combines at a microscopic level.

Early experiments employed SC leads to contact a metallic or SC island with a size of a few hundred nanometers. Such mesoscopic islands are generally too large to display a significant energy discretization, but small enough for a notable Coulomb repulsion to be present, characterized by E_U. In the absence of superconductivity, electrostatic interactions dominate the transport, restricting it to single-particle tunneling processes and giving rise, in equilibrium, to the emergence of discrete charge states that can impede the flow of current even at finite biasing voltages (the so-called Coulomb blockade effect). In the resulting ground state (GS), the island contains a well-defined number of electrons, which fixes the fermionic parity of the system depending on its occupancy (even or odd). Now, when turning the electrodes into SC state, proximization arises, typically characterized by the Josephson coupling scale, E_J (that depends on Δ and the tunnel resistances). While electrostatic effects oppose to tunneling processes involving more than one particle (at low energies), proximity effect favors the formation of ABS that enable the transmission of CPs through the device, establishing a supercurrent at zero-bias. The evident antagonism between these two phenomena define two separated transport regimes, and the specific conduction features of each sample depends only on the particular E_U/E_J ratio. This ratio can be modified by changing the island size, the SC materials employed and the transparency of the tunnel barriers, allowing to access a regime dominated by Coulomb blockade ($E_U/E_J >> 1$) or another in which the island is completely proximized ($E_U/E_J << 1$). Interestingly, theoretical predictions indicated that the proximity effect present in junctions owning a $E_U/E_J \sim 1-10$ ratio would strongly depend on the parity of the charge state conforming the GS of the system. Predictions could be corroborated by fabricating island junctions following a transistor geometry, as to include a gate electrode that allows to control the island's chemical potential, μ_{Isl}, via its capacitive coupling, changing the filling number of the island and, thus, the GS parity [59]. The

switching current emerging in superconducting single-electron transistors at such intermediate regime showed a periodic structure, repeating every time the number of electrons in the island is changed by either 1 or 2 (depending on the temperature), and ranging from a maximum value along the gate range corresponding to odd occupations to a minimum value along the gate range corresponding to even ones [129, 130, 9]. The interplay between electrostatic and proximity effects was shown to influence the formation of the ABS for different values of μ_{Isl}, generating gate-dependent Josephson supercurrents that emerge at subgap energies, bypassing Coulomb blockade.

Novel transport features and properties emerge if the nanoisland is replaced by a QD, owning a DOS that consists in a discrete set of electronic states, analogous to molecular orbitals. These QD orbitals play a fundamental role in determining the transport properties of the SC-QD-SC junction, since the ABS can only develop at specific energies. Proximity effect is no longer defined in terms of E_J, but according to the specific tunnel couplings γ_L and γ_R of each QD level to the SC leads. The large on-dot Coulomb repulsion and level spacing achieved by employing colloidal QDs (like metallic nanoparticles or molecules of a few nanometers in diameter), together with the relatively weak couplings that usual contacting techniques provide, contribute to canceling out higher-order processes, as well as proximity effect. The resulting conduction is dominated by Coulomb blockade, fairly resembling measurements for the normal state of the leads but displaying distinct features corresponding to the gapped quasiparticle DOS characteristic of SCs [1, 3]. In contrast, small charging energies and level spacings, and large couplings can be obtained in junctions contacting larger QD objects, like carbon nanotubes (CNTs) or nanowires (NWs). In these junctions the proximization of the nanostructure is promoted, enabling for the establishment of gate-dependent Josephson supercurrents through the device at zero bias [6] (similarly to nanoisland-based junctions) and also at specific energies due to multiple ARs through the QD levels [11, 7, 8]. Even more intriguing behaviors arise in SC-QD-SC junctions at intermediate coupling regimes, in which Kondo effect also comes into play. This phenomenon manifests exclusively at odd charge states, originated by the antiferromagnetic exchange interaction exerted between the spin of the unpaired electron at the QD and the conduction electrons at the leads. The resulting spin correlations arise in the normal state, being characterized by the Kondo energy, $k_B T_K$ (which, in turn, depends on μ_{QD}, E_U and γ). While promoting higher order effects, this interaction favors an electronic order distinct from the SC pairing at the dot and locally at the leads. A complex competition is then established between Kondo effect and superconductivity, giving rise to two possible electronic configurations of different nature: magnetic (singlet) or superconducting (doublet), which can be adopted by the SC-QD-SC system as its GS and excited state (ES), depending on the governing phenomenon. If they both have a similar strength, the ES appears at low energies, laying within the SC gap and allowing for the transmission of CPs, constituting an ABS of magnetic origin and specific properties called Yu-Shiba-Rusinov (YSR) state [10]. A quantum phase transition (QPT), where the GS and the ES of the system undergo an inversion, can be experimentally realized by subjecting the system to external parameters that change the relevant energy scales, for example, with a gate voltage [5, 12, 13, 14, 15]. Surprising behaviors predicted to emerge from this interplay, like the inversion of the supercurrent direction at the QPT, have been experimentally observed in pioneering experiments [16, 17, 18, 19, 20].

SPECTROSCOPY OF YU-SHIBA-RUSINOV STATES

The local competition between the SC pairing and Kondo correlations originated by a magnetic impurity (in other words, an oddly-occupied QD) has been the subject of intense research in the last decade. This interest stems from the prediction of Majorana physics arising in proximized mesoscopic structures exhibiting a spin texture varying in space, as NWs owning a large spin-orbit coupling [21], or nanometric islands integrated by magnetic molecules/adatoms [22]. Special attention has been given to junctions consisting of a QD coupled to a single SC lead in such Kondo regime, as they constitute the elementary brick of the more complex Majorana systems, and their study can provide a direct insight on the fundamental properties arising from this interplay.

Opposite to symmetrically coupled SC-QD-SC junctions (where simultaneous correlations extending

between the dot and both leads determine the transport), a large asymmetry in the coupling can make both the Kondo and SC correlations to vanish at the weakly coupled lead, therefore acting as an spectroscopic probe that can measure the spectral features of the correlated SC-QD system at the other side of the junction. In this way, the local electronic DOS of SC-QD systems have been measured in several experiments by implementing a weakly coupled electrode in SC-QD-SC junctions based on CNTs [23, 24, 25, 26], NWs [27, 28, 29, 30] and self-assembled nanocrystals [31], as well as its dependence on μ_{QD} for a transistor geometry. An equivalent asymmetric disposition can be achieved with scanning tunneling microscopes (STMs) [32, 10], proving to be an excellent platform for the study of this interplay thanks to its spatial resolution [33] and the possibility of tuning the couplings of the system [34, 35]. Different phenomenologies have been observed in both experimental approaches (solid state devices and STM) due to the distinct hierarchies of energy scales that characterize the particular SC-QD system. In relevance, electromigration junctions (EMJs), which provide a valid platform for contacting small QDs (like molecules or nanoparticles), can also be made of SC materials. The resulting SC-QD-SC junctions obtained by electromigration are generally characterized by relatively large values of E_U and E_δ (similarly to the molecules studied by STM), while including a gate electrode (as usual in mesoscopic devices), constituting a bridge between these two communities.

Scarce experimental works showing YSR physics measured in electromigration transistors can be found in the literature [39, 36], firstly because of the stochasticity of the contacting procedure, and also due to the experimental difficulties generally involved when working with SC materials: fast oxidation rates and reduced malleabilities (detrimental for the electromigration process). While these studies employed proximized gold EMJs, which inevitably broadens the SC-DOS, spectroscopies measured in the state-of-the-art EMJs developed at Institut Néel reproduce the BCS lineshape faithfully, with an abrupt energy gap and keen coherence peaks, as they are entirely made of aluminum [37]. For this, customized filtering systems have been installed along the electrical lines of our dilution cryogenic setups, allowing to perform electromigration in-situ at a temperature of 4 K and avoiding the oxidation of the pristine aluminum contacts. The SC-QD-SC junctions obtained by employing metallic nanoparticles display a marked hierarchy of well-separated energy scales, such that $E_U \gg E_\delta \gg \Delta$. As the temperature is reduced below these characteristic energies, thermal broadening is avoided, and hybridization becomes the main limitation to the spectroscopic resolution [38]. Moreover, the divergence of the SC-DOS at the coherence peaks contributes to sharpening conductance features, constituting an ideal system to perform precise electronic spectroscopies. During my work, I have electromigrated several hundreds of constrictions, observing the predominance of either extremely weak or intermediate coupling regimes. A few of these samples displayed a sufficiently large coupling asymmetry to exhibit a YSR spectrum, being probed at an exceptionally high resolution. The conduction of these samples was characterized both for the N and SC state of the leads, allowing for a detailed analysis of both the Kondo and the YSR resonances, and their evolution when subjecting the system to external magnetic fields (B) and at different temperatures. While similar studies have been previously done in CNT-based [40] and NW-based [41, 42] junctions, a previously unnoticed displacement of the QPT gate position, V_G^{QPT}, at low B fields was observed in our experiments. The feasibility of using external B fields as an experimental knob allowing to traverse the QPT has already been reported in SQUID-arranged devices, tuning the SC phase across the SC-QD-SC junction [43]. However, the SC phase is unaffected in our system (in the absence of a SC loop), and the upturn delineated by V_G^{QPT} when increasing B is rather attributed to the interplay between the Zeeman splitting of the doublet state and the suppression of the SC gap [44], constituting a novel behavior that demonstrates the feasibility of tuning a SC-QD system across the QPT with an external B field.

TURNSTILE OPERATION OF THE SC-QD-SC TRANSISTOR

In a separate research line, a vast amount of experimental activity has been devoted to conceive devices where the flow of current can be controlled down to the single electron level. Common to all of them is the concept of confining electrons individually in a system that can be operated with an AC

voltage signal oscillating at a high frequency, f (typically in the radiofrequency, RF, regime) ideally sustaining a "single-electron turnstile" current at a precise value of ef. A great variety of mesoscopic systems have been engineered for performing such charge pumping experiments, (metallic arrays of tunnel junctions, 2-dimensional electron gases and MOSFET devices), some of them largely tested and optimized, reaching accuracies with a deviation smaller than 1.0×10^{-6} [45].

A decade ago, it was demonstrated that a SC junction contacting a nanoisland can also be operated as a single-electron pump, by driving μ_{Isl} with an RF signal applied to the gate electrode [46, 47]. Such system takes advantage of the gapped SC-DOS (that suppresses resonant tunneling of electrons at low bias), which is overcome electron-by-electron when the oscillating signal is turned on. Furthermore, our group has demonstrated that SC-QD-SC transistors made by electromigration also display turnstile behaviors, when operated in the same way [48]. Following this direction, the main technical aspects of my work, in terms of sample fabrication and adaptation of the measurement setup, were devoted to improve the accuracy of charge pumping experiments. Unfortunately, while turnstile behaviors were observed in several devices, a complete characterization could never be done due to experimental problems of diverse character. However, a summary of the working principle and several turnstile experiments are presented at the end of this manuscript, showing remarkable improvements in the frequency range of operation with respect to previous experiments.

OUTLINE

- **Chapter 1**: As the tunnel barriers between the QD and the leads are arbitrarily fixed during electromigration, it is of paramount importance to understand the main transport processes taking place at the different coupling regimes, allowing to recognize and classify each device, and perform an adequate analysis for the extraction of the physical parameters. Therefore, we start with an extended discussion summarizing the state of the art on electronic transport in QD junctions at different coupling regimes, both for the N and the SC state of the leads.
- **Chapter 2**: The fabrication procedure of the electromigration constrictions, gated with a waveguide electrode designed to improve the frequency range of the turnstile operation, is described in detail. An statistical analysis of electromigration, as well as a description of the different QD deposition methods employed and their optimization are also provided here.
- **Chapter 3**: In this chapter, we introduce our cryogenic transport setups. While the samples studied in the main text were measured in cryostat B (owning a coil for the application of external B-fields), we illustrate here the installation of RF lines and the in-situ molecule evaporator unit in cryostat A (employed for the charge pumping experiments), together with the implementation of home-made bias-tee elements in the sample-holders for coupling DC and RF signals at the gate electrode of the samples.
- **Chapter 4**: This chapter collects all the measurements performed with a static gate voltage (acquired in cryostat B). While SC-QD-SC transistors in a weak coupling regime are briefly discussed, the main focus of the chapter lays in the analysis of the Kondo and YSR spectra observed in asymmetrically-coupled samples. Leaning on the theoretical discussion given in chapter 1, the extraction of the energy scales from the measurements is explained in detail, together with the characterization and analysis of their B-field and temperature dependence.

1 Electronic transport in quantum-dot junctions

The electronic transport of mesoscopic and nanometric devices combining different quantum phenomena strongly depends on the relative values of the typical energy scales characterizing them, becoming apparent if the temperature is low enough. Depending on the coupling, Coulomb Blockade and Kondo constitute the main effects determining the electronic transport processes in systems composed by a quantum dot contacted to bulk metallic electrodes through tunneling barriers.
Additional electronic correlations arise for the superconducting state of the contacting leads, greatly modifying the conduction features and properties of the quantum-dot junction. For relatively weak couplings, the large charging energy suppresses the tunneling of Cooper pairs, restricting the transport to single-electron processes and leading to a sequential current that replicates the lineshape of the quasiparticle density of states in the superconductors. For stronger couplings, two microscopic states of different nature arise locally at the quantum dot site, stemming from the competition between Kondo effect and superconductivity, reflected in the conduction of the junction by the emergence of Yu-Shiba-Rusinov sub-gap states.

Contents

1.1 Introduction to electronic transport in quantum dots

The behavior of metals and semiconductors has been historically described from the perspective of the Fermi liquid theory, in which the Coulomb interactions between electrons are neglected and the ions integrating the solid are replaced by a periodic potential that mimics the crystalline lattice [49]. Although these approximations may result oversimplified in specific cases, the simplicity of the free-electron model, and its quantitative agreement with many experimental results, makes common its use to describe the transport through macroscopic conductors, according to Ohm's law. However, when decreasing the size of conducting elements down to the micrometer/nanometer scale, deviations from Ohm's law start appearing, as quantum effects (like energy discretization, exchange interaction, quantum tunneling...) start emerging and dominating the electronic transport. We start this section with a short remainder of the free-electron gas model, generally employed to describe the bulk electrodes and contacting leads of nanodevices (1.1.1). After that, we comment on general modifications of this model that are required to broadly explain how the transport of electrons takes place in mesoscopic devices (1.1.2). Then, we present the concept of a quantum dot, explaining the role that Coulomb repulsion plays in devices contacting such a nanostructure, and enumerate the energy scales that determine their transport features (1.1.3). We finish the section by introducing the second-quantization formalism commonly employed to describe the transport through tunnel junctions (1.1.4).

1.1.1 The free-electron gas model

To measure the electronic transport through extremely small devices, these are commonly contacted by bulk-like metallic electrodes/leads, called reservoirs, which are soldered to macroscopic wires connecting the device with the measuring instruments. Reservoirs are considered to be in thermodynamic equilibrium and well described by the free-electron model: electrons behave as particles that propagate freely through the solid (known as quasiparticles[1] or quasielectrons, referred to as electrons along this manuscript for simplification purposes) with a certain effective mass m^*, and a wavefunction in the form of a plane wave modulated by a Bloch function. The shape of the unit cell restricts the values of allowed wave numbers k, resulting in a band structure that associates the electron energies E, with the momenta $p = \hbar k$ imposed by the crystalline lattice. A electronic density of states per unit energy and volume (DOS, represented here by D) can be derived:

$$D(E) = \frac{1}{\pi^2 \hbar^3} \sqrt{2m^{*3}E}. \tag{1.1.1}$$

Here, E_F is the Fermi energy, and the origin of energies is taken at the bottom of the conduction band E_B (Fig. 1.1a), defining the conduction's half-bandwidth as $W = E_F - E_B$. The occupation

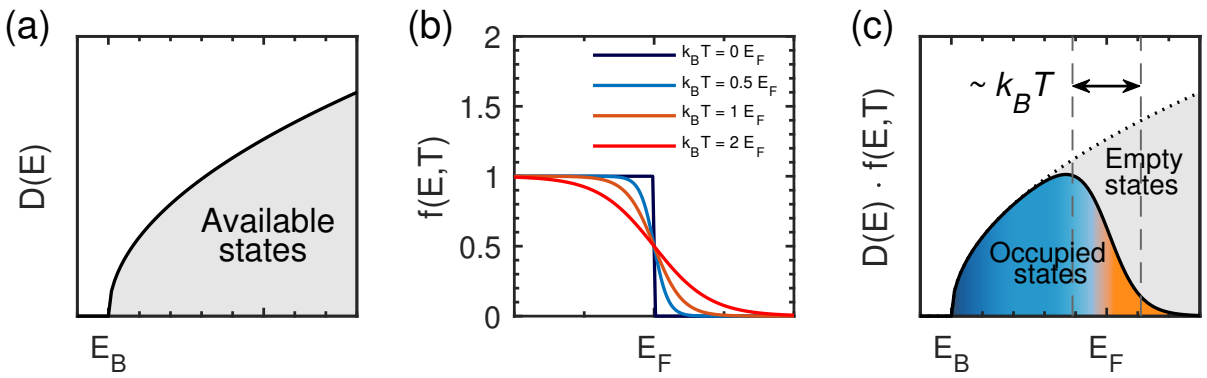

Fig. 1.1: (a) Density of states per unit energy and volume as a function of energy in the free-electron gas model. (b) Fermi-Dirac distribution, plotted for different temperatures. (c) Electronic occupation as a function of energy, at a temperature of $k_B T = 0.1 E_F$. A finite temperature induces a smearing around E_F over an energy range $\approx 4 k_B T$

[1] Quasiparticles can be seen as electrons surrounded by a positively charged cloud.

probability of a state of certain E is given by the Fermi-Dirac distribution, which accounts for the fermionic nature of electrons, imposing Pauli's principle, so that two of these particles cannot occupy the same state, or equivalently, cannot have the same quantum numbers (spin degeneracy is already included in Eq. 1.1.1):

$$f(E) = \frac{1}{1 + e^{(E-E_F)/k_B T}}, \tag{1.1.2}$$

where T is the temperature of the system and k_B is the Boltzmann's constant. The temperature dependence of f (depicted in Fig. 1.1b) implies that the ground state is only reached at $T = 0$, while at $T \neq 0$ thermal excitations can lift electrons to energies above E_F, resulting in a smearing of the distribution on the order of $k_B T$ (Fig. 1.1c). In this way, the distribution on energies of the electronic population is given by $D(E) \cdot f(E,T)$ and the total number of particles in the system can be obtained by integrating the whole expression as $\int D(E) \cdot f(E,T)\ dE$.

1.1.2 Electron confinement in mesoscopic systems

The electrical resistance of macroscopic objects is determined by scattering events (typically with crystalline defects, phonons and localized impurities) that change the microscopic state of the colliding electron. The average distance that electrons can travel without altering its quantum state is called, on the whole, the mean free path. In fact, different mean free paths can be defined attending to the conservation of a certain quantum property (energy, momentum, phase,...) as distinct types of scattering may change only some of them. The overall resistance of a macroscopic system is dictated by the mean free path over which the electron's momentum is conserved, following Ohm's law.

Mesoscopic devices are electronic circuits integrated by structures of sizes small enough ($L \lesssim 1000$ nm) for electrons to conserve their momentum when traversing them, where transport is ballistic, and Ohm's law does not hold anymore. Quantum confinement effects may appear for further size reduction in, at least, one dimension ($d = x, y, z$), transforming the electrons' wave functions into stationary waves along the confining direction, with discretized wave numbers and energies:

$$k_d = n_d \frac{\pi}{L_d}, \tag{1.1.3}$$

$$E_d = \frac{(\hbar k_d)^2}{2m^*} = \frac{\hbar^2 \pi^2}{2m^*} \left(\frac{n_d^2}{L_d^2} \right). \tag{1.1.4}$$

with $n_d = 1, 2, ...$ Accordingly, the DOS becomes discretized at the confined dimensions into the conventional particle-in-a-box energy levels, while keeping a continuous character along the other dimensions. Thus, the energy dependence of the DOS changes with the system's dimensionality (being no longer described by Eq. 1.1.1), classifying nanoscopic objects as 2D, 1D or 0D, according to the number of non-confining dimensions. Each of these energy levels constitute a propagating mode or channel (generally characterized by a momentum k and a spin σ), through which electrons can traverse the nanostructure. Even for perfectly ballistic systems, energy modes show a finite resistance in actual experiments, reflecting the finite reflection probability of electrons at the contact interfaces due to the abrupt potential variation generally appearing between the 3D metallic reservoir and the nanostructure. The characteristic resistance of a single mode is equal to $h/2e^2 \approx 12.9$ kΩ (or 25.8 kΩ, if we consider non-spin-degenerated channels) defining the quantum of resistance, or equivalently, the quantum of conductance as $2e^2/h \approx 77.5$ μS.

In practice, nanostructures may contain impurities or defects that cancels out perfect ballisticity, and are often contacted to the reservoirs by tunnel barriers. In general, these elements can reduce the transmission of different channels, not necessarily by the same quantity. The cleverness of Landauer formulation resides in defining a transmission matrix, T, accounting for the different transmissivity of each channel (k, σ), expressing the total conductance of the device as

$$G = \frac{2e^2}{h} \sum_{k,\sigma} T_{k,\sigma}. \tag{1.1.5}$$

The generality of this formula allows to describe the conductance of two-terminal nanodevices, replacing Ohm's law in mesoscopic and quantum nanoelectronics (a broad overview on transport in mesoscopic systems can be found in Ref. [50], while Ref. [51] describes the derivation and application of Landauer's formalism in detail).

1.1.3 Relevant energy scales in quantum-dot devices

A quantum dot (QD) can be defined as a structure able to accumulate electrons, being so tiny that the addition/extraction of a single electron from/to it involves a non-negligible energy cost, due its extremely small capacitance, thus allowing to control the number of electrons in the nanostructure down to the single particle level. This effect, explained in the frame of classical electrostatics, can be approached by first reminding the definition of capacitance, $C = Q/V$, as the capability of a regular capacitor to accumulate an amount of charge, Q, in each of its plates, by the establishment of a potential difference, V, between them. It shall be noticed, as well, that any additional charge in a piece of metal distributes homogeneously over the whole surface due to Coulomb repulsion. Therefore the capacitance of a system depends on its geometry (shape and size), and on the dielectric medium surrounding it. As the previous capacitance definition requires two electrodes, single metallic object are rather characterized by their self-capacitance. For example, a metallic sphere of radius R suspended in vacuum (owning a dielectric permeability of ε_0) is characterized by a self-capacitance of $C_{self} = 4\pi\varepsilon_0 R$. The electrostatic energy necessary to charge it with Q is obtained by integrating the following expression:

$$E_C^{self} = \int_0^Q V dq = \int_0^Q \frac{q}{C_{self}}\, dq = \frac{Q^2}{2C_{self}} = \frac{Q^2}{8\pi\varepsilon_0 R}. \tag{1.1.6}$$

The inverse proportionality between E_C^{self} and R reflects the fact that larger spheres have bigger surfaces where Q can spread, requiring a lower energy input for the same amount of charge. Indeed, the electrostatic energy involved in charging a macroscopic metallic object with one electron ($Q = -e \approx -1.6 \times 10^{-19}$ C) is so minuscule that single-electron charging effects are imperceptible and buried within thermal noise, even at cryogenics temperatures. However, as the sphere size is reduced, E_C^{self} grows, reaching well-detectable values of about 0.3 eV for a sphere of $R = 2.5$ nm. Nevertheless, contacting a QD to bulk electrodes (reservoirs) through tunnel junctions, leads to the formation of capacitors between the dot and each electrode. The energy "per electrode" required for injecting/extracting a single electron from the QD is also calculated from the integral in Eq. 1.1.6, but replacing C_{self} by the total capacitance of the system, C, equal to the summation of all capacitors:

$$E_C = \frac{e^2}{2C}. \tag{1.1.7}$$

In this sense, defining a QD in terms of E_C is subjective and subordinated to what is considered a non-negligible energy. In fact, metallic nanoislands of sizes ranging between $100 - 1000$ nm already display a well measurable charging energy. Historically, the term of "quantum dot" was coined within the field of mesoscopic electronics, to name nanometric structures whose DOS is discretized into energy levels due to a strong spatial confinement [52]. While single-electron charging effects had already been characterized and well understood the continuous progress in nanofabrication techniques allowed to made structures each time smaller and smaller, at some point reaching a detectable energy discretization, initially observed in electron droplets formed in two-dimensional electron gases (2DEG). While nowadays it is possible to fabricate metallic nanoislands displaying a measurable discretization (of sizes ~ 10 nm), the scope of this term has spread, also reaching self-assembled nanostructures like semiconducting nanowires (NWs) and carbon nanotubes (CNTs), metallic or semiconducting nanoparticles and nanocrystals, or single molecules. Actually, the research area studying the electronic transport through such tiny objects has bifurcated from mesoscopic electronics, conforming a new field called quantum nanoelectronics.

In spite of the disparity of all the previously mentioned experimental configurations, the underlying physics governing the transport through QDs are unique, and the different conduction features observed in the distinct approaches can be linked to different hierarchies of the energy scales present in each QD junction. Following the historical progression, we gradually introduce the energy scales characterizing these systems down to our superconducting-quantum dot transistors.

JUNCTIONS CONTACTING METALLIC ISLANDS

The first realizations of devices observing the charge discretization effects discussed above were achieved by contacting metallic islands patterned by lithography with relatively large typical sizes ($L \sim 0.1 - 1$ μm) and containing a considerably high number of electrons ($\sim 10^7$). While this size is small enough to observe single-electron charging effects, energy levels could not be resolved in these pioneering samples as the spacing in energy discretization (Eq. 1.1.4). The characteristic scales determining the transport features in these samples are

- **The charging energy** (E_U): is defined as the energy required to add/remove an electron from the QD. Although the expression in Eq. 1.1.7 is ordinarily found in the literature, works studying Kondo effect commonly define this quantity as $E_U = 2E_C = e^2/C$ (which is the convention adopted in this text).
- **The thermal energy** (k_BT): it establishes the energetic distribution of electrons both in the QD and at the contacting electrodes, which is often taken as unique and determined by the temperature of the sample through the Fermi-Dirac function (Eq. 1.1.2). At this point it is worth to mention that certain QD systems can exhibit a poor electron-phonon coupling deriving from its reduced size, and a significant difference may be displayed between the temperature at the dot and the reservoirs [53].
- **The tunnel couplings** (γ): A certain tunneling rate, Γ, is associated to the specific tunnel barriers that form the QD junction, defining the average time between tunneling events as $1/\Gamma$, for the electrons crossing the barrier. While in experiments on nanoisland junctions the tunneling rate is often related with a characteristic tunnel resistance (see section 1.2.1), a characteristic energy scale can be heuristically associated to such rate in QD junctions from the Indetermination principle and accounting for the magnitude of the hybridization of energy levels. This energy, referred to as the tunnel coupling, is defined here as $\gamma = \hbar\Gamma/2$ (discussed in more detail in section 1.2.2).

The relative values of these energy scales define three different regimes of operation. First of all, the thermal energy at room temperature (≈ 25 meV) is usually much larger than any of the other energies requiring to cool down the samples (such that $E_U \gg k_BT$) for observing single-electron charging effects. The junctions can be categorized according to the relative value of γ, as being in a weak-coupling regime ($E_U \gg k_BT \gg \gamma$), an intermediate coupling regime ($E_U \gg \gamma \gg k_BT$), or a strong-coupling regime ($\gamma \gg E_U \gg k_BT$). The transport properties of the QD junction vary strongly from one regime to another, giving rise to completely different features for the relative value of γ (general overviews and comparisons of the typical phenomenology observed in each of the three regimes is given in Refs. [54, 55]). Note that two different coupling regimes may be present simultaneously in the same device, as γ between the QD and each electrode can be totally different, generally depending on the fabrication process.

JUNCTIONS CONTACTING QUANTUM DOTS

Nowadays it is now possible to contact structures as tiny as molecules ($L \sim 1$ nm). One consequence of such size reduction lies in the natural increase of E_U, lifting up the operation temperature at which single-electron charging effects can be observed [56, 57]. More interesting from a fundamental perspective is the discretization of the QD-DOS. The key length scale here is related with the *De Broglie* wavelength (defined for the free electrons of a Fermi liquid as $\lambda_D = p/h = 2\pi/k$).

As higher energy states present a larger degeneration, the mean De Broglie wavelength is generally close to the Fermi wavelength $\lambda_F = 2\pi/k_F$. Commonly, well separated levels can be resolved for QDs displaying a typical size of $L \sim 10\lambda_F$, introducing an additional relevant scale that gives raises to specific transport features:

- **The mean level-spacing** (E_δ): between electronic spin-degenerate energy levels, which can be estimated, for metallic nanoparticles, to be around $\frac{2\pi^2\hbar^2}{mk_FV}$, where m is the electron mass, k_F is the Fermi wavenumber, and V is the particle's volume [1].

In general, such levels are spin-degenerated and involve a spatial probability distribution around and inside the QD, as atomic orbitals. Atomic-scale irregularities gain importance due to the reduced size of actual QDs, leading to ergodic and non-uniform distributions of the orbital energies in each particular sample, limiting the validity of the previous E_δ expression for an order-of-magnitude estimation.

HYBRID SUPERCONDUCTING-QUANTUM DOT JUNCTIONS

When a metal enters the superconducting (SC) phase, electrons couple together into the so-called Cooper pairs (CPs) due to an attractive interaction mediated by the phonons of the crystalline lattice. Such SC pairing correlations are characterized by

- **The superconducting energy** (Δ): is the (negative) bound state energy per electron forming a Cooper pair, in turn constituting the half-amplitude of the energy gap of forbidden states opening around E_F in the SC-DOS and the modulus of the SC order-parameter.

While superconductivity manifests equally in different materials presenting the SC phase transition, significant differences appear in the characteristic value of Δ. As we employ aluminum contacts, we restrict the discussion to conventional (type I) superconductivity, in which Δ is a constant parameter. The introduction of SC correlations in the electrodes of a QD junction strongly modifies its transport properties, as the charge discretization imposed by Coulomb repulsion opposes to the simultaneous tunneling of the two electrons forming a CP, favored by proximity effect.

1.1.4 Electronic transport in tunnel junctions

A generic tunnel junction consist of two objects (metallic, in general) separated by an insulating barrier thin enough for displaying a sufficiently high electron tunneling probability to originate detectable currents. The band structure of the objects on both sides of the barrier, called 1 and 2, fixes the respective electronic momenta, k and q, and DOS, ϵ_k and ϵ_q. Such system is usually described with a hamiltonian accounting for all electronic states at each object, and including a tunneling term, H_T, that comprises all possible tunneling processes (one electron occupying an initial state in 1 cross the barrier, ending up in a final state at 2). This interacting component is generally expressed as:

$$H_T = \sum_{k,q} \left(\tau_{k,q} a_k^\dagger c_q + \tau_{k,q}^* a_k c_q^\dagger \right), \tag{1.1.8}$$

where $a_k^\dagger$ ($c_q^\dagger$) and a_k (c_q) represent the creation and annihilation operators in 1 (2), and $\tau_{k,q}$ are the tunneling amplitudes, fixed by barrier properties (thickness, work function, etc) and related to the transmission matrix elements of Eq. 1.1.5. Here, we assume that the probability of each tunneling process, $T_{k,q} \propto \tau_{k,q}$, is solely determined by the electronic energies of the initial and final states (or equivalently momenta, k and q), dropping any dependence on other quantum numbers like the spin.

Opposite to structures directly connected by metallic links, the employment of tunnel barriers as a contact method carries along a drastic decrease in the transmission probability, leading to tunneling amplitudes $T_{k,q} \ll 1$, which results in conductances $G \ll 2e^2/h$. Thus, H_T can be considered as a perturbation, allowing to calculate the probability of a certain tunneling event by applying Fermi's golden rule: an electron in 1 with energy ϵ_k may tunnel into any of all possible empty states in 2 (of

energies $\sum_q \epsilon_q$). The total rate for electrons tunneling in this direction is obtained by extending the summation over all occupied states in 1:

$$\Gamma_{1\to 2} = \frac{2\pi}{\hbar} \sum_{k,q} |\tau_{k,q}|^2 \langle a_k^\dagger a_k c_q^\dagger c_q \rangle \delta(\epsilon_q - \epsilon_k), \tag{1.1.9}$$

The Dirac delta function, $\delta(x)$, appearing in this expression restricts the calculation to processes in which the electron's energy is conserved, i.e., elastic or first-order tunneling. Equivalently, it is possible to write down the expression for the rate in the opposite sense, $\Gamma_{2\to 1}$, and obtain the net current flowing through the junction from their difference, relating it with the amplitudes $\tau_{k,q}$ that characterize the particular barrier. Generally, the calculation of tunneling rates can be a rather complicated task as it requires to count occupied and empty states in the objects at both sides of the barrier. However, an analytical rate expression can be obtained for specific systems, under certain approximations.

ELASTIC TUNNELING IN A BULK TUNNEL JUNCTION

We consider now a system in which a tunnel barrier separates two bulk metallic objects over which a certain voltage difference V_B is applied. These objects (called source S and drain D) display a continuum DOS (as defined in Eq. 1.1.1), and the respective hamiltonians describing their quantum states are $H_S = \sum_k \epsilon_k a_k^\dagger a_k$ and $H_D = \sum_q \epsilon_q c_q^\dagger c_q$. The tunneling interaction between them is described by adding the interactive term (in Eq. 1.1.8) to the total hamiltonian of the system: $H = H_S + H_D + H_T$. If a certain biasing voltage V_B is applied to S, their electrons will experience an increment in energy of magnitude $-eV_B$ with respect to the Fermi level of D (taken as the origin of energies). The effect of the voltage difference in the calculation of the tunneling rates is included replacing ϵ_k by $\epsilon_k - eV_B$ in Eq. 1.1.9.

To give an analytical expression for the tunneling rates, we shall express them on their integral form. In this formalism, the Fermi-Dirac distributions in the electrodes are $f(\epsilon_k) = \langle a_k^\dagger a_k \rangle$ and $f(\epsilon_q) = \langle c_q^\dagger c_q \rangle$ (equal to each other as we consider both electrodes to be at the same temperature). Taking into account that the summations over quantum states can be converted into integral over the energy as $\sum_k = \int D_S(\epsilon_k) d\epsilon$ and $\sum_q = \int D_D(\epsilon_q) d\epsilon$, the transmission matrix needs to be expressed as a function of energy $\tau_{k,q} = \tau(E)$. The resulting integral is canceled for the whole energy range, except for the filled states of the initial (donor) electrode, and the empty states of the final (collector) electrode, which lie inside the bias window. For solving the resulting integral, the energy dependence of the transmission function is often taken as constant $\tau(E) \approx \tau$, attributing equal tunneling probabilities to electrons with different energies. Additionally the slow energy-variation $\sim \sqrt{E}$ allows to approximate the DOS by their values at the Fermi energy: $D_{S,D}(E) = D_{S,D}(0)$, as long as the voltage applied is small compared with the bandwidth of the leads ($V_B \ll W = E_F - E_B$). Carrying out these approximations[2], analytical expressions are obtained for both rates:

$$\begin{aligned}
\Gamma_{S\to D}(V_B) &= \frac{2\pi}{\hbar} \int |\tau(E)|^2 D_S(E - eV_B) D_D(E) f(E - eV_B)[1 - f(E)] dE \\
&\approx \frac{2\pi |\tau|^2 D_S(0) D_D(0)}{\hbar} \int f_S(E - eV_B)[1 - f_D(E)] dE \\
&\approx \frac{V_B}{eR^T} \left(\frac{1}{1 - e^{-eV_B/k_B T}} \right),
\end{aligned} \tag{1.1.10}$$

$$\begin{aligned}
\Gamma_{D\to S}(V_B) &= \frac{2\pi}{\hbar} \int |\tau(E)|^2 D_S(E - eV_B) D_D(E) f(E)[1 - f(E - eV_B)] dE \\
&\approx \frac{-V_B}{eR^T} \left(\frac{1}{1 - e^{eV_B/k_B T}} \right),
\end{aligned} \tag{1.1.11}$$

[2] By using the identity $\int_{-\infty}^{\infty} f(x)(1 - f(x + a)) dx = \int_{-\infty}^{\infty} f(x - a)(1 - f(x)) dx = a/(1 - e^{-a/k_B T})$ [58]

defining the tunnel resistance of the barrier as $R^T = \hbar/2\pi e^2|\tau|^2 D_S(0)D_D(0)$. The net current flowing through the system is determined from the difference of both tunneling rates multiplied by the charge involved in each transfer process ($-e$), taking the usual convention of electrons flowing from D to S as the positive sense of tunneling (equivalent to consider the current flowing from S to D as positive):

$$I_{bulk}(V_B) = -e(\Gamma_{D\to S} - \Gamma_{S\to D}) = \frac{V_B}{R^T}\left(\frac{1}{1-e^{eV_B/k_BT}} + \frac{1}{1-e^{-eV_B/k_BT}}\right), \tag{1.1.12}$$

where it can be observed that an ohmic linear dependence, as $I_{bulk} = V_B/R^T$, is reached in the high bias limit ($|eV_B| \gg k_BT$), identifying the integral coefficients with the characteristic tunneling resistance, R^T, of the junction.

As explained later, the nanoisland junction is regarded as two tunnel junctions on-series, where the differences between the island's and the leads' chemical potentials are expressed in terms of the capacitive couplings of the system. The tunneling rates are calculated in terms of these differences, allowing to give analytical expressions for the sequential current.

1.2 Quantum dot junctions in the normal state

In the late 80's, *Fulton and Doland* [59] were exploring the conduction of a small metallic island patterned by lithography, employing the spontaneous oxidation of the structure surface to form tunneling barriers, contacting it to the reservoir electrodes by overlapping them with the island using a shadow-angle evaporation technique (Fig. 1.2a). The small size of the island (800×50 nm^2) allowed them to observe a current suppression in characteristic I-V curves, opening a Coulomb gap around zero-V_B as a consequence of Coulomb repulsion at the island. The inclusion of a third capacitively-coupled but not tunnel-coupled lead (acting as a gate electrode) could be used to show the modulation of the Coulomb-gap extension and access different single-electron charging states, coining the name of "Fulton-Dolan electrometer", popularized later as the "single-electron transistor" (SET). In a radically different but simultaneous research line, the observation of periodic conductance fluctuations arising sporadically in 2DEG-based narrow-channel transistors leaded the group of *Kastner et al* to modified the transistor lithographic pattern to further investigate this phenomenon [63]. By including constrictions along the narrow-channel (Fig. 1.2b), artificially created tunnel barriers induce the formation of an electron droplet at the center of the channel, effectively acting as a nanoisland, and allowing them to link the conductance fluctuations with single-electron charging effects [60]. The great versatility of such 2DEG-based samples, in which customized designs of lithographically patterned electrodes make possible to define electron droplets with an arbitrary shape, size and position, resulted in a rapid follow-up of this experiment. Novel electrode arrangements were implemented shortly after, for example including a gate electrode to control independently the tunnel barriers and the island's chemical potential [61], as well as more complex devices involving single-electron transfers between on-series QDs allowing, for example, to generate a turnstile current [62] (see Fig. 1.2c).

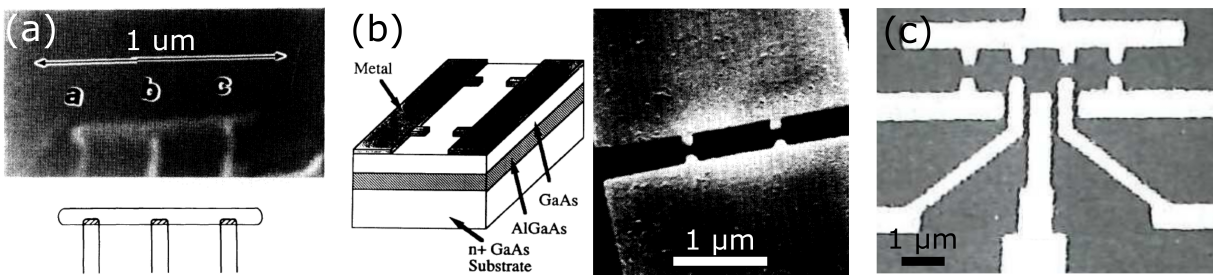

Fig. 1.2: Several pictures and schematics of (a) of a metallic island connected to three electrodes by oxide tunnel junctions (extracted from [59]), (b and c) electrodes patterned on a semiconducting heterostructure, forming a QD junction in the 2DEG below the surface (extracted respectively from [60] and [61, 62]).

All these samples involved island/droplet structures of a size ~ 1 μm, small enough to display clear signatures of single-electron charging effects for a weak tunnel coupling to the electrodes. However, the size of these island-like dots was still too large to achieve a significant energy discretization, and the observed DOS was essentially continuous. Accordingly, we begin this section by presenting the Orthodox model (also called Constant Interaction model) describing the Coulomb blockade effect and tunneling current for an island in a SET (gated) configuration (1.2.1), employed to extract various sample parameters from our measurements. Then, we center our attention on discrete-spectrum QD junctions, explaining the consequences of energy discretization in the model and relating the current with the tunnel coupling scales, γ (1.2.2). The stochastic nature of the electromigration technique used to fabricate our QD transistors impede us to predefine/tune the tunnel barriers (randomly fixing the values of γ). As the main focus of this thesis lies on the characterization of samples displaying a strong coupling asymmetry (reaching intermediate/strong coupling regimes on one side), we finish this section giving a brief overview on higher-order processes (1.2.3), focusing on the Kondo effect and its phenomenology in QD junctions (1.2.4).

1.2.1 Single-electron transistor: the weak-coupling regime

In the weak-coupling regime ($E_U \gg k_BT \gg \gamma$), electronic transport in junctions contacting a nanoisland is governed by the Coulomb repulsion between electrons at the central electrode, which give rise to single-electron charging effects. This is the operation regime of the standard single-electron transistor (SET), in which the number of electrons in the island can be controlled by means of its capacitive coupling to the gate electrode. The application of different voltages to the gate allows to block or permit the electrical conduction through the nanostructure for a certain biasing voltage, switching the device on and off, similarly to field-effect transistors (FET). However, the different physical origin that drives electronic transport in these two types of transistor results in distinct behaviors that separate them: the appearance of gate-modulated periodic oscillations (Coulomb oscillations), the staircase aspect of the characteristic I-V_B curve and the establishment of an electron-by-electron on-state current constitute the typical behaviors that characterizes the SET, all encompassed in the so-called Coulomb blockade effect. This effect has been studied in detail over the past decades, along with the development of the Orthodox theory, which accounts for the Coulomb interaction of electrons in the island by imposing a charging energy of constant value that needs to be payed for tunneling events to take place. While the origins of this model dates back to the 70's [64], multiple expansions have been implemented, for example, by *Averin and Likharev* [65], who associated the Coulomb Blockade effect initially observed in granulated media with the single-electron tunneling processes appearing nanoisland tunnel junctions, later including the effect of a gate electrode [66].

COULOMB BLOCKADE EFFECT IN A SINGLE-ELECTRON TRANSISTOR

The equivalent circuit considered within this Orthodox picture simplifies the junction structure, considering that the tunnel barriers connecting the nanoisland to the leads (source, S, and drain, D), are characterized by capacitances (C_S and C_D) and tunnel couplings (γ_S and γ_D) of constant values. In the SET configuration, a gate electrode (G) is also present in the device, being close enough to the island to be capacitively coupled to it (C_G), but sufficiently far to neglect any tunneling processes between them (Fig. 1.3a). In such system, $C = C_S + C_D + C_G$ is the total capacitance of the island, determining its charging energy.

We start by considering the equilibrium situation, in which both electrodes S and D are connected to the same electrical potential (ground), so that their chemical potentials are balanced, $\mu_S = \mu_D$. In an initial transitory state, tunneling processes take place until the island's chemical potential is also balanced with those of the electrodes, fixing its equilibrium charge at $Q = -eN$, expressed as an integer number of electrons. However, as the island have a significant charging energy, tunneling electrons may not be able to completely compensate its chemical potential, and an arbitrary, sample-dependent offset may appear in its electrostatic potential. This offset can be represented by an

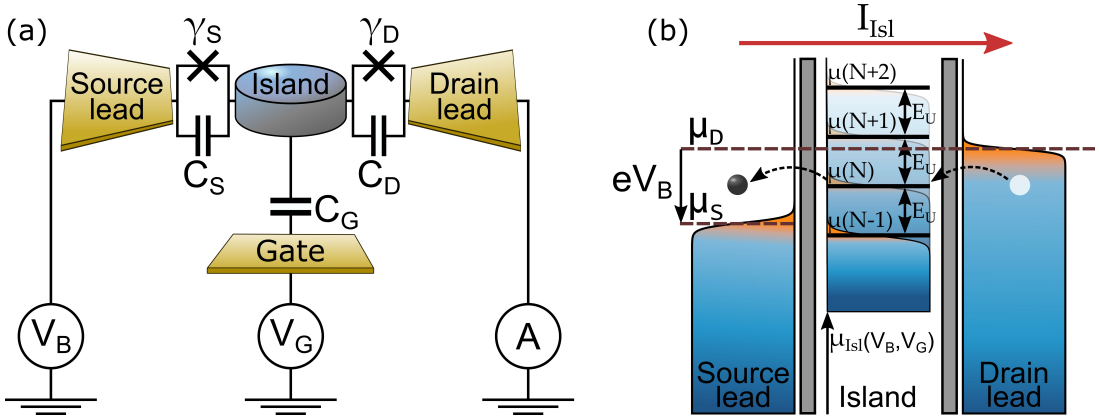

Fig. 1.3: Schematic (a) and chemical potential diagram (b) of an island-like SET, where the DOS of the central electrode is continuum and charge states arise due to the charge discretization induced by Coulomb blockade.

charge-offset constant equal to eN_{offset}, necessarily being a fractional number (smaller than the charge of one electron, so that $0 < |Q_{\text{offset}}| = eN_{\text{offset}} < e$). The resulting electrostatic potential of the island at equilibrium is the written as

$$V_{Isl}^{eq} = \frac{Q}{C} + \frac{Q_{\text{offset}}}{C} = \frac{-eN}{C} + \frac{-eN_{\text{offset}}}{C}, \tag{1.2.13}$$

Although such offset is systematically present in actual samples, it can be compensated by the application of a certain gate voltage, and therefore this term is generally neglected in the theoretical model (taking $Q_{\text{offset}} = 0$ for the rest of the description).

By applying finite voltages to S, D and G (V_S, V_D and V_G respectively) the island's electrostatic potential is influenced via its capacitive couplings by an amount $V_{ext} = (C_S V_S + C_D V_D + C_G V_G)/C$. The island's electrostatic potential is then obtained from the addition of the equilibrium component plus the externally induced one:

$$V_{Isl}(V_{ext}) = V_{Isl}^{eq} + V_{ext} = \frac{Q + Q_{ext}}{C} = \frac{-e}{C}(N + N_{ext}). \tag{1.2.14}$$

defining the externally induced charge as $Q_{ext} = -eN_{ext} = C_S V_S + C_D V_D + C_G V_G$. As the total charge on the island, $Q + Q_{ext}$, depends on the external voltages applied, it becomes possible to change the number of electrons blocked in it by applying sufficiently high voltages. To understand how the number of electrons in the island changes, it is necessary to calculate the electrostatic energy of the system:

$$\begin{aligned} U_T(N, V_{ext}) &= \int_{q=0,v=0}^{Q,V_{ext}} (V_{Isl}dq + qdv) = \frac{(eN)^2}{2C} - eNV_{ext} \\ &= \frac{(Q - Q_{ext})^2}{2C} - \frac{Q_{ext}^2}{2C} = \frac{Q_{\text{eff}}^2}{2C} - \frac{Q_{ext}^2}{2C}. \end{aligned} \tag{1.2.15}$$

where the origin of energies is defined for a configuration of zero additional electrons in the island, so that $U_T(N = 0) = 0$, and we have defined the effective charge in the island as $Q_{\text{eff}} = -eN_{\text{eff}} = Q - Q_{ext}$. Despite the fact that Q_{eff} can be varied continuously with the external voltages applied, the actual number of electrons in the island N can only adopt integer values, as individual electrons cannot partially tunnel into the island. This effect puts in evidence the granular nature of the electrical charge, deriving from the strong localization that an electron suffers when tunneling into the island (collapsing its wave function in space). Differently from the classical example of a free-electron colliding with a potential barrier which divides its wave-function into a transmitted and a reflected parts (resulting from the ondulatory nature of the electron at both sides of the barrier), the localization effect of the small island imposes the total transmission or reflection of the electron.

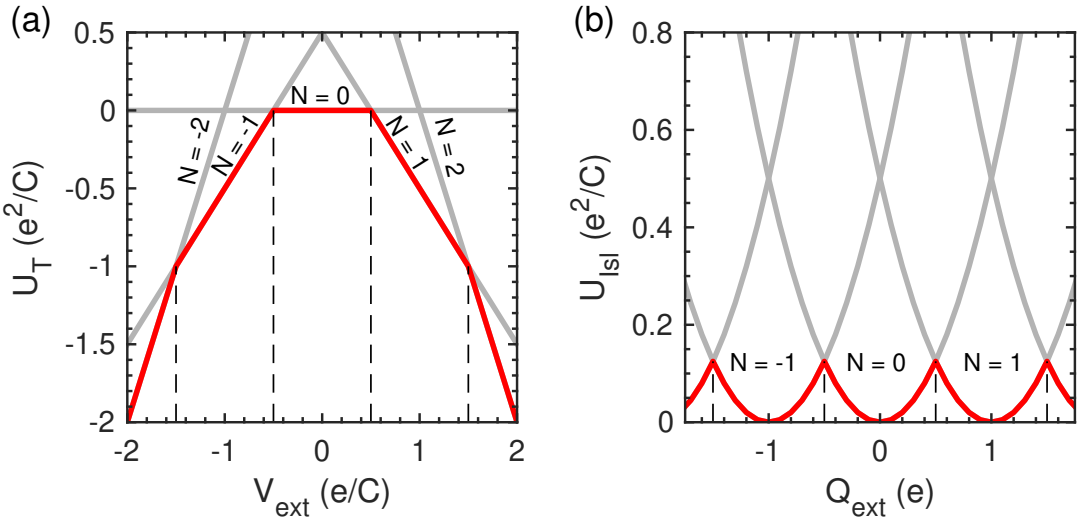

Fig. 1.4: (a) Total electrostatic energy of a SET as a function of V_{ext}. (b) Electrostatic energy of the island as a function of Q_{ext}. Both quantities in (a) and (b) are represented for different number of electrons in the island (N, neglecting the experimental offset $N_{\text{offset}} = 0$). The electrostatic energy of constant-N states (solid grey lines) intersect at specific degeneracy points (vertical dashed lines), revealing the transitions from one charge state to the next one. In equilibrium, the system is found in the lowest available energy state (red line).

To infer at which values of V_{ext}, the induced Q_{eff} is large enough for the number of electrons in the island to actually change, it is necessary to calculate as well the electrostatic energies for a different number of electrons blocked at the island in equilibrium ($V_{ext} = 0$). This can be done by a simple substitution of N by $..., N-1, N+1, ...$ in the generic formula (Eq. 1.2.15), obtaining the values of $..., U_T(N-1, 0), U_T(N+1, 0), ...$ Accordingly, when V_{ext} is sufficiently high for the electrostatic energy of a given N to become equal to the equilibrium energy of a subsequent configuration ($U_T(N, V_{ext}) = U_T(N-1, 0)$ or $U_T(N, V_{ext}) = U_T(N+1, 0)$) the charge in the island changes by one electron. This can be observed by representing U_T as a function of V_{ext}, which leads to a set of straight lines (one for each value of N) of different slope (Fig. 1.4a). As the system always tends to be in the lowest-energy state available (red line), it can be observed that N remains constant over a certain range of V_{ext}, resulting in the generation of charging states, arising as a consequence of the granular nature of electrical charge. Intersections between different charge states happen at regular increases of $\Delta V_{ext} = e/C$, signaling the precise points where the system is degenerated in between two charge states (degeneracy points). When crossing through a degeneracy point, the charge state of the system changes by one electron. The energy increment that the system requires to change its charge state is found to be $\Delta U_T = e^2/C$ (not appearing at the state $N = 0$, since it has been taken as the energies origin).

It is interesting to notice that, when expressing Eq. 1.4 in terms of Q_{ext} instead of V_{ext}, the electrostatic energies corresponding to the capacitor plates of the island (U_{Isl}) and at the leads (U_l) decouples, obtaining:

$$U_{Isl} = \frac{Q_{\text{eff}}^2}{2C} = \frac{(Q - Q_{ext})^2}{2C} \qquad \text{and} \qquad U_l = \frac{Q_{ext}^2}{2C}. \tag{1.2.16}$$

By representing U_{Isl} as a function of Q_{ext}, a set of parabolas appears for the different charge states (Fig. 1.4b). Similarly, intersections signal the points at which the charging state of the system changes, appearing at half-integer values of $N_{ext} = e(..., -1.5, -0.5, 0.5, 1.5, ...)$.

Each of these charge states can then be associated with a certain chemical potential, defined in classical thermodynamics as the amount of energy per particle, calculated from its total internal energy and number of particles. Therefore, the chemical potential in our QD-junction system is equal

to the variation of the total electrostatic energy induced by the addition of one electron to the island:

$$\mu_{Isl}(N) = U_T(N) - U_T(N-1) = \frac{e^2}{C}\left(N - \frac{1}{2}\right) - eV_{ext}. \tag{1.2.17}$$

Although this chemical potential is defined for the whole device (employing the total electrostatic energy of the system, U_T), it is commonly attributed to the island, as it depends for the number of electrons N blocked in it. The energy required to change the island's charge by one electron (charging energy) can be extracted as the difference of the island's chemical potentials for consecutive charge states:

$$E_U = \mu_{Isl}(N) - \mu_{Isl}(N-1) = \frac{e^2}{C}, \tag{1.2.18}$$

constant for any consecutive charge states considered.

Charge states are generally depicted as a set of grades $(..., N-1, N, N+1, ...)$ in the energy diagram of the junction (Fig. 1.3b). For the establishment of non-zero net current through the island, a configuration, in which at least two charge states are accessible, needs to be reached (by acting in the external voltages that define V_{ext}). Individual electrons traverse the device consecutively, constituting a sub-poissonian flow that gives raise to a telegraphic process known as sequential or resonant tunneling. The electronic transport through the junction is then correlated with the number of electrons in the island, the origin of such electronic correlations being the Coulomb repulsion [67]. In this way, Coulomb Blockade allows to control the current down to the single-particle level, generating a one-by-one electron stream, where the system oscillates between two consecutive charge states.

SEQUENTIAL CURRENT IN A SINGLE-ELECTRON TRANSISTOR

The chemical potentials differences in the nanoisland junction have to be defined for calculating the tunneling rates, allowing to derive the total net current flowing through the system when a certain biasing voltage is applied. Despite the symmetric biasing condition generally considered in theoretical works, it is more common, in experiments, to apply the total biasing voltage, V_B to the source electrode, S, (identifying $V_S = V_B$), while keeping the drain electrode, D, grounded, as it is connected to an ammeter (so that $V_D = 0$). The energies origin is taken at $\mu_D = 0$ for convenience, while the biasing voltage results in an opposite-sign imbalance at the source chemical potential, $\mu_S = -eV_B$. Hence, the externally-induced voltage is reduced to $V_{ext} = (C_S V_B + C_G V_G)/C$, allowing to rewrite the expression for the chemical potential of the island containing N electrons at equilibrium as:

$$\begin{aligned}\mu_{Isl}(N, V_B, V_G) &= \frac{e^2}{C}\left(N - \frac{1}{2}\right) - e\frac{C_S}{C}V_B - e\frac{C_G}{C}V_G = \\ &= -e\alpha_B V_B - e\alpha_G(V_G + V_G^N),\end{aligned} \tag{1.2.19}$$

where the gate value of the degeneracy point between the charging states $N-1$ and N is defined as $V_G^N = (-e/C_G)(N - 1/2)$. The non-dimensional constants $\alpha_B = C_S/C$ (sometimes represented by η in the literature), and $\alpha_G = C_G/C$, constitute the bias and gate coupling parameters (also known as lever arms), establishing the linear dependence of $\mu_{Isl}(V_G, V_B)$ on the external voltages.

For calculating the net sequential current, the system is split into two separate junctions (between the island and each lead, S and D), characterized by independent tunneling rates, Γ_S and Γ_D. These rates can be obtained by applying Fermi's golden rule, considering the chemical potential difference at the corresponding junction (as indicated in section 1.1.4). In a situation where the equilibrium charge state of the island is N, and external voltages are applied to the device in ranges such that $-E_U \leq e\alpha_B V_B \leq E_U$ and $-E_U \leq e\alpha_G V_G \leq E_U$, only three charging states ($N-1, N$ and $N+1$) are possible. For N electrons being initially in the island, and a tunnel event moving one electron

in/out of the island from/to the lead $l = S, D$, the chemical potential differences are [66, 68]:

$$\begin{cases} \Delta E_S^{in}(N) = \mu_{Isl}(N+1) - (-eV_B) = (e^2/C)(N+1/2) - e\alpha_G V_G + (1-\alpha_B)eV_B, & \text{(1.2.20a)} \\ \Delta E_S^{out}(N) = \mu_{Isl}(N) - (-eV_B) = (e^2/C)(N-1/2) - e\alpha_G V_G + (1-\alpha_B)eV_B, & \text{(1.2.20b)} \\ \Delta E_D^{in}(N) = \mu_{Isl}(N+1) = (e^2/C)(N+1/2) - e\alpha_G V_G - e\alpha_B V_B, & \text{(1.2.20c)} \\ \Delta E_D^{out}(N) = \mu_{Isl}(N) = (e^2/C)(N-1/2) - e\alpha_G V_G - e\alpha_B V_B. & \text{(1.2.20d)} \end{cases}$$

The chemical potential differences in the processes bringing the island from $N-1$ and $N+1$ states back to N ($\Delta E_S^{in}(N-1)$,$\Delta E_D^{in}(N-1)$ and $\Delta E_S^{out}(N+1)$,$\Delta E_D^{out}(N+1)$) can be equivalently derived. By plugging these energy differences into Fermi's Golden rule 1.1.9 the respective tunneling rates can be obtained:

$$\Gamma^N_{S(D)\to Isl} = \frac{1}{e^2 R^T_{S(D)-Isl}} \int f_{S(D)}(E - eV_{S(D)})[1 - f_{Isl}(E + \Delta E^{in}_{S(D)}(N))]dE, \quad \text{(1.2.21)}$$

$$\Gamma^N_{Isl\to S(D)} = \frac{1}{e^2 R^T_{S(D)-Isl}} \int f_{Isl}(E + \Delta E^{out}_{S(D)}(N))[1 - f_{S(D)}(E - eV_{S(D)})]dE. \quad \text{(1.2.22)}$$

A kinetic expression based on the master equation can be written in terms of the tunneling rates [69]. The evolution rate of P_N (the probability of finding the system in the charge state N) is defined as the difference between the probability of processes driving the system from $N-1$ or $N+1$ states back into N minus the probability of processes driving the system from N into $N-1$ or $N+1$, all of them being multiplied by the corresponding rate:

$$\frac{dP_N}{dt} = P_{N-1}(t) \sum_{l=S,D} \Gamma^{N-1}_{l\to Isl} + P_{N+1}(t) \sum_{l=S,D} \Gamma^{N+1}_{Isl\to l} - P_N(t) \sum_{l=S,D} \left(\Gamma^N_{Isl\to l} + \Gamma^N_{l\to Isl}\right). \quad \text{(1.2.23)}$$

A closed system of detailed balanced equations is formed by also considering the corresponding expressions for the time evolution of P_{N-1} and P_{N+1}. As V_B is kept small, successive charging states (P_{N-2}, P_{N+2}) are neglected. If the voltages applied to the SET are kept constant (stationary case), the probability P_n of all considered charge states ($n = N-1, N, N+1$) is constant, and their time evolution (Eq. 1.2.23) is equal to zero. By applying a normalization condition ($\sum_n P_n = 1$), the system can be solved, and the current flowing through the device can be calculated for different V_B and V_G values. The resulting map shows Coulomb blocked regions, and on-state areas where a finite current is enabled by double charging-state degeneracy (either between $N-1 \rightleftarrows N$, or $N \rightleftarrows N+1$), reaching a triple charging state degeneracy ($N-1 \rightleftarrows N \rightleftarrows N+1$) only at the highest values of the V_B range considered. In such a stationary situation, the expression for the current can be written in terms of the total tunneling rates as:

$$I_{Isl}(V_B, V_G) = -e(\Gamma^T_{D\to Isl} + \Gamma^T_{Isl\to S} - \Gamma^T_{S\to Isl} - \Gamma^T_{Isl\to D}), \quad \text{(1.2.24)}$$

where $\Gamma^T_{l\to Isl} = \sum_n \Gamma^n_{l\to Isl}$ for $n = N-1, N, N+1$, equivalently defined for the opposite tunneling direction ($Isl \to l$). The dependence on V_B and V_G is included in the $\Delta E_l^{in/out}$ parameters, allowing to map the current over these variable voltages. The current map constitutes an stability diagram of the SET, where regions with a fixed charge state (blocking the current) intercalate with conduction regions where charge states are degenerated and a finite net current is established by sequential tunneling. The characteristic diamond-like structure emerges as a consequence of the linear dependence of $\mu_{Isl}(V_G, V_B)$. The magnitude of the sequential current is determined by the tunneling resistances $R^T_{S(D)-Isl} = \hbar/2\pi e^2 |\tau_{S(D)}|^2 D_{S(D)}(0) D_{Isl}(0)$ of both barriers. Although many transport channels are generally involved due to the continuous DOS of the island, the low transmission caused by the reduced tunnel probability leads to resistances generally much higher than the spin-degenerated quantum of resistance ($R^T_{S(D)-Isl} \gg h/2e^2$), setting the weak-coupling regime condition, necessary for the clear observation of individual charge states.

STABILITY DIAGRAM OF THE SINGLE-ELECTRON TRANSISTOR

The stability diagram of standard SET devices can be reconstructed from the measurement of its V_B-V_G map of current (Fig. 1.5): white diamonds at low V_B represent the Coulomb blockaded regions where a fix number of electrons in the island impedes the current flow (Fig. 1.5a), the red and blue diamonds depict conduction regions of positive and negative current respectively. Periodic Coulomb oscillations appear when sweeping the V_G across several degeneracy points $V_G^{N-1}, V_G^N, V_G^{N+1}$,... (Fig. 1.5b). The characteristic $I - V_B$ curves at constant V_G show a zero-current range around zero-V_B, known as Coulomb gap, until the edge of the diamond is reached (Fig. 1.5c and d). Inside the diamonds, the current shows a linear ohmic dependence on V_B determined by $R^T_{S(D)-Isl}$, with stepwise increments each time an additional charge degeneracy (signaled by darker diamonds) is accessed, laying inside the V_B-window.

The capacitances of a SET device can be extracted from the measurement of such current map [70, 71]. While the value of E_U determines the diamonds half-extension in bias, the positive and negative diamond slopes, β^+ and β^-, corresponds to the alignment of μ_{Isl} with the E_F of the transport leads; $\mu_S = -eV_B$ and $\mu_D = 0$. By imposing $\mu_{Isl} = \mu_S$ and $\mu_{Isl} = \mu_D$ in Eq. 1.2.19, linear relations between V_B and V_G delineating the diamond edges are obtained. While the independent term in the resulting formulas accounts for the gate positions of the degeneracy points positions $(V_G^{N-1}, V_G^N, V_G^{N+1}$,...), the proportionality factors between V_B and V_G represent the slopes of the diamond edges, which depend on the characteristic capacitances of the system as:

$$\beta^+ = \frac{C_G}{C_D + C_G} \text{ (for } \mu_{Isl} = -eV_B) \qquad \text{and} \qquad \beta^- = \frac{C_G}{C_S} \text{ (for } \mu_{Isl} = 0), \tag{1.2.25}$$

The gate coupling parameter, α_G, defined in Eq. 1.2.19, relates variations in the gate voltage, ΔV_G, with shifts in the island's chemical potential, since $\Delta\mu_{Isl} = \alpha_G \Delta V_G$. Having determined E_U, the α_G parameter can be extracted from the gate-width of the diamond (the separation between neighboring degeneracy points is equal to $E_U/e\alpha_G$). Notably, the large values of E_U present in our QD transistors precluded us both from reaching two consecutive degeneracy points within the whole experimentally accessible V_G range, as well as the observation of the diamond extension in bias since the application of large values of V_B can easily destroy the junctions. Consequently, a complete picture of a whole diamond could not be obtained, impeding the direct determination of E_U. Nevertheless, the gate coupling α_G and the capacitive coupling asymmetry of S and D could be extracted from the extracted slopes as:

$$\frac{C_D}{C_S} = \frac{\beta^-}{\beta^+}\left(1 - \beta^+\right) \qquad \text{and} \qquad \alpha_G = \frac{\beta^+\beta^-}{\beta^+ + \beta^-}. \tag{1.2.26}$$

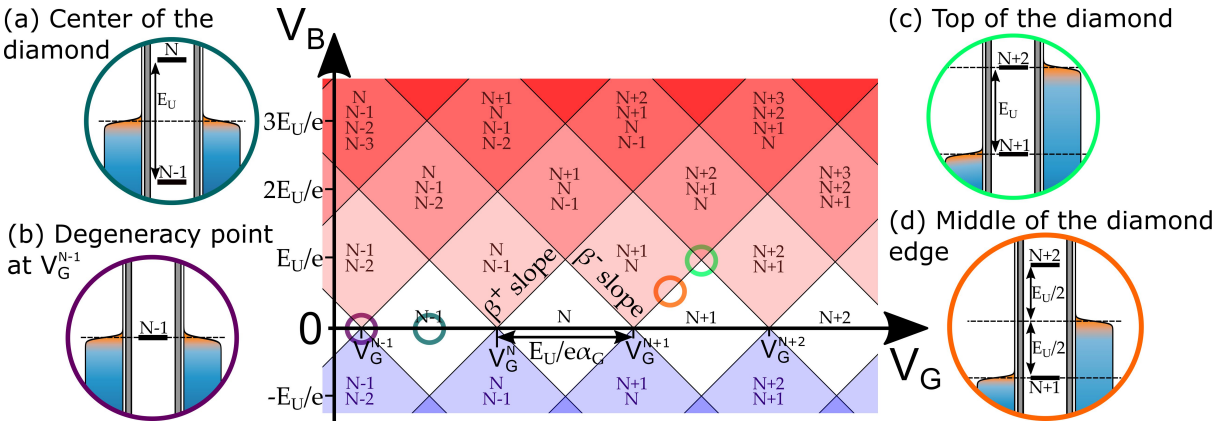

Fig. 1.5: Stability diagram of a standard SET. The diamond-shaped regions correspond to different charge states of the system, as indicated. The energy configuration of the QD junction is depicted at several key positions: (a) the $N-2$ to $N-1$ degeneracy point, (b) the center of the $N-1$ blocked diamond, (c) the top corner of the $N+1$ blocked diamond and (d) one of the $N+1$ diamond edges.

The charge discretization phenomena observed in SET devices contacting island-like QDs (containing many electrons and a continuous DOS) is well described by the Coulomb blockade effect as explained from the Orthodox theory perspective. Some modifications need to be introduced, however, when considering QDs owning a discrete energy levels.

1.2.2 Quantum-dot transistor: transport through discrete energy levels

For observing a significant energy discretization in the QD-DOS, sizes comparable to the Fermi wavelength of the material they are made of need to be reached. In semiconducting heterostructures, the Fermi wavelength, λ_F, can be as large as few tens of nanometers, facilitating the emergence of discrete energy levels for relatively large electron droplets defined in a 2DEG system (already for sizes around 100 nm [72]). On the contrary, $\lambda_F \sim 0.1$ nm in most metals, requiring to reduce the dot's size down to a few nanometers at much. Specific fabrication techniques, like electromigration, have been developed in the last decades, allowing to contact individual QDs of such a reduced size, like metallic nanoparticles or molecules. The resulting energy levels are spin-degenerated and involve a spatial probability distribution around and inside the QD, in the same way as atomic orbitals, being possible to address them individually if their spacing is large enough.

COULOMB BLOCKADE IN A QUANTUM-DOT TRANSISTOR

The description of the Coulomb Blockade effect in QD transistors requires slight modifications of the equations presented previously to account for the energies of the orbitals in the dot. In fact, rather than spin-degenerated orbitals that can take more than one electron, the formal description is done by considering non-spin-degenerate single-particle levels E_n, as the charge discretization imposed by Coulomb Blockade merges together with the discrete orbitals in the QD-DOS. The total electrostatic energy of the system is written as:

$$U_{QD}(N) = U_T(N) + \sum_{n=1}^{N} E_n = \frac{e^2}{2C}(N - N_{ext})^2 - \frac{(eN_{ext})^2}{2C} + \sum_{n=1}^{N} E_n. \tag{1.2.27}$$

and the chemical potential is calculated in the same way as previously done,

$$\begin{aligned} \mu_{QD}(N, V_B, V_G) &= \frac{e^2}{C}\left(N - \frac{1}{2}\right) + E_N - e\frac{C_S}{C}V_B - e\frac{C_G}{C}V_G = \\ &= -e\alpha_B V_B - e\alpha_G(V_G + V_G^N), \end{aligned} \tag{1.2.28}$$

the degeneracy point being located at $V_G^N = (-e/C_G)(N - 1/2) - E_N/e\alpha_G$. The energy required to add an electron to the QD now depends on the separation between consecutive levels:

$$E_{add}(N) = \mu_{QD}(N) - \mu_{QD}(N-1) = \frac{e^2}{C} + E_N - E_{N-1} = E_U + E_\delta(N), \tag{1.2.29}$$

Although the electrostatic description is similar to the nanoisland case, the essential disparity between their continuous DOS and the discrete-spectrum of QDs lead to fundamental differences appearing in the transport features and properties of both kinds of devices. On one hand, the energy levels at conduction collapse the wave function of tunneling electrons into the corresponding quantum state at the dot. On the other hand, the drastic reduction of internal scattering processes in the QD fixes its electronic distribution among the levels at sufficiently low temperatures, restricting their availability for contributing to the sequential current. While such transport properties are discussed later, here we focus on the resulting modifications that they cause in the transport maps of QD transistors with respect to nanoisland SETs. Firstly, the N-dependence of the level spacing, $E_\delta(N) = E_N - E_{N-1}$, originates non-uniform separations between consecutive degeneracy points, as $e\alpha_G(V_G^{N-1} - V_G^N) = E_U + E_\delta(N)$ [73] (appreciable in Fig. 1.6a). In fact, the spin-degeneracy of the actual orbitals in QDs vanishes the spacing, $E_\delta(N) = 0$, typically for odd filling factors, N. Secondly,

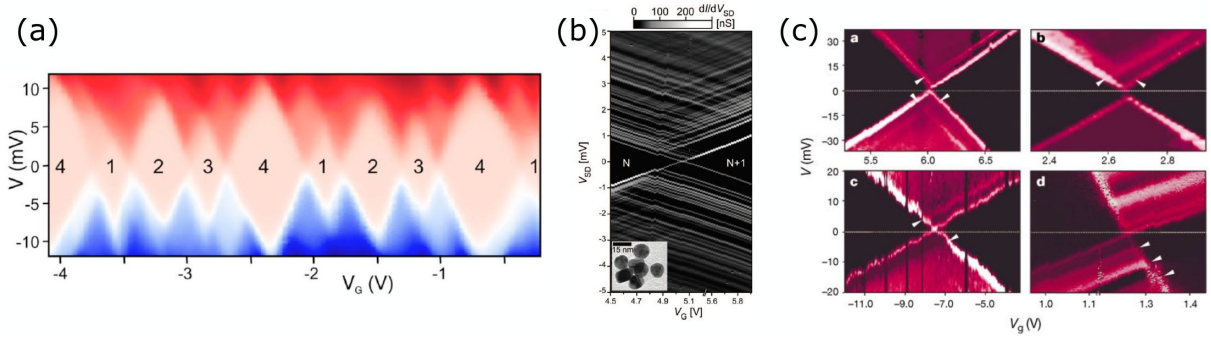

Fig. 1.6: Current and differential conductance maps of QD transistors where the dot structure is (a) a metallic single-walled CNT, showing a non-uniform spacing between the gate positions of subsequent degeneracy points (extracted from [73]), (b) a 15-nm-diameter metallic nanoparticle presenting several electronic excitations caused by the inclusion of addition energy levels withing the bias window (extracted from [76]), and (c) a C60 molecule, displaying a few vibrational excitations (extracted from [74]).

the current inside on-state regions becomes completely staircase-shaped, showing additional lines running parallel to the diamond edges as subsequent orbitals enter the V_B-window (typically displayed by devices contacting metallic nanoparticles, Fig. 1.6b). Like this, the E_δ values of subsequent orbitals can be extracted either from the bias voltage at the intersection between the corresponding line and the diamond edge, or from the separation between consecutive degeneracy points. Vibrational modes of the QD, more commonly observed in molecular devices, can also promote the dot's conduction when the applied V_B corresponds to their excitation energy of resonance, appearing also as lines running parallel to the diamond edges [74, 75] (Fig. 1.6c).

In a closer view of the phenomenology exhibited by these nanometer-scale SETs, the smaller size of the central electrode generally carries along a higher sensitivity to parameters taken as constant in the Orthodox theory. For example, the charging energy scale E_U may suffer significant increases as more and more electrons are loaded in the dot [77]. Important differences can also appear in the capacitive and tunnel couplings to the leads of different energy levels belonging to the same QD [78, 79]. In addition, as the leads generally present a size much bigger than the dot itself, they can induce a screening of the V_G-generated electrical field, leading to a non-linear dependence of $\mu_{QD}(V_G)$, i.e., an effective variation of $\alpha_G(V_G)$. However, the characterization analysis in all kinds of QD transistors is generally first-approached from the perspective of the Orthodox theory, as the magnitude of these deviations is generally sample-dependent and needs to be analyzed for each particular case [80].

SEQUENTIAL TUNNELING IN A QUANTUM-DOT TRANSISTOR

The overlapping of charge and energy discretization (respectively caused by Coulomb blockade and quantum confinement), requires to meet conditions concerning both spacings scales, E_U and E_δ, for activating the dot's conduction [66, 58]. We restrict the discussion to the typical regime of our samples: $E_U \gtrsim E_\delta$, in which a few levels can contribute to the dot's conduction at a single charge state [81]. The description of the resulting sequential tunneling is approached similarly to the nanoisland case, by considering three available charging states $(N-1, N, N+1)$ in a given V_G range, and transitions between them are caused by first-order tunneling processes supported by the single-particle energy levels laying in the V_B range considered. For N electrons being initially at the dot and a tunnel event moving one electron in/out of the QD from/to the lead $l = S, D$, the chemical potential differences between a particular QD single-particle level (n, of energy E_n) and the leads are:

$$\begin{cases} \Delta E_S^{in}(N,n) = \mu_{QD}(N+1) - (-eV_B) = (e^2/C)(N+1/2) - e\alpha_G V_G + (1-\alpha_B)eV_B + E_n, \\ \Delta E_S^{out}(N,n) = \mu_{QD}(N) - (-eV_B) = (e^2/C)(N-1/2) - e\alpha_G V_G + (1-\alpha_B)eV_B + E_n, \\ \Delta E_D^{in}(N,n) = \mu_{QD}(N+1) = (e^2/C)(N+1/2) - e\alpha_G V_G - e\alpha_B V_B + E_n, \\ \Delta E_D^{out}(N,n) = \mu_{QD}(N) = (e^2/C)(N-1/2) - e\alpha_G V_G - e\alpha_B V_B + E_n. \end{cases}$$

Several considerations need to be taken into account for writing the tunneling rate equations. First of all, the discrete QD-DOS is expressed as a set of Dirac-delta functions, $D_{QD} = \sum_n \delta(E - E_n)$. Secondly, the electronic distribution function is discretized as well: the possibility of the QD to take/deliver an electron to/from the leads is modulated with the probability of each level to be occupied (so that it cannot take an electron from the leads, but it can deliver it) or empty (vice versa). The tunneling rates between the leads and the nth level are expressed in terms of its occupation number, m^n_{occ}, being equal to $0(1)$ if the level is empty (filled), replacing the usual Fermi-Dirac distribution function by a Kronecker's delta:

$$\begin{aligned} \Gamma^{N,n}_{S(D)\to QD} &= \frac{2\pi|\tau_{S(D)}|^2 D_{S(D)}(0)}{\hbar} \int f(E - eV_{S(D)})\delta(E - \Delta E^{in}_{S(D)}(N,n))\delta_{m^n_{occ},0}\, dE = \\ &= \frac{2\gamma_{S(D)}}{\hbar}\, \delta_{m^n_{occ},0}\, f_{S(D)}(\Delta E^{in}_{S(D)}(N,n) - eV_{S(D)}), \end{aligned} \tag{1.2.31}$$

$$\begin{aligned} \Gamma^{N,n}_{QD\to S(D)} &= \frac{2\pi|\tau_{S(D)}|^2 D_{S(D)}(0)}{\hbar} \int [1 - f(E - eV_{S(D)})]\delta(E - \Delta E^{out}_{S(D)}(N,n))\delta_{m^n_{occ},1}\, dE \\ &= \frac{2\gamma_{S(D)}}{\hbar}\, \delta_{m^n_{occ},1} \left[1 - f_{S(D)}(\Delta E^{out}_{S(D)}(N,n) - eV_{S(D)})\right], \end{aligned} \tag{1.2.32}$$

where $\gamma_{S,D} = \pi D_{S,D}(0)|\tau_{S,D}|^2$, are the tunnel couplings between the dot and each respective leads, considered here as independent of the particular level addressed. The rates $\Gamma_{S,D}$ show a plateau-shape dependence on the voltages, with a Fermi-Dirac smearing on the sides. The maximum value at the plateaus flat summit, $\Gamma_{S,D} = max(\Gamma^{N,n}_{QD\to S,D})$, is usually taken as a characteristic rate of the junction, related to the coupling as $\gamma_{S,D} = \hbar\Gamma_{S,D}/2$.

Likewise the nanoisland case, a generic expression for the current flowing through an individual n level can be expressed in terms of its tunneling rates. To obtain the total net current, it is necessary to sum this expression up to the maximum number of levels in the dot considered (n_{max}) and over all possible configurations of the N electrons present in the dot, distributed among all the levels ($\{m^i_{occ}\} = \{m^1_{occ}, m^2_{occ}, ...\}$):

$$I_{QD} = -e \sum_{n=1}^{n_{max}} \sum_{\{m^i_{occ}\}} P(\{m^i_{occ}\}) \left(\Gamma^{N,n}_{D\to QD} + \Gamma^{N,n}_{QD\to S} - \Gamma^{N,n}_{S\to QD} - \Gamma^{N,n}_{QD\to D}\right), \tag{1.2.33}$$

where $P(\{m^n_{occ}\})$ is the stationary probability of each $\{m^n_{occ}\}$ electronic configuration. Interestingly, at equilibrium ($V_B = 0$), the probability distribution of each configuration is well described the Fermi-Dirac function only for temperatures much greater than the levels' energy difference, allowing transitions between them. However, as soon as the thermal energy becomes considerably lower than the average level spacing ($E_\delta \gg k_B T$), electronic transitions are greatly reduced and the equilibrium configuration is better described by the distribution of Gibbs.

When a biasing voltage is applied driving the system out of equilibrium, tunneling events continuously change the charge state between $N-1, N$ and $N+1$, and the electronic configuration in the QD deviate from Gibbs distribution. Expressions for the time evolution of each non-equilibrium configuration probability, $P(\{m^n_{occ}\})$, can be written using the master equation approach. For constant V_B and V_G, the kinetic equations are equal to zero and only stationary configurations are possible,

whose probabilities can be calculated by solving the corresponding system of detailed balance equations (one equation per single-particle level). Solutions were found by *Averin et al* for the asymmetric dot-scales ($E_U, k_BT \gg E_\delta$ and $E_\delta, k_BT \gg E_U$), allowing them to obtain the $I-V_B$ curves of the QD junction [66], and to take the effect of a relaxation rate at the QD into consideration [82]. Separately, *Carlo Beenakker* included a gate electrode in this picture and, by introducing a linear-in-V_B deviation of the stationary configurations' probabilities from the equilibrium distribution, he developed a linear-response theory describing the transport in the QD transistor at the zero-V_B limit for different energy-scale hierarchies [58], discussed in the following.

CONDUCTION AND HYBRIDIZATION OF A SINGLE ENERGY LEVEL

One of the most remarkable differences arising in the transport features of QD junctions compared to nanoisland-based devices stems from the spin degeneracy of the orbitals in the QD. The resulting effects manifest at the on-state conduction regions when the sequential current is conveyed by an single QD orbital. Large relative values of E_U and E_δ are required, in comparison with the thermal energy, which must be kept small to avoid thermal excitations in the QD, keeping its electronic distribution at the ground state: all the orbitals are completely filled up to a lowest unoccupied orbital, which carries the current. For an accurate description, the total coupling ($\gamma_T = \gamma_S + \gamma_D$), must be the lowest energy scales of the system, suppressing higher-order processes. The resulting hierarchy ($E_U \gtrsim E_\delta \gg k_BT \gg \gamma_T$) is necessary to restrict the current to sequential tunneling processes conveyed by a single orbital, addressed individually at the corresponding charge-degeneracy point (V_G^n) within biasing-range such that $0 < |eV_B| < E_\delta$.

Considering a double spin degeneracy ($\uparrow$ and $\downarrow$), the orbital under consideration can be either empty or half-filled (Fig. 1.7a or b, respectively). By solving the rate equations in this energy-scale regime and taking into account the effect of the spin degeneracy, *Bonnet et al* deduced simple expressions for the current[3] in both cases [83]. If the orbital is initially empty (Fig. 1.7a), the first sequential tunneling event (lead $\rightarrow QD$) can transfer an electron of spin either $\uparrow$ and $\downarrow$. However, the fixation of the electron's spin at the QD reduces, in the second sequential event ($QD \rightarrow$ lead), the number of accessible states in the lead to just half of its total DOS (considering a spin-balanced conduction band). An asymmetry appears in the current expression, depending on the direction of the electron transfer ($S \leftarrow QD \leftarrow D$ for $V_B > 0$, or $S \rightarrow QD \rightarrow D$ for $V_B < 0$):

$$I^{n,+}_{QD(\textit{empty})} = \frac{4e}{\hbar}\,\frac{\gamma_S\gamma_D}{\gamma_S+2\gamma_D} \qquad \text{and} \qquad I^{n,-}_{QD(\textit{empty})} = -\frac{4e}{\hbar}\,\frac{\gamma_S\gamma_D}{2\gamma_S+\gamma_D}, \tag{1.2.34}$$

as a consequence of such spin-induced bottleneck caused in the second sequential tunneling event. On the contrary, if the orbital is already half-filled (Fig. 1.7b), the spin-induced bottleneck is originated at the first sequential tunneling event. The expression for the sequential current at different bias signs are then reversed:

$$I^{n,+}_{QD(\textit{half})} = \frac{4e}{\hbar}\,\frac{\gamma_S\gamma_D}{2\gamma_S+\gamma_D} \qquad \text{and} \qquad I^{n,-}_{QD(\textit{half})} = -\frac{4e}{\hbar}\,\frac{\gamma_S\gamma_D}{\gamma_S+2\gamma_D}. \tag{1.2.35}$$

While in the ideal case of identical couplings ($\gamma_S = \gamma_D$), the spin-bottleneck acts equally in both tunneling directions and for both QD orbital occupations (resulting in equal currents intensities for $\pm V_B$), an additional tunneling bottleneck, stemming from an asymmetry in the coupling characterizing each lead, usually comes into play in actual samples. In fact, at a given orbital occupation, and for a V_B polarity such that the sequential tunneling event of spin-reduced probability coincides with the lead displaying a weaker coupling, both bottlenecking effects add up, reducing the corresponding current step significantly with respect to that one measured at the opposite bias [84]. These relations are extremely useful as they provide a straightforward method for extracting the tunnel couplings from the measurement of the current at a degeneracy point of a QD transistor.

[3] Note that the formulas in Ref. [83] are expressed in terms of the tunneling rates, $\Gamma_{S,D}$, while here we present them as a function of the couplings, taking into account that $\gamma_{S,D} = \hbar\Gamma_{S,D}/2$.

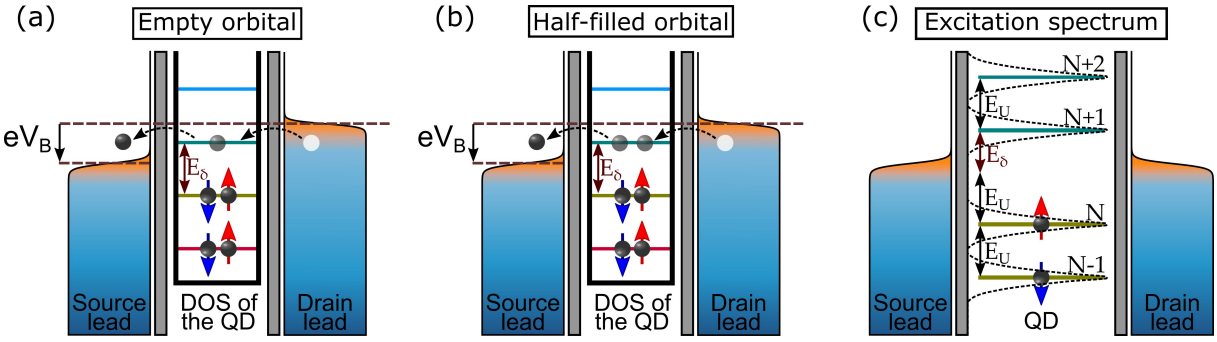

Fig. 1.7: Energy schematics showing a voltage-biased QD junction, where the conduction is carried out by a spin-degenerated orbital being initially: (a) empty and (b) half-filled (charge states are not shown explicitly in these sketches). (c) The charging states of the junction overlap with the discrete orbitals, originating unequally spaced degeneracy points. The thermal/lifetime broadening is qualitatively indicated by the dotted lines.

Regardless of the coupling differences and the conducting orbital occupation, the current asymmetry disappears at the $V_B \to 0$ limit and the linear-response theory developed by *Beenakker* [58] allowed him to derive an expression relating the tunnel couplings with the top-conductance of the Coulomb resonance of the single-particle level, appearing when sweeping V_G through the corresponding degeneracy point (V_G^n):

$$G^n_{max} = \frac{\mathcal{G}_n e^2}{4k_BT}\frac{\Gamma_S\Gamma_D}{\Gamma_S+\Gamma_D} = \frac{\mathcal{G}_n e^2}{\hbar}\frac{1}{2k_BT}\frac{\gamma_S\gamma_D}{\gamma_S+\gamma_D}, \tag{1.2.36}$$

Here, $\mathcal{G}$ accounts for the spin degeneracy, equal to 1(2) if the orbital is empty (half-filled). This relation is, in principle, equivalent to the single-level current expressions above, so that it cannot be used independently to extract the tunnel coupling but it provides an alternative method. In addition, this theory also describes the lineshape of the resonance peak as:

$$G^n_{QD} = \left.\frac{I}{V_B}\right|_{V_B\to 0} = G^n_{max}\cosh^{-2}\left(\frac{e\alpha_G(V_G - V_G^n)}{2k_BT}\right). \tag{1.2.37}$$

While the zero-temperature divergence of this formula makes it not suitable to describe the conduction in this limit, it reproduces accurately the widening caused by the thermal smearing (originated by the Fermi-Dirac distribution of electrons in the electrodes), leading to a full-width at half-maximum (FWHM) of the resonance peak around $3.5k_BT/e\alpha_G$ at the weak coupling regime considered ($E_U \gtrsim E_\delta \gg k_BT \gg \gamma_T$). On one hand, this result explains the finite width of Coulomb oscillations observed in measurements despite the alleged Dirac-delta character of the levels in the QD-DOS (Fig. 1.7c). On the other hand, it settles a theoretical upper boundary for the maximum spectroscopic resolution that can be achieved with contacting leads in the normal (N) metallic state, as limited by the thermal broadening.

In theory, even at a low-temperature regime (such that $E_U \gtrsim E_\delta \gg \gamma_T \gg k_BT$, where Eqs. 1.2.37 and 1.2.36 do not hold anymore) the FWHM of Coulomb resonances saturates at a finite value. Actually, the finite tunneling rates existing between the dot and the leads carry along an intrinsic widening of the spectral lineshape of the orbitals, known as life-time broadening, proportional to the corresponding coupling scales ($\gamma_{S,D}$). The hybridization that the QD orbitals undergo, as a consequence of their finite coupling to the continuum of electronic states in the DOS of the leads, broadens them, loosing their Dirac-delta character even at zero temperature. In fact, this limit is studied in chapter 6 of Ref. [51], from the perspective of the Landauer-Buttiker formalism. By expanding the single-level transmission coefficients of conduction channels for small couplings, at $T = 0$, a Lorentzian-like broadening is obtained

$$\tau_n(E) = \frac{\Gamma_S\Gamma_D}{\Gamma_S+\Gamma_D}\,\mathcal{L}_n(E) = \frac{\Gamma_S\Gamma_D}{\Gamma_S+\Gamma_D}\left(\frac{1}{\pi}\frac{\Gamma_T/2}{([E-E_n]/\hbar)^2+(\Gamma_T/2)^2}\right), \tag{1.2.38}$$

where $\Gamma_T = \Gamma_S + \Gamma_D$ is the total tunneling rate, and $\mathcal{L}$ is a Lorentzian function centered at the energy E_n of the corresponding nth level (taken as the energies origin). The resulting conductance peak at the Coulomb resonance inherits the Lorentzian (Breit-Wigner) shape [58]:

$$G^n_{QD}(E) = \frac{\mathcal{G}_n e^2}{h} \frac{\Gamma_S \Gamma_D}{\Gamma_S + \Gamma_D} \mathcal{L}_n(E) \qquad \text{and} \qquad G^n_{max} \frac{\mathcal{G}_n e^2}{\hbar} \frac{4\gamma_S \gamma_D}{(\gamma_S + \gamma_D)^2} \tag{1.2.39}$$

displaying a finite lifetime broadening that remains even at zero temperature. In this limit, the Coulomb peak displays a FWHM equal to the total tunnel rate $\hbar\Gamma_T$, establishing the maximum spectroscopic resolution reachable in N-state QD junctions. The resonance's top-conductance is renormalized with the coupling amplitudes, saturating for symmetric tunnel ($\gamma_S = \gamma_D$) at the conductance quantum, $2e^2/\hbar$, for doubly spin-degenerated orbitals ($\mathcal{G}_n = 2$).

1.2.3 Higher-order transport processes

So far we have only considered first-order elastic tunneling processes, which usually constitute the main contribution for the current in the weak coupling regime. However, as the tunnel couplings of the QD junction increases, so does the probability of higher-order processes to take place. Such higher-order processes can be understood as a set of single-electron tunneling events, each of them happening with a probability modulated by $\gamma_{S,D}$, depending if they involve an electron transfer between the QD and S or D. By considering a unique coupling scale $\gamma \approx \gamma_S \approx \gamma_D$ for simplicity, the total probability of a particular higher-order process composed of $\mathcal{N}$ single-electron events is then proportional to $\gamma^{\mathcal{N}}$, as it can be derived by applying Fermi golden's rule to the ensemble of events that compose it [86]. Hence, second-order processes (composed of just two single-electron tunneling events) emerge earlier for increasing couplings. In specific QD junctions, second-order processes are easily observable, also called cotunneling processes, which enable the conduction of the device inside the Coulomb blocked regions. Although the total energy of the system is conserved in all cases, cotunneling processes are often classified as being elastic (if the QD electronic distribution is kept in the ground state configuration, shown in Fig. 1.8b) or inelastic (if the QD ends up in an excited state, illustrated in Fig. 1.8c). In an experiment done on a 2DEG-QD transistor, *De Franceschi et al* showed the apparison of both types of cotunneling [85]. A non-zero net current caused by elastic cotunneling takes off as soon as a finite bias is applied, generating a bias-dependent conductance background inside the blocked diamonds, regardless of the parity of the charging state (occupation of the conduction orbital). Differently, inelastic cotunneling takes place only at even-N charge states, as one tunneling

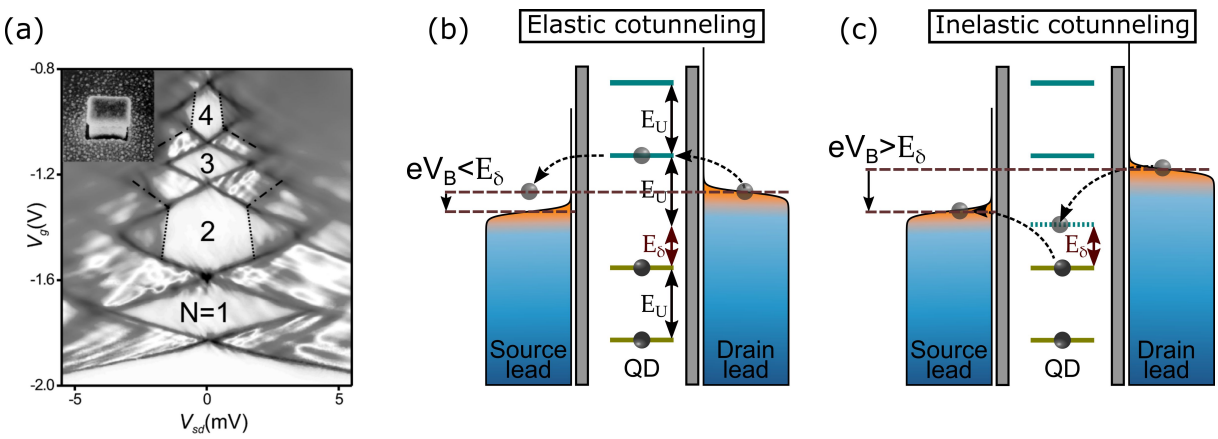

Fig. 1.8: (a) Differential-conductance map of a QD transistor (shown in the inset), showing the simultaneous presence of Coulomb diamonds and cotunneling features, indicating the QD occupation at each charge state (extracted from Ref. [85]). (b) Tunneling path of the elastic cotunneling process, in which one electron tunnels from S to D through a higher-energy single-particle level. (c) Tunneling path of the inelastic cotunneling process, in which one electron tunnels from S to an excited state in the QD, while the electron at the highest orbital tunnels out of the QD to D.

event addresses the subsequent orbital in the QD (at an energy of E_δ with respect to the conduction orbital). Consequently, inelastic cotunneling emerges in the transport map at even diamonds, with a sharp onset at $|eV_B| = E_\delta$ (Fig. 1.8a). After an inelastic cotunneling process has taken place, the QD is left in an excited state, requiring for the QD deexcitation to restart the process. As 2DEG-QDs are embedded inside an heterostructure, the decay is easily achieved by the significant rate of electron-phonon interactions in these kind of devices. Interestingly, the reduced phonon-mediated tunneling rate associated results in a smaller broadening of the corresponding conductance feature with respect to diamond edges, leading to an increased spectroscopic resolution (down to 10 μeV of FWHM) at the inelastic-cotunneling conductance onsets. On the contrary, the large charging energy characteristic of our QD transistors ($E_U \sim 10 - 100$ meV), makes both kinds of cotunneling effects to be generally inappreciable in our measurements.

The master-equation approach previously employed to calculate the sequential current takes into consideration exclusively first-order processes. *Meir and Wingreen* derived a general expression for the current, accounting for processes up to a predefined order, by describing the tunneling processes in the QD junction system under the Keldysh formalism, employing the Green function method [87]. The Landauer-type formula obtained with this approach takes into consideration the lifetime broadening of the QD orbitals and the probability-enhancing effect that it exerts on higher-order processes.

1.2.4 Kondo effect: the intermediate-high coupling regime

Similarly to superconductivity, the origin of Kondo effect lies on its phenomenological discovery while carrying out low-temperature experiments, popularized in the first half of the last century thanks to the technological achievement of Helium liquefaction. Again, the subject under study was the electrical resistance R of metals which, in the Fermi-liquid theory, is associated with scattering processes of different nature that own distinct temperature dependences. The electron-phonon interaction, scaling as T^5, is the main resistance source at ambient conditions, vanishing rapidly as the temperature is decreased. The electron-electron interaction scales as T^2, dominating over the phonon scattering at low temperatures. These two contributions lead to a monotonic decrease of the resistance with T, and vanish in the zero-T limit, where R levels off to a finite residual value, R_0, determined by the presence of defects and impurities (temperature-independent scattering sources). However, it was reported that Ag and Au wires often show a resistance increase below a certain T, attributed to different degrees on the purity of the metal [88]. This behavior remained unexplained for 30 years, until *Jun Kondo* developed a model to describe the global consequence that the spin-scattering effects induced by magnetic impurities has on in the electrical resistance of the system [89] (in the frame of perturbations' theory for a small magnetic interaction). It turned out later that impurities of magnetic materials, like Fe or Mn, are naturally present in noble metals, explaining why this anomalous resistance increase was not observed in similar wires made of non-noble elements.

Kondo's model is based on the antiferromagnetic exchange interaction, J, established between the electrons in the conduction band of the continuous metallic medium and a magnetic impurity[4]. The usual expression for the tunneling hamiltonian (Eq. 1.1.8) can be transformed to explicitly show its dependence on J as

$$H_T = J\boldsymbol{s_B}\boldsymbol{S_0} = \frac{J}{2}\sum_{k,k',\sigma,\sigma'} c^\dagger_{k'\sigma'}\boldsymbol{\sigma}_{\sigma',\sigma}c_{k\sigma}\cdot\boldsymbol{S_0}, \tag{1.2.40}$$

where $\boldsymbol{S_0}$ is the spin of the impurity and $\boldsymbol{s_B}$ is the average spin of the conduction-band electrons at the impurity site ($\boldsymbol{r_0}$), which can be expressed in terms of the creation/annihilation operators as $\boldsymbol{s_B}(\boldsymbol{r_0}) = 1/2(c^\dagger(\boldsymbol{r_0})\boldsymbol{\sigma}c(\boldsymbol{r_0}))$ (where $\boldsymbol{\sigma}$ represent Pauli's matrix). By tackling the problem using a linear-response theory, Kondo computed the spin-scattering probability, obtaining a logarithmic dependence of the resistance of an impurity-contaminated wire with temperature:

$$R(T) = R_0\left(1 - 2JD(0)\ln\left(\frac{k_BT}{W}\right) + ...\right), \tag{1.2.41}$$

[4] In this convention, the interaction is antiferromagnetic for $J > 0$, and $J < 0$ refers to ferromagnetic interaction.

where R_0 is the residual resistance at $T = 0$, while $D(0)$ and W are the DOS at E_F of the metal medium and its conduction half-bandwidth. As the temperature is decreased below W/k_B, a logarithmic increase of the resistance is obtained, eventually diverging for $T \to 0$. In fact, by considering following higher-order scattering processes, and summing up the main contributions, *Alekséi Abrikosov* arrived to an approximate expression for the overall resistance [90], showing an even stronger divergence at the zero-temperature limit:

$$R(T) \approx \frac{R_0}{[1 + 2JD(0)\ln(k_B T/W)]^2}. \tag{1.2.42}$$

From this formula, it is possible to estimate the magnitude of the divergence at different temperatures, independently from the system's particular resistance. The so-called Kondo temperature,

$$k_B T_K \approx W\sqrt{2JD(0)}\exp\left\{-\frac{1}{2JD(0)}\right\}, \tag{1.2.43}$$

identifies the energy scale that characterizes such Kondo effect and indicates the temperature at which the perturbation in Eq. 1.2.41 becomes of order one. Similar expressions in the literature differ by a $\sqrt{2}$ multiplicative factor depending on the definition of J

Logically, Kondo's perturbation approach is unsuitable for describing the system at low temperatures ($T \lesssim T_K$) as the exchange interaction becomes dominant and cannot be treated as a perturbation anymore. Parallel in time, *Phil Anderson* was studying the same problem from the local perspective (with the Hartree-Fock method), considering a single atomic-like magnetic impurity tunnel coupled to the metallic medium [93]. He proposed an alternative way for describing the low temperature limit, by applying a scaling theory and representing Kondo's systems by a coarse-grained model, that becomes coarser when reducing the temperature [94]. Inspired by this idea, *Kenneth Wilson* developed a numerical technique based on the renormalization group theory for computing this scaling approach [95] (known as numerical renormalization group method, or NRG). This non-perturbative technique allowed him to describe the Kondo system accurately at the zero-temperature limit, constituting a central part of the work for which he was awarded a Nobel prize. His results were corroborated afterwards, when particular solutions of the Kondo model could be finally found analytically [96, 97]. In the elusive low-temperature regime ($T < T_K$), Kondo effect is understood as a many-body phenomenon in which the free-electrons in the conduction band of the metal congregate around the impurity to screen out its magnetic field (Fig. 1.9a). This agglomeration of screening electrons,

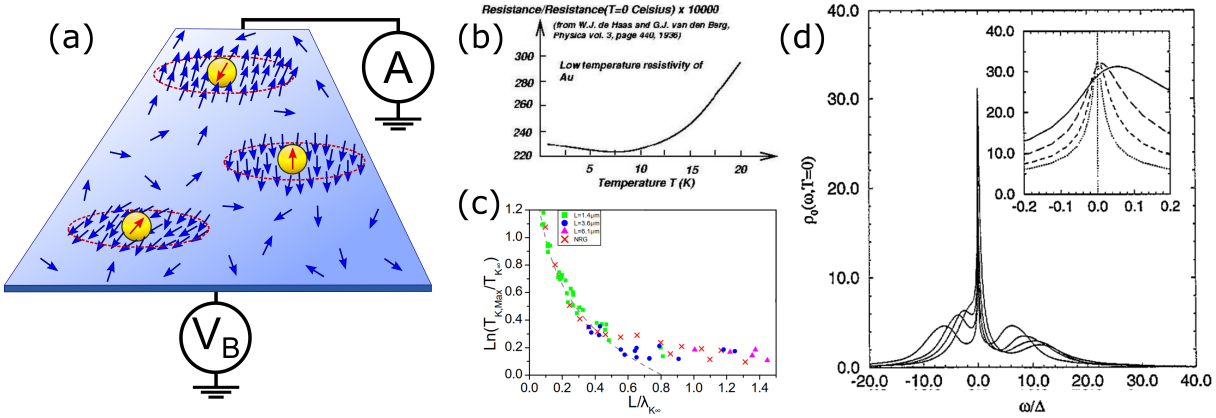

Fig. 1.9: (a) Magnetic impurities in a metallic wire are screened by electrons in the conduction band, acting as scattering centers for $T < T_K$. (b) Resistance measurement of an Au wire containing magnetic impurities, showing an upturn around 7 K (extracted from [88]). (c) A magnetic QD embedded in a Fabry-Perot interferometer of variable cavity-length, L, allows to measure a Kondo cloud's extension of to $\lambda_K \sim 1$ μm (extracted from [91]). (d) Spectral function of a Kondo-correlated QD (obtained by NRG simulations), displaying a Kondo resonance at E_F and satellite Coulomb peaks for different values of the level depth, ϵ_0 (extracted from [92]).

known as the Kondo-cloud, owns a total average spin equal and opposite to that of the impurity. A spin-singlet local ground state (with a bonding energy of $k_B T_K$) is then established mutually between the metal and the impurity, conforming a spin-correlated system. The length scale $\lambda_K \sim \hbar v_F / k_B T_K$ (where v_F is the Fermi velocity) determines the spatial extension of the spin correlations in the metallic media (in other words, the extension of the Kondo cloud). However, the exponential decay of Kondo correlations intensity at distances larger than λ_F and its sensibility to detection systems makes difficult to probe the Kondo cloud away from the impurity. Only recently, specifically-designed samples involving measuring systems of reduced invasiveness, have demonstrated a Kondo cloud extension up to a few μm away from the impurity in 2DEG systems [91] (Fig. 1.9c). Although all the electrons in the metallic band participate in the screening process, a more efficient screening is granted by high-energy electrons (around E_F). The different screening contributions results in a locally modified metallic DOS close to the impurity, manifesting itself in the spectrum of the system as a resonance peak pinned at the Fermi-level (reproduced by NRG simulations, as shown in Fig. 1.9d), which constitutes a distinctive and identifying feature of Kondo-correlated systems.

KONDO EFFECT IN QUANTUM-DOT TRANSISTORS

In tunnel junctions contacting a magnetic QD at an intermediate coupling regime ($E_U \gg \gamma_T \gg k_B T$) the QD-lead distance starts to be short enough for a significant J interaction to be established between the electrons in both objects. Spin correlations extend locally over Kondo-coupled electrodes (Fig. 1.10a), imposing a common ground state at each QD-lead system that originates remarkable differences in the transport features with respect to weakly coupled junctions. These correlations intensify as the ratio E_U/γ_T decreases and govern the transport completely at the strong-coupling regime ($\gamma_T \gg E_U \gg k_B T$). Paradoxically, opposite to the resistance increase observed for impurities embedded in a continuous medium, the correlated state in the QD-junction geometry (where the impurity constitutes a link between two semi-continuous metallic media) results in a surprising enhancement of the dot's conduction, well described by the single-impurity Anderson's model (SIAM) [98, 99]. A vast amount of Kondo-assisted transport has been reported in QD junctions over the last three decades, thanks to the experimental accessibility for contacting each time smaller dot structures that results in a higher localization of the unpaired-spin and a narrower QD-lead gap that strengthen the coupling. Some examples of QD junctions that may display Kondo-correlations include 2DEG systems [100, 101, 102], CNTs [103], and different kinds of colloidal QDs like metallic nanoparticles [104], fullerenes [105, 106] or wire-like molecules [107, 108], as well as magnetic adatoms investigated by STM [109], just to name a few. More exotic systems may exhibit additional features, like low-intensity satellite resonances originated by electronic excitations at the dot [110] or a twofold main resonance appearing for integer-spin impurities [78, 111].

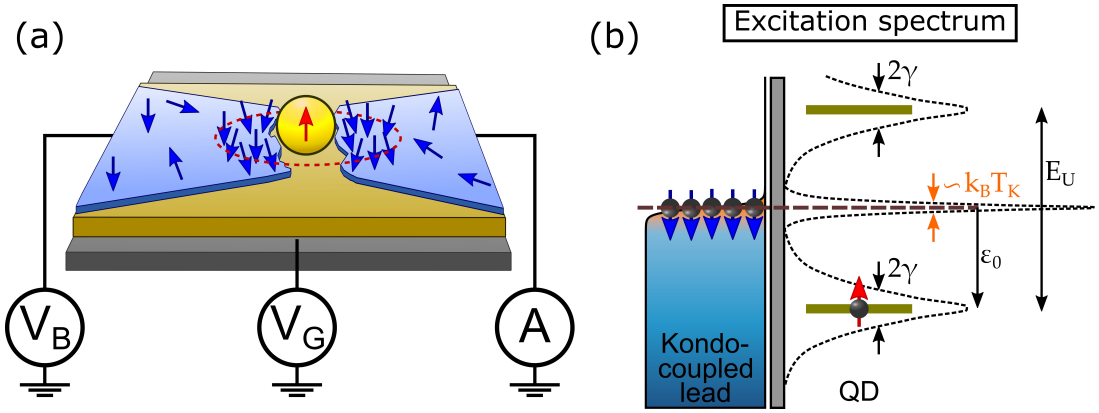

Fig. 1.10: (a) Kondo effect develops in a QD junction, induced by an unpaired spin at the dot. A common Kondo-singlet ground state extend locally over both leads for relatively symmetric couplings. (b) Energy diagram of a system formed by a metallic reservoir Kondo-coupled to an oddly-occupied QD, as considered in Anderson's model.

The SIAM simplifies the QD by considering a single spin-degenerated resonant orbital which can be empty, half-filled or completely filled (with respective occupation numbers of $N = 0, 1, 2$). If half-filled, oddly occupied orbital adopts a doublet configuration (either $\Psi_0 = |\uparrow\rangle$ or $|\downarrow\rangle$) whose unpaired spin confers the dot a magnetic character (regardless of the material it is made of), leading to the formation of an opposite-spin Kondo cloud at the electrode. The QD-lead forms a spin-correlated system, adopting a local screening ground state described as a Kondo-singlet, $|\Psi_K\rangle$. The magnetic character is lost for an even filling factor (corresponding to singlet dot-states of $\Psi_0 = |0\rangle, |\uparrow\downarrow\rangle$ for $N = 0, 2$), making the spin correlations to vanish and the Kondo cloud to dissolve. The combination of the orthodox theory with the Hartree-Fock approach to the many-body problem allows the SIAM to describe the QD-lead system along the three charge states ($N = 0, 1, 2$). While analytical solutions of the model have been found well-inside the charge states, at the diffuse frontier of the degeneracy points Kondo effect merges with first-order processes allowed by Coulomb blockade, and NRG simulations are required to reproduce the system's behavior. Each electrode in the QD junction is accounted for in the standard SIAM hamiltonian by a pair of terms H_N^l and H_T^l, (respectively describing the free-electrons of momentum $\kappa = k, q$ assuming an s-wave character at each lead, $l = S, D$, and their respective tunnel interaction with the QD, $\gamma_{S,D}$), that share the same dot component, H_0 (representing the two single-particle levels of the dot's d-like orbital):

$$\begin{aligned} H &= H_N^l + H_0 + H_T^l \\ &= \sum_{\substack{\sigma,\kappa=k,q \\ l=S,D}} \epsilon_\kappa c_{\kappa\sigma}^\dagger c_{\kappa\sigma} + \sum_\sigma \left(\epsilon_0 d_\sigma^\dagger d_\sigma\right) + E_U d_\uparrow^\dagger d_\uparrow d_\downarrow^\dagger d_\downarrow + \sum_{\substack{\sigma,\kappa=k,q \\ l=S,D}} \left(\tau_\kappa c_{\kappa\sigma}^\dagger d_\sigma + \tau_\kappa^* d_\sigma^\dagger c_{\kappa\sigma}\right), \end{aligned} \tag{1.2.44}$$

The level depth, ϵ_0, is the chemical potential of the QD orbital, and $\epsilon_{\kappa=k,q}$ are the energy of free-electrons at each lead, all measured with respect to an origin taken at E_F^D of the drain (as depicted in Fig. 1.10b for a single electrode). Indeed, ϵ_0 corresponds to a shifted μ_{QD} (defined in Eq. 1.2.28), by taking the V_G origin at a gate value of $V_G^0 = (-e/C_G)(N - 1/2) - E_N/e\alpha_G$, where the charge degeneracy between $N = 0$ and $N = 1$ is located:[5]

$$\epsilon_0(V_B, \widetilde{V}_G) = \mu_{QD}(N, V_B, V_G - V_G^0) = -e\alpha_B V_B - e\alpha_G(V_G - V_G^0). \tag{1.2.45}$$

Through a canonical transformation, *Schrieffer and Wolff* demonstrated the relation between the conduction-band spin-operator $\boldsymbol{s_B}$ in Kondo's hamiltonian, with the microscopic QD parameters considered in the SIAM [112]. This allows to express the exchange interaction of the QD with each respective lead and its corresponding interacting hamiltonian component as the sum of two terms, associated with the energies of the two single-particle levels of the dot (at ϵ_0 and $\epsilon_0 + E_U$, as indicated in Fig. 1.10b) [99, 113]:

$$JD(0) \sim \gamma \left(\frac{1}{\epsilon_0 + E_U - \epsilon_\kappa} + \frac{1}{\epsilon_\kappa - \epsilon_0}\right), \tag{1.2.46}$$

$$H_T \sim \sum_{\kappa,\kappa',\sigma,\sigma'} \left(\frac{\gamma}{\epsilon_0 + E_U - \epsilon_{\kappa'}} c_{\kappa\sigma'}^\dagger c_{k'\sigma} d_\sigma^\dagger d_{\sigma'} + \frac{\gamma}{\epsilon_{\kappa'} - \epsilon_0} c_{\kappa'\sigma} c_{\kappa\sigma'}^\dagger d_{\sigma'} d_\sigma^\dagger\right). \tag{1.2.47}$$

Two tunneling events constituting an inelastic cotunneling process appear explicitly in this form of the interactive hamiltonian, creating (annihilating) an electron κ, σ' (κ', σ) in one lead and annihilating (creating) it at the dot. Such Kondo-induced cotunneling, in which the unpaired electron at the dot is inter-exchanged with one from the cloud in the lead, arise as a consequence of an increased localization of screening electrons around the impurity, boosting up the probability of such a higher-order processes to happen. Each cotunneling process carries along a spin-flip of the system, easily understood by decomposing it in single-electron tunneling events: an electron from the cloud at $\epsilon_{\kappa'}$ tunnels into the half-filled dot at the available level of energy $\epsilon_0 + E_U$ (first term in H_T, indicated

[5] Under this convention for the energies origin and the dot's chemical potential, the values adopted by the level depth are such that $0 < \epsilon_0 < E_U$ for $N = 0$, $-E_U < \epsilon_0 < 0$ for $N = 1$ and $-2E_U < \epsilon_0 < -E_U$ for $N = 2$.

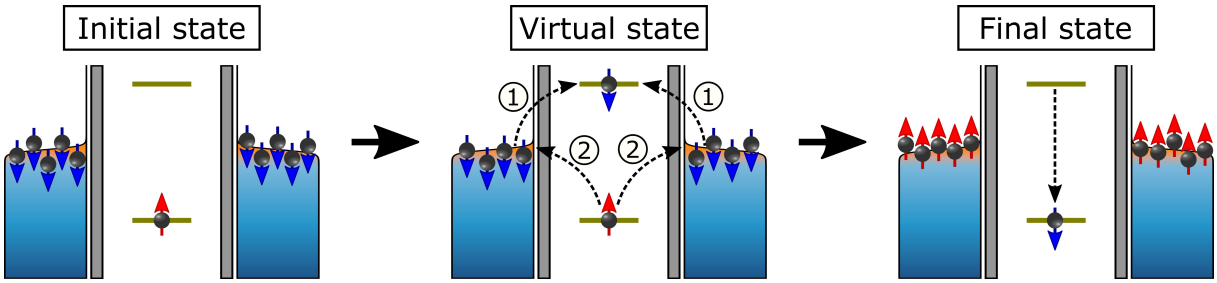

Fig. 1.11: Energy diagram of a symmetrically Kondo-coupled QD junction showing the induced cotunneling process, exchanging electrons with both leads and resulting in a spin-flip of the system. In the virtual state, the order of the tunneling events determines if the excitation is electron-like (1-2) or hole-like (2-1).

in Fig. 1.11b as event 1), or the unpaired electron in the QD, at ϵ_0, tunnels out into the lead at its Fermi level, $\epsilon_{\kappa'}$ (second term of H_T, marked in Fig. 1.11b as event 2). The continuous occurrence of spin-flipping cotunneling processes establish a tunneling resonance between the QD and the electrons at E_F of the lead, with a time-averaged total spin of the system $\mathcal{S} = 0$, being the Kondo-singlet state a superposition of both possible spin configurations of the cloud-dot.

Considering now a second Kondo-coupled electrode, spin-correlations will extend over it equivalently. The cotunneling resonance can occur simultaneously between the QD and both leads, bypassing Coulomb blockade. An overall increase of the dot's conduction with respect to non-magnetic charge states is obtained, specially strong at $V_B = 0$, where the Fermi levels of both leads are aligned (Fig. 1.11). Hence, Kondo effect manifests as a conduction resonance at zero-bias, emerging along odd-occupation diamonds, with an amplitude renormalized by the coupling parameters, expressed in the zero-temperature limit as

$$G_0 = \frac{2e^2}{h}\,\frac{4\gamma_S\gamma_D}{(\gamma_S+\gamma_D)^2}, \tag{1.2.48}$$

reaching the unitary limit for a symmetric coupling ($\gamma_S = \gamma_D$). The binding energy of the cloud-dot singlet state, i.e., the Kondo energy scale k_BT_K (indicated in Fig. 1.10b) determines the resonance width. Actually, as the exchange interaction, J, depends on all other microscopic energy scales (Eq. 1.2.46), the corresponding scale k_BT_K also inherits a dependence on these quantities, resulting in screening clouds of distinct characteristics for different values of E_U, γ, ϵ_0. Two different regimes are defined attending to the level depth position at the odd-diamond (delimited by the charge degeneracy points at $\epsilon_0 = -E_U$ and $\epsilon_0 = 0$):

- **The Kondo regime** ($-E_U + \gamma < \epsilon_0 < -\gamma$). The resonant level is buried well below E_F. The behavior of the system is well described by the Kondo model solution, and the resonance appears well-developed and isolated at zero-V_B. In particular, several works carry out studies at $\epsilon_0 = -E_U/2$ (at the precise center of the odd diamond), where both resonant and empty levels of the QD are at the same distance from E_F, preserving particle-hole energy symmetry.
- **The Mixed-Valence (MV) regime** ($-\gamma < \epsilon_0 < 0$ or $-E_U < \epsilon_0 < -E_U + \gamma$): appearing as the system approaches one of the degeneracy points, and the Kondo and Coulomb conductance resonances merge together, combining the corresponding tunneling processes. The description of the system grows in complexity, and NRG simulations are required for an accurate description of the system.

For a very specific energy-scale hierarchy, such that ($W \gtrsim E_U \gg \gamma \gg k_BT$), and at the Kondo regime ($-E_U + \gamma < \epsilon_0 < -\gamma$), *Haldane* extended the analytical formula of k_BT_K found in Kondo's model (Eq. 1.2.43), expressing it in terms of the SIAM microscopic parameters [114], as

$$k_BT_K \sim \sqrt{\frac{\gamma E_U}{2}}\exp\left\{\frac{\pi\epsilon_0(\epsilon_0+E_U)}{2\gamma E_U}\right\}, \tag{1.2.49}$$

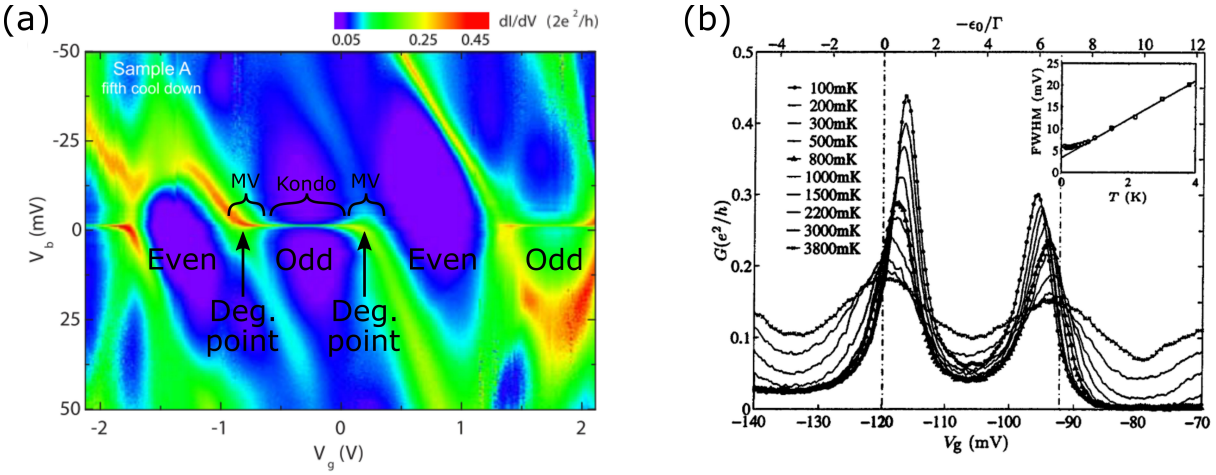

Fig. 1.12: (a) Conductance map of a QD transistor made with a C60 molecule, showing the presence of zero-V_B Kondo resonances at the odd-occupation diamonds (extracted from [105]). (b) Temperature dependence of the zero-V_B Kondo ridge in an 2DEG-based QD transistor, measured across an odd charge state, where the dashed lines signal the degeneracy points (extracted from [101]).

The multiplicative factor in this k_BT_K definition depends on the particular value of ϵ_0 and changes for different ratios between W, E_U and γ[6]. Consequently, a certain variability in the criterion chosen to define k_BT_K is commonly found in the literature. Empirically, this scale is often extracted from the resonance's width, taking k_BT_K as FWHM, FWHM/2, FWHM/3 or similar. Despite the precise value of such prefactor, the gate electrode present in QD transistors allows to map the zero-V_B resonance as a function of $\epsilon_0(V_G)$, forming a ridge that extends over the entire V_G-range of the odd-state diamonds (Fig. 1.12b). The exponential dependence of $k_BT_K(\epsilon_0)$ is reflected in the measurement as a variation in the resonance's lineshape along the Kond ridge. Such variation is qualitatively captured by Eq. 1.2.49 around the odd diamond center if the QD junction display the corresponding energy scale regime ($W, E_U \gg \gamma \gg k_BT$), but it deviates as the degeneracy points are approached (entering the MV regime, as indicated in Fig. 1.12a). Inside the even-occupation diamonds, the magnetic character of the QD vanishes and the Kondo resonance disappears. A more reliable method for deducing the accurate values of T_K lies in studying the evolution of the resonance's top-conductance, when an additional correlation-destroying parameter (like temperature, as shown in Fig. 1.12b) is gradually introduced.

UNIVERSAL EVOLUTION OF THE KONDO CONDUCTANCE

It has been demonstrated that the amplitude of the zero-V_B conductance through the QD caused by Kondo effect only depends on the relative value of k_BT_K and the characteristic energy scale of the perturbation ($E_x = g\mu_BB, k_BT, eV_B$ for magnetic field, temperature and biasing voltage respectively). Different tendencies are followed the relative magnitude both effects (characterized by such E_x/k_BT_K relative scale):

- **For high-energy disrupting effects** ($E_x \gg k_BT_K$): Essentially, the cloud formation is not fully developed in this regime, and the magnetic impurity acts as an inelastic scatterer, leading to a conductance of the form $G(E_x) \sim 1/\ln^2(E_x/k_BT_K)$, in agreement with the results derived by Kondo and Abrikosov at the high temperature limit ($k_BT \gg k_BT_K$) previously discussed.
- **For low-energy perturbations** ($E_x \ll k_BT_K$): *Nozières* showed that the electrons forming the cloud behave as a Fermi liquid, acting as an elastic scatterer [115]. In this regime, the conductance follows $G(E_x) \sim G_0(1 - C(E_x/k_BT_K))^2$, where C is a constant that depends on the type of the perturbation.

[6] Only at particle-hole symmetry ($\epsilon_0 = -E_U/2$) a precise value of 0.182 for the multiplicative factor has been obtained, leading to $k_BT_K = 0.182E_U\sqrt{8\gamma/\pi E_U}\exp\{-\pi E_U/8\gamma\}$ [113].

While there is no analytical model that describes the transition from the perturbation to the high-energy range, *Costi et al* applied Wilson's NRG method to obtain the behavior of an Anderson's system at finite temperatures [92]. It was found that the zero-V_B NRG conductance at the Kondo regime follows a tendency described as

$$G(E_x) \sim G_0 \; F(E_x/k_B T_K) + G_{\text{Bgnd}}. \tag{1.2.50}$$

While G_0 (the peak's top-conductance for a negligible perturbation, $E_x \approx 0$) and G_{Bgnd} (accounting for a conductance background caused by additional tunneling processes) depend on the particular sample under study, the generic function F (different for distinct kinds of perturbations) only depends on the Kondo scale of the system, constituting the main reason why $k_B T_K$ is called an universal energy scale. In the particular case of a temperature perturbation ($E_x = k_B T$), *Goldhaber-Gordon et al* phenomenologically found a particular form of the F function, able to fit the temperature evolution of the NRG conductance at various values of the level-depth (within the Kondo regime) [101]. For magnetic impurities owning a semi-integer spin, it has the form:

$$G(T) = G_0 \left(\frac{T^2}{T_K^2} \left(2^{1/s} - 1\right) + 1 \right)^{-s} + \; G_{\text{Bgnd}}, \tag{1.2.51}$$

where s is a fitting parameter that reproduces best the NRG-generated data for a value of 0.22. This empirical expression offers an alternative method of extracting T_K by fitting it to the experimentally measured temperature-dependence of the Kondo resonance maximum (like those represented in Fig. 1.12b), being equivalent to NRG calculations but at lower computational costs.

1.3 Quantum dot junctions in the superconducting state

The inclusion of SC materials in the fabrication processes of mesoscopic and nanodevices, allow to study superconductivity at a microscopic level. The employment of aluminum has become generalized due to the feasibility offered by this material to create tunnel junctions, and the conventional superconductivity that it presents, well described by the BCS theory, in general. In this way, we start this section by giving a brief overview on the BCS theory and the typical phenomenology observed in SC devices made of aluminum (1.3.1). Following the discussion in the previous section, we continue by describing the electronic transport in weakly coupled SETs and QD transistors with SC leads, focusing on the single-energy-level conduction regime (1.3.2). Finally, we explain how the concurrence of Kondo-like and superconducting-pairing correlations in more strongly coupled devices results in a competition of superconductivity and Kondo effect to establish the ground state of the system, giving raise to the emergence of Yu-Shiba-Rusinov (YSR) states (1.3.3).

1.3.1 BCS theory and aluminum-based superconducting devices

Almost 50 years passed from the experimental discovery of superconductivity before the development of a theory that could explain the phenomenon. The so-called BCS microscopic theory is built on the basis of establishing an attractive interaction, $V_{k,k'}$, in a free-electron gas, which couples electrons of opposite momenta ($|k,\uparrow\rangle$ and $|-k,\downarrow\rangle$) together [116]). Hence, superconductors (SCs) are described by the usual free-electron gas hamiltonian plus an attractive term, as

$$H_{SC} = \sum_{k,\sigma} \epsilon_k c^\dagger_{k,\sigma} c_{k,\sigma} - \sum_{k,k'} V_{k,k'} c^\dagger_{k,\uparrow} c^\dagger_{-k,\downarrow} c_{-k',\downarrow} c_{k',\uparrow}. \tag{1.3.52}$$

At the superconducting (SC) state of matter, pairs of electrons couple together forming singlets bound states known as Cooper pairs (CPs). The ingenuity of this theory resides in employing a self-consistent mean-field approach to relax the constraint on the total number of electrons in the system, N, treating the occupancy $\langle c^\dagger_{-k,\downarrow} c^\dagger_{k,\uparrow} \rangle$ of a given k-state statistically. Systems with a large N

display small occupancy fluctuations, allowing this approximation to describe them accurately. The mean-field hamiltonian is

$$H_{SC} = \sum_{k,\sigma} \epsilon_k c^\dagger_{k,\sigma} c_{k,\sigma} - \sum_k \left(\widetilde{\Delta}_k \, c^\dagger_{k,\uparrow} c^\dagger_{-k,\downarrow} + \widetilde{\Delta}^*_k \, c_{k,\uparrow} c_{-k,\downarrow} \right), \tag{1.3.53}$$

where the origin of energies is taken at the Fermi level and the quantity $\widetilde{\Delta}_k = -\frac{1}{N} \sum_{k'} V_{k,k'} \langle c^\dagger_{-k',\downarrow} c^\dagger_{k',\uparrow} \rangle$ is defined as the bounding energy per electron in a CP (requiring an amount of energy of $2\Delta_k$ to break the bound state). The ground state of a superconductor can be then written as:

$$\Psi_{SC}(\varphi) = \prod_k \left(|u(k)| + |v(k)| e^{i\varphi} c^\dagger_{k,\uparrow} c^\dagger_{-k,\downarrow} \right) |\phi_0\rangle \,, \tag{1.3.54}$$

where $|\phi_0\rangle$ is the vacuum state and the coefficients represent the probability of the pair $(k\uparrow, -k\downarrow)$ to be occupied ($|v|^2$) or empty ($|u|^2$), implying $|v|^2 + |u|^2 = 1$. These complex coefficients differ by a phase φ, and their amplitude is derived by applying the variational method, obtaining

$$|v(k)|^2 = \frac{1}{2}\left(1 - \frac{\epsilon_k}{E_k}\right) \qquad \text{and} \qquad |u(k)|^2 = \frac{1}{2}\left(1 + \frac{\epsilon_k}{E_k}\right), \tag{1.3.55}$$

where the energy of excitations resulting from the breakage of a CP is defined as $E_k = \sqrt{\Delta_k^2 + \epsilon_k^2}$. Excitations in a SC are different from their counterparts in a regular Fermi liquid: they consist in a superposition of an electron and a hole of opposite momenta. Such excitations (known as Bogoliubov quasiparticles, BQP) can be addressed, for example, by injecting a single electron to the superconductor, occupying one slot of the CP while the other is empty, constituting an excitation that eventually couples with another BQP, decaying into the SC ground state, $\Psi_{SC}(\varphi)$. Temperature or electromagnetic radiation can lead to the generation of BQP, whose number decrease exponentially as $k_B T$ is decreased below Δ, only vanishing completely for $T = 0$.

Due to their bosonic nature, the CPs in the SC form a Bose-Einstein condensate, sharing the same ground state (Eq. 1.3.54), no matter the size of the system, and resulting in a rather unique example of a macroscopic quantum phenomenon. This state of matter is reached as the temperature is reduced under a critical value, below which the phonons start mediating the attractive interaction, constituting a phase transition of second order. The order parameter of such transition

$$\widetilde{\Delta}_k = \Delta(k) e^{i\varphi}, \tag{1.3.56}$$

is a complex number defined by a modulus equal to the CP bonding energy per electron, $\Delta(k)$, and the SC phase, φ (introduced in Eq. 1.3.54). While φ is constant along the SC system, $\Delta(k)$ can display variations with respect to the momentum, k, of the electrons that integrate each CP. In the case of conventional (type I) superconductivity, the attracting interaction is constant ($V_{k,k'} = V$), leading to the spatial isotropy of $\Delta(k) = \Delta$ in the k-space. As a matter of fact, and in agreement with the local approximation done in the mean-field theory, the determination of φ leads to the uncertainty on the number of CPs in the system, as established by Heisenberg's relation for charge and phase.

Different SC materials display distinct values of the SC energy scale, Δ, typically ranging around $\Delta \sim 0.1 - 1$ meV. As it is the bounding energy of CPs, it also represents the minimum energy required to create an elemental BQP excitation, manifesting in the quasiparticles' DOS (SC-DOS or D^{SC}) as an energy gap opening around E_F. The SC-DOS, $D^{SC}(E_k)$, describes the energies at which single-electrons can be injected/extracted from the SC (forming a BQP). In continuous notation, it is common to normalize the SC-DOS with the normal-state DOS (N-DOS) of the corresponding material as

$$\frac{D^{SC}(E)}{D(E)} = \mathrm{Re}\left(\frac{|E|}{\sqrt{E^2 - \Delta^2}} \right), \tag{1.3.57}$$

being exponentially close for $|E| \gg \Delta$. In contrast, close to the Fermi level, $D^{SC}(E)$ displays a strong dependence on energy delineating a 2Δ gap of forbidden states around E_F and diverging singular points right on the gap sides (called SC coherence peaks).

SUPERCONDUCTING NANODEVICES BASED ON ALUMINUM

In the early 60's, *Ivar Giaever* demonstrated that the gapped structure of the SC-DOS (in Eq. 1.3.57) can be spectroscopically probed in a mesoscopic tunnel junction. Ever since, the incorporation of SC materials has become extraordinarily common in mesoscopic and nanodevices, promoting the progression of this research area. Not only mesoscopic tunnel junctions enable to perform spectroscopic studies of different types of superconductivity and its response when subjected to perturbations (like temperature, external magnetic field, etc) but also the operation of more complex nanodevices benefit or is entirely based on specific SC properties (like SC qubits, SQUIDS, nanoresonators, electronic thermometers and coolers, etc). The development of such hybrid devices is partly due to the compatibility of aluminum with fabrication processes and setups: its SC phase transition occurs at accessible cryogenic temperatures (around 1.2 K), and its rapid oxidation and the robustness of the oxide layer makes of it an ideal material for creating SC tunnel junctions. These physical properties together with its cheap price and the conventional superconductivity displayed by Al, have turned it into the main material at use for these purposes. However, as more precise and accurate devices have been developed, it has been realized that the employment of this metal can be a double edged sword.

Since long it has been known that thin metallic films present a modified band structure, mainly deriving from border effects that distorts in the crystalline lattice. The resulting DOS experiences an overall single-level reduction and looses its smooth energy dependence, adopting a spiky lineshape [119]. Consequently, strong modifications arise in the SC-state properties (like Δ and T_c) reaching values counter-intuitively larger than the nominal ones in bulk-SC [120]. In fact, it has been predicted that quantum confinement also plays a role when the thickness is shrunken down to a few Å, introducing oscillations in the values of such parameters as function of the thickness [121]. Besides these generic behaviors, it has been shown that thin films of Al prepared by thermal evaporation present a polycrystalline structure integrated by grains of very different sizes ($\sim 10 - 100$ nm) and chaotic arrangement, strongly depending on the deposition parameters [122] (the vacuum level during evaporation, the nominal deposition rate value and typical fluctuations around it, and the purity of the initial Al target). Such granularity leads to a disordered porous morphology that oxygen can partially penetrate, oxidizing the exposed grain boundaries and conforming an oxide matrix with metallic/SC nuclei distributed inside it. The disorder of Al thin films is reflected in its electrical properties as an increase in the film resistivity which, for example, can be enhanced by increasing the O_2 partial pressure during the evaporation, eventually reaching the metal-insulator transition, when the film's DOS drops to zero at E_F. Surprisingly, it has been shown both in theory [123] and experiments [124] that SC remains robust against such disorder even beyond the metal-insulator transition, breaking down at a certain point [125]. Furthermore, nanostructured Al films have been predicted to display Andreev-type subgap resonances, attributed to diverse phenomena, all of them linked with disorder and quantum confinement. Recent measurements in highly-disordered Al films, both with an STM [126] and using SC resonators [127] have, indeed, confirmed the presence of such disorder-induced subgap resonances.

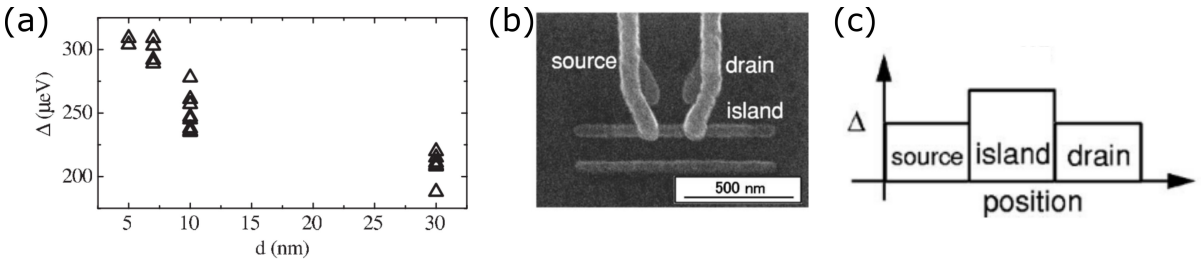

Fig. 1.13: (a) SC gap measured in Al tunnel junctions of different thickness, d. (extracted from [117]). (b) SEM picture of an all-aluminum SET. Tunnel junctions separate the island from each lead, done by in-situ oxidation during the preparation process. (c) The smaller thickness of the island with respect to the leads (shown in b) results in a SC gap profile along the device length (b and c images have been extracted from [118]).

Although one would guess that disorder effects are necessarily detrimental for the operation of Al-based SC devices to a greater or lesser extent, there exist some examples taking advantage of such deviations from the BCS behavior. The thickness-dependence of the SC gap in Al, increasing above 300 μeV in thin films of a few nanometers (doubling its nominal bulk value of $\Delta = 170$ μeV, as shown in Fig. 1.13a), allows to engineer a gap profile over the device employing films of different thicknesses [118, 117] (Fig. 1.13b and c). Other interesting applications stem from the increased kinetic inductance achieved in highly-granular Al SC resonators [128], all in all, contributing to the popularity of granular Al for its consolidation as a rediscovered material to be exploited. Even our Al breaking junctions may benefit from an disorder-induced increase of resistivity for the rather aggressive electromigration required (see section 2.4.2). As a general conclusion, when working with SC thin Al layers, it is highly advisable to characterize its properties, as non-negligible deviations may appear with respect to its bulk values.

1.3.2 Superconductor-quantum dot transistors in the weak-coupling regime

The prompt generalization of Al as the predominant fabrication material to create tunnel junctions leaded to its employment in some of the first experimental conceptions of nanoisland SETs [129, 130]. These early demonstrations settled the basis to create SC-SET devices (with either the leads, or the island or both are made of Al) in which certain energy scales, like E_U or γ could be controlled, up to some extent, in the fabrication process. Nowadays, SC-SETs are fabricated routinely and incorporated into larger and more complex circuits, typically for charge detection purposes [131, 132, 133, 134]. Fine resolution lithographic techniques enable to build SC-SETs of moderate charging energies ($E_U \sim 1-10$ meV), significantly larger than the SC gap of the thin Al layers their structures are made of ($\Delta = 170 - 340$ μeV). The simultaneous tunneling of the two electrons that integrate a CP is forbidden by the strong Coulomb repulsion at the island in SC-SET devices displaying such a relative scale ($E_U \gg \Delta$), restricting the transport to single electrons, that create electron/hole QP excitations in the SC leads.

THE SUPERCONDUCTING SINGLE-ELECTRON TRANSISTOR

In analogy with our SC-QD-SC transistors, we consider a SC-SET consisting of a N-state island weakly coupled to the S and D leads, in the SC state (being Δ_S and Δ_D the respective gaps, here considered equal, $\Delta_S = \Delta_D = \Delta$, for the sake of simplicity). The gap aperture in the SC-DOS around E_F induces a strong current suppression that adds up to Coulomb blockade, resulting in a gate-dependent total spectroscopic gap, $\Omega(V_G)$, with a minimum value of 4Δ at the degeneracy points and a maximum value of $4\Delta + 2E_U$ at the center of the diamonds. The system is formally described similarly to the N case: two tunnel junctions between the island and each lead are considered, and the current can be calculated by means of the master equation approach [47]. Superconductivity in the leads is taken into account by including the SC-DOS, $D^{SC}(E)$, in the corresponding rate expressions (Eqs. 1.2.21 and 1.2.22). The $I - V_B$ curves at different V_G can be calculated, tracing out the SC-SET current map (Fig. 1.14a). As the SC-DOS saturates to the N-DOS for $E \gg \Delta$, the current flowing through the SC-SET device recovers the characteristic N-state linear dependence on the tunnel resistance at biasing voltages well above Ω. At the spectroscopic gap border (for $|eV_B| \approx \Omega$), the sharp divergence of the SC-DOS at the leads is smoothed because of the thermal smearing of the Fermi-Dirac distribution in the N-state island.

An infinitely sharp divergence of the SC-DOS at $|E| = \Delta$ arise only at zero temperature in the BCS theory, and implies an infinite lifetime τ of the BQP excitations. In contrast, a dynamic equilibrium is expected in experiments (at finite temperature), in which CPs are continuously being excited into BQPs above the gap, eventually recombining back into pairs due to inelastic scattering with phonons [135]. Finite values of τ cause a certain broadening of the SC-DOS, smoothing the divergences, and such dynamic equilibrium ensures the presence of BQP above the SC gap that originate a finite tunneling current in SC tunnel junctions at biases below the spectroscopic gap. By decreasing the

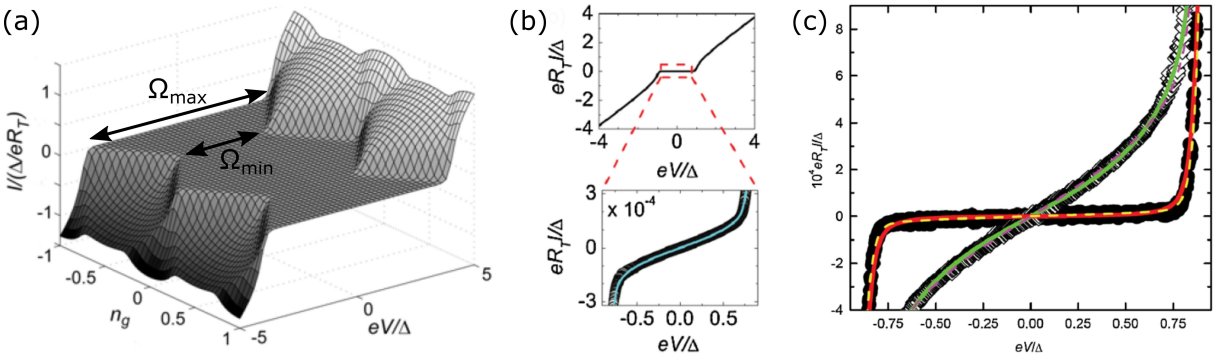

Fig. 1.14: (a) Current map of a SC-SET obtained by simulating the system following the master equation approach at a finite temperature, considering equal gaps in both leads, Δ and a N-state island of charging energy $E_U = 2\Delta$ (extracted from [47]). (b) Typical $I - V_B$ curve measured in a SC-Insulator-N junction, displaying a linear leakage of current below the gap ($\Delta = 200$ μeV) well-described by the Dynes model (cyan line) for $\vartheta = 1.8 \times 10^{-4}\Delta$ (extracted from [138]). (c) $I - V_B$ curve measured in SC-Insulator-N junctions without (open symbols) and with (solid symbols) a ground plane, well reproduced both by a Dynes-model (dashed lines) or by a finite-temperature master equation approach (solid lines), accounting for the junction's leads capacitance to the ground plane (if present).

sample temperature well below Δ, the equilibrium population of BQPs becomes exponentially small, leading to larger lifetime values, as confirmed by low-temperature measurements performed in bulk-Al tunnel junctions (extending over a certain area) obtaining values of $\tau \sim 10^{-5}$ s for $k_BT = 0.1 \times \Delta$ [136]. However, similar studies carried out in granular Al showed that disorder decrease this characteristic time a few orders of magnitude, demonstrating that electron-electron interactions (increased by disorder) also affects the CP lifetime [137]. Regardless of the scattering source, the associated energy scale $\vartheta = h/\tau$, also called Dynes parameter (being $\vartheta \sim \Delta \times 10^{-6}$ for bulk Al, and varying between $\Delta \times (10^{-2}$ and Δ for highly granular Al), can be included in the expression of $D^{SC}(E)$, as a generic broadening factor accounting for any kind of CP breaking effect, by replacing $E \to E + i\vartheta$. In general, the non-negligible subgap current observed in SC-junction systems (like the SC-SET) measured for $k_BT \ll \Delta$ is convincingly described by a phenomenologically Dynes-broadened version of the SC-DOS (Fig. 1.14b). Nevertheless, it should be kept in mind that additional parasitic effects can equally originate the excitation of BQPs, and attributing the whole subgap current leakage to Al disorder might be a risky argument. In Refs. [138, 139], it was demonstrated that the subgap current leakage can be explained by the presence of residual electromagnetic radiation in the sample cavity, developing a model to describe this effect, perfectly consistent with the phenomenological Dynes-broadened SC-DOS (Fig. 1.14c). In this work, the group of *Pekola et al* also shows how the inclusion of an on-chip ground plane around the mesoscopic tunnel junction shields it and diminish very significantly the subgap leakage current.

THE SUPERCONDUCTING-QUANTUM DOT TRANSISTOR

As for SC-QD-SC transistors in a weak-coupling regime, the pioneering work of *Ralph et al* settled the basis on the study of this kind of systems. The employment of an original sample geometry allowed them to contact individual metallic nanoparticles with Al leads, dodging the oxidation problem already in the mid 90's [1]. The particles' size ($2-15$ nm) was adjusted in their fabrication process, obtaining SC-QD-SC transistors displaying large energy spacings ($E_U \approx 5$ meV and $E_\delta \approx 0.5$ meV) and small couplings at the tunnel barriers ($\gamma_T \gtrsim 10$ μeV), created by the controlled oxidation of the sample. Experiments demonstrated a mild hierarchy of energy scales (such that $E_U \gg E_\delta \gtrsim \Delta \gg k_BT \gtrsim \gamma_T$), indicating a relatively weak-coupling regime. On one hand, a large relative scale of E_δ/Δ impedes to the SC transition of the Al particles, conserving the spectral features of usual QDs [2]. On the other hand, large values of E_U/Δ and E_U/γ_T opposes to the double occupation of the QD at low V_B, inhibiting the transport of CPs by higher-order processes and restricting the transport to mainly first-order tunneling of single electrons (forming BQPs at the leads).

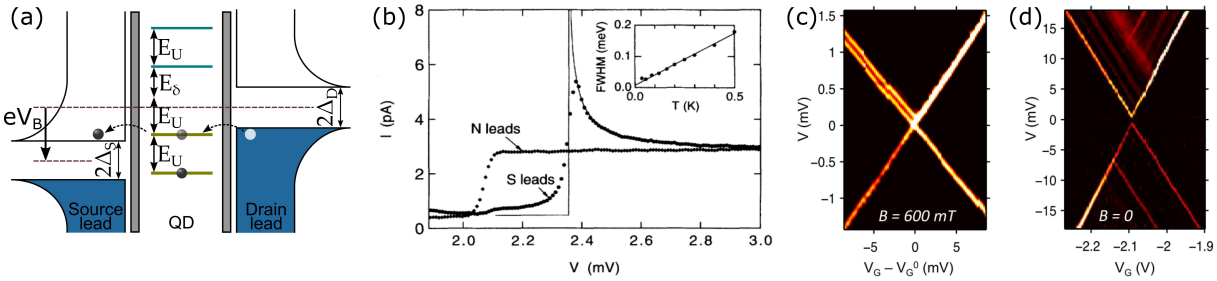

Fig. 1.15: (a) Energy diagram of a SC-QD-SC junction. A single-particle energy level at the QD is aligned with the coherence peaks at both leads, corresponding to the apex of the on-state conduction diamond of a transistor. (b) Current step at the DE of a QD junction with leads in the N and SC state, the solid line being a fit to the BCS DOS. Inset: FWHM of the corresponding N-state conductance peak as a function of temperature. The linear fit has a slope of slope $3.7/;k_B$ (extracted from [1]). (c,d) dI/dV_B maps around a degeneracy point of an aluminum QD transistor made by electromigration, respectively at the N (zoomed-in) and SC (zoomed-out) state (extracted from [38]).

The current flowing throw weakly coupled SC-QD-SC junctions is proportional to the convolution of the SC-DOS in both leads. This is a direct consequence of applying Fermi's Golden rule to a system owning a discrete spectrum represented by Dirac's delta functions. The delta functions evaluate the integral of the tunneling rate expressions (Eqs. 1.1.10 and 1.1.11) at the energy of each energy level, establishing a proportionality between Γ and the SC-DOS in the leads. If E_U and E_δ are sufficiently large, the contribution of each individual level appears separately, and the sequential current replicates the BCS profile at the single-level conduction regime (for $2\Delta < |eV_B| < 2\Delta + E_\delta$). Consequently, the diamond edges (DEs) are sharpened for the SC state of the leads, as they correspond to the alignment of the energy levels at the QD with the coherence peaks at the one of the leads, and with both of them at the diamond apex signaling the degeneracy point (Fig. 1.15a). By applying a magnetic field (B), the sample could also be characterized for the N-state of the leads (Fig. 1.15b), showing a displacement in V_B of the diamond onset, corresponding both to capacitive effects and the opening of the SC gap around zero-bias. By measuring the differential conductance, dI/dV_B, of the samples in the N-state, the conductance peak corresponding to the diamond onset displayed a linear temperature dependence close to $3.5\ k_BT$, indicating the thermal limit of the spectroscopic resolution (inset of Fig. 1.15b). However, the linear tendency saturated at low temperatures, pointing towards the lifetime broadening as the limiting factor at temperatures of 30 mK. On the other hand, the FWHM of the conductance peak measured for the SC-state of the electrodes presented a FWHM 10 times smaller, reflecting the sharp current increase at the alignment of the QD energy level with a coherence peak at one lead. These observations put into manifestation the improvement in the spectroscopic resolution that the divergences of the SC-DOS generates in weakly coupled QD transistors.

While the samples studied in Refs. [1] and [2] simply consist on SC-QD-SC junctions, the addition of a gate electrode was implemented shortly after [3], allowing to measure the transport map of the resulting QD transistor. Additionally, we present the dI/dV_B map of an all-aluminum QD transistor created by electromigration within our group, respectively for the N and SC state of the leads (Fig. 1.15c and d). One diamond edge (DE) on panel c appears Zeeman-split as a consequence of the large B applied, allowing to determine the parity of the QD (odd at the left of the degeneracy point, located around $V_G = -2.1$ V). At the SC state, an spectroscopic gap $\Omega_{SC} \approx 4\Delta$ opens around zero bias, observed at the degeneracy point. The DEs become sharper, as well as subsequent electronic excitations inside the diamond, as a consequence of the enhanced spectroscopic resolution (note, however, the difference in the voltage ranges of both graphs).

STABILITY DIAGRAM OF THE SUPERCONDUCTING-QUANTUM DOT TRANSISTOR

The diamond structure appearing in the transport maps of weakly coupled QD transistors puts into manifestation the dependence of the dot's chemical potential, μ_{QD} (or level depth, ϵ_0, corresponding to take the origin of energies at a degeneracy point), on V_B and V_G. By measuring the transport map

of a QD transistor, both for the N and SC state of the leads, a certain shift can be observed in the position of the DEs, stemming from the opening of the SC energy gap of magnitude 2Δ around the Fermi level of the leads. While such displacements are almost inappreciable in a large variety of QD systems, the generally larger spectroscopic resolution achieved with metallic nanoparticles, further enhanced by the SC state of the leads, makes these small effects of capacitive origin to become apparent in the corresponding SC-QD-SC junctions.

In the N-state, the apexes of the lower and upper on-state diamond (respectively appearing at positive and negative bias) touch each other at $V_B = 0$ signaling the precise gate value, V_G^0, of the degeneracy point. In the SC-state, the spectroscopic gap $\Omega_{SC} = 4\Delta$ opening around zero bias impedes the electron flow at charge degeneracy (Fig. 1.16a). Conduction can be reached by applying a bias voltage overcoming the gap, such that $|eV_B| \geq 2\Delta$. Under ideally symmetrical conditions (symmetric biasing voltage, so that $V_S = -V_D = V_B/2$, symmetrical dot-lead capacitances, $C_S = C_D$ and symmetrical SC-gaps in both leads, $\Delta_S = \Delta_D$), the application of a finite V_B does not disturb the QD level position, and the apexes of the conduction diamonds in SC-state are found at the exact same gate value, V_G^0. However, actual QD junctions often present asymmetries in these parameters, and an asymmetrically biasing configuration (such that $V_S = V_B$ and $V_D = 0$) is commonly employed to measure them. The V_B-shifts displayed by the DEs when transiting from the N to SC state in ungated and symmetrically biased SC-QD-SC junctions were characterized in Ref. [1]. By considering an uniform gap (taking $\Delta_S = \Delta_D = \Delta$) they demonstrated that displacements in the V_B coordinate are modulated by $(C_S{+}C_D)/C_S$ and $(C_S{+}C_D)/C_D$ factors (depending on the V_B sign), relating them with the capacitive asymmetry. In the case of asymmetrically biased junctions, further deviations with respect to these V_B-shifts values appear. In the following, we extend their derivation for calculating the misalignment of the conduction-diamond apexes in asymmetrically biased SC-QD-SC transistors.

We start by considering an SC-QD-SC junction in equilibrium ($V_B = 0$), tuned at the gate value of a certain charge degeneracy point, V_G^0, as shown in Fig. 1.16a. To overcome the SC gap and reach the apexes of the on-state diamonds, it is necessary to apply a biasing voltage of $\Delta V_B^0 = 2\Delta/e$. By doing so, a variation is induced at the dot's level depth with respect to its zero-bias value, $\epsilon_0(0,0)$, caused by the bias lever arm, α_B (as indicated in Eq. 1.2.28 and highlighted in magenta in Fig. 1.16b). The magnitude of this variation is

$$\Delta\epsilon_0 = \epsilon_0(0,0) - \epsilon_0(\Delta V_B^0, 0) = e\alpha_B \Delta V_B^0 = \left(\frac{2C_S}{C_S + C_D + C_G}\right) \Delta. \tag{1.3.58}$$

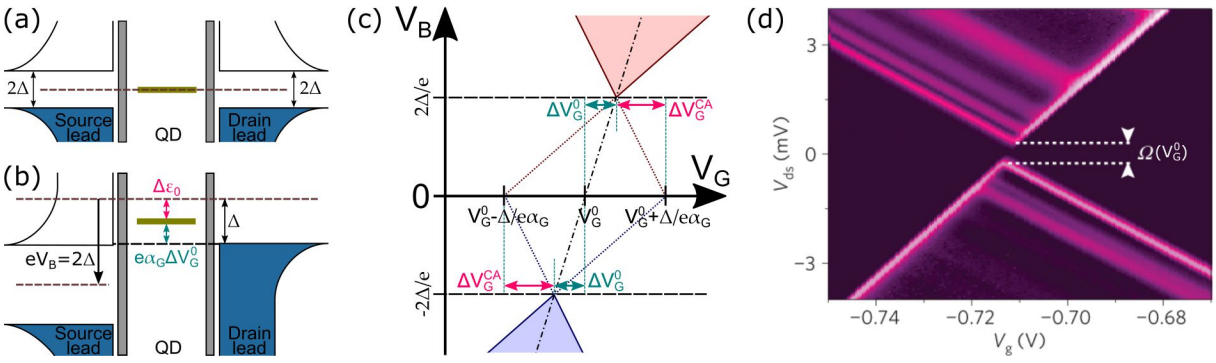

Fig. 1.16: (a) Energy diagram of an SC-QD-SC transistor at a degeneracy point for $V_G = V_G^0$ and $V_B = 0$ V. (b) When asymmetrically biasing the junction by $V_B = 2\Delta/e$, the bias coupling induces a level-depth shift of $\Delta\epsilon_0$. A certain gate detuning of ΔV_G^0, aligning the level with the coherence peaks (black dashed line) is required to reach the conduction point. (c) Illustrative stability diagram SC-QD-SC transistor, indicating the zero-V_B position of the degeneracy point and the V_G-shifts of the diamond apexes caused both by the bias lever arm ($DeltaV_G^{CA}$) and the asymmetric biasing configuration ($DeltaV_G^0$). The dashed-dotted black line indicates the position of $\epsilon_0 = 0$ at finite V_B. (d) dI/dV_B map of an aluminum QD transistor contacting a C_{60} molecule, made by electromigration, highlighting the spectroscopic gap and diamond apexes misalignment at charge degeneracy (extracted from [39]).

Such level-depth shift can be translated into a certain gate offset, ΔV_G^{CA}, calculated as

$$\begin{aligned} \left|\epsilon_0(0, \Delta V_G^{CA})\right| = \Delta\epsilon_0 \rightarrow e\alpha_G \Delta V_G^{CA} = e\alpha_B \Delta V_B^0 \rightarrow \\ \rightarrow \Delta V_G^{CA} = \frac{\alpha_B}{\alpha_G}\, 2\Delta/e = \frac{2C_S}{C_G}\, \Delta/e. \end{aligned} \tag{1.3.59}$$

If we assume that ΔV_B^0 to induce a significant variation of the level depth, then the resulting horizontal displacement is negligible ($\Delta V_G^{CA} \approx 0$), and the gate voltage variation necessary to reach conduction is simply equal to the SC gap of the drain electrode, $\Delta V_G^0 = \Delta/e\alpha_G$. On the contrary, if the effect of the bias lever arm is taken into account, the value of this gate detuning is reduced by an amount of ΔV_G^{CA}, as shown in Fig. 1.16b and c, leading to a separation of the diamond apexes appearing in the measurement equal to

$$\begin{aligned} \Delta V_G^0 = \Delta/\alpha_G e - V_G^{CA} = \left(\frac{C_S + C_D + C_G}{C_G}\right) \Delta/e - \frac{2C_S}{C_G}\, \Delta/e = \\ = \left(\frac{-C_S + C_D + C_G}{C_G}\right) \Delta/e. \end{aligned} \tag{1.3.60}$$

The biasing and capacitance asymmetries results in the apparison of the conduction-diamonds apexes at a gate value between V_G^0 and $V_G^0 \pm \Delta/e$, equal and opposite in sign for both on-state diamonds. If N-state data cannot be accessed, the value of V_G^0 can be simply obtained from the midpoint between the two apexes. Ideally, a voltage biasing condition can be engineered to compensate the capacitance asymmetry, removing the bias lever arm effects. This simple calculation can be further generalized for the case of asymmetric SC energy gaps, and relations for the V_B-shifts of the DEs can also be extracted[7] by combining the V_G-shifts obtained here with the relations for the diamond edges slopes in Eqs. 1.2.25.

Several studies on electromigration QD transistors contacting metallic nanoparticles followed the experiments of *Ralph et al* in the following years [140, 141, 76, 142]. Nowadays, molecular transistors made by electromigration, using different kinds of molecules as the central nanostructure have become more popular. Previous experiments done within our group have studied the conduction of C60 molecules in the presence of SC leads, by employing electromigration constrictions of either pure aluminum or proximized-gold [39]. Peculiarly, the conductance features observed in such devices often presented relatively large linewidths around $100\ \mu$eV, well above the N-state thermal threshold ($3.5k_BT \approx 24\ \mu$eV for $T = 80$ mK), even at SC state (Fig. 1.16d). While such increased linewidths are commonly observed in single molecule transistors, the origin of such broadening is uncertain. Nevertheless small scale effects such as the misalignment of the apexes of the on-state diamonds is still observable in the transport map at the SC state of these devices.

HYBRIDIZATION IN A SUPERCONDUCTOR-QUANTUM DOT TRANSISTOR

Weakly coupled SC-QD-SC transistors created by the electromigration of our all-aluminum junctions (after the deposition of a colloidal solution of 5 nm diameter gold particles), display a rather unique set of energy scales, owning a pronounced hierarchy, such that $E_U \gg E_\delta \gg \Delta \gg k_BT \gg \gamma_T$. A relatively sharp SC-DOS at the leads is revealed in the characteristic curves, showing a sequential current at the on-state diamonds that presents a BCS lineshape, with an abrupt gap and keen coherence peaks (Fig. 1.17a). The strong suppression of current inside the spectroscopic gap indicates a vanishingly small number of BQPs at the leads, as expected for $k_BT \ll \Delta$. However, the smoothed decay of the current at the DE manifest a low but finite tunneling probability right below the SC gap edge (Fig. 1.17b). To understand the origin of the softened current decay, fits based on models accounting for different phenomena have been performed prior to my work

[7] The V_B-shift values obtained by *Ralph et al* in Ref. [1] can be reproduced by considering symmetric biasing ($V_S = -V_D = V_B/2$) and the corresponding modification on the level depth formula (Eq. 1.2.45) as $\epsilon_0 = -e\alpha_S V_S - e\alpha_D V_D - e\alpha_G \widetilde{V}_G$, where α_S, D are source/drain lever arms.

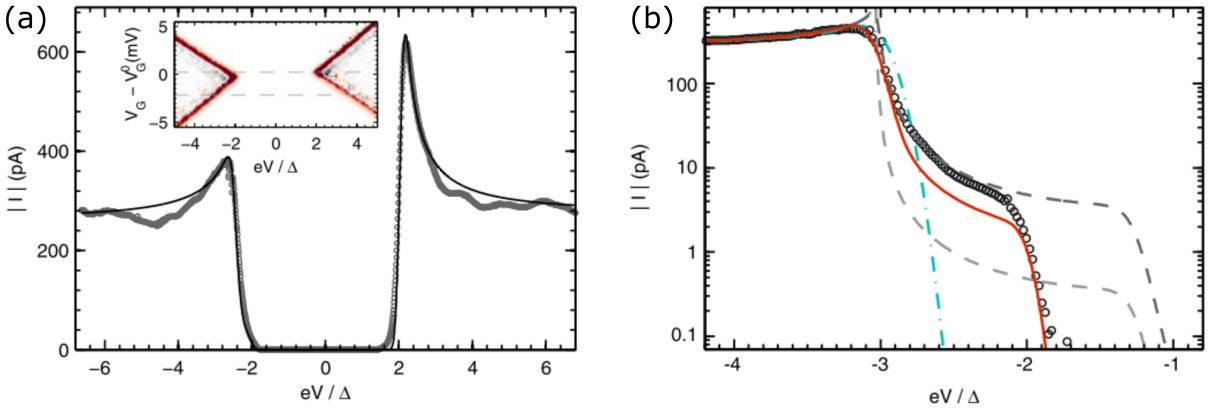

Fig. 1.17: (a) $|I| - V_B$ trace at V_G^0 in an aluminum SC-QD-SC transistor made by electromigration, fitted by the Green-function cotunneling model. Inset: dI/dV_B map of the device around charge degeneracy, indicating the line cuts displayed in (a) and (b) graphs. (b) Log-scale graph of $|I| - V_B$ zooming in at the diamond edge. Fitting curves are based on the Green-function cotunneling model (red solid line) and sequential tunneling considering a Dynes-broadened BCS-DOS for values of $\vartheta = 10^{-2}\Delta$ and $10^{-3}\Delta$ (grey dashed lines) or a ~ 10 μV Gaussian noise (cyan dashed-dotted line). Best-matching was found for the cotunneling model, while the slight underestimation is attributed to non-equilibrium effects (extracted from [38])).

As it was explained at the end of section 1.2.2, sequential tunneling processes between the energy levels in the dot and N-state leads are described by a constant coupling parameter, γ. In fact, the relative flatness of the N-DOS, $D(0)$, around the Fermi-level results in an uniform hybridization of the QD levels for any voltages applied (Lorentzian spectral function of regular shape). In contrast, the strong dependence on energy of the SC-DOS, $D^{SC}(E)$, around E_F is expected to introduce significant variations of the hybridization for distinct values of the chemical potential difference, ϵ, between the dot and each SC lead (identical to ϵ_0, but defined for a single lead). Consequently, the tunneling probability is no longer constant, but a function of ϵ, defined as $\widetilde{\gamma}(\epsilon) = \gamma D^{SC}(\epsilon)/D(0)$. Such energy-dependent couplings are considered in Green-function methods developed for calculating the conduction in SC-QD-SC junctions [143, 144], which also account for cotunneling contributions up to an arbitrary higher-order (above which the corresponding Green functions are truncated). The expression for the current carried by a single spin-degenerate level derived from the Green-function cotunneling model in the weak-coupling regime considered

$$I(V_B, V_G) = \frac{4e}{h}(2 - n_{QD}) \int [f_S(E - eV_B) - f_D(E)] \times \frac{\widetilde{\gamma}_S(E - eV_B)\widetilde{\gamma}_D(E)}{(E - \epsilon_0(V_B, V_G))^2 + [\widetilde{\gamma}_S(E - eV_B) + \widetilde{\gamma}_D(E)]^2} \, dE, \tag{1.3.61}$$

was determined by *Kang*. The on-dot Coulomb repulsion is taken into account in the prefactor $(2 - n_{QD})$, where n_{QD} is the QD's filling factor, expressing the probability of the QD level to be filled for a given configuration of applied voltages. A self-consistent expression for $n_{QD}(V_B, V_G)$, including all possible energy-conserving cotunneling processes up to the truncated order [145], allows to calculate this quantity independently and compute the current. Indeed, the current decay at the DE of the SC-QD-SC transistors is well captured by the cotunneling model (red solid line in Fig. 1.17b), whereas the master equation approach cannot reproduce it neither when considering Dynes-broadened SC-DOS at the leads (grey dashed lines) nor when introducing a Gaussian noise (blue dashed lines) [38]. It is then possible to claim that a hard BCS-like SC-DOS is present in our devices, and to dismiss noise-induced broadening effects in our cryogenic set-ups (owning highly-filtered electrical lines) and the spectroscopic resolution in these devices is only limited by the lifetime broadening inherent to a finite tunnel coupling.

1.3.3 Emergence of Yu-Shiba-Rusinov states in the Kondo-coupling regime

The presence of impurities in a free-electron gas introduces local disruptions at the periodic potential of the crystalline lattice. The electrons in the band tend to congregate around the impurity for screening it, so that the potential recovers its periodic structure, giving raise to Kondo effect. In the case of a superconductor (SC), such screening process is carried out by CPs, leading to a local reduction of their bounding energy with respect to the corresponding bulk value (Δ) as a consequence of the attractive interaction exerted by the potential deep induced by the impurity. The local SC-DOS around an impurity may then display quasiparticle excitations at energies below Δ, generically called Andreev bound states (ABS). In the case of magnetic impurities, the potential fluctuation is amplified by the exchange interaction, J, and the specific ABS receive the name of Yu-Shiba-Rusinov (YSR) states [146].

Instead of considering an impurity embedded in a continuous medium (whose sole presence already disrupts the potential), an interesting case arises when magnetic impurities are placed on top of a SC surface. The potential disruption is then purely magnetic, being exclusively caused by J, and YSR states arise locally in the area below it [147] (Fig. 1.18a). For sufficiently large couplings, SC-QD junctions may display this behavior, as the spin, S_0, of the unpaired electron at odd-occupation charge states grants the dot a magnetic character. The formal description of such Anderson-type impurities is done from the perspective of the SIAM, replacing the N-state electrode in Anderson's hamiltonian (Eq. 1.2.44) by a superconductor (Eq. 1.3.53). Kondo's hamiltonian is a particular case of the SIAM hamiltonian (for $E_U \to \infty$ and $-E_U < \epsilon_0 < 0$) whose superconducting version is obtained equivalently, leading to

$$\begin{aligned} H &= H_{SC} + H_0 + H_T \\ &= \sum_{k,\sigma} \epsilon_k c^\dagger_{k,\sigma} c_{k,\sigma} - \sum_k \left(\widetilde{\Delta}_k \, c^\dagger_{k,\uparrow} c^\dagger_{-k,\downarrow} + \text{h.c.} \right) + \sum_\sigma \epsilon_0 d^\dagger_\sigma d_\sigma + E_U d^\dagger_\uparrow d_\uparrow d^\dagger_\downarrow d_\downarrow + \\ &+ \frac{J}{2} \sum_{k,k',\sigma,\sigma'} c^\dagger_{k'\sigma'} \boldsymbol{\sigma}_{\sigma\sigma'} c_{k\sigma} \cdot \boldsymbol{S_0} \end{aligned} \tag{1.3.62}$$

This SC version of Kondo's hamiltonian was diagonalized independently by *Lu Yu* [148], *Hiroyuki Shiba* [149] and *A. I. Rusinov* [150, 151]. In Kondo's hamiltonian, the spin in the QD is classical, equivalent to a local magnetic field as its quantum mechanical and dynamical properties are neglected ($J \to 0$ and $S_0 \to \infty$, so that their product is finite). Briefly, the solutions obtained by Yu, Shiba and Rusinov describe a set of quasiparticle excitations arising locally in the SC state of the medium due to scattering of the CPs with the impurity. The energy dispersion of the lowest excited state (LES) was obtained to follow a tendency of the form

$$E_{YSR} = \Delta \frac{1-\zeta^2}{1+\zeta^2}, \tag{1.3.63}$$

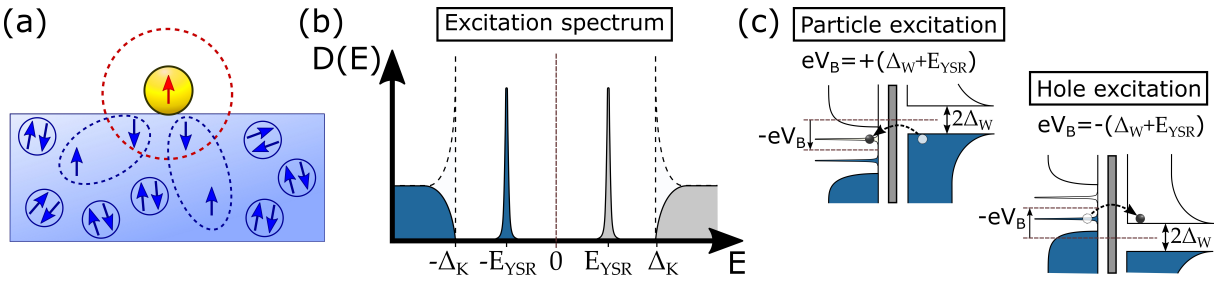

Fig. 1.18: (a) The screening process of a magnetic impurity on a SC substrate results in a local weakening of the CPs pairing energy. (b) Local excitation spectrum of a magnetic impurity coupled to a superconductor, displaying YSR resonances at sub-gap energies of $\pm E_{YSR}$ that accumulate most of the BCS spectral weight. (c) Energy configurations required to probe the hole/particle resonances of the YSR state with a weakly coupled SC electrode characterized by a gap Δ_W.

where $\zeta = JS_0\pi D(0)/2$ is a positive quantity and thus, the LES shall always be found lying below the SC gap, Δ. If the SC considered is sufficiently large (containing a large number of particles), for the mean-field approach to be valid, the LES can be accessed equivalently by injecting/extracting an electron to/from the system. Under this approximation, the LES excitation manifests as two sub-gap resonances (of particle-like and hole-like characters respectively) emerging at symmetric energies of $\pm E_{YSR}$ in the excitation spectrum of the correlated system, and accumulating a certain part of the BCS particle/hole spectral weight depending on the strength of J (leading to a local flattening of the coherence peaks of the SC-DOS, as illustrated in Fig. 1.18b). Therefore, the energy spectrum of the SC-QD system can be spectroscopically probed, for example, with the SC-tip of a STM (Fig. 1.18c) allowing for the experimental observation of the YSR resonances.

EXPERIMENTAL MANIFESTATION OF THE YU-SHIBA-RUSINOV RESONANCES

In the last couple of decades, extensive experimental work have been devoted to characterize a large variety of dot-like nanostructures strongly coupled to superconductors, gradually revealing the richful phenomenology that these systems can display, as many energy scales are involved ($E_U, E_\delta, \Delta_{S,D}, \gamma_{S,D}, k_B T_K^{S,D}$, labeling both S and D electrodes) and distinct ratios between them are obtained in different sample configurations. Heading devices exploring the combination of Kondo effect and superconductivity were generally based on semiconducting NWs and CNTs, symmetrically coupled to a pair of SC electrodes. The high transmission probability of CPs in devices displaying relatively strong $\gamma_{S,D}$ and low E_U resulted in the complete SC proximization of the dot structure, reaching the so-called Fabry-Pérot regime where a supercurrent flows through the device at zero-bias and several multiple-Andreev reflections (MARs) appear at finite biases [5, 11, 6, 7, 8]. Regardless of the sample, these conduction features presented a periodic gate modulation, previously observed previously in SC-SET devices [9], largely decreasing their amplitude at even charge states of the QD, putting into manifestation the importance of the QD occupation parity in the charge transport mechanisms. Later on, the SC proximity effect was weakened in QD devices increasing E_U, where the conductance features at odd charge states evolve into a large Kondo resonance imposing over the SC gap [12]. Certain works reach intermediate values of E_U, relative to $\gamma_{S,D}$, obtaining QD transistors were proximity effect display a strength similar to Kondo effect. In these samples, YSR states arise, appearing duplicated as four conductance resonances in the characteristic curves, as the spin-correlations of the dot extended over both SC leads of the junction [14, 13, 23, 26]. Consequently, the transport was completely correlated and the YSR spectrum of both leads appear convoluted in the conductance measurement. More recent experiments have been able to measure

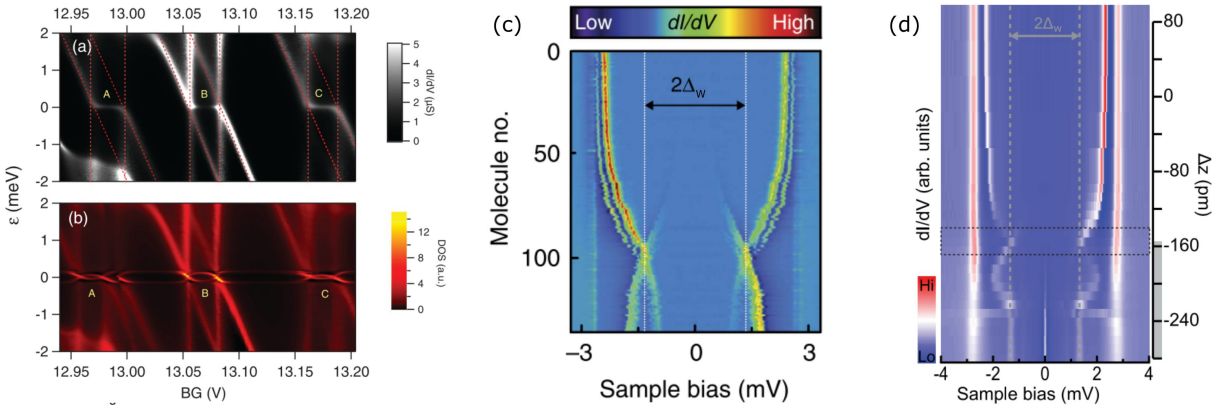

Fig. 1.19: dI/dV_B and DOS maps of a CNT-QD stronly coupled to a lead in the N (a) and SC (b) state, probed by a weakly-coupled N-state lead. The zero-V_B Kondo resonances emerging along the diamonds of odd parity (labeled as A, B and C) at the N state evolve into YSR resonances at the SC state (extracted from [25]). (c) dI/dV of 137 magnetic molecules on a SC substrate recorded by an STM and artificially ordered. (extracted from [34]) (d) dI/dV of single magnetic molecule measured with an STM at various tip-sample distances. (extracted from [35])

the YSR spectrum by reducing the coupling scale of one of the leads into the weak-coupling regime, acting as a probe that performs spectroscopy on the SC-QD correlated system at the other side of the SC-QD-SC junction [31, 24, 25, 29, 30, 41]. Such these systems could study the continuous evolution of the YSR spectrum for different values ϵ_0 tuned via a gate electrode. Furthermore, the zero-V_B Kondo resonance was recovered in measurements for the N state of the leads, reached by suppressing superconductivity with an external magnetic field (Fig 1.19a and b), allowing for the determination of the Kondo energy, $k_B T_K$, and moreover, to characterize the transition from the Fabry-Perot to the Kondo regime [28] (as the magnetic field gradually reduces Δ, weakening the proximity effect).

In these asymmetrically coupled junctions, the energy scales characterizing the Kondo-coupled lead (Δ and γ) are fundamentally involved in determining the transport properties of the system, while the weakly-coupled electrode (characterized by γ_W and Δ_W) simply constitutes a way for probing the spectrum. In fact, such asymmetric configuration matches naturally the arrangement of STM set-ups, in which a N/SC tip can be adjusted at tunable distances over the sample, which can be prepared as a clean SC surface, covered by self-arranged layers magnetic molecules or adatoms that establish arbitrarily strong couplings to the substrate. Actually, YSR resonances were already being investigated by STM a few years before their first observation in solid state devices [32]. Many interesting features have been measured in STM experiments, for example, strong asymmetries in the spectral weights of both YSR resonances that oscillates with the distance from the impurity [33], or the simultaneous presence of several resonances arising from the complex orbital structures of specific magnetic molecules [152]. Fitting our discussion, the group of *Franke et al* demonstrated the coupling-dependence of E_{YSR} by addressing molecules owning slightly different Kondo-couplings to the substrate with an STM, showing that both resonances may display a crossing at zero-energy[8] stemming from the competition between Kondo effect and superconductivity [10]. A diagram displaying the continuous evolution of E_{YSR} and capturing the crossing point can then be reconstructed by adding together the spectrum of different molecules [34], or tuning γ on a single molecule by pushing it down with the STM tip [35] (Fig 1.19c and d).

Superconducting molecular transistors fabricated by electromigration have also been proven as a valid candidate to study YSR resonances, if the molecule happen to dispose in the right asymmetric coupling configuration [39, 36] (Fig. 1.20a). The large relative value of the dot's spacing scales (E_U and E_δ) in such devices is comparable to the molecular junctions studied by STM. Besides, electromigration QD transistors are not likely reach the large couplings that can be achieved with CNTs and NWs (in which the SC lead is directly deposited on top of the nanostructure along the fabrication process). Altogether makes that proximity effect is severely reduced in QD transistors made by electromigration. When couplings happen to be strong enough to generate significant Kondo correlations with one lead, the other lead is normally weakly coupled, allowing to perform

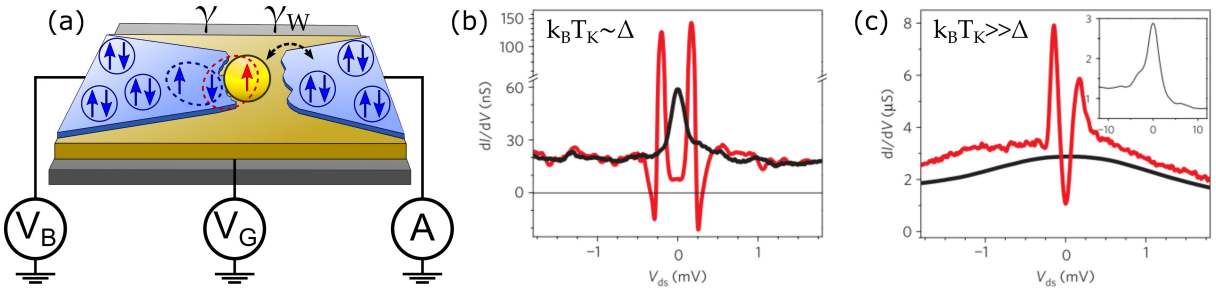

Fig. 1.20: (a) In an asymmetrically coupled SC-QD-SC transistor, Kondo correlations extend solely over the strongly coupled lead, while the weakly coupled electrode acts as a tunnel probe. (b and c) dI/dV spectra measured at constant V_G in superconducting electromigration junctions contacting individual C_{60} molecules. While a Kondo resonance develops in the N state (black), YSR resonances appear in the SC-state spectrum (red). Inset: zoom-out showing the entire Kondo resonance range. (adapted from [39])

[8] Note that, since these STM measurements are performed with a SC tip, a $2\Delta_W$ gap opens around zero-V_B, which need to be subtracted (deconvoluted) for obtaining the actual spectrum of the molecule-substrate system

spectroscopy of the resulting well-developed YSR states at the SC state (Fig. 1.20b), which may even appear buried below a Kondo resonance that imposes over the SC gap for an larger value of the strong coupling scale (displaying a residue of the YSR state at the summit, as it can be observed in Fig. 1.20c). Despite the lack of control on the couplings during the fabrication of electromigration devices, they offer a rather unique platform for the characterization of the YSR resonances, as they combine the energy-scale hierarchy typical of molecular junctions with a gate electrode. Furthermore, the spectroscopic resolution can be much increased with respect to the measurements shown in Figs. 1.20 by replacing the proximized-gold contacts in these experiments by pure aluminum ones, and employing metallic nanoparticles rather than molecules (which have systematically presented present large linewidths well above the thermal limit).

SUPERCONDUCTIVITY VS. KONDO EFFECT: THE 0-π TRANSITION

The YSR resonances could already be predicted by solving the SC-Kondo hamiltonian that considers a classical spin. Nevertheless, an accurate description of the experiments discussed above requires the consideration of a quantum spin. On one hand, for an effective screening of the QD's magnetism, the formation of a BQPs at the SC lead is required. Like this, Kondo correlations exert a disruptive influence on the superconductivity at a strongly coupled lead, establishing the formation of a screening cloud and constituting a Kondo-like singlet local state. On the other hand, the SC pairing correlations oppose to the accumulation of quasiparticles, keeping electrons bounded by pairs into CP singlets. At the same time, the SC proximity effect favors the extension of pairing correlations at the dot. Although both effects relies on the existence of a Fermi surface at the free-electron gas, the origin of the driving forces and the resulting many-body quantum state are different. A complex competition between both phenomena that depends on the relative value of the relevant energy scales: E_U, γ, ϵ_0 and Δ. To simplify the picture, only k_BT_K and Δ are sometimes considered, including the first three scales into the Kondo energy. Although this is not formally correct, and k_BT_K is defined in the absence of a prefactor, it is common to restrict the discussion to the relative values of this two scales for simplification purposes. In this sense, the establishment of one of the two possible regimes and the corresponding ground states, arising from this interplay, might be ascribed to the k_BT_K/Δ ratio, one of them being characterized by the prevalence of magnetism (for $k_BT_K \ll \Delta$), or superconductivity for the other (for $k_BT_K \gg \Delta$):

- **Free-spin doublet ground state: the weak J limit** ($k_BT_K \ll \Delta$). The CPs are robust against a weak exchange interaction, and the local SC pairing energies are slightly affected, resulting in an spectrum where YSR resonances lay exponentially close to the gap edge. The SC gap depletes the quasiparticle DOS around E_F, suppressing Kondo screening and the unpaired spin at the QD remains unscreened, so that the system adopts a doublet ground state $|\Psi_\sigma\rangle$ configuration: either $|\uparrow\rangle$ or $|\downarrow\rangle$, with a time-averaged local spin of $\mathcal{S} = 1/2$.
- **Kondo-screening singlet ground state: the strong J limit** ($k_BT_K \gg \Delta$). In this regime, the exchange interaction is strong enough to impose over the SC pairing. However, the resulting singlet is fundamentally different from the Kondo-singlet in the N-state. An electron of the broken pair binds together with the electron at the dot, forming a CP on their own that resonates between the QD and the SC. The wave function of the two resulting eigenstates $|\Psi_\pm\rangle$ (one of them conforming the ground state) is equivalent to a SC singlet, displaying a time-averaged local spin of $\mathcal{S} = 0$ and an spectrum where the YSR resonances also approach the gap edge. Paradoxically, while this regime is characterized by Kondo effect governing the system, the corresponding ground state is BCS-like due to proximity effect, characterized by CPs resonating between the reservoir and the QD.

At the intermediate regime, where $k_BT_K \sim \Delta$, both states $|\Psi_\sigma\rangle$ and $|\Psi_\pm\rangle$ own similar energies. The lowest one constitutes the GS of the system, while the other one becomes the LES. The YSR resonances show up at the corresponding energy difference, $E_{YSR} = E_{LES} - E_{GS}$, lying well below

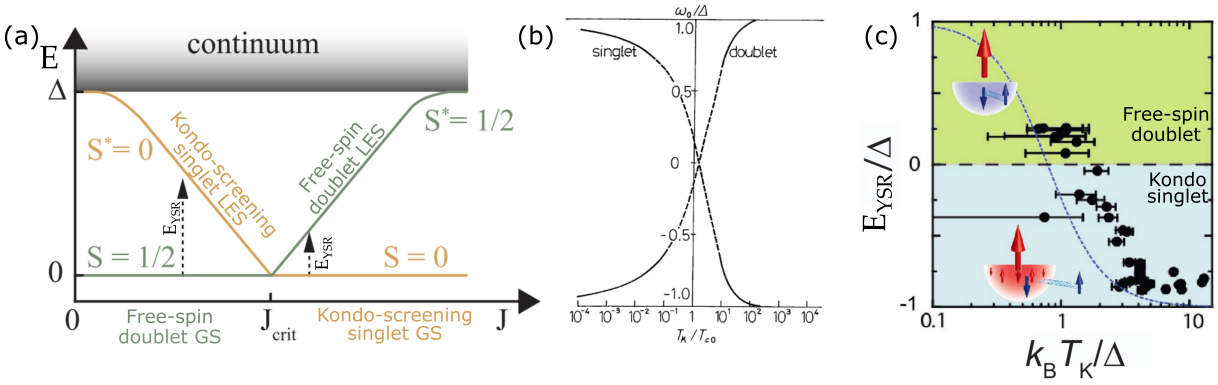

Fig. 1.21: (a) Quasiparticle excitation diagram indicating the nature of the GS and LES, which cross at the QPT, for $J = J_{crit}$, changing the spin of the system (adapted from [147]). (b) The energies of the singlet and doublet cross for $k_BT_K/\Delta \sim 1$, resulting in an inversion of the GS (extracted from [156]). (c) Correlation between k_BT_K/Δ and E_{YSR} measured with an STM in several molecular adsorbates, extracting k_BT_K from the FWHM/2 of the N-state Kondo resonance. The dashed blue line corresponds to Eq. 1.3.64 (adapted from [147]).

Δ. By applying a certain V_B, such that the probing electrode reaches the resonances at $\pm E_{YSR}$, the correlated system is brought from the GS to the LES each time an electron is injected/extracted to/from the probe, eventually relaxing back to the GS, generating a sub-gap current. If the k_BT_K/Δ ratio is tuned from a regime where $k_BT_K/\Delta \ll 1$ to a regime where $k_BT_K/\Delta \gg 1$, for example by tuning J (and consequently k_BT_K), both YSR resonances display cross at zero-energy. This crossing point, where E_{YSR} drops to zero, identifies a the critical value of $J = J_{crit}$, where the system undergoes an inversion of the singlet-doublet states, where the GS at one regime becomes the LES at the other, carrying along a change in the system's average spin by an amount of $\Delta\mathcal{S} = \pm 1/2$ (Fig. 1.21a). Although this transition constitutes a no more than a level-crossing, such GS-LES swapping is often referred to as a quantum-phase transition in the literature [153, 154] (QPT in the remainder). The exchange coupling is considered as the order parameter, and the average spin of the GS is contemplated as the control parameter (abruptly switching from 0 to $1/2$, indicating a first-order transition). Similar transitions are observed by lifting the spin-degeneracy of confined electrons in a QD with an external magnetic field [155], or in Kondo systems with integer spin [111].

The problem of the quantum spin was firstly solved by *Tafimusa Matsuura* [156], obtaining a relation describing the energy dispersion of the YSR resonances at the strong coupling regime ($k_BT_K \gg \Delta$). In his solution, the parameter ζ in Eq. 1.3.63 is be expressed as

$$\zeta = \frac{\pi\Delta}{4k_BT_K}\left[1 + \ln\left(\frac{4k_BT_K}{\pi\Delta}\right)\right], \tag{1.3.64}$$

Although this relation is only strictly valid at the strong coupling limit, it can be extended towards the intermediate regime, displaying the crossing of the YSR resonances qualitatively, for $(k_BT_K/\Delta)_c \sim 1$ (Fig. 1.21b). In fact, the YSR resonance-crossing reconstructed from STM measurements on differently coupled molecules follow the same tendency (Fig. 1.21c). The zero-energy crossing of the YSR resonances constitutes the main transport feature indicating the phase transition in the SC-QD correlated system, probed with a weakly-coupled lead. In contrast, if this electrode is also strongly coupled, the transport across the junction becomes completely correlated, enabling the transport of resonating CPs through the QD that establish a supercurrent across the junction [157]. The QPT manifest in such symmetrically coupled SC-QD-SC junctions as sign inversion of the SC order parameter, corresponding to a π-shift in the phase difference, φ, of the SC wave function of both leads at the doublet-GS phase of the system [158] (Fig 1.22a and b). Such shift of the SC-phase implies a reversal of the supercurrent flowing through the QD when tuning the system across the QPT into the doublet-GS region, as it has been demonstrated by several measurements carried out in SQUID devices (with symmetrically coupled SC-QD-SC junctions conforming one or both of the weak links in the SC loop) [16, 17, 18, 19, 20, 25, 43] (Fig 1.22c and d).

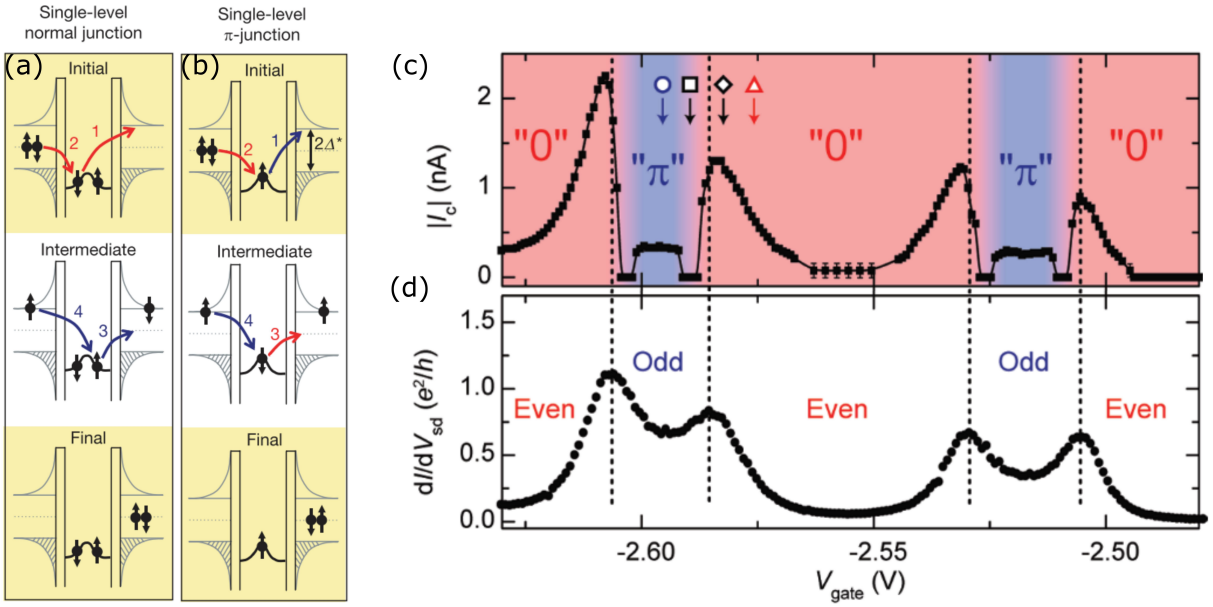

Fig. 1.22: (a and b) Decomposed Kondo-assisted MAR. (a) While the singlet GS preserves the SC phase, ϕ, of the CP, (b) the doublet GS introduces a π-shift in the phase of the CP tunneling through (adapted from [17]). (c and d) A SQUID formed by a QD junction and a tunable barrier allows to measure the absolute critical current $|I_C|$ when sweeping V_G across several charge states. (c) An inversion of the I_C sign, corresponding to a supercurrent reversal, is observed at the gate values corresponding to the center of odd charges states, (d) which display a Kondo ridge in the usual voltage-biasing conductance measurement at the N state. (adapted from [18]).

ANALYTICAL SOLUTIONS AND NRG SIMULATIONS

Already for a classical spin, *A. I. Rusinov* predicted the spatial oscillations of the YSR resonances spectral weight when varying the distance from the impurity [150, 151], experimentally confirmed many years later [33]. For the quantum-spin case, a general solution valid for all possible energy-scale hierarchies and describing precisely the spectral features of the system, has not been found up to the date. An analytical description of the problem is possible when the on-dot repulsion is completely neglected [159] ($E_U \to 0$, commonly known as the non-interacting limit). At this regime, Coulomb blockade effect vanishes and proximity effect imposes a SC singlet state at the dot, dismissing for the possibility of stabilizing a doublet state. If a finite E_U is considered, approximated solutions can be obtained for specific limits by employing analytical techniques [160] (such as mean-field theory or perturbation expansions).

Nevertheless, the superconducting atomic limit (in which $W \gg \Delta \gg E_U \gg \gamma$) constitutes a particularly interesting case as analytical expressions for both the doublet and singlet states can be inferred. By means of the Green-function formalism, an effective local hamiltonian for the dot component is derived from the SC-SIAM:

$$H_0^{\text{eff}} = \sum_\sigma \epsilon_0 d_\sigma^\dagger d_\sigma - \left(\gamma_\varphi e^{i(\varphi_S+\varphi_D)/2}\, d_\uparrow^\dagger d_\downarrow^\dagger + \text{h.c.}\right) + E_U \left(\sum_\sigma d_\sigma^\dagger d_\sigma - 1\right)^2, \tag{1.3.65}$$

where the additional term accounts for the SC proximity effect induced at the dot by the two SC leads forming the junction (S and D, considering a symmetric coupling). The resulting on-dot pairing amplitude is expressed as

$$\gamma_\varphi = \frac{2\gamma_T}{\pi}\ \arctan\left(\frac{D}{\Delta}\right)\ \cos\left(\frac{\varphi_S - \varphi_D}{2}\right), \tag{1.3.66}$$

being proportional to the total tunnel coupling $\gamma_T = \gamma_S + \gamma_D$ and depending on the difference of the respective SC phases, φ_S and φ_D (a single value for the SC gap at both electrodes is considered,

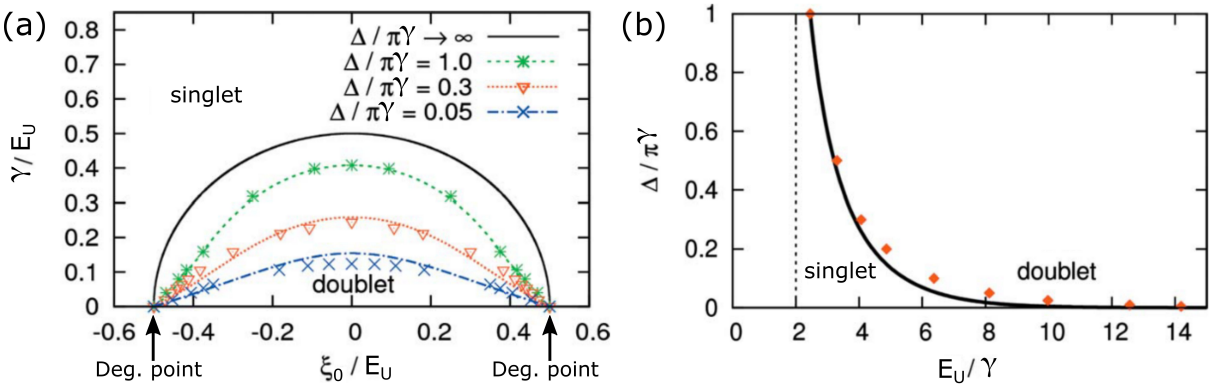

Fig. 1.23: Phase diagram of the QPT as a function of the symmetric level depth (a) and the microscopic parameters of the system (b) for the particle-hole symmetry point $\xi_0 = 0$. The black line in (a) illustrate the analytical result obtained for the SC-atomic limit, signaled in (b) by the asymptotic dashed line. The colored markers/lines represent NRG/perturbative data obtained for intermediate values of the relative scales (adapted from [162]).

$\Delta_S = \Delta_D = \Delta$). The total hamiltonian resulting when plugging H_0^{eff} in the SC-SIAM can be diagonalized by a Bogoliubov transformation, obtaining four possible eigenstates [161, 162]. Two of them correspond to a doublet state $|\Psi_\sigma\rangle = |\uparrow\rangle$ or $|\downarrow\rangle$, with equal energies of $E_\uparrow = E_\downarrow = E_\sigma = \xi_0$, where $\xi_0 = \epsilon_0 + U/2$ represents the level depth, measured from the particle-hole symmetrical point. The other two states are

$$\begin{aligned} |\Psi_+\rangle &= u_0\,|\uparrow\downarrow\rangle + v_0^*\,|0\rangle\,, \\ |\Psi_-\rangle &= -v_0^*\,|\uparrow\downarrow\rangle + u_0\,|0\rangle\,, \end{aligned} \tag{1.3.67}$$

where

$$u_0 = 1/2\sqrt{1+\xi_0/\sqrt{\xi_0^2+\gamma_\varphi^2}} \qquad \text{and} \qquad v_0 = 1/2\sqrt{1-\xi_0/\sqrt{\xi_0^2+\gamma_\varphi^2}} \tag{1.3.68}$$

corresponding to BCS-like singlets, being their respective eigenenergies equal to $E_\pm = E_U/2 + \xi_0 \pm \sqrt{\xi_0^2+\gamma_\varphi^2}$. Four YSR resonances appear at energies of $\pm a_0$ and $\pm b_0$, obtained from the energy difference of the effective hamiltonian's eigenstates

$$\begin{aligned} a_0 &= E_- - E_\sigma = \frac{E_U}{2} - \sqrt{\xi_0^2+\gamma_\varphi^2}, \\ b_0 &= E_+ - E_\sigma = \frac{E_U}{2} + \sqrt{\xi_0^2+\gamma_\varphi^2}. \end{aligned} \tag{1.3.69}$$

While $\pm b_0$ describes two YSR resonances appearing at higher energies, $\pm a_0$ corresponds to the low-energy pair, eventually crossing for $a_0 = 0$, or equivalently, for $\xi_0^2 + \gamma_\varphi^2 = E_U^2/4$, giving the analytical expression for the boundary separating both phases (black line in Fig. 1.23a). Despite the diverging Δ value considered in this limit and the consequent enhancement of proximity effect, the presence of a finite E_U, being much larger than γ, makes possible to stabilize a single spin at the dot, allowing for the existence of a doublet-GS phase.

By applying the NRG method, a few theoretical studies have explored the QPT in SC-QD correlated systems at specific regimes, described either from the perspective of the SC-Kondo model (classical spin) or the SC-SIAM (quantum spin). In the first case, a critical value of $(k_B T_K/\Delta)_c \approx 0.3$ has been obtained for the occurrence of the QPT at a weak-coupling limit, such that $\Delta, E_U \gg \gamma$ [163, 164], decreasing down to $(k_B T_K/\Delta)_c \approx 0.2$ as the coupling is increased [113]. In the later case, the transition at the weak-coupling regime was found around $(k_B T_K/\Delta)_c \approx 0.42$ [158], in agreement with the qualitative value of $(k_B T_K/\Delta)_c \sim 1.0$ found at the strong-coupling regime by *Matsuura* [156]. Similar but consistently larger critical values of $(k_B T_K/\Delta)_c \approx 0.6 - 0.8$ have been

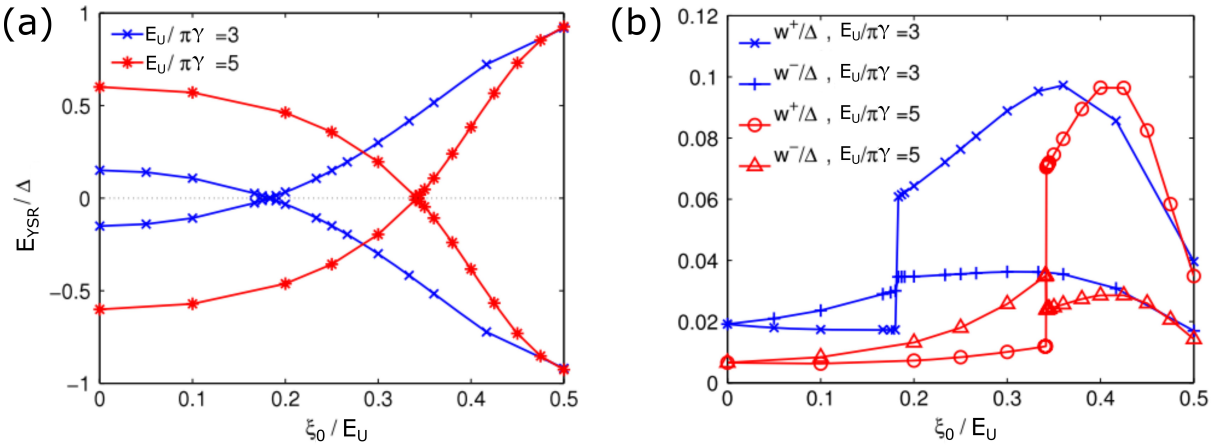

Fig. 1.24: Energies (a) and spectral weights (b) of the YSR resonances as a function of the level depth between one degeneracy point and the center of the odd-diamond, extracted by NRG simulations for two different values of the relative scale $E_U/\pi\gamma$, fixing $\Delta = 0.01$ and $\pi\gamma = 0.2$. (extracted from [161])

obtained experimentally from changes in the tendency of the relative conductance at the SC and N state in symmetrically coupled devices [5, 12, 28], or by observing the zero-energy crossing of the YSR resonances in asymmetrically coupled devices [26, 30]. Even larger values of $(k_BT_K/\Delta)_c \approx 1.0$ have been typically reported in molecular junctions measured by STM [10, 165]. Actually, all such discrepancies are attributed to a certain variability of the prefactor in the Kondo scale k_BT_K considered at each study, as it is defined differently at the various theoretical frameworks [166], and diversely extracted from experimental data. In spite of the lack of agreement, the settlement of an universal criterion is not simple, since it is not always possible to measure certain quantities in specific experimental configurations or numerical approaches, together with the absence of a fixed expression of k_BT_K, valid for any regime. In that sense, k_BT_K is generally taken as a approximate quantity, and special care must be taken when comparing the Kondo scales of different works.

An extended NRG study of the quantum SC-QD system was done by *Bauer et al* providing a description for the full parameter range from the weak to the strong coupling [161]. Together with the energy dispersion and spectral features of the YSR states (Fig. 1.24a and b), they obtained the phase boundary separating the doublet-GS and singlet-GS phases for different relative values of the microscopic energy scales (colored dots in Fig. 1.23a and b). The calculated trajectories of the phase boundary in the E_U/γ vs ξ_0/E_U plane, for different values of Δ/γ, reach the maximum E_U/γ value at the particle-hole symmetric point ($\xi_0 = 0$ or $\epsilon_0 = E_U/2$), coinciding with the saturation of E_{YSR} and the minimum of the spectral weights ($w^{\pm}$). At the singlet-GS phase, $w^{\pm}$ reach a maximum value with the shape of a broadened kink, displaying an inversion of their relative value at the QPT, as well as sudden drop in intensity, further decreasing up to particle-hole symmetry. A couple of years after the publication of this work, a framework applying a perturbation theory to the SC-atomic limit discussed above demonstrated the obtainment of quantitatively similar results [162], presenting slight deviations but resulting more practical than the computationally demanding NRG simulations (colored lines in Fig. 1.23a and black line in b).

2 Sample fabrication and electromigration

Selectively contacting individual metallic particles or molecules of only a few nanometers in size would involve the fabrication of electrode structures so small that are currently unreachable by available lithographic technologies. Breaking junctions provide a suitable alternative, despite the stochastic nature of the cracking procedures that impede sample reproducibility and own relatively moderate yields of successful fabrication of a stable junction system. Separately, the employment of standard metallic lines, made by lithography, for the on-chip transmission of radio-frequency signals down to mesoscopic devices can induce high power losses that are strongly frequency-dependent, detrimental for an accurate control of the incoming signal at the device site, as well as introducing a notable increment of the electromagnetic noise in the sample environment. Specifically adapted designs, like the grounded coplanar waveguide, can ensure a flat transmission of radio-frequency signals along the line over a wide range of frequencies.
In this chapter, we explain in detail the bottom up approach followed for the implementation of a radio-frequency-compatible local back gate electrode combined with previously developed electromigration breaking junctions, entirely made of aluminum and optimized for contacting colloidal nanoparticles, while signaling the difficulties found in the whole procedure and the key points to avoid them. At the end of the chapter, we comment on the characterization of the electromigration process and show the aluminum-compatible quantum-dot deposition methods tried out, indicating the corresponding success rates and identifying the critical parameters that allow to improve them.

Contents

2.1 Introduction to the fabrication of quantum-dot transistors

The empirical concept of a quantum dot (QD) has evolved from its first experimental realizations, more than 30 years ago, as lithographically patterned metallic islands and isolated electron droplets in semiconducting heterostructures of sizes $\sim$ 100 nm, up to the present, accordingly to the gradual progression of nanofabrication technologies allowing to create and contact structures each time smaller. A wide variety of solid state devices have been developed to study the electronic transport through QDs, displaying clever sample geometries and adapted QD deposition methods or growing procedures. The minuscule size of colloidal QDs, such as few-nanometers diameter metallic particles or molecules (called this way as they are usually stored in colloidal solutions), enables to reach the large-charging-energy limit and obtain well-separated electronic energy levels, when contacted by tunnel junctions to a pair of transport electrodes.

At the beginning of this section, we briefly review general breaking-junction approaches, that provide the most common and experimentally accessible way to connect individual colloidal QDs with a macroscopic circuit (2.1.1). Then, we introduce the concept of electrostatic gating as a method to control the chemical potential of mesoscopic objects, enumerating the most common gate-electrode configurations and their compatibility with distinct breaking junctions geometries (2.1.2). After that, we comment on the feasibility of employing superconducting (SC) materials for creating breaking junctions (2.1.3). Finally, we define our strategy for fabricating SC-SET contacting individual colloidal QDs, including an adapted gate electrode for the transmission of AC signals in the radio-frequency (RF) range (2.1.4).

2.1.1 Breaking junctions for contacting individual quantum dots

Contacting colloidal QDs remains a challenging task, since the typical sizes involved (1–10 nm diameter of the dot, plus distances below 1 nm for the contacting tunnel barriers) remain one order of magnitude smaller than the shortest lithographically accessible resolution. The first successful approach addressing individual molecules was achieved in the late 80's by the group of *Aviram et al*, who used a scanning tunneling microscope (STM) to investigate surfaces functionalized with molecular mono-layers [167]. Posterior progression in the field suggested the possibility of creating single-molecule junctions by crashing the STM tip into the functionalized substrate and then retrieving it gently, gradually breaking the formed constriction (Fig. 2.1a). By employing bi-functional linear molecules owning chemically active terminals at both extremes, and a tip made of specific metals reacting with the molecular terminals, it is likely to reach a situation in which a single molecule ends up bridging the tip and the substrate, right after the metallic weak link is completely broken(as done in Refs. [168, 169, 170]).

The success and feasibility of such STM-breaking junctions (STM-BJs) settled the concept of a weak metallic link, functionalized with molecular mono-layers, then artificially broken under controlled conditions, as a suitable method for obtaining single-molecule junctions. It should be mentioned that the rapid progression on these systems stems from the employment of gold (Au), owning a very special set of properties that includes a very specific reactivity (that facilitates the attachment of molecules to its surface), high malleability (favoring its atomic rearrangement during the breaking procedure), and lack of oxidation (tolerating its exposure to ambient conditions and simplifying sample manipulation), which makes it an ideal platform for the development of breaking junctions. Based on STM-BJs, different kinds of solid state devices, in which two massive electrodes are connected by a thin narrow constriction (of typical cross sections around 100×10 nm^2), are fabricated by lithography following bottom-up approaches. According to each different geometry, specific techniques have been developed to break each particular kind of constriction in a controlled fashion, opening a nanometric fissure that separates both leads. Prior to or directly after the breaking procedure, a deposition of colloidal QDs can be carried out on the surface (by a self-assembled molecular mono-layers, direct drop-casting or by thermal evaporation), so that a QD can eventually fall in the crack, sandwiched between both leads and connected to them by tunnel junctions. By applying a biasing voltage,

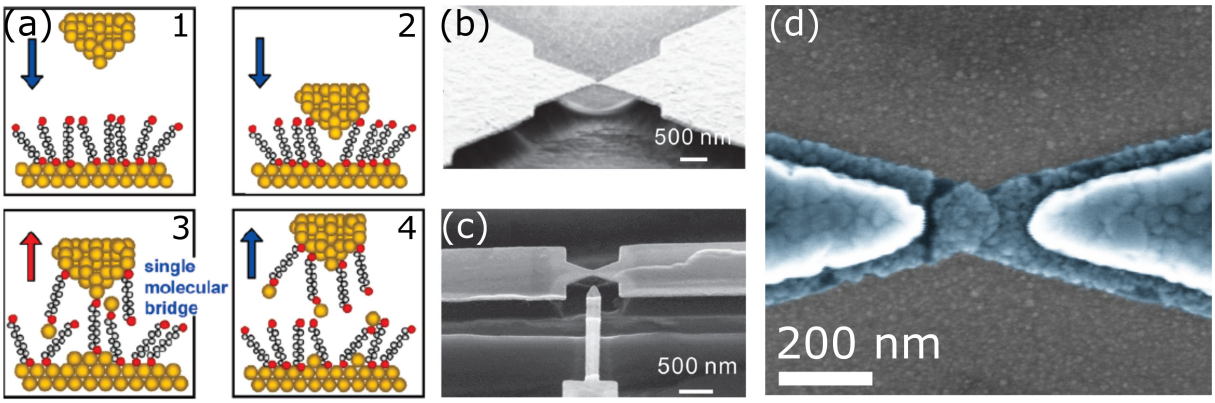

Fig. 2.1: (a) Schematic illustrating the steps of the STM breaking junction technique: 1-Approaching. 2-Touching the surface forming molecular contacts. 3-Pulling. 4-Breaking. (extracted from [175]). (b) SEM image of a MCBJ showing the freestanding metal bridge on an flexible isolating substrate (extracted from [178]). (c) SEM image MCBJ with a side gate electrode (extracted from [179]). (d) False-colored SEM image of an aluminum EMBJ after electromigration has been carried out, showing the formation of a nanometric gap at the thin constriction.

V_B, across such QD junction, the conductance through the dot can be measured in a two-terminal geometry. Compensating the lack of spatial flexibility granted by scanning probes setups, integrated devices benefit from an improved mechanical stability and introduce the possibility of creating more complex devices that connect the QD junction to other circuit elements, for example, a gate electrode, conforming a QD-based single-electron transistor (QD-SET).

Mechanically-controllable breaking junctions (MCBJ), initially conceived to study the conductance of quantum point contacts, were successfully employed to obtain single-molecule devices for first time in the late 90's [171], self-assembled on the electrodes from a colloidal suspension. The principle of operation of MCBJs consist on exerting a physical tension on the sample substrate (for instance pushing the substrate from below with a piezoelectric element) that pulls the constriction-connected leads in opposite directions, gradually reducing the constriction section and finally breaking it apart, similarly to STM-BJ (Figs. 2.1b and c). Diverse experimental work has been carried out ever since in both experimental systems (MCBJ and STM-BJ) [172], studying the transport properties of the QD junction as a function of the leads spacing [173, 174], modifying its tunnel coupling [106] and even managing to rearrange the QD-lead contact geometry and align the molecule [175, 176, 177].

In 1999, a new breaking procedure, based on an old-known phenomenon called electromigration, emerged as an alternative way for creating nanometrically separated electrodes [180]. In short, this technique consist on imposing an increasing current flow between the leads connected by a weak link, that will eventually break the constriction due to the momentum transfer of the moving electrons to the static metallic ions (see Fig. 2.1d). If the process is carried out in a controlled manner, nanometric fissures can be engineered. Opposite to STM and MCBJ, the absence of mechanically moving parts in electromigration breaking junctions (EMBJ) disables the option of moving or rearranging the QD. On the other hand, its main advantage resides in the possibility of including a relatively-well coupled gate electrode that can be used to modify the chemical potential of the dot, allowing to study its transport properties over this different degree of freedom. Albeit the presence of a colloidal QD in the opening crack seems very improbable, the yields of success found in EMBJ experiments (1–10%) suggest a tendency of nanoparticles and molecules to bridge the gap when electromigration takes place. However, up to the date, it is thought to be a random process over which we have no control, and no future perspectives of massive production of QD junctions using EMBJ can be drawn at the moment.

2.1.2 Gated-quantum-dot electromigration junctions

The concept of the gate electrode is on the foundations of quantum nanoelectronics. By applying a voltage, V_G, to the gate electrode it is possible to tune the chemical potential of a quantum

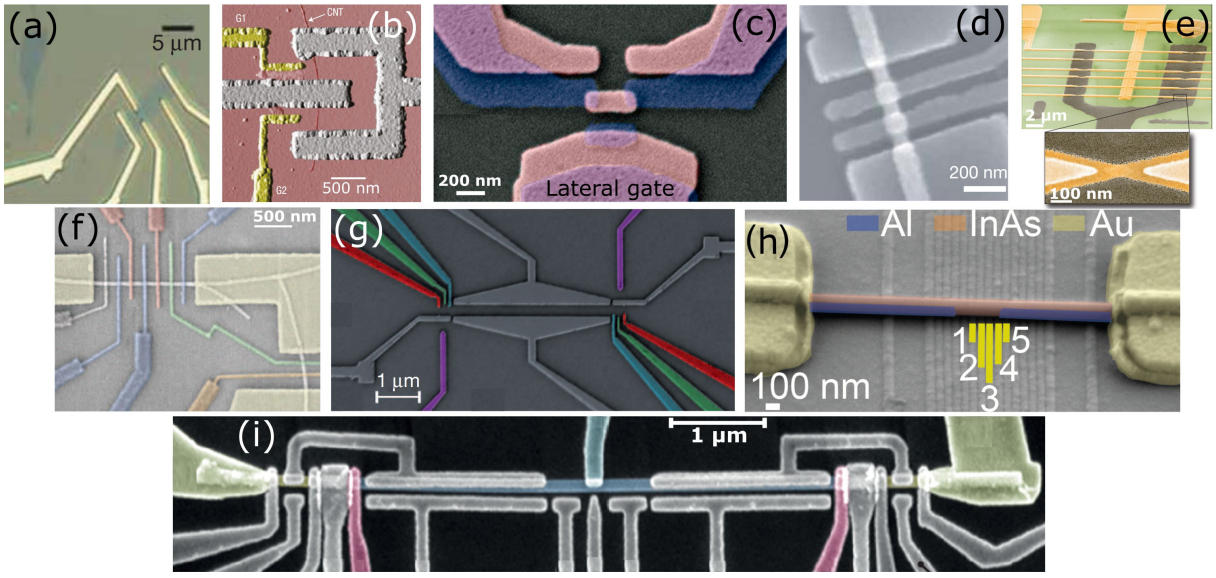

Fig. 2.2: (a) Graphene quantum-hall bar on a doped-Si wafer with a 300 nm SiO_2 coating layer. A voltage is applied to the doped silicon substrate, acting as a planar back gate (extracted from [181]). (b) CNT-based SQUID device in which the doped-Si substrate is employed as a planar back gate, while the two yellow electrodes are sidegates (extracted from [16]). (c) The chemical potential of a metallic nanoisland (central pink segment) is controlled by a sidegate following the classical SET configuration (extracted from [47]). (d) Topgates patterned on an InAs NW defining a QD in between them. (extracted from [17]). (e) Local horse-shoe shaped back gate (dark grey) with Au electromigration constrictions on top. (extracted from [182]). (f) Several local top gates patterned on a Si/Ge NW. The blue electrodes define two QDs on series, while the red ones are used to control their chemical potentials (extracted from [183]). (g) Several topgates on a GaAs heterostructured substrate define a complex potential landscape in the 2DEG layer several nm below the surface, including two QDs (red, green and blue). (extracted from [184]). (h) Several backgates define and control two on-series QDs in an InAs NW (extracted from [185]). (i) Several top and lateral gate electrodes patterned on a InAs/Al NW conform a device consisting of two on-series SC nanoislands coupled to smaller nanoislands, in the normal (N) state, at the sides of the NW that act as SETs for charge detection (extracted from [186]).

objects capacitively coupled to it. In this sense, the quality of a gate electrode is defined by the gate capacitive coupling parameter (α_G, that determines the chemical potential change due to a certain V_G shift) and the avoidance of a leakage current to/from the transport electrodes. The implementation of gate electrodes owning different geometries have been developed along with the progression in nanofabrication technologies. Different kinds of gate electrodes can then be adapted and combined depending on the nature of the sample and the particular phenomena to be measured:

- **Planar back-gate**: the extended use of doped-Si wafers with a topping thermal oxide layer enables to employ the conducting silicon bulk as a for the global gating of nanostructures placed/fabricated on top. The thickness of the thermal oxide (~ 100 nm) determines the gate coupling, commonly valid for relatively large mesoscopic structures, like 2D-material micrometric flakes or carbon nanotubes or nanowires, but far too weak for tiny colloidal QDs. Devices employing this gating method are shown in Figs. 2.2a and b.
- **Local top-gate**: also called topgates, these are dead-end electrical lines patterned by lithography, generally used for local depletion/accumulation of electrons in semiconducting nanostructures. Complex potential landscapes, such as electron droplets acting as QDs, can be induced at the 2DEG by fabricating multiple topgates following specific designs (Figs. 2.2d, f, g and i).
- **Lateral gate**: also known as sidegates, being as well dead-end electrical lines patterned by lithography, can be used in devices involving quantum objects large enough to provide a significant gate coupling at lithographically-accessible distances (Figs. 2.2b, c and i).
- **Local back-gate**: Also referred to as backgates, are again dead-end electrical lines patterned by lithography, generally covered with a thin oxide layer for their electrical isolation from the structures patterned on top (Fig. 2.2e and h).

As explained in the previous chapter (1.2.1), the charge state of the dot in a QD junction following the three-terminal SET configuration can be modified by sweeping V_G. Common SET devices involving lithographically-defined QDs, such as metallic nanoislands [47], electron droplets defined in a two-dimensional electron gas (2DEG) [184], in semiconducting nanowires (NW) [17, 185, 186] or carbon nanotubes (CNT) [16], are fabricated incorporating local top and lateral gate electrodes, generally obtaining relatively large gate couplings (up to $\alpha_G \sim$ 1–10%) that allow a few charge states to be addressed. In contrast, gating colloidal QDs in breaking junctions is not so simple, as the large size of the constriction electrodes with respect to the few-nanometers dots, screen the gate electric field inside the nanogap, resulting in much lower gate couplings. To maximize this parameter, local backgates covered by extremely thin oxide layers (of about 10 nm) are employed in EMBJs, leading to typical capacitive couplings to the gate of $\alpha_G \approx 1\%$.

The scope of creating gated and re-arrangeable QD junctions that combines the spatial resolution of STMs, the fine and stable tunnel coupling modification and QD geometry rearrangement of MCBJs, and the chemical potential tuning with the gate present in EMBJs, has fueled the exploration of exotic experimental configurations. In scanning probe setups, limited gating methods like in-situ aqueous-solution media (that provides electrochemical gating of specific redox molecules) [187, 188], and artificial arrangements of individual atoms close to the junction [189] have been demonstrated so far. Future perspectives may introduce STM-compatible samples that include lithographically patterned gate electrodes. In a parallel research line, diverse approaches have studied the feasibility of adding a gating electrode in MCBJs. By including a backgate [190] or sidegate [179] a moderate influence over the $I - V_B$ characteristics has been reported, even managing to change the QD's charge state [191]. Although the gate couplings achieved are around one order of magnitude below EMBJs ($\alpha_G \sim 0.1\%$) more recent experiments have managed to implement a local backgate along the weak link bridge ("sandwich" configuration) [192, 193, 194, 195] enhancing the gate coupling to values closer to the typical ones obtained in EMBJs.

2.1.3 Superconductor-quantum-dot electromigration junctions

In the last 20 years, the implementation of SC-QD hybrid devices, in which the macroscopic quantum state of superconductivity (SC) is combined with electron confinement at the dot, have boosted up to explore novel transport properties arising in these systems. Nevertheless, intrinsic difficulties are found in the usage of conventional superconductors, as most of them oxidize rapidly even at medium vacuum. Such aspect does not collide for the fabrication of devices based on CNTs [16, 18, 20] or semiconducting NWs [6, 17, 196] or nanocrystals [12, 31], as the SC material can be directly deposited on top of the nanostructures to form the contact. The fabrication procedures of junctions contacting metallic nanoislands take profit of this property as they are based in shadow angle evaporations, intercalated with controlled oxidation processes enabling to control the tunnel barrier of the island contacts [46, 47]. However, the employment of SCs to fabricate breaking junctions have turned out to be not so straightforward. On one hand, it is not clear that a proper electromigration, leading to the formation of nano-spaced electrodes, can be performed in SC materials. On the other, the extremely high O_2 reactivity displayed by most conventional SCs requires to carry out the breaking procedure in-situ under, at least, high-vacuum conditions.

As a consequence of these drawbacks, only a few examples on the experimental conception of SC breaking junctions exist in the literature, which employ proximized-Au at the constriction [39, 36]. In fact, the presence of a sharp BCS-like DOS with an abrupt energy gap, that leads to a total suppression of current at energies below the SC gap, Δ, is mandatory for the turnstile operation of SC-QD-SC SET junctions (see Annex A). In this research line, previous students at Néel Institute have optimized the fabrication process of state-of-the-art electromigration constrictions entirely made of Al [37], which were proven successful for contacting colloidal QDs [38]. Furthermore, charge pumping measurements were performed in some of these samples, demonstrating their feasibility as a electron-turnstile devices [48], though showing a reduced frequency-range of operation, attributed to the lack of a RF-adapted gate electrode.

2.1.4 Fabrication objectives

The main nanofabrication objective of this project is to implement a RF-compatible gate electrode matched at the impedance of the cryogenic RF lines (50 Ω). This task can be accomplished by the inclusion of a ground plane, thus requiring the modification of the previous EMBJs sample design. Moreover, the high dielectric permittivity of intrinsic Si (three times larger than usual doped-Si substrates) allows to design impedance-matched gate electrodes wide enough to harbor the EMBJ structures on top, replacing previously employed doped-Si substrates. Additionally, the replacement of alumina (Al_2O_3) as the gate and ground plane oxide insulation layer by zirconia (ZrO_2) enabled us to pattern bonding lines by optical lithography thanks to its resistance against the developing chemical agents used in the process, besides providing an increased gate coupling due to its larger relative dielectric permittivity.

Few hundreds of individual chips (basic unity that can be cooled down at a time) containing a total of 30 electromigration constrictions each (augmented with respect to previous sample designs) could be prepared simultaneously in a three-step lithography process, increasing the probability of successful electromigration per cool down. The design and adjustment of the whole fabrication process parameters (summarized in Annex D) were the fruit of a close collaboration with the postdoctoral researcher *David M. T. van Zanten* and the technical staff composing the NANOFAB platform.

2.2 Waveguide gate electrode fabrication

The design of the gate electrode must be done according to the following key points: while the local back-gate is the only gating geometry compatible with electromigration that provides sufficiently large couplings to access different charging states in colloidal QD junctions, its design must be arranged to warrant an adequately flat transmission of RF signals from the sample-holder connectors. Several configurations commonly employed in micro-electronics for conceiving a waveguide electrodes are reviewed at the beginning of this section (2.2.1). Then, we described the lithography process, which employ a bi-layer resist technique to achieve a highly flatness of the structures that integrate the gate layer to avoid inducing failures on the EMBJs that will be patterned on top (2.2.2). Finally, an oxide layer is used to cover the gate structures, providing the electrical insulation from the junctions (2.2.3).

2.2.1 Transmission line geometries

Precisely RF-driven QD junctions require an accurate control of the AC signal arriving to the gate electrode. A good-quality RF line becomes essential to ensure the proper transmission of the signal from the wave-generator, into the cryostat and down to the gate electrode of the sample. Impedance discontinuities appearing in RF lines between the central conductor and the grounded coaxial jacket generate standing waves along the line, leading to a frequency-dependent transmission coefficient, amplifying or attenuating the oscillation amplitude in segments of the line matched at different impedances. To avoid the formation of standing waves, RF component and cables are meticulously designed and tested to present nominal impedance values, standardized at 50 Ω. In past experiments, it was observed that the chemical potential oscillation induced in some QD junctions displayed a strong dependence on the signal's frequency (see Annex A), pointing towards an impedance mismatch. Measurements performed with a vector network analyzer reaffirmed the good state of the cryogenic RF line, localizing the mismatch at the sample-holder stage. The capability of identical sample-holders and micro-bonding wires for properly transmitting RF signals in similar experimental setups, then leaded us to suspect about the gate electrode as the mismatching spot. At the beginning of my project, we started investigating how to implement an impedance-matched gate electrode (acting as a waveguide) imitating transmission line designs. A detailed description on the propagation of AC signals in transmission lines and several effects that may induce variations of the gate coupling parameter for AC signals can be found in Annex B.

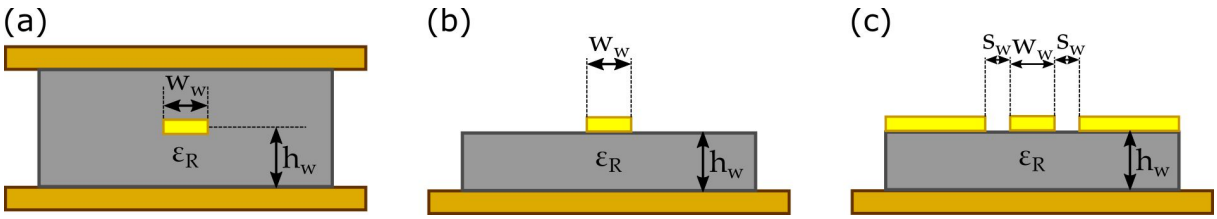

Fig. 2.3: a) Cross-section of a stripline geometry. The RF signal is carried by the central strip, embedded in an insulator, sandwiched in between two ground planes on the top and bottom. b) Cross-section of a microstrip geometry. The RF signal is carried by the central strip, patterned on an insulating substrate placed on a bottom ground plane. c) Cross-section of a GCPW geometry. The RF signal is carried by the central strip, patterned on an insulating substrate in between two coplanar ground planes (right and left), and a bottom ground plane.

The small size and planar structure of integrated circuits in the variety of micro and nanoelectronic devices makes impossible the use of coaxial cables, commonly employed in macroscopic electronics to carry AC signals. At this scale, coaxial cables are replaced by transmission lines: metallic strips patterned on substrates by lithographic processes that act as a waveguide for the oscillating signal, minimizing losses in form of radiation and keeping a high-quality transmission over a certain frequency range. In answer to the public demand of electronics reaching larger bandwidths, reduced noise and produced at lower costs, different designs have been developed, among which the following stand out:

- **Stripline**: This classical configuration, also called triplate line (Fig. 2.3a), was developed during World War II [197]. It consists in a thin flat metallic strip buried in an insulator (ideally air) sandwiched between two parallel ground planes. The width of the waveguide strip (w_w), its distance with respect to the ground planes (h_w) and the relative permittivity of the insulator (ε_R) determine the impedance of the ensemble. This design provides for environmental noise immunity and little power losses, allowing a high-frequency performance up to 10 GHz.
- **Microstrip**: The microstrip configuration (Fig. 2.3b) was developed a few years after [198] as a more compact and cost-efficient alternative to the strip line. In this case the metallic strip is fabricated on a substrate placed on top of a single grounded metallic plate. Despite displaying significant power losses at high RF frequencies due to the different dielectric constants of the two surrounding media and inducing unintentional cross-talks if other circuit components are not well-arranged, microstrips are widely used in different applications up to a few GHz.
- **Co-planar waveguide (CPW)**: The CPW configuration was designed in the late 60s [199]. This geometry adds a couple of broad ground planes on both sides of the transmission line to the microstrip design. It introduces an easily-modifiable parameter: the spacing between the coplanar ground planes and the transmission line (s_w). By properly setting the values of w_w and s_w, it is possible to adjust the impedance of the transmission line for different substrates (h_w and ε_R), ensuring a high-transmission over a larger bandwidth (up to several GHz) than its little brother; the microstrip. Later designs include a ground plate under the substrate, baptized as grounded coplanar waveguide (GCPW or conductor-backed CPW, Fig. 2.3c). Interestingly, innovative designs based on a waveguide integrate by arrays of SQUIDs allow the external modification of the CPW line impedance with a magnetic field [200].

The adaptability offered by the CPW design, optimizable for different frequency ranges, together with its open geometry makes it a perfect substitute of conventional microstrips, becoming popular in the field of quantum nano-electronics, specially for experiments that require large bandwidths (for instance, the transmission of ultrashort RF pulses for single-electron manipulation [201]). In fact, as pointed out in sections 1.3.2, the presence of electromagnetic noise in the sample environment induces the broadening of the SC density-of-states sharp features, generating a sub-gap leakage current in SC-SETs that is enhanced when these devices are operated as turnstiles due to power losses if using a microstrip gate. Not only a broader bandwidth can be achieved by adding ground planes following the CPW configuration, but it has also been demonstrated that the sub-gap current is greatly inhibited as a consequence of reduced power losses in the waveguide gate [138, 202].

Taking advantage of the adjustable impedance offered by the CPW geometry, we started several fabrication tests for its implementation in our EMBJ samples as the gate electrode. Simulations were done to select the preferred substrate material and determine the precise dimensions of the CPW design, matching it at the 50 Ω standard. Opposite to the classically used doped-Si wafers with a relative permittivity around 3.9, intrinsic-Si provides a three times larger dielectric constant ($\varepsilon_R^{Si} = 11.9$) permitting a 1-$\mu$m-wide 50-$\Omega$-matched gate electrode, broad enough to comfortably hold EMBJs on top. Intrinsic-Si wafers available in the market have a typical thickness of h_w = 275 μm, for which our simulations establish a CPW structure of sizes of w_w = 3.8 μm and s_w = 2.3 μm (details on the simulation can be found in Annex C). When the whole fabrication process is finished and single chips containing constrictions ready for electromigration are diced out to be individually cooled down and tested, a conducting glue (silver paste model 4929N) is used to glue the chips on the metallic plate of the sample-holder that provides the bottom ground plane of the GCPW configuration. Additional benefits resulting from the ground planes in the sample include a better thermal conduction for heat evacuation during electromigration, and the formation of capacitors at the bonding lines of the junctions acting as on-chip high frequency filters.

2.2.2 Coplanar waveguide gate lithography

Local back gates of nanoelectronic devices must be fabricated as flat as possible. Conventional lithographic processes based on a single resist layer often induces upstanding edges (top row of Fig. 2.4). Such spiky ridges result detrimental for a vertical flow on successive lithographies, as they can easily create disconnections in the structures patterned on top or short-circuits with the electrodes below. A bi-layer technique for optical lithography developed at the Nanofab platform of Néel Institute allows to create an undercut in the resist mask (bottom row of Fig. 2.4), avoiding the formation of upstanding edges: first, a thick bottom layer of resist (LOR3A), sensitive to the developer agent, is spin-coated on the substrate. Then, a second layer of photo-resist (S1805) is spin-coated on top. After the insulation, the sample is submerged in the chemical developer, which will immediately dissolve the insulated pattern on the top photo-resist, and will gradually eat away the exposed areas of the bottom resist. The developing time, the resist thicknesses and the exposure dose are the key parameters to create a stable undercut that will prevent the contact between the metal deposited on the substrate

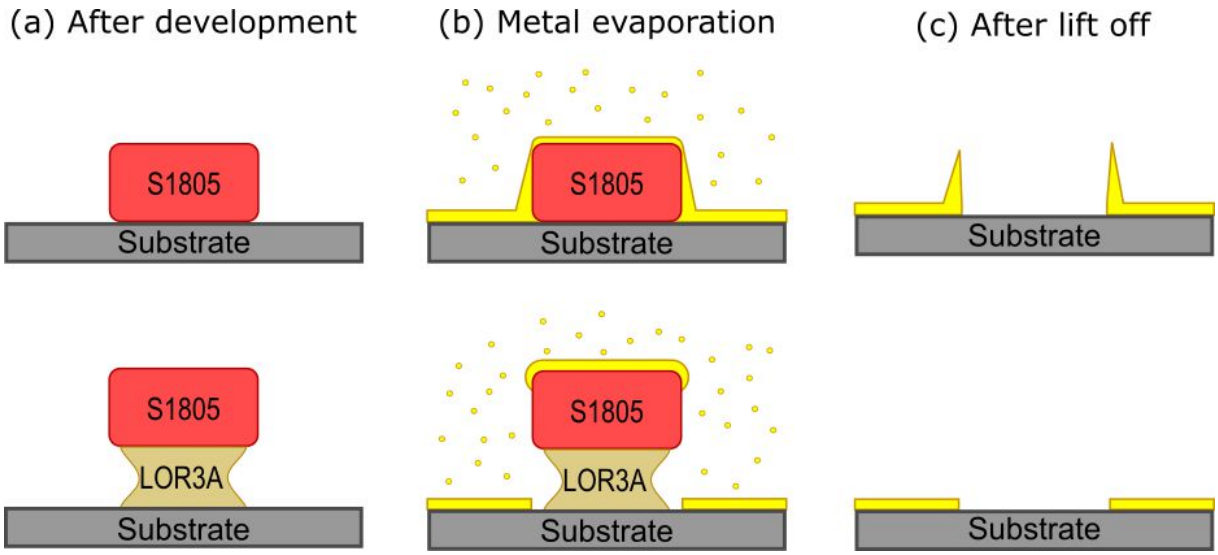

Fig. 2.4: Illustration of the last steps of an optical lithography process for two different samples with a single photo-resist layer (top) and an optical bi-layer resist (bottom). (a) The high sensitivity of the lower bi-layer resist to the developer agent creates an undercut, non-existent in the single resist layer sample. (b) The presence of the undercut avoids the deposition of metal on the sides of the resist mask. (c) The metal deposited on the sides of the resist (top sample) creates upstanding edges, absent when an undercut is present (bottom sample).

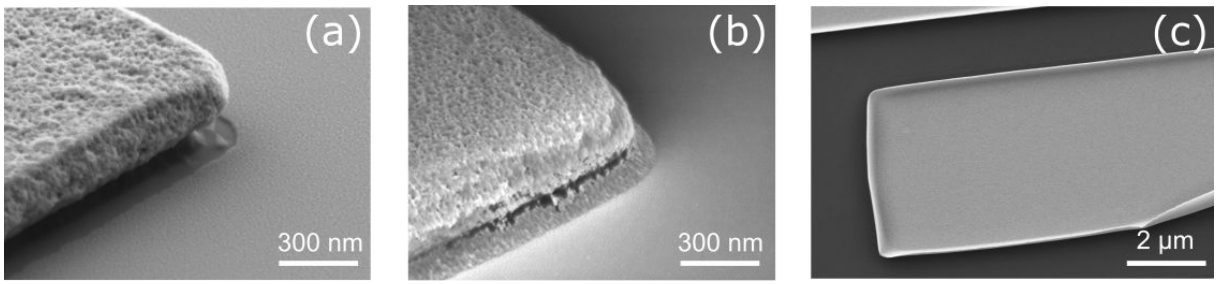

Fig. 2.5: SEM images of structures made by optical lithography. (a) The adjustment of the bi-layer parameters provides a sufficiently large and stable undercut leading to a flat metallic structure on the substrate. (b) Too short development times can originate a reduced undercut, allowing the metal to deposit on the resist wall. (c) The whole edge of the gate electrode is bended upwards when employing a single-resist layer.

and on top of the resist bi-layer (Fig. 2.5a). These parameters need to be adjusted depending on the total area of exposure of each particular design, otherwise the resulting undercut might be too large and collapse during the metal evaporation or too small and unable to prevent upstanding edges (Fig. 2.5b). As in our CPW design two thin resist lines (around 2.3 μm wide) are surrounded by a heavily insulated large area corresponding to the ground plane, the unintentional partial insulation of the resist lines by proximity due to laser beam deflection is high, inducing upstanding edges all over the structure (Fig. 2.5c) if the most straightforward single-resist layer approach is employed.

Our CPW design includes a gate electrode large enough to support 30 EMBJ per chip (each chip contains one gate). Few compact arrangements were prepared for commercial 2-inches intrinsic-Si wafers, maximizing the number of chips per disk (150–250). Several tests were done to optimize the parameters of the bi-layer optical lithography. In short, the surface is cleaned by an O_2 dry reactive ion etching plasma (RIE) and the resists are spin-coated and baked. The insulation is done with a Heidelberg laser lithography machine, with a minimum resolution of 1 μm, slightly below the smaller sizes of our CPW design. Precise alignment with the crystalline axis of the wafer must be done to facilitate its later dicing into individual chips. After the exposure, the wafer is developed and we proceed with the evaporation of a Ti-Au layer using an electron-beam metal evaporator. Finally, we put the sample into lift off solvents that remove the remaining mask. Pictures showing the CPW structure integrating the gate layer of a single chip can be seen in Fig. 2.6, including cross-shaped markers used in the alignment of subsequent lithography steps. A detailed recipe containing the adjusted values of all the parameters in the process can be found in Annex D (Tab. D.1).

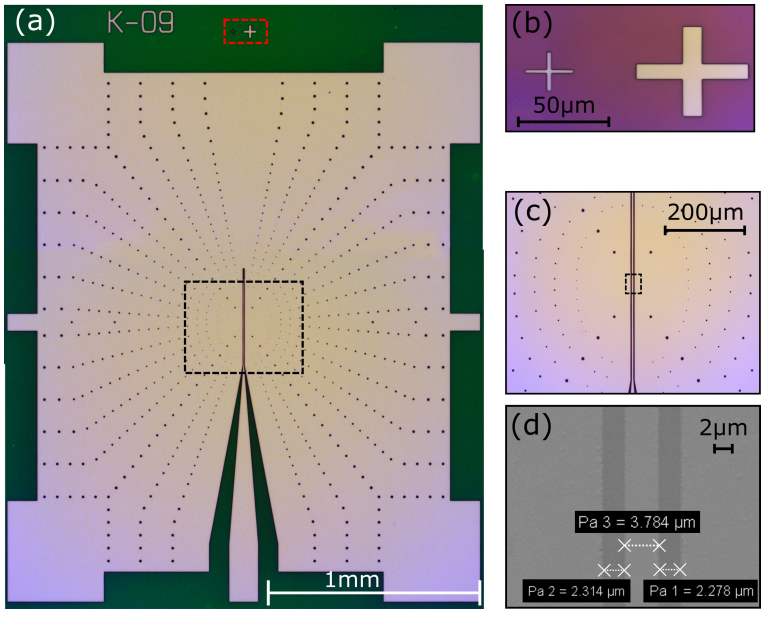

Fig. 2.6: Optical microscope image of an individual chip after finishing the first lithography step. (a) The gate electrode is patterned in between a large rectangular ground plane, following a CPW configuration. (b) Zoom-in at the red dashed square in (a) showing the alignment markers for following lithography steps. (c) Zoom-in at the black dashed square in (a), the width of the gate electrode and its spacing with the ground plane is kept constant along its whole length. (d) SEM picture zooming-in at the black dashed line square of (c). The dimensions of the gate electrode are $w_w \approx 3.8$ μm and $s_w \approx 2.3$ μm.

2.2.3 Gate oxide insulation

Traditionally, the silicon industry use SiO_2 as the insulating layer for gate electrodes in MOSFET transistors, where the gate coupling is determined by its relative dielectric permittivity ($\varepsilon_R^{SiO_2} = 3.9$) and its thickness (usually thermally grown SiO_2 layers of a few hundred nanometers). The increasing complexity of integrated circuits (envisioning 3D structures and vertical architectures) soon demanded for a conformal insulation of the metallic structures. Initially, elements made of aluminum were used for this purpose, oxidizing its surface at controllable oxygen pressures. However, undesired detrimental effects, such as low breakdown voltages or current leakages, arising from the small thickness of this natural oxide (∼2 nm), have promoted the development of oxide deposition techniques like chemical vapor deposition (CVD) or atomic-layer deposition (ALD) in the last decades. These processes allow to deposit an oxide layer of a preselected material on an arbitrary surface atomic layer by layer, controlling the thickness down to the atomic scale up to few hundreds of nm of total thickness. The resulting deposition is conformal and uniform along the whole sample surface, ensuring the complete insulation of the structures underneath and the conservation of a relatively flat surface for fabricating of structures on top. The possibility of growing layers of high-κ dielectrics ($\varepsilon_R^{high-\kappa} > \varepsilon_R^{SiO_2}$) [203] regardless of the sample surface composition or morphology has been key for the success of these methods. The employment of oxides as Al_2O_3 ($\varepsilon_R^{Al_2O_3} = 9$), or more recently HfO_2 and ZrO_2 ($\varepsilon_R^{HfO_2}, \varepsilon_R^{ZrO_2} \approx 25$) [204] has become increasingly common, although the characterization of their electrical properties is still a research field on its own, as it has been demonstrated that actual values of $\varepsilon_R^{high-\kappa}$ depends strongly on the parameters of the deposition process [205, 206].

As the ALD method reduces the concentration of impurities in the oxide while keeping the amorphous structure, necessary for a high-quality electrically-insulating layer (ensuring high breakdown voltages and small leakage currents [207, 208, 209]), it has been our preferred oxide growth approach. Among our material choices, previous students' experience indicate that Al_2O_3 oxide gets etched by common chemical developers (MF26A), and observations of unexpected resistivity increases in thin Al films when deposited on top of HfO_2 due to unknown causes leaded us to use of ZrO_2, since it did not show any conflicts with the fabrication process while owning a high-κ dielectric character. Actually, the good quality of the insulating layer is of paramount importance and its deposition is a critical fabrication step: on one hand, a few-nm oxide must insulate effectively an area of about 4 mm^2 (total area of the gate/ground plane structures), advocating for large thicknesses to avoid the appearance of short-circuits between the gate/ground-plane and the junctions, which will completely invalidate the whole wafer. On the other hand, thin oxide layers provide larger α_G to the colloidal QDs in the junctions that will be obtained eventually. It was pointed out by *Supriyo Datta*, that the gate coupling dependence on the oxide thickness saturates around 10 nm for a tapered electrode geometry, below which α_G is mostly inhibited by the screening of the nano-spaced electrodes in an electromigration junction [210]. Significant work was done to adjust the oxide deposition parameters, and a fair compromise for this trade-off was found for oxide thicknesses of $L_{ox} \approx 18$ nm, corresponding to 180 iterative steps of the growth procedure shown in Annex D (Tab. D.2). The electrical characterization of the resulting ZrO_2 layers is shown in section 2.4.2.

2.3 Electromigration constrictions fabrication

The circuit constituting our EMBJs is fabricated in two lithography steps. Large structures, such as the bonding pads and access lines, are firstly patterned by deep ultra-violet (DUV) optical lithography using a hard mask aligner (offering a reduced minimum resolution of a few μm but fast insulation times of about 30 s). In the second step, the nanometer-sized constrictions are patterned on top of the gate electrode and connected to the access lines by electron beam lithography (EBL) owning a 10-nm resolution. A bi-layer technique is used again for both lithographies, in the case of the access lines to avoid upstanding edges that may result in poor contacts with the junctions lines (2.3.1), and in the case of the EMBJs being strictly necessary (2.3.2) as a shadow-angled metal evaporation

technique is employed to fabricate the aluminum constrictions below the resist undercut (2.3.3). At the end of this section we dedicate a few paragraphs commenting on the gradual deterioration of our aluminum samples after their fabrication, relevant for their storage (2.3.4).

2.3.1 Access lines optical lithography

The access lines of the electromigration junctions include a bonding pad area, where each line can be bonded to the sample-holder pads and connected to the cryostat lines. The bonding area must stick out of the ground plane, as the micro-bonding procedure is rather aggressive and could easily break the ALD oxide layer creating short-circuit with the ground plane, if the bonding areas would have been patterned on top of it. The metallic structures constituting the access lines mount on top of the oxide-covered ground plane, extending the bonding pads towards the central part of the sample, where the constrictions will be patterned later. A DUV optical aligner is used in hard contact mode to insulate the bonding-pads-access-lines (BPAL) pattern on the sample. A bi-layer resist was also employed in this step to avoid the generation of upstanding edges and ensure good electrical contact of the access lines with the constriction lines. A chromium photo-mask incorporating the BPAL design, as well as alignment markers patterned in the gate lithography step for a precise alignment was ordered and has been employed for the fabrication of all samples in this thesis. The optical aligner counts with a 500 W Cd/Xe lamp of 240-365nm wavelength and a minimum resolution $\sim 2\mu$m. Once the exposure finished, wafer were developed and metallized with a Ti-Au layer constituting the bonding pads and access lines, then put into solvent to remove the remaining resist (Fig. 2.7). Further details on the lithography process parameters can be found in Annex D (Tab. D.3).

ON-CHIP LOW-PASS FILTERS

The access lines design was outlined taking into account their overlapping area with the ground plane, ranging between $A_{AL} = 0.06 - 0.1$ mm^2, depending on the line number (1–32). The zirconia layer sandwiched in between forms a plane capacitor to ground, effectively acting as an on-chip low-pass filter (LPF) beneficial for noise filtering. Considering an oxide thickness of $L_{ox} \approx 18$ nm and assuming realistic permittivity of $\varepsilon_R^{\mathrm{ZrO_2}} \approx 18$ [211], we can expect filters with capacitances in the range of $C_{AL} = \varepsilon_0 \varepsilon_R^{\mathrm{ZrO_2}} A_{AL}/L_{ox} \approx 500 - 900$ pF. Electrical characterization of the sample shows a total access line resistance of $R_{AL} \approx 50\ \Omega$ from the bonding pad to the junctions, in agreement with our expectations, leading to a LPF cut-off frequency of $f_c^{LP} = 1/(2\pi R_{AL} C_{AL}) \approx 0.5 - 3$ MHz, added up to the noise filtering circuitry in the cryostat lines.

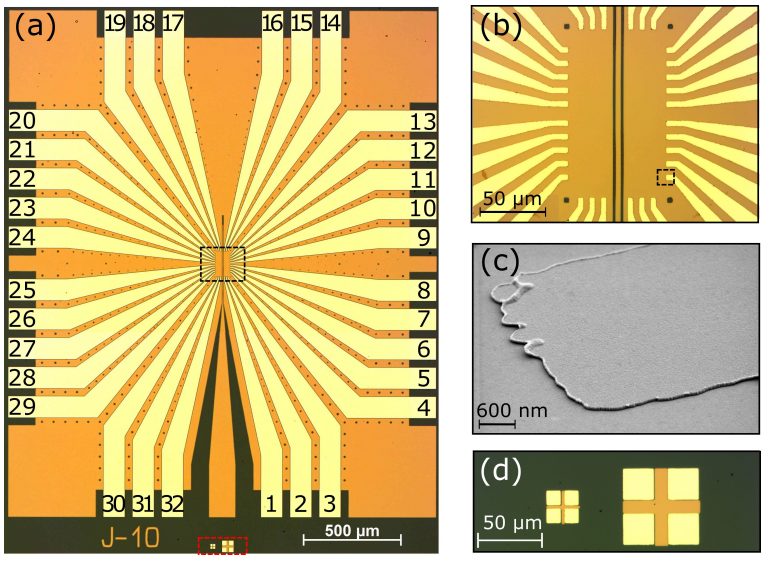

Fig. 2.7: Optical microscope image of an individual chip after the second lithography step. (a) The bonding lines (numbered 1-32) mount on top of the oxide-covered ground plane, providing access to the central part of the chip. (b) Zoom-in at the central part of the chip (black dashed square in (a)). (c) SEM picture of one bonding line ending (black dashed line square in (b)). The bi-layer resist technique employed minimizes the generation of upstanding edges. (d) Zoom-in at the marks used for the DUV lithography alignment (red dashed square in (a)). The cross-like marks are patterned at the gate lithography step, and aligned with square patterns in the DUV lithography step.

2.3.2 Constrictions electron-beam lithography

Reducing the dimensions of three-terminal devices down to the scale of colloidal QDs (few nm) has revealed the apparition of size-scaling issues that effectively reduce the gate coupling. A detailed analysis performed by *Datta et al* studying the electric field screening effect of nano-spaced contacting leads showed that the geometrical shape of the junction (parametrized by the nanogap spacing s and width d, and the electrode thickness t and angle θ) plays a mayor role determining α_G, as important as the oxide layer parameters: dielectric permittivity ε_R^{ox} and thickness L_{ox} [210] (Fig. 2.8). Although electromigration does not allow a precise control on the nanogap typical sizes (s and d), the shape of the metallic constriction enable to reach a certain reproducibility for fixed parameters of the electromigration procedure. A few key points regarding the design of electromigration constrictions to obtain nanogaps of similar sizes and improve the chances of having large α_G, are listed below:

- The whole nanometer-sized constriction must be fabricated on top of the gate electrode localizing the nanogap creation on this area.
- The constrictions must be connected to the extreme of the access lines (previously patterned by DUV lithography in our case). Ideally, the total accessing lines must have a negligible resistance, so that when applying a tension the main voltage drop happens across the constriction (necessary for a correct evolvement of electromigration).
- For the constriction design, tapered shapes (with $\theta < 120°$) and section sizes no bigger than ~ 10 nm height and ~ 100 nm wide are preferred in order to minimize the electric field screening of the contacting leads. For constrictions fulfilling these conditions, the minimum oxide thickness can be fixed to $L_{ox} = 10nm$.

We based our fabrication procedure on the method developed by *Park et al* [180], consisting on the exposure of a bi-layer resist combined with a two shadow-angled and one perpendicular metal evaporations, resulting in thin and narrow constrictions over a length ~ 100 nm, connected to bulky access lines. While the design and fabrication of Au constrictions has been optimized at Néel Institute for more than a decade [182, 39], several tests has been done to extend this technique for all-aluminum constrictions in the last years, showing the feasibility of employing this material likewise for creating QD junctions by electromigration [37, 38, 48]. In this context, I inherited the newborn fabrication recipe for Al constrictions and implemented it for the CPW gate design, trying to optimize further the success rate of electromigration.

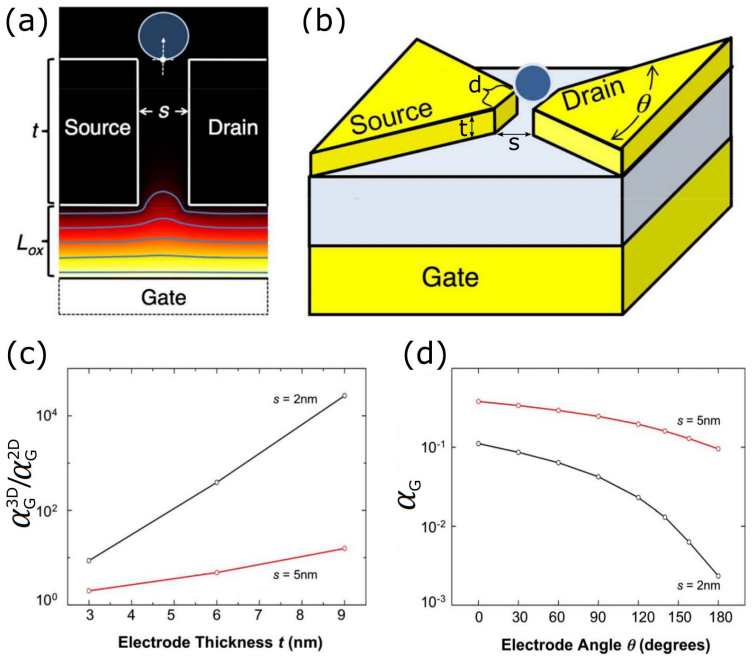

Fig. 2.8: (a) Equipotential (blue lines) and electrostatic potential (color map) of the gate electrode in a three-terminal QD device, obtained by finite element simulations. (b) Schematic of a three-terminal QD device indicating the electrode geometrical parameters that influence the gate coupling, α_G. (c) The gate coupling ratio of a 3D ($\theta = 120°$) and 2D ($\theta = 180°$) electrode geometry increases with the electrode thickness, t and decreases with the spacing s. (d) A tapered shape of the electrodes increases the gate coupling. All these images have been extracted from [210].

2.3.3 Constrictions metalization

Bow-tie shaped constrictions are designed with an electrode apex angle of $\theta_{EM} = 30°$ and total length of $l_{EM} = 200$ nm (Fig. 2.9a). The EBL was performed on a bi-layer resist with a bottom layer of PMMA/MMA 6% AR-P 617 (thickness of $t_{res}^{bot} \approx 290$ nm) and top layer of PMMA 3% (thickness of $t_{res}^{top} \approx 140$ nm). The presence of an MMA copolymer in the bottom resist layer makes it more sensitive to the electron beam exposure. In this way, patterns can be insulated in the lower resist (that will get etched away with the chemical developer) keeping the upper resist in place and creating, for instance, resist bridges of nanometric size. By slightly increasing the beam dose at the exposure of the constrictions, the lower resist can be effectively insulated in the surrounding area by proximity (Fig. 2.9a). When introducing the sample in the developer chemical, the agent will eat away the proximity-insulated lower resist around the apex of the constriction, leaving the upper resist intact and creating a top-resist bridge at the center of the bow-tie design (Fig. 2.9b). Dose and development tests were carried out to create an undercut significantly greater than $l_{EM}/2$, but keeping a stable resist bridge. By rotating the sample with respect to the longitudinal direction of the resist bridge, metal can be deposited in the area below the resist bridge (Fig. 2.9c). The constriction length and the resists heights fix the minimum angle for the tilted metal evaporation to $\varphi_{ev} > \tan^{-1}(l_{EM}/2t_{res}^{bot}) = 19°$. Several batches of chips were fabricated with different shadow-angled evaporation parameters: at angles of $\varphi_{ev} \pm 23°, 24°$ and $25°$ and thicknesses of $t_{ev} = 13, 14$ and 15 nm, for electromigration tests (discussed in the following section). For these combinations, we expect an effective thickness of the aluminum layers forming the constriction in a range of $t_{EM} = t_{ev}\cos(\varphi_{ev}) = 11.8 - 13.6$ nm (Fig. 2.9d). The resist bridge over the constriction covers it from a last perpendicular evaporation, performed to increase the thickness of the accessing lines, reducing its resistance and ensuring a good contact with the previously DUV-patterned access lines. Finally, the sample was put into lift-off solvent to remove the remaining resist. The resulting constriction structures are shown in Fig. 2.10. The adjusted parameters for the whole lithography process are recapitulated in Annex D (Tab. D.4).

Our chip design contains a couple of linear constriction arrays per chip (corresponding to lines 1-16 and 17-32 in Fig. 2.10a). Each bonding pad is connected to two constrictions at the same time (forming a T shape). During the electromigration process, if a QD junction is detected at one of the constrictions, the constrictions on the sides must be electromigrated in order to equate the

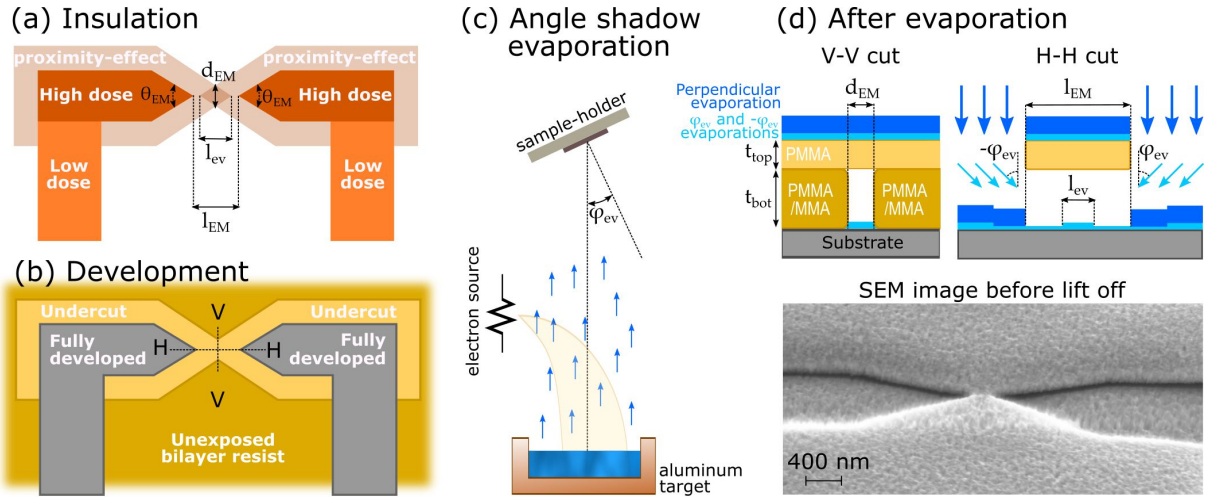

Fig. 2.9: (a) Bow-tie shape constriction design fixing the geometrical parameters of the constriction (θ_{EM}, d_{EM} and l_{EM}). The constriction-sides are exposed using a higher dose inducing the insulation of the lower resist by proximity effect. (b) An undercutted resist bridge is created on top of the constriction site (central part of the bow-tie design). (c) Tilting the metal evaporator sample-holder a certain angle, φ_{ev}, allows to deposit metal below the resist bridge. (d) Cross-section cuts showing two thin, angled metal evaporations (at φ_{ev} and $-\varphi_{ev}$, light blue) form a constriction below the resist bridge. A third perpendicular evaporation provide thick access lines. An SEM picture of a constriction before lift-off shows the existent undercut, creating a gap between the metal on the resist layer and on the substrate.

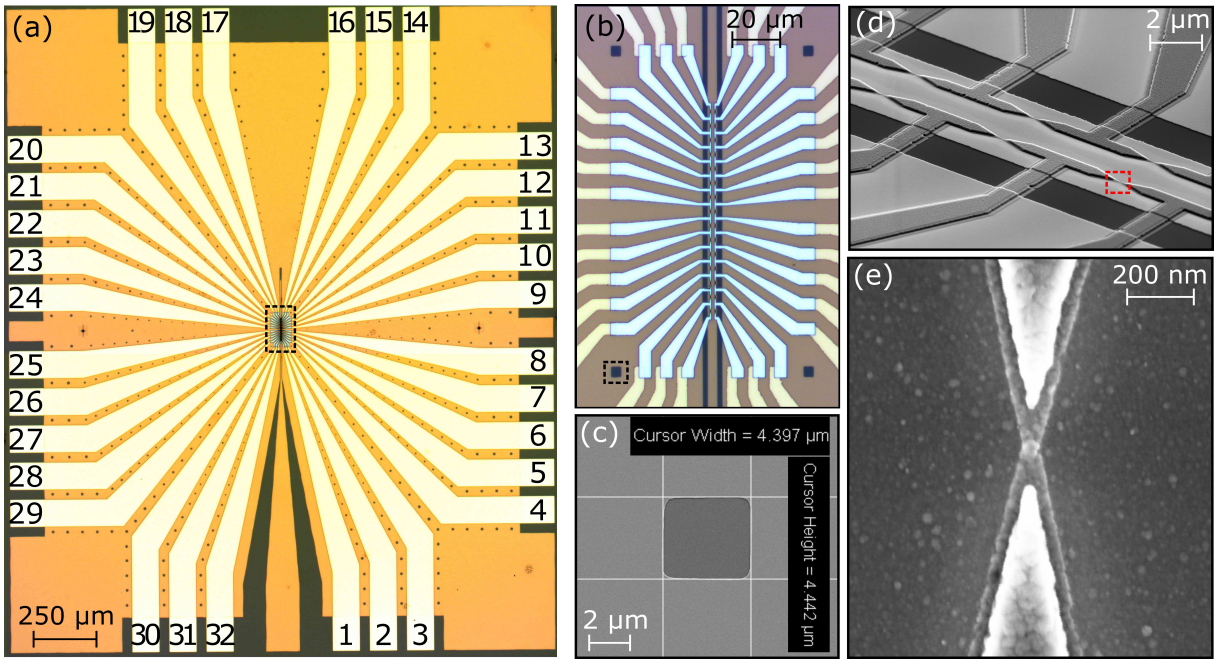

Fig. 2.10: Optical microscope image of a single chip after the third lithography step. (a) Aluminum constrictions have been fabricated on the central part of the sample (dashed square) (b) The constrictions are placed on top of the gate electrode and connected to the bonding lines. Four square holes patterned in the ground plane on the four sides of the EBL write-field serve as on-chip alignment marks. (c) SEM picture zooming-in at the dashed line encompassing a square hole in (b), with a side length of ≈ 4.5 μm. (d) SEM picture zooming-in at the aluminum constrictions. (e) SEM Zoom-in at a single constriction (indicated in (d) with a red dashed square), that allow us to measure the constriction's set of geometrical parameters: $l_{EM} \approx 200$ nm, $l_{ev} \approx 40 - 60$ nm, $\theta_{EM} \approx 30°$. Grey dots found around the structure are thought to be resist residues.

capacitances to the gate and ground of the source and drain accessing lines, as parasitic effects may appear otherwise (see Supp. Mat. of [48]). This compact arrangement maximizes the number of constrictions per chip, increasing the chances of obtaining a QD junction per cooldown. Alignment marks, consisting on 4.5 nm square holes, were patterned on the ground plane during the gate lithography step, on the area around the constrictions (Fig. 2.10c). These markers allowed for an on-chip calibration of the electron beam close to the corresponding writefield, immediately before the constrictions exposure, avoiding misalignments due to beam drifts in long time exposures.

2.3.4 Sample storage

After the constrictions' lithography step is finished, we spincoat a thick layer of resist that protects the thin aluminum constrictions from oxidation (bare Al constrictions completely oxidize after 24 hours otherwise). The sample is then diced and the individual chips are simply stored in plastic boxes until the cryogenic measurement setup is available. Actually, in the course of our work, we have found that the series resistance of the access lines, measured from one bonding pad to the next one across the constriction, increases at a rate of $\approx 50 - 100$ Ω/month. The gradual formation of purple plague (an Al-Au intermediary compound with poor electrical conductivity) at the overlapping contact of around 25 μm^2 between the Al and Au access lines is believed to be the cause of this sample aging (Fig. 2.11a and b). This effect, stemming from Au atomic diffusion into Al, reduces the chances of performing a successful electromigration due to the appearance of an on-series resistance in the access lines on the order of the constrictions resistance. To avoid the purple plague formation, we stopped the process after the Au access lines fabrication, diced the 2" inch wafer into pieces containing several single chips, and proceed with the last lithography step (EBL of the constrictions and Al evaporation) in one piece every month, restricting our cool downs for chips containing fresh and pristine Al breaking junctions. Alternatively, we also tried storing fully-fabricated samples in liquid N_2 (using vacuum bags) to reduce

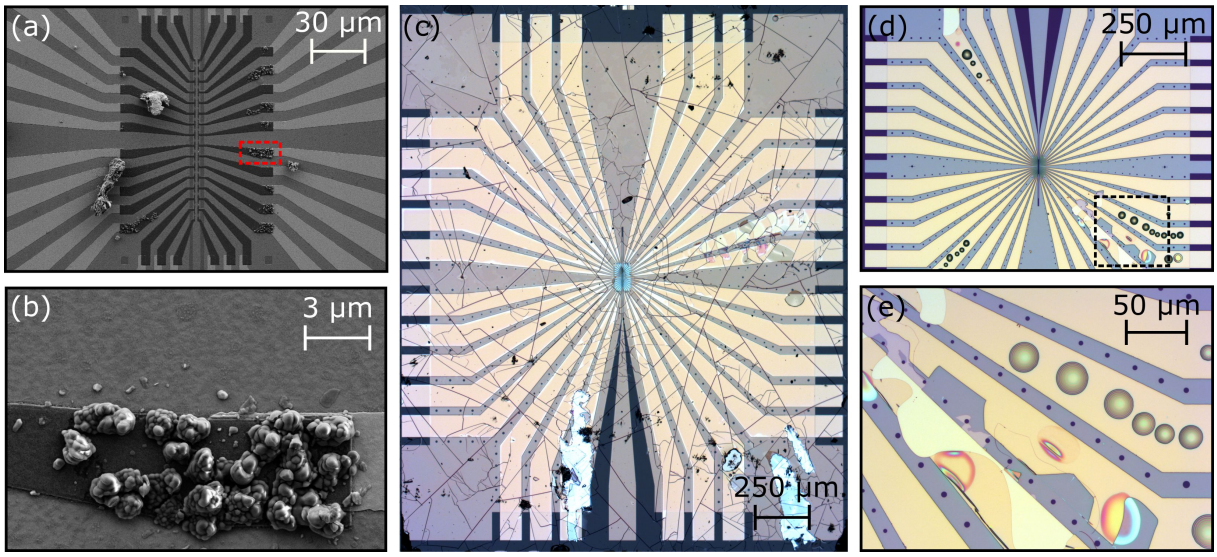

Fig. 2.11: (a) Optical microscope picture of a sample after the bonding lines DUV lithography process. (b) Zooming-in at the black dashed line square in (a), we can observe damages caused in the oxide layer when removing the mask after the insulation, as well as, bubbles formation in the oxide layer below certain bonding lines after the metal evaporation, both of them causing direct connection of the corresponding bonding pads to the ground plane. (c) Optical microscope picture of a chip stored in liquid N_2 for a few months. The protective resist layer on top is cracked and the aluminum constrictions completely oxidized. (d) SEM picture of aluminum constrictions that were deposited a few months ago. Several connections of Al-Au bonding lines present evident formation of purple-plague compound (e) Zoom-in at an Al-Au bonding lines connection indicated by a red dashed line square in (d). The purple-plague covers the totality of the contact surface, increasing the resistance of the access line.

the temperature-enhanced gold diffusion and delay the purple plage formation. However, we found that the protective resist cracks at N_2 temperatures (Fig. 2.11c) and the constrictions in samples stored this way were not conducting at all, indicating a complete oxidation of the aluminum.

Other difficulties appeared over the optimization of the whole fabrication process, mainly related with the fragility of the ALD oxide layer. Although the hard-contact mode of the DUV mask aligner (at the access lines lithography step) helps to reach a better alignment and an adequate insulation of the bi-layer resist, it can cause damages in the oxide layer, making it to peel off the sample's surface when removing the mask after the exposure. Also at this fabrication step, we observed that a non-negligible amount of chips presented bubbles below the access-lines area right after the metal evaporation. We attribute the bubble formation to heating sample surface during the metal deposition, inducing the physical desorption of gases trapped in interstitial positions at the oxide layer (possibly residual gasses of the ALD growth process, as H_2). Such damages in the oxide layer generally result in short-circuits of the corresponding access line to the ground plane (Figs. 2.11d and e), invalidating its employment for electromigration. Replacing the DUV by laser lithography significantly increases the fabrication time but it will remove these problems from the process. A careful calibration of the DUV aligner hard-contact mode is highly advisable otherwise.

2.4 Electromigration constrictions characterization

Electromigration was discovered by *Gerardin* in 1861 when studying the electrical properties of metallic alloys. This phenomenon remained untouched for 100 years until the first systematic measures, carried out by *Seith and Wever* in the early 50s, revealed that the nature of electromigration depends on the dominant charge carriers (electron or holes), and could be reversed [212]. In the following decades, different groups identified the relation between the driving force and the charge carriers momentum, coining the name of electron wind [213, 214]. The study of electromigration advanced steadily until it was identified as the cause of disconnection of aluminum lines in integrated circuits, threatening the

growth of the young semiconductor industry [215]. The general interest in electromigration boosted up, being characterized in detail at industrial laboratories while a theory describing the phenomenon was developed (summarized in Ref. [182]). The chance of taking advantage of electromigration for the fabrication of nano-spaced electrodes was first explored in the late 90's by the group of *Park et al* [180]. The stunning success of their experiment conducted an abrupt introduction of electromigration in molecular electronics, establishing as one of the main fabrication methods due to its gate-electrode compatibility. Constrictions made of pure Au [74, 107, 108, 140, 76, 105] or Au-based alloys [75, 78] have been widely employed for the fabrication of three-terminal molecular devices ever since, as the high atomic mobility and diffusion of this metal facilitates the process, and different techniques allowing to break the constriction progressively and in a controlled fashion have been developed (recapitulated in Ref. [37]). The employment of different materials for the fabrication of nano-spaced electrodes by electromigration (like Ag [216], Pb [217], Pd[218], Pt[219], or even graphene [220, 221]) has been demonstrated in the last decade. However, the employment of superconducting (SC) materials in electromigration junctions remains challenging nowadays, the high O_2-reactivity of most superconductors (that leads to an immediate oxidation of the junction contacts if the constriction is exposed to the atmosphere during or after the breaking procedure) being the main obstacle. Some groups have managed to create proximized-SC molecular transistors by including a thick layer of SC material (either Al [39] or MoRe [222, 36]) in direct contact, nearby the Au constriction. However, the highly accurate charge-pumping experiments in a SC-SET requires a sharp gap in the leads' DOS, not achieved in proximized metals. Nevertheless, previous students in our group have demonstrated the feasibility of obtaining QD junctions by electromigrating constrictions entirely made of aluminum [37, 38, 48], constituting the main antecedent of my thesis work. To avoid the oxidation of the nano-gap (taking place in a matter of seconds even at medium or feeble high-vacuum levels [223]), the electromigration process was carried out in-situ inside the cryogenic measurement setup, at a temperature of 4 K and under ultra-high vacuum conditions ($\sim 10^{-8}$ mbars).

Although electromigration can be described with an analytical model, the particular nanostructuration of the metal at the constriction (defects, grains, oxidized grain boundaries,...) makes impossible to predict the evolution and size of the nanogap. The electrical resistance of the constriction, R_{EM} (fixed by the combination of both metallic disorder and geometrical sizes), can provides a general idea of its quality and feasibility for a successful breakage. In fact, after electromigration, nanogaps display a non-uniform width around or below 1 nm at some spots that allows direct tunneling between both electrodes (even in the absence of a QD, or bypassing it otherwise), resulting in a certain shunt resistance, R_{sh}, consistently present in all our in-situ broken constrictions. Typical values of R_{sh} were also used to evaluate and determine the quality of the nanogap. In an effort to optimize the obtainment of QD devices, a few parameters regarding the fabrication of constrictions (namely the angle and thickness of the shadow evaporation) were varied for performing tests along the electromigration of real samples, both at temperatures of 300 K and 4 K. Following a phenomenological approach, the data obtained from the systematic physical and electrical characterization of the constrictions has been treated statistically to help us fabricate and conduct electromigration in the desired way, i.e., aiming for values of R_{sh} ranging from 1 MΩ to few GΩs, as determined favorable for trapping nanoparticles by previous experience in our group.

2.4.1 Physical characterization

The geometrical parameters of our electromigration constrictions, fixed during the fabrication process (l_{EM}, l_{ev}, d_{EM}, θ_{EM} and t_{EM}), partially determine the resistance of the constriction R_{EM} together with the particular Al-disorder present at each actual constriction. Systematic SEM observations revealed that the EBL-patterned constrictions display sizes variations in the following ranges: $l_{EM} = 195-225$ nm and $\theta_{EM} = 29-31$, attributed to slight unintended irregularities in the dose factor, the resist thickness and age or development time. However, no significant correlation of R_{EM} or R_{sh} could be strictly linked to these variations. Regarding our fabrication tests, constrictions made with different evaporation angles of $\varphi_{ev} = 23°, 24°$ and $25°$ presented different sizes of the angled evaporation

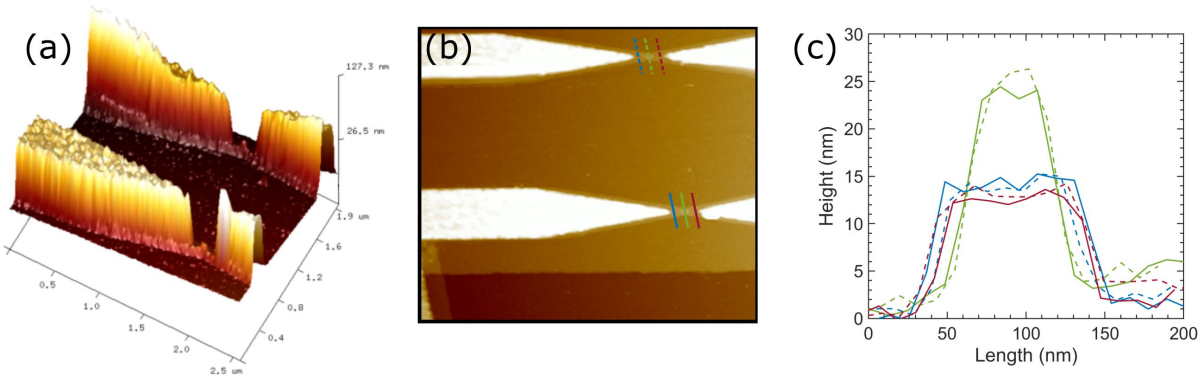

Fig. 2.12: AFM scan of two nearby electromigration constrictions where 14.5 nm of Al were evaporated at $\varphi = 25°$. (a) 3D plot. (b) 2D plot. (c) Line cuts performed along the constriction (as indicated in b) show that the thinnest points of the constriction are ≈ 13 nm thick while the region where they overlap is ≈ 25 nm thick. A surface roughness of ~ 2 nm indicates the granularity of aluminum.

overlapping, ranging between $l_{ev} = 45 - 65$ nm and $d_{EM} = 60 - 80$ nm. Again, we did not observe a significant dependence of both R_{EM} and R_{sh} for identical electromigration routines, finally sticking to $\varphi_{ev} = 25°$ as the standard angle of our recipe. Once the angle was fixed, samples with different total evaporation thicknesses of $t_{ev} = 13, 14$ and 15 nm, leading to effective constriction thicknesses of $t_{EM} = 11.8, 12.7$ and 13.6 nm were tested. The AFM measurements in Fig. 2.12 show that, although the average thickness corresponds to our estimations, the high granularity of the Al deposited induces roughness fluctuations of ± 2 nm, at least. While room temperature and in-situ electromigration worked out properly for all three thicknesses, we observed an slight increase on the total number of junctions displaying $R_{sh} < 1$ MΩ for $t_{ev} = 13$ nm. The evaporation thickness was finally settled to $t_{ev} = 14.5$ nm, leading to an effective constriction thickness of $t_{EM} = t_{ev} cos(25°) = 13.1$ nm. In all these tests, the evaporation rate was always kept constant at 0.05 Å/s with an evaporator vacuum around $3 \times 10^{-}6$ mbar, expecting similar Al nanostructuration in all samples.

2.4.2 Electrical characterization

The large resistance per unit length present at the constrictions (R_{EM}/l_{EM}) in comparison with the rest of the circuit (access lines, sample-holder pads and micro-bonding wires, cryogenic setup wires and connectors,...) makes electromigration to take place precisely at this spot, on top of the gate electrode. In short, to perform electromigration we apply a voltage tension between the lines connected to the sides of a constriction, flowing a current through it. The high value of R_{EM}/l_{EM} originates local Joule heating of the metal and increases its temperature, favoring the movement of the metallic atoms that integrate the constriction. By increasing the voltage/current, the constriction temperature also increases, eventually enabling the displacement of the ions pushed away by electron scattering, leading to a constriction narrowing until the link is completely broken. Although heating up the metal is necessary, an uncontrolled temperature increase will lead to melting or even exploding the constriction. The art of electromigration for creating nano-spaced electrodes resides in the regulation of the process, reaching a regime where the temperature is enough to allow ions displacement but insufficient to melt it down. When this regime is reached, electromigration takes place rapidly, requiring a sufficiently real-time measurement system (controlled with a fast feedback loop) that stops the voltage ramp and drops it to zero as soon as a targeted resistance is reached. The maximum voltage applied in such process, V_{Break} (called the breaking voltage) is also used as an indicative parameter, slightly correlated with resulting R_{sh} values. Rough estimations on the sample quality of a given badge can be done by characterizing its typical values of R_{EM} and V_{Break} in a room temperature probe station prior to their cool down, saving the precious cryostat time and cryogenic resources.

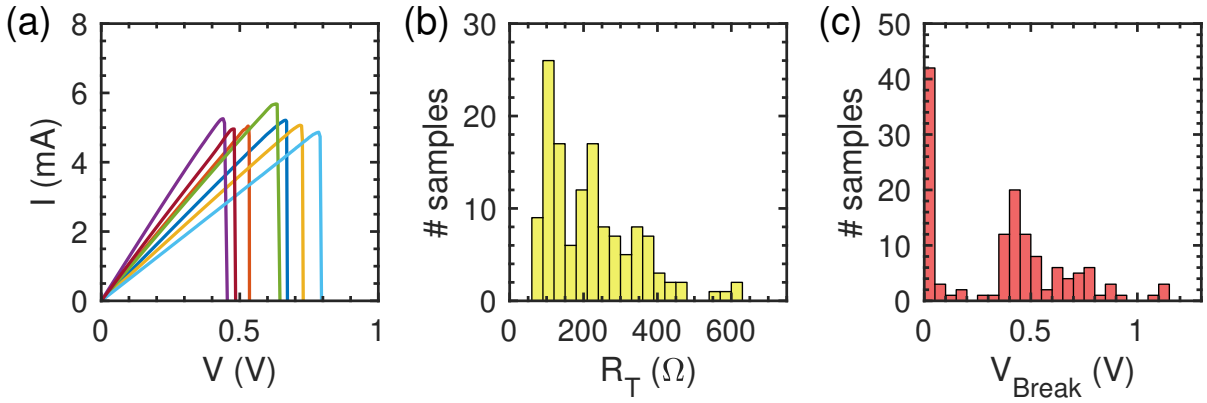

Fig. 2.13: (a) Few illustrative curves showing electromigration at ambient conditions done by ramping the biasing voltage. Histograms on 135 constrictions electromigrated this way show characteristic values for (b) the total resistance of the constriction (measured between consecutive access lines) of 80–500 Ω and (c) breaking voltages of $V_{Break} = 0.3 - 1.1$ V. A relatively large number of constrictions broke right after the voltage ramp started.

ELECTROMIGRATION AT ROOM TEMPERATURE

Systematic characterization of sets of individual chips was done after each EBL lithography with a probe station at room temperature, T_R, to test the quality of the constrictions. Measurements performed in a single chip between consecutive bonding pads across a single constriction, usually showed a total resistance in the range of $R_T = 80$ and 300 Ω (Fig. 2.13b). Measurements between nonconsecutive lines across a few constrictions of the array, showed resistances increasing by a typical amount of $R_{EM} = 40$ Ω per constriction. As the average constriction length was measured to be around 200 nm, characteristic values of $R_{EM}/l_{EM} \approx 2.5 \times 10^8$ Ω/m are found for our junctions. The typical resistance of the access lines is obtained as $R_{AL} = (R_T - R_{EM})/2 = 20 - 130$ Ω (attributed to slight misalignments between the DUV and EBL lithographies that reduce the effective Al-Au contact area). As access lines own an average length of 1 mm, typical resistances per unit length around $2 - 13 \times 10^4$ Ω/m are found for the access lines, much smaller than at the constrictions. A voltage-bias feedback routine was implemented with the help of the PhD student David Wander, allowing us to electromigrate the constrictions at T_R (Fig. 2.13a) and extract representative breaking voltage values (Fig. 2.13c). Constriction batches showing an R_T in the range of 80 and 300 Ω, usually break at voltages of $V_{Break} = 0.4 - 0.7$ V at T_R (for voltage ramping speeds of 5 mV/s) and often provide R_{sh} in the desired range when electromigrated in-situ. In addition, we consistently found that constrictions a few weeks old presented values of R_T up to 400 Ω or above, and often broke as soon as the voltage ramp starts, impeding electromigration and attributed to the detrimental effects specified in section 2.3.4.

ELECTROMIGRATION AT CRYOGENIC TEMPERATURES

In-situ electromigration was performed in the cryostat with a 2-terminal configuration under high vacuum conditions and cryogenic temperatures of 4 K. We employed a voltage-biasing feedback algorithm developed by *E. Bonet, C. Thirion and R. Picuerel*, executed by an Adwin Gold II DAC-ADC converter that counts with a 500 kHz processor (see section 3.2.1). Employing this instrument, the voltage was ramped up at speeds settled between 1–50 mV/s, while recording the current (converted to an amplified voltage using a Femto low-noise amplifier in full bandwidth mode). We fix the reset condition for conductances smaller than $2e^2/h$, stopping the voltage ramp and rapidly returning it to zero (within 10 μs). Right before reaching the reset condition, we generally observed a sudden drop of the current happening at breaking voltages between 0.5 and 2 V (Fig. 2.14a and b). The change in the typical V_{Break} values at room and cryogenic temperatures are due to the relative temperature difference between the constriction and the environment. Most EMBJs showed resistances well below $h/2e^2$ after a single launching of the breaking procedure, indicating the total constriction breakage and

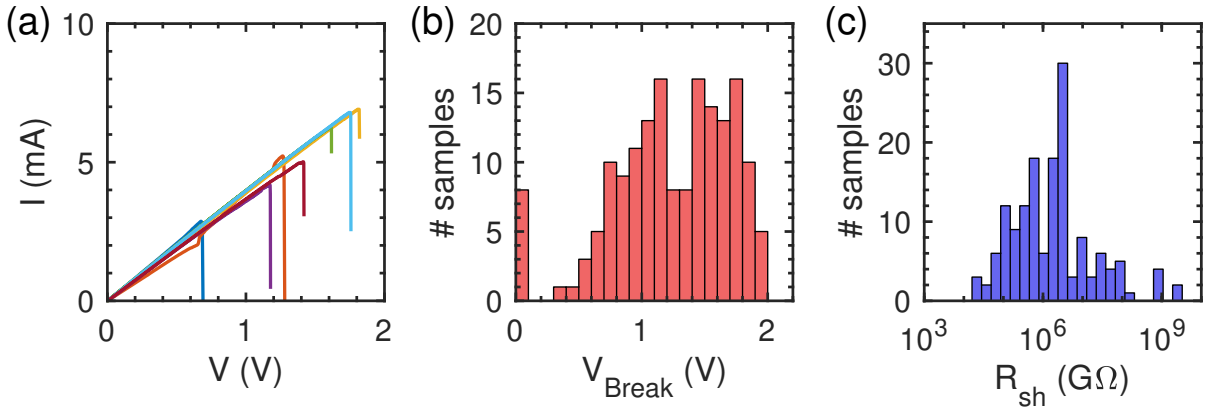

Fig. 2.14: (a) Few illustrative curves showing typical in-situ electromigration at a temperature of 4 K. Histograms on 170 constrictions electromigrated this way show characteristic values for (b) the breaking voltage of $V_{Break} = 0.5 - 2$ V, and (c) tunnel resistances R_{sh} distributed from few tens of KΩs up to a few GΩs. Most tunnel resistances are congregated in the range of $0.1 - 100$ MΩ.

entrance into the tunneling regime. Approximately half of the tunnel junctions reach the target values of $R_{sh} \sim 1 - 10.000$ MΩ (Fig. 2.14c). Although little correlation could be found between V_{Break} and the resulting R_{sh}, we observed that chips containing constrictions breaking around $V_{Break} = 0.4 - 0.7$ V at T_R and $V_{Break} = 1.5 - 2$ V at 4 K, often lead to R_{sh} in the targeted range.

ALD OXIDE LAYER CHARACTERIZATION

To characterize the ZrO_2 layer deposited by ALD on top of the gate electrode and ground plane, we start by electromigrating all the constrictions in an individual chip in order to isolate the access lines from each other. Then, we measure the oxide characteristic curve by applying a voltage tension, V_G, to the gate and measuring the current, I, at a bonding pad. The measurements in Fig. 2.15a, acquired using a probe station at ambient conditions, show that the oxide in most samples can hold voltages higher than 15 V, although some access lines undergo an electrical breakdown or showed

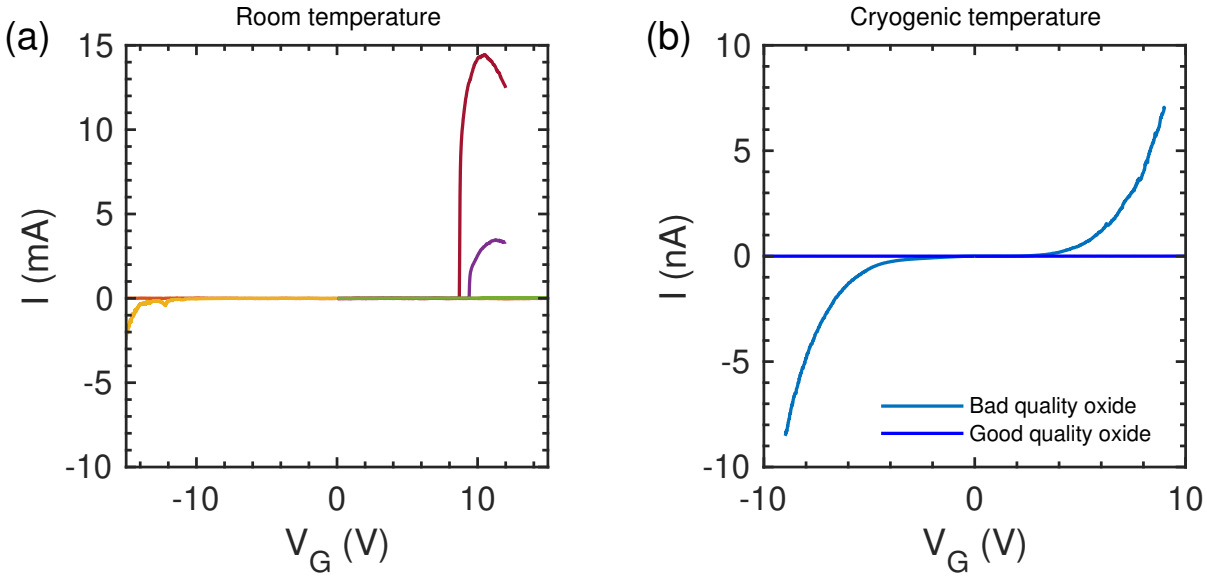

Fig. 2.15: Few representative I-V characteristic curves obtained by applying a voltage V_G to the gate while measuring the current at the access lines of isolated constrictions. (a) Measurements done at room temperature reveal that the oxide layer in some samples present breakdown voltages in the range of $|V_G| = 8 - 15$ V, while others are stable above 15 V. (b) Measurements taken at a temperature of 4 K show the stability of the oxide in the range of $V_G = \pm 10$ V (dark blue line), while some chips displayed a few-nA leaking current as soon as some V_G was applied (light blue line).

a significant leaking current at voltages between 8–15 V, imposing the upper boundary that can be safely applied on V_G without damaging the oxide. Same measurements carried out in the cryostat, at temperatures of 4 K, (2.15b) demonstrate that the oxide layer in most chips was robust for $|V_G| \leq 10$ V at low temperatures, leading to an oxide resistance of $R_{ox} > 1$ TΩ (dark blue line). Nevertheless, a small number of samples showed current leaks of few nA, which indicate the bad quality of the oxide layer present in them (light blue line). Although these two behaviors were commonly found in samples fabricated together, they can be attributed to local damages of the oxide during the rest of the fabrication process, as explained in section 2.3.4.

2.5 Quantum dots deposition methods

The first devices based on few-nm QDs were conceived in the late 60's, prepared by connecting two metallic electrodes by a tunnel barrier containing multiple metallic nanoparticles, grown by the evaporation of a thin metallic film on the oxide barrier, that agglomerates under the influence of the surface tension small particles. Global transport properties of the nanoparticles could be studied in such samples, like their transition into the S state [224], and the first experimental signatures of charge quantization due to Coulomb blockade [225, 226]. Around 30 years later, the development of the first electronic lithography technologies made possible, although not straightforward, the fabrication of electrodes with a nanometric separation (~ 10 nm). Diverse methods for fabricating and contacting individual few-nm nanoparticles arose in the following years, for example, the group of *Ralph et al.* implemented the sub-mono layer evaporation approach in a novel sample geometry, allowing them to contact particles individually in a two-terminal configuration [1], adding a third gating electrode shortly after [3]. Separately, the group of *Klein et al.* imported the self-assembled mono-layer (SAM) technique, initially employed in STM experiments to measure the conductance of single molecules of a self-assembled layer [167, 227, 228]. The SAM method consists on functionalizing the surface of Au electrodes with linker molecules containing a double -thiol (SH) ending group, chemically bounding to the leads on one side (forming a mono-layer that covers their whole surface) and, by introducing the sample into a colloidal solution of metallic nanoparticles, to the particles on the other side, eventually bridging the nano-spaced electrodes [229, 4] (Fig. 2.16a). Rather uniform distributions with a well-controlled density, and the firm attachment of the particles to the surface turned the SAM method into the main deposition technique for the conception of few-nm QD junctions in the 90's allowing to address individual and stable nanoparticles with a STM tip [230, 231], to approach the single-molecule limit in gated devices [232] or to obtain QD junctions by electromigration [180].

As the nanomaterials industry grows, diverse and cheaper products (colloidal solutions of different kinds of nanoparticles, on-demand customized molecules,...) have become available in the market, fueling research projects that combined the SAM method with breaking junctions. On one hand, some groups focused on the optimization of the nanoparticle-trapping process, taking advantage of the non-neutral electrical charge of metallic particles in specific colloids combined with functionalizing molecules owning charged ligands (replacing the -thiol by -amine groups) [76] or using dielectrophoretic

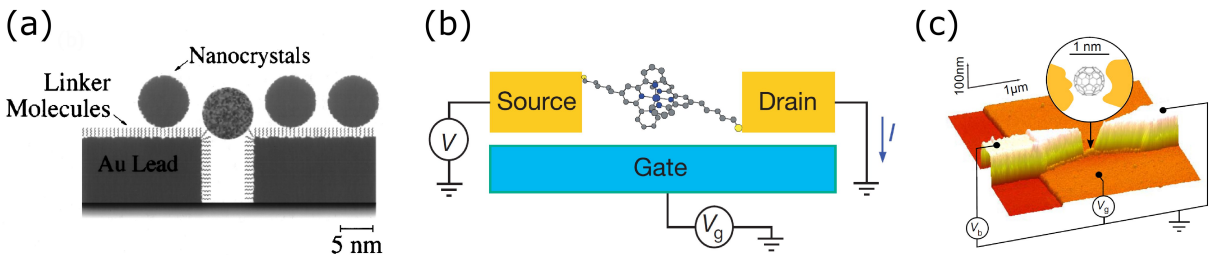

Fig. 2.16: (a) In the SAM technique, bifunctional linker molecules functionalizing nano-spaced electrodes bound chemically to the nanoparticles forming a stable QD junction (extracted from [229]). (b) A single linker molecule forms a bridge between nano-spaced electrodes (extracted from [108]). (c) A colloidal suspension of fullerenes drop-casted onto an electromigration constriction results in a QD junction after electromigration (extracted from [105]).

forces [233]. On the other hand, the SAM method was further developed, replacing the usual nanoparticle in the junction by just one single molecule of the mono-layer, which assumes the role of the QD [234] (Fig. 2.16b). Remarkable work was done following this approach: thanks to the variability of the chemical species in the molecules, novel energy scale hierarchies could be reached, achieving regimes of large tunnel couplings, charging energies and level spacing, making possible to observe and characterize vibrational [75] and electronic excitations [78] and the manifestation of the Kondo effect in gated QD junctions [108, 107, 235]. More versatile prospects were explored after that, for example, by manually drop-casting the colloidal suspension directly on the bare sample surface, skipping the functionalizing mono-layer. Despite its simplicity, this approach also turned out to be suitable for conceiving QD junctions, although it involved a significantly lower success rate than the classical SAM technique. The drop-casting method opened up a sea of possibilities, since it did not present any constraints regarding the electrodes material and any kind of molecules/nanoparticles could be employed. At first, numerous devices characterizing the transport properties single C_{60} fullerenes emerged, both in MCBJs and EMBJs (Fig. 2.16c), allowing to map the vibrational structure of this textbook molecule [74], study the Kondo phenomenology that it presents [236, 106, 105, 111], and the modification of its conduction features when coupled to ferromagnetic [237] or superconducting electrodes [39]. Up to the present, a vast amount of studies have been carried out employing diverse types of molecules, some of them owning more exotic phenomena like engineered orbital structures [238] or intrinsic magnetism [239].

Unfortunately, it was observed by previous students that the entire Al structures of our EMBJs get rapidly corroded in the presence of the acid media of SAM nanoparticle solutions [37], dismissing this possibility. The preferred choice were commercial nanoparticle solutions (in organic solvents), directly drop-casted on the samples prior to the insertion of samples in the cryostat for in-situ electromigration, that resulted in a yield of success $\sim 3\%$. In the course of my work, we tried to optimize the solution drop-casting procedure (2.5.1), as well as other compatible QD deposition approaches (2.5.2 and 2.5.3), intended to improve the success rate. In all cases, the QD deposition was done on chips containing recently fabricated Al EMBJs (one month at most), since the progressive degradation of Al-Au contacting interfaces at the access lines hinds electromigration. Additionally, we note that to avoid the oxidation of the Al constrictions, the whole chip preparation process (removal the protective resist, QD deposition, gluing and micro-bonding the chip to the sample-holder and its insertion into the cryostat) must be done within the same day.

2.5.1 Colloidal suspension drop-casting

The simplest and quickest method for performing a QD deposition is by drop-casting some droplets of a colloidal solution directly on the surface of the sample and blow dry it. This approach was chosen by previous students, due to its straightforwardness and the incompatibility of Al with the SAM technique. To create the colloidal solution, 1 mg of commercial powder of 5 nm Au nanoparticles functionalized with dodecanethiol ligands [240] was dispersed in 500 μL of pure toluene, obtaining a highly concentrated stock solution, of about $\mathcal{C}_{stock} = 2$ g/L. Small amounts of testing solution (further diluted) were prepared from the stock one and were employed in to carry out QD depositions. The drop-casting procedure pursued initially consist of the following steps:

1. Sonicate the colloidal solution at maximum power for, at least, 30 minutes (using an ELMA TI-H-10 sonication machine).
2. While holding the chip in the air with a tweezer, cast a $\sim$10 μL droplet of the colloidal solution onto the its surface (using a micro-pipette).
3. Lay the chip down, on top of a clean-room tissue and remove the liquid away from chip immediately, by blow-drying its surface with a pressurized N_2 gun at high intensity. The blow-drying process must be done rapidly, as soon as the sample touches the tissue to avoid the nanoparticle agglomeration (generally happening if the solution is let to self-evacuate by capillary forces).
4. Repeat the process from point 2 until the targeted number of droplets (typically 10) is reached.

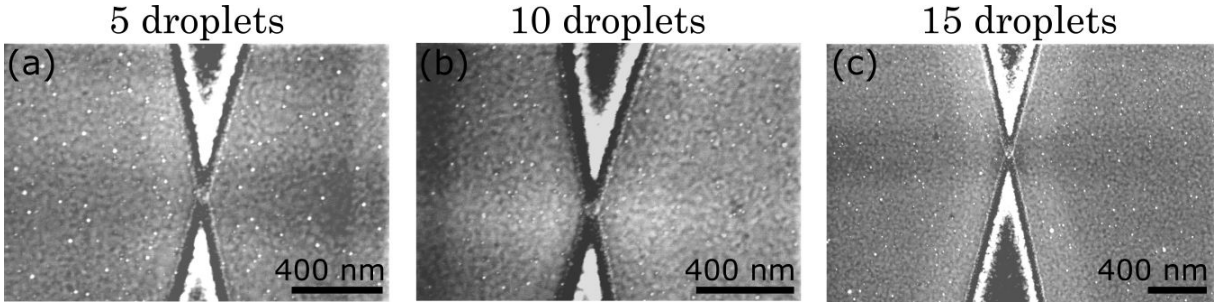

Fig. 2.17: SEM images of electromigration constrictions after drop-casting a colloidal solution of nanoparticles (with a concentration of 0.125 μg/μL) following the procedure described above for: (a) 5 droplets, (b) 10 droplets and (c) 15 droplets. The images reveal an almost identical surface density of nanoparticles on the flat areas and the absence of them on top of the Al constrictions.

In sight of the limited success rate found for this method in the past, we conveyed several tests intended to optimize the drop-casting procedure in terms of total number of droplets casted, conduction of the blow-drying proceeding and solution concentration. Additionally, it has been demonstrated that different tunnel coupling between the QD and the leads in molecular junctions can be reached by employing molecules with distinct terminal groups [108, 241]. In the spirit of favor stronger couplings in our devices, a similar commercial solution of Au nanoparticles functionalized shorter -thiol ligands (octanethiol), was tried over. While this product was already dispersed in organic solvents (toluene, in principle) by the manufacturer, low-concentration solutions were prepared and tested in the same way, following the drop-casting procedure. However, we observed a systematic increase on the constriction resistances up to few tens of kΩ minutes after the QD deposition, possibly indicating that the solvents attacked the Al and disabling it as a viable option.

DROPLETS TEST

Starting from the highly concentrated stock solution ($\mathcal{C}_{stock} = 2$ μg/μL), a testing solution was prepared by further diluting 50 μL from the stock into 750 μL of pure toluene ($\mathcal{C}_1 = 0.125$ μg/μL). Five, ten and fifteen droplets from the test solution were casted on three different chips following the initial drop-casting procedure. In posterior SEM pictures of the three chips we could observe that a radically small number of nanoparticles (tiny bright dots in Fig. 2.17) was found on top of the Al conforming the constriction in all three cases, also revealing that the resulting surface density of particles depends little on the number of droplets casted with this procedure. Equivalent tests were repeated for different testing solution concentrations of 0.25 and 0.5 μg/μL, but no significant difference was observed.

BLOW-DRYING TEST

The little dependence of the nanoparticles surface density on the number of droplets leaded us to believe that most of the particles were removed in the blow-drying step. Subsequent tests were performed with the same testing solution ($\mathcal{C}_1 = 0.125$ μg/μL). This time, instead of the quick and vigorous blow-drying action done as soon as the sample touches the clean-room tissue after casting each droplet, let the solution slip away from the sample surface into the tissue by capillarity (taking around 5 seconds, while some leftovers remain on the sample's surface). Although this modification greatly increased the particles surface density and its presence on top of the Al constrictions, most of them appear agglomerated (Fig. 2.18a, b and c). In fact, junctions overcrowded with particles are thought to be more likely to display charge-offset switches, appearing spontaneously in the gate voltage, observed in some of our QD junctions (shown in section 4.1.2). Random charging/discharging of other nanoparticles nearby the electromigration gap may modify the electrostatic environment around the actual particle bridging the junction, inducing instabilities on the gate control of the QD chemical potential and making impossible to perform steady transport measurements.

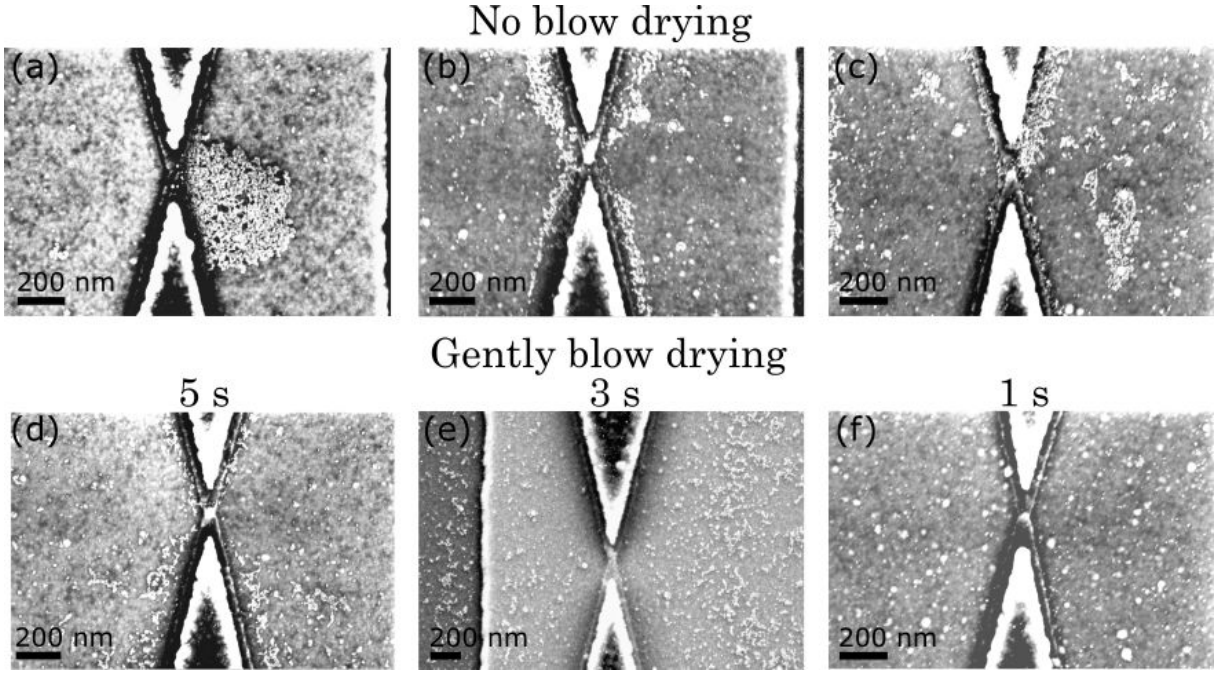

Fig. 2.18: SEM images of electromigration constrictions after drop-casting 5 droplets from a colloidal solution of nanoparticles (with a concentration of 0.125 μg/μL) following the procedure described above but completely avoiding the blow drying step (a, b and c) or by gently blow-drying 5, 3 and 1 seconds after the sample touches the clean room paper surface (d, e and f, respectively). While in the no-blow-drying case the nanoparticles are completely agglomerated around the constriction structures, in the gently blow-drying case the deposition presents low agglomeration that decreases with decreasing waiting time, and some particles are present on top of the Al structures. The smaller bright dots in the pictures are identified as nanoparticles, while bigger circular structures are attributed to resist residues.

We identified the blow-drying step as the critical parameter that determines the quality of the QD deposition in terms of clustering and surface density. There is a trade-off between an aggressive blow-drying, that reduces the surface density (and accordingly the possibilities of getting a particle trapped at the nano-gap), but leads to higher changes of getting stable QD junctions, as most of the particles are isolated. In contrast, the removal of the blow-drying step may result in higher success rates, but a lower quality of the sample in terms of gate stability. In further tests, we observed that gently blow-dried samples (starting the flow a few seconds after the chip is let resting on the clean-room paper but before all the solution slips away by capillarity) present a surface density that remains high, while the agglomeration decreases significantly, depending on the waiting time (Fig. 2.18d, e and f). Finally, we settled the waiting time at 2 seconds to optimize the trade-off between agglomeration and surface density. Unfortunately, we do not count with specialized equipment to regulate precisely the blow-drying process, and although decent degrees of reproducibility were observed, an automatic blow-drying process would help ensuring the uniformity of the depositions.

SOLUTION CONCENTRATION TEST

Under the flag of increasing the surface density of particles while keeping a low agglomeration, two additional test solutions of higher concentration than the initial one ($\mathcal{C}_1 = 0.125$ μg/μL) were prepared by diluting 50 μL of the stock solution in 250 and 500 μL of toluene (obtaining concentrations of $\mathcal{C}_2 = 0.25$ μg/μL and $\mathcal{C}_3 = 0.5$ μg/μL). The initial drop-casting procedure, modified by gently blow-drying after 2 s of waiting time, was repeated for 5 droplets of each solution in three different chips. The SEM images revealed nanoparticles surface densities greatly increasing for higher solution concentrations (Fig. 2.19). Particles could be observed clearly placed on top of the Al constrictions, while little agglomeration was present. The chip prepared using the $\mathcal{C}_3$ solution displayed an average of more than 10 well-spaced nanoparticles on top of the constrictions, giving rise to a good compromise of surface density and small agglomeration, at first sight.

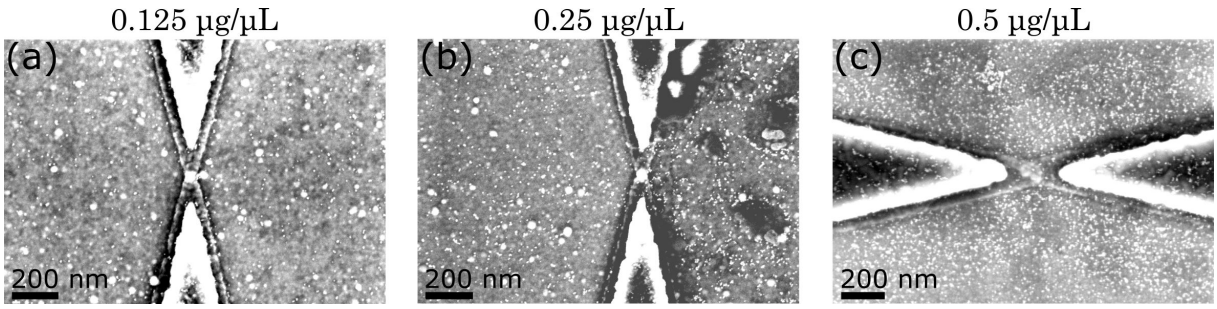

Fig. 2.19: SEM images of electromigration constrictions after drop-casting 5 droplets (with a blow-drying waiting time of ≈ 2 s) from three colloidal solutions of nanoparticles with different concentrations concentration of (a) 0.125 μg/μL, (b) 0.25 μg/μL and (c) 0.5 μg/μL. Low-agglomeration nanoparticle densities increase for higher colloidal solution concentrations, leading to an optimal surface distribution for 0.5 μg/μL (c). The smaller bright dots in the pictures are identified as nanoparticles, while bigger circular features are attributed to resist residues.

OPTIMIZED DROP-CASTING PROCEDURE

After these tests we can conclude that the main factor affecting the nanoparticles distribution on the sample's surface is the blow-drying procedure. While a short blow-drying waiting time can avoid the particle's agglomeration, the concentration of the colloidal solution can be adjusted to reach decent surface densities, rather than by drop-casting larger numbers of solution droplets. The resulting optimized procedure can be written as follows:

1. Sonicate the colloidal solution ($\mathcal{C}_3 = 0.5$ μg/μL) at maximum power for, at least, 1 hour (using an ELMA TI-H-10 sonication machine).
2. While holding the chip in the air with some tweezers, cast a 10 μL droplet of the colloidal solution onto the its surface (using a micro-pipette).
3. Prepare the pressurized N_2 gun ready for blow-drying and lay the chip down onto a piece of clean-room paper tissue (keeping the tweezers holding it).
4. After the chip touches the tissue and capillary forces start evacuating the liquid, wait for approximately 2 seconds, then gently blow dry the remaining liquid on the sample surface.
5. Repeat the process from point 2 until 5 droplets have been drop-casted.

Most of the samples used for drop-casting tests were also cooled down and electromigrated in-situ, resulting in some of the QD junctions measurements presented in chapter 4. Once the optimized procedure described above was reached, we stick to these steps for the rest of the colloidal QD depositions. Overall, we electromigrated at 4 K more than 300 constrictions prepared by drop-casting colloidal solutions of dodecanethiol-capped, 5 nm, Au nanoparticles, out of which we observed clear and stable QD conduction signatures in 14 of them, deriving a total success rate of about 5%. However, considering merely the samples in which the QD deposition was done following the optimized procedure, we estimate an increased success rate up to $\sim$10%.

2.5.2 In-situ evaporation of fullerenes

Inspired by ultra-high vacuum setups allowing to carry out in-situ surface preparation processes (see, for example, references [234, 10]), we designed and fabricated an ohmic-heating molecule evaporator as a removable unit, attachable to the cryostat sample cavity (shown in section 3.1.5). The quench condensation method, consisting on in-situ evaporations of molecules at cryogenic temperatures, has been long employed for depositing C_{60} fullerenes [242] and proven successful for the obtainment of QD junctions in samples containing nano-spaced electrodes [243], motivating us to try this approach in an attempt to improve the success rate of the drop-casting method. We employed a commercial Pt resistor (lumped element) as the evaporator heating device, whose resistance displays a well-known linear temperature dependence, allowing to control the temperature and calibrate the evaporation process. A 10 μL droplet of a C_{60} colloidal solution in toluene (with a relatively high concentration

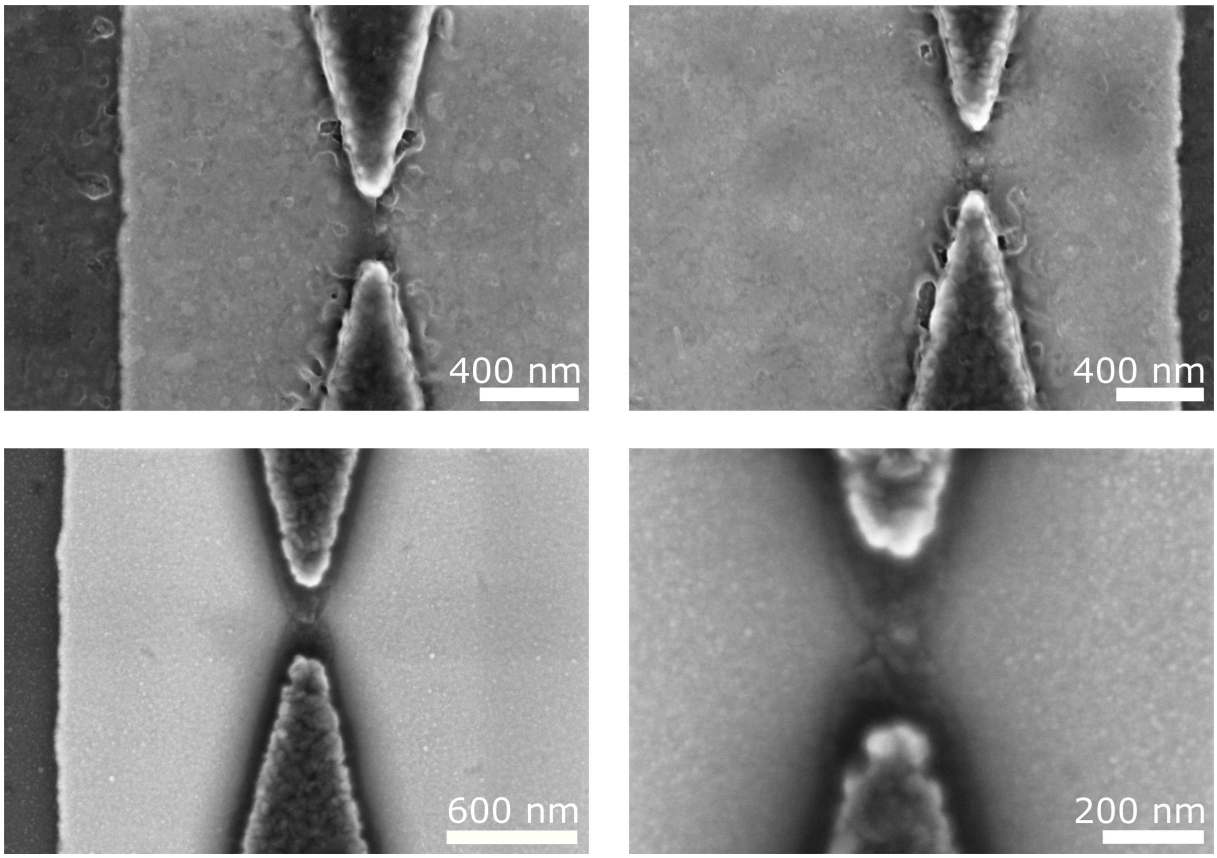

Fig. 2.20: SEM images Al constrictions electromigrated at low temperatures, employed in the optimization the in-situ C_{60} evaporation procedure. (a,b) During the evaporator calibration, long-lasting evaporations over a total time of 45 minutes resulted in a molecular layer covering the whole sample surface. (c,d) After a degassing process of about 20 minutes, few consecutive flash evaporations of 30 s were performed on two samples in two different cool downs. Apart from a slight fuzziness with respect to bare Al constrictions images, no indicative details of the success of the evaporation can be appreciated.

of $\mathcal{C}_{C60} = 1\ \mu g/\mu L$) was casted on top of the Pt resistor and let for the solvent to evaporate. Several tests were performed, initially in a high-vacuum toy setup at room temperature on bare silicon substrates, and later in the cryostat at 4 K on chips containing Al constrictions. Although the desorption temperature of fullerene molecules depends both on the fullerene type and the adsorption surface, it is commonly found in literature that the desorption rate is maximum around $T = 250 - 500$ °C [244]. As we look towards depositions of a sub-mono layer, to avoid the agglomeration of molecules, we aimed for short evaporation times at the onset of the desorption rate (typically for $T = 200 - 250$ °C). SEM images of samples exposed to uninterrupted long evaporation times of 45 minutes showed blurred constrictions, pointing towards a layer of molecules completely covering the sample surface (Figs. 2.20a and b). After several calibration tests, we outlined an evaporation procedure based on consecutive flash evaporations of 30 s duration. While samples prepared this way do not present any clear features indicating the presence of C_{60} molecules (Figs. 2.20c and d), the aluminum appears blurrier than in naked constrictions, which may be an indication of successful evaporations. A complete explanation of the evaporator calibration and the flashing procedure can be found in Annex E.

Along the calibration tests of few molecule evaporator versions, one successful QD junction, and clear QD conduction features in two more, were observed from the electromigration and exploration of a total of 33 constrictions. The reduced yield of success can possibly be ameliorated by optimizing the evaporation procedure. In any case, we consider that insufficient junctions have been measured to be conclusive about this success rate, and tests with a larger sampling rate must be carried out.

2.5.3 Metallic sub-mono layer evaporation

As explained at the beginning of this section, the evaporation of thin metallic layer (~ 1 nm) on a substrate can turn into few-nm nanoparticles formed due to the surface tension, covering the whole sample surface. Following the funding fathers' steps, we also tried the metallic sub-mono layer approach, to explore another possibility that may increase the QD junctions yield of success. Several tests on the evaporation of thin gold films on electromigration constrictions made of Al, Au and Pt were carried out together with Bivas Dutta and Danial Majidi (PhD students in our group). Since Au and Pt are noble metals that do not oxidize, electromigration of constrictions made of these materials can be carried out either at ambient or cryogenic temperatures, allowing to deposit the metallic sub-mono layer after electromigration in the first case. In both cases, the surface of the sample was cleaned by a RIE oxygen plasma procedure of 10 W power for 5 s, right before the sub-mono layer evaporation. Both approaches showed an extraordinarily high yield of success ($\sim 70\%$) and, although many of these QD junctions displayed constant charge-offset gate switches, some of them are stable and precise measurements could be taken [245, 219]. We observed that the typical particle-size (and therefore the surface density) depends on the evaporated thickness. The sub-mono layer thickness was optimized in this respect, finding the best compromise for a yield of success and a decent electrostatic stability of the samples for 1.2 nm of Au, evaporated at a rate of 0.05 Å/s.

In the case of Al constrictions, electromigration must always be carried out in-situ under high-vacuum, to avoid the oxidation of the nanogap contact leads. Same tests were performed in Al constrictions (Fig. 2.21b), by cleaning the sample with a RIE process, evaporating 1–2 nm of Au and electromigrating the constrictions at 4 K. Although electromigration seemed to work out properly in 36 constrictions, retrieving the usual values for V_{Break} and R_{sh}, and the current across the broken constriction often displayed a certain dependence on V_G, we could never obtain a properly coupled QD junction. We attribute this lack of success to the fact that electromigration in Al occurs in a rather violent way, in opposition to Au breaking junctions, probably tearing apart the sub-mono layer formed on top of the constriction (Fig. 2.21c).

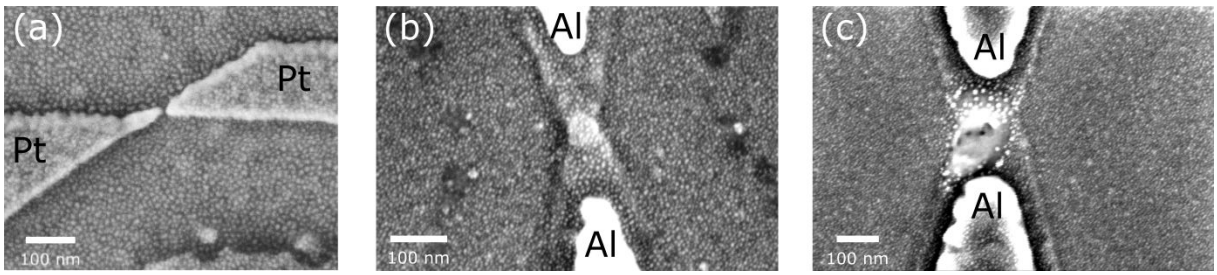

Fig. 2.21: SEM images of electromigration junctions after the evaporation of a sub-mono layer of Au that collapses into nanoparticles of $\sim 5-10$ nm diameter due to surface tension. (a) Electromigration junction made of Pt after breaking the constriction (extracted from [245]). (b) Before electromigrating the Al constriction, its surface is completely covered by nanoparticles. (c) After electromigrating the Al constriction, nanoparticles seem to have scattered away from the nanogap, looking slightly bigger and brighter, possibly due to Au sub-mono layer melting down during the breaking process.

3 Experimental implementation

As quantum physics studies nature in the limit of small length scales, the typical energies that drives the behavior of particles (like electrons) in such quantum systems are often extremely low, resting negligible with respect to the thermal energy at room temperature. Commonly, fluctuations at ambient conditions are large enough to completely bury the signature of quantum effects, making them inappreciable. Most of experimental setups devoted to the study of quantum physics require of an enclosed environment, where samples can be isolated from ambient noise (light radiation, pressure waves, mechanical vibrations, temperature,...) and cooled down to temperatures close to absolute zero, so that quantum effects become distinguishable and measurable.
A cryostat (or cryogenic refrigerator) is a device created to fulfill this objective, allowing to maintain samples cold and isolated while measurements can be pursued. Moreover, since the presence of superconducting leads is on the basis of our study (typically aluminum display a critical temperature around 1.2 K) and keeping their contact surfaces unoxidized after electromigration is a must, the low-temperature and high vacuum conditions reached in cryogenic setups are doubly required in our case. Here we will briefly review the cryostats employed in this project, commenting on the improvements performed on them and the implementation of our measurement setup.

Contents

3.1 Cryogenic transport setup

The cryostats at our disposal are two inverted dilution refrigerators, named A and B (Fig. 3.1). Opposite to the classical cryostat arrangement where the samples are attached to a dipstick that is inserted into a He^4 bath, the peculiar design and functioning of inverted dilution refrigerators (also called Sionludi, a verlan inversion for dilution) reminds of an Italian coffee kettle, as the cryostat is mounted on top of a He^4 Dewar vase. A vacuum shielded pipe connects the bottom of the Dewar vase with a He^4 pot, placed inside the cryostat and connected on the other side to a He^4 recovery line. By creating an over-pressure in the Dewar vase containing liquid He^4, the fluid ascends through the pipe, reaching and filling the He^4 pot, resembling the boiling water reaching to the upper side of Italian kettles when the pressure in the lower part increases when heating it up. Sionludis are separated in concentric stages, characterized by different self-established equilibrium temperatures during its operation, being colder as the stage is closer to the center of the cryostat (matrioshka structure). Each stage counts with an horizontal metallic plate, where radiation shields are fixated and wires are thermalized. We can distinguish between the hotter/outer stages (at temperatures of 80 K, 20 K and 4 K, reached automatically by the cryostat isolation quality and the temperature gradient between T_R and the He^4 pot) and the colder/inner stages. Dilution refrigerators are based on a He^3/He^4 mixture that flows inside and out of the cryostat through a closed-circuit pipes system, with the help of pumps and compressors. Along circulating through the circuit, the mixture undergoes a thermodynamic cycle, reaching different equilibrium temperatures at the distinct parts of the circuit: 1 K at the still stage, 200 mK at the cold stage and the lowest (base) temperature, around 50-80 mK, is reached at the mixing chamber stage, to which sample is attached (see the schematic shown in Fig. 3.7). The He^4 pot open circuit provides a fast cooling of the cryostat stages down to 4 K when starting the cool down process from room temperature, and a strong pre-cooling of the circulating mixture injected into the cryostat. The Sionludi concept was developed and patented by our laboratory (Néel Institute in Grenoble) and a few generations of cryostats attending to slight different designs have been fabricated locally in the past years. While we will not discuss the exact details of the Sionludi operation, more details on these subjects can be find in the theses of *Norbert Moussy* [246] and *Stefan Thiele* [247].

The configuration and functioning of both Sionludis A and B is equivalent (despite owning a slightly different design), including an identical sample-holder receptacle so that the same sample-holders can be use indistinctly. First, we briefly describe their structure, as necessary to understand the key points regarding the installation of electrical lines performed along my work (3.1.1). Both Sionludis were mostly wired by previous students, including the thermometry system at the cryostat stages and highly filtered but electromigration compatible DC measurement lines (3.1.2), as well as a coil for the generation of perpendicular magnetic fields in the sample stage of cryostat B (allowing us to characterize our aluminum junctions in the normal state at low temperatures). During my project, I mainly worked in cryostat A, where we installed three radio-frequency (RF) lines, one of them devoted for the AC-driven turnstile measurements (3.1.3). Home-designed PCB plates were ordered and then manually prepared as sample-holders, including the soldering of RF connectors and a lumped-element bias-tee circuit necessary for a proper coupling of the gate electrode AC and DC signals at a sample-holder bonding pad (3.1.4). A couple of DC lines were also installed in cryostat A, providing the power for a home-made molecule evaporator unit that we fabricated and tested in our samples (3.1.5).

3.1.1 Thermal isolation and radiation screening

To reach temperatures close to absolute zero, the heat conduction between the outer part of the cryostat (room temperature shield or vacuum bell) and the central base temperature stage (colored in dark blue in Fig. 3.7) should be minimized. Diffusive thermal conduction is canceled by pumping vacuum in the system, reaching a high-vacuum level $\sim 10^{-8}$ mbar thanks to cryosorption at temperatures of 4 K or below. To reduce the thermal conduction by black-body radiation, each of the outer cryostat stages is equipped with a radiation screening shield, consisting on a hollow copper cylinder with a polished and gold-plated surface to avoid oxidation, keeping it highly reflective.

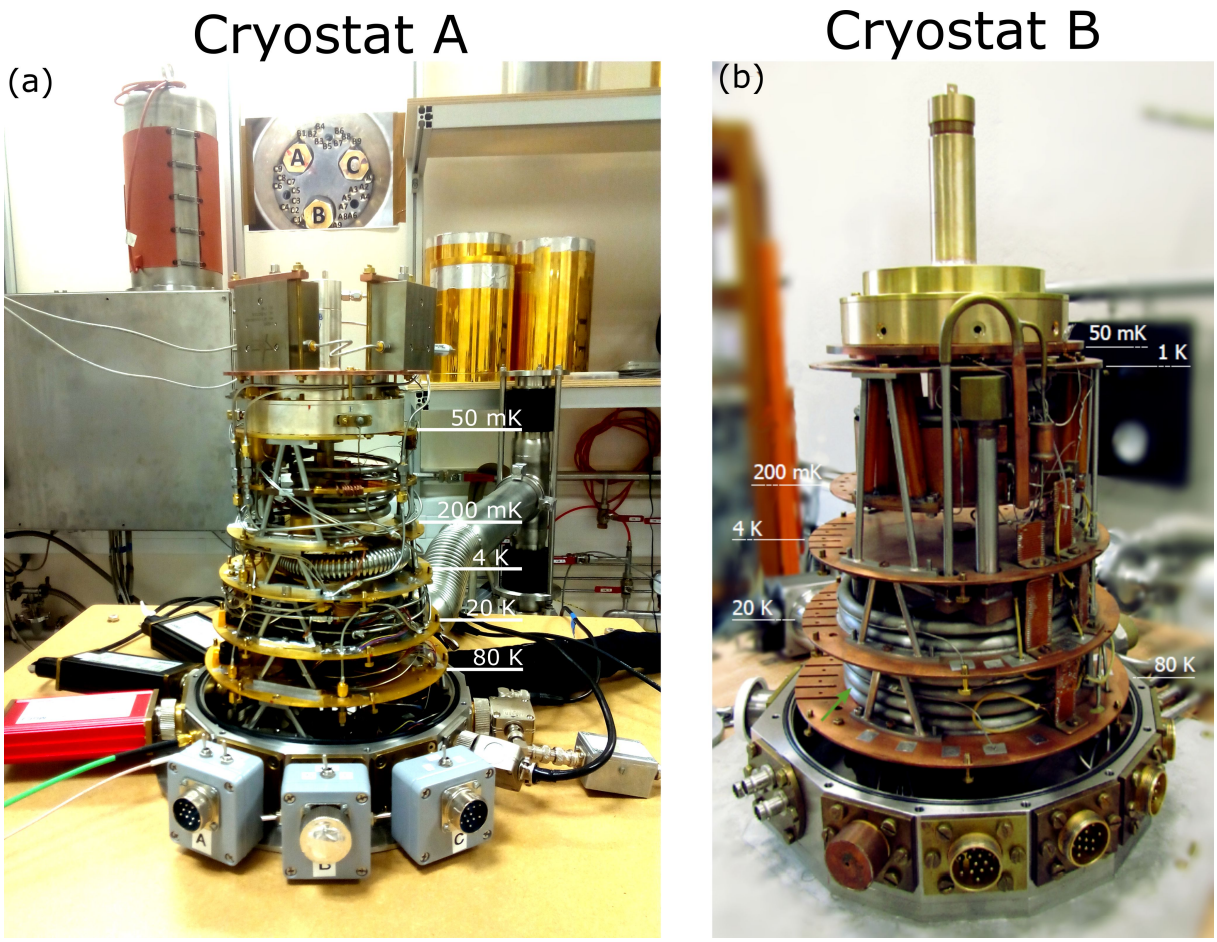

Fig. 3.1: Pictures of the Sionludi cryostats employed, indicating the different temperature stages in (a) cryostat A and (b) cryostat B. In the top-left corner of (a) we can see the grey vacuum bell with a red heating jacket around it, and in the top-right corner the three gold-plated radiation screening shields of the warm stages (80, 20 and 4 K).

The base temperature stage of our Sionludis consist on a hollow copper disk-shaped block, gold or silver coated, with an upstanding central cylinder where the sample-holder receptacle is located (see Fig. 3.3). The whole chunk is attached to the He^3/He^4 mixing chamber, and its inside is divided in two separate cavities providing two well-shielded environments at base temperature (pictures taken before to the closure of the base temperature stage of cryostat A are shown in Fig. 3.2). The cavities are isolated from each other, being the initial cavity used for filtering the DC measurement lines and its thermalization at base temperature, while the sample-holder is plugged and connected to the filtered and thermalized measurement lines at the second, "clean" sample cavity. An schematic layout of the whole cryostat structure and electrical lines can be seen in Fig. 3.7.

3.1.2 Electromigration-compatible measurement DC lines

The small values of typical currents and voltages involved in transport measurements of mesoscopic devices require adequate shielding and extensive filtering of the electrical lines to reduce the noise/signal ratio as much as possible. Unshielded wires may absorb electromagnetic black-body radiation from the warmer stages of the cryostat on their way from the room temperature connectors to the sample stage, increasing the noise in the measurement. The 27 DC lines in each cryostat are divided into 3 capillary coaxial coverage, that act as screening shields protecting the wires from black-body radiation at intermediate cryostat stages. Apart from protecting the wires from the pick-up of ambient radiation inside the cryostat, the self-radiation that wires carry from its connection to measuring instruments at room temperature must also be filtered out. For this, the capillaries are filled with eccosorb [248]

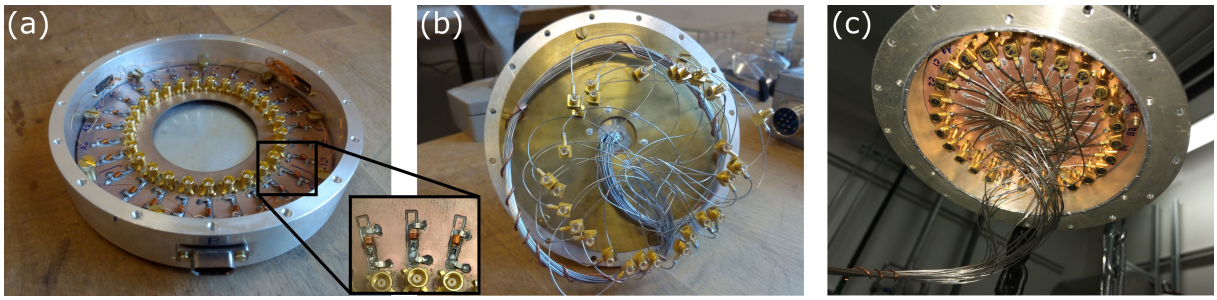

Fig. 3.2: (a) Inside the initial cavity of cryostat A, the DC measurement lines are connected to π-filters attached to a PCB plate fixed on the cavity surface. Inset: Zoom-in at the π-filters. (b) Thermocoax wires feed-through from the initial cavity into the sample cavity. (c) Bottom-view of the sample cavity showing the second PCB plate attached to the top surface, connecting the thermocoax cables to copper wires that bring the DC measurement lines to the sample-holder receptacle connectors. Pictures courtesy of Bivas Dutta.

(a dissipative dielectric used for a first filtering step) while thermal anchors are used to thermalize them at each cryostat stage. At the base temperature stage, each DC line is connected to a π-filter soldered in a PCB plate (with a cut-off frequency around 10 MHz) that removes most of the high-frequency noise in the lines and thermalizes it at base temperature in the initial cavity, shown in Fig. 3.2a. ThermoCoax coaxial cables [249], connected to the π-filters, bring the DC lines into the sample cavity across a feed-through passage, shown in Fig. 3.2b. In the sample cavity, the ThermoCoax cables are connected to copper wires soldered to a second PCB plate (Fig. 3.2c), which bring the DC lines to the spring connectors in the sample-holder receptacle (Fig. 3.3a). The total length of each line is about 3 m and shows a total resistance around 100-200 Ω, displaying negligible resistances per unit length with respect to our Al constrictions ($\sim 10^8$ Ω/m).

As the electromigration voltage ramp requires a good transmission for bandwidths up to of ~ 1 MHz, no direct low-pass filter with similar cut-off frequencies can be included in the DC lines. Our peculiar filtering strategy, based on dissipative dielectrics (eccosorb) and lossy cables (ThermoCoax), is specifically designed for achieving compatibility between in-situ electromigration and a filtering system ensuring a low-noise electrical setup as necessary for precise turnstile measurements. In fact, the non-linearity of this filtering system makes the fast reset of the electromigration voltage ramps to get smoothed out, and the breaking procedure cannot be performed in a gradual and progressive way (opposite to electromigration experiments employing modern feedback algorithms that allows a precise control on the breaking procedure [250]). However, a rather aggressive electromigration may be favorable for our purposes, opening nanogaps wide enough to fit 5 nm nanoparticles in them.

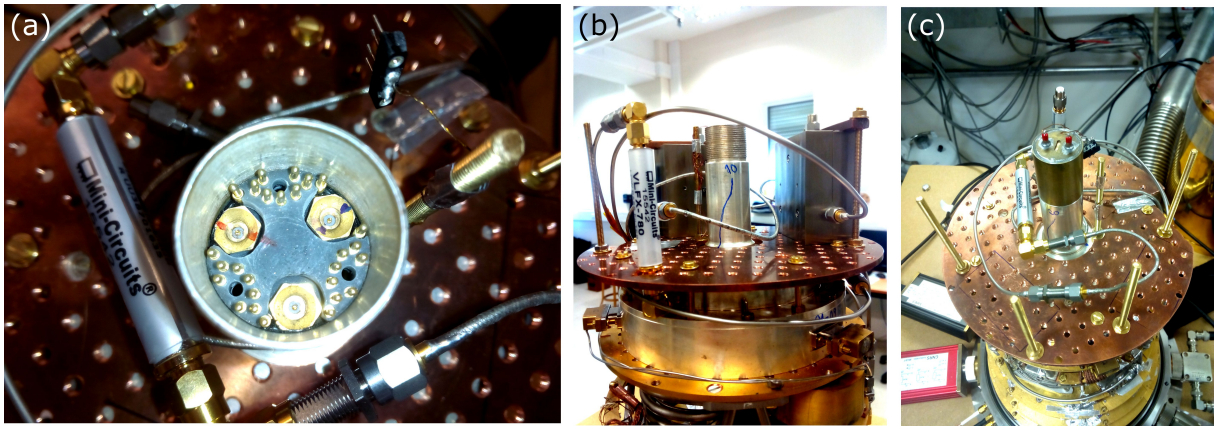

Fig. 3.3: (a) Top-view of the sample-holder receptacle (identical in cryostats A and B) showing the 27 spring connectors that correspond to the DC lines, and three SMP connectors that can carry RF signals. (b) Back-view of the base temperature stage of cryostat A, showing the RF circulators and filters installed at the base temperature stage (for RF_I and RF_O lines). (c) Top-view of the base temperature stage showing the molecule evaporator unit in place, closing the sample cavity cylinder (circulators were removed for the clarity of the picture).

3.1.3 Installation of radio-frequency lines

Electrical lines intended to carry an AC signal are commonly conceived as a conducting wire placed inside a grounded coaxial shield, separated by a dielectric media. While the coaxial shield protects the inner conductor from the absorption of external noise and prevents the emission of part of the AC signal power in form of radiation, the presence of a solid dielectric fixes the inner conductor at the center of the cable, ensuring a constant impedance to ground along the whole cable length. Any damage or discontinuity of the dielectric or the coaxial shield will create a local impedance mismatch resulting in the generation of standing waves in the line and/or power losses. Hence, the good-quality of cryogenic RF lines used for AC-driven experiments is extremely important, especially in blind configurations involving dead-end electrodes, like our gate, since there is no indicator of the characteristics of the signal arriving at the sample other than the QD turnstile current itself. Three RF lines were set up in cryostat A during my PhD, one of them, RF_G, devoted to provide the AC signal, V_G^{AC}, to the gate electrode in our EMBJs (as explained in Annex A), and two others (RF_I and RF_O) for a different project involving transmission experiments in RF nanoresonators. For this purpose, semi-rigid MicroCoax cables [251], were manually prepared, adapting them to the cryostat space constraints (including careful bending, cutting and soldering SMA connectors). As the RF_I and RF_O lines need of substantial low-temperature RF equipment (high-frequency-bandwidth low-pass filters, attenuators circulators and amplifiers), a copper platform was designed and fixed at the base temperature stage of cryostat A, providing a basement for the installation and thermalization of these circuit elements (shown in Fig. 3.3b and c). At the base temperature stage, the three RF lines are brought directly into the clean sample cavity by SMA feed-through connectors, where three copper coax cables of 10 cm connect each line to the three SMP receptacles at the sample-holder stage (Fig. 3.3a). As the RF_I and RF_O lines has not been used in any of the measurements presented in this thesis, we have omitted their representation in Fig. 3.7 and they will not be further discussed.

Thermal anchors (blue arrows in Fig. 3.4a) and SMA jack-to-jack connectors (green arrows in Fig. 3.4b) were settled at each temperature stage to thermalize the coaxial jackets of the RF lines. Differently, thermalization of the inner conductor is achieved by employing attenuators (red arrows in Fig. 3.4c), collaterally diminishing the oscillation amplitude of the AC signal. The attenuation factor, At, specification gives the relation between the amplitude of the input and output voltage signals through the attenuator:

$$At = 20\log\left(\frac{V_{in}}{V_{out}}\right) \rightarrow V_{in} = 10^{At/20}V_{out}, \tag{3.1.1}$$

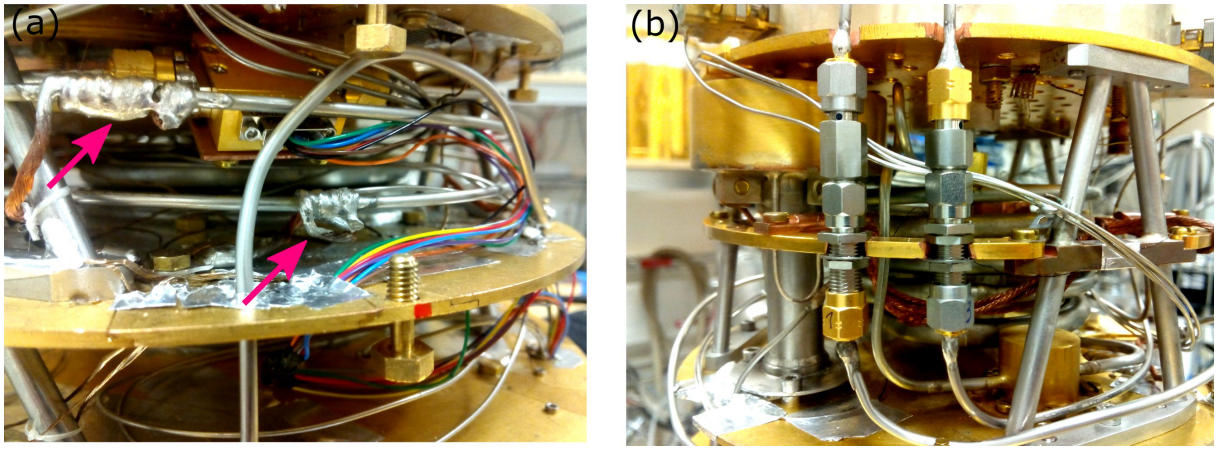

Fig. 3.4: (a) Examples of thermal anchors in two RF lines (pink arrows). The low temperature RF amplifier (LNF-LNC0.3_14A model) for the RF_O line can be seen in the background of the image, attached to the upper 4 K stage. (b) SMA jack-to-jack connectors and attenuators employed for the fixation and thermalization of RF_I and RF_O lines at the 200 mK stage, and the attenuation of the corresponding signals.

The inner conductor of the MicroCoax cables is made of a CuBe alloy, characterized by a low thermal conductivity that helps establishing a thermal gradient in the cable and minimize the heat load to the base temperature stage. In this sense, only two attenuators of -10 dBm (at the 4 K stage, and at base temperature right before entering the sample cavity) were needed to bring the RF_G to the sample-holder receptacle without observing a significant base temperature increase. In fact, it is important not to overkill the V_G^{AC} signal with several attenuators as colloidal-QD junctions typically display relatively small gate couplings ($\alpha_G \sim 0.1\%$), which can result further reduced for AC signals (for a detailed analysis on the comparison of α_G^{AC} and α_G, see Annex B).

3.1.4 Broadband bias-tee sample-holder

The characterization of the DC properties of our QD junctions is done by applying a DC voltage, V_G, to the gate electrode. After such preliminary characterization, to perform charge pumping measurements, an AC signal, V_G^{AC}, must be applied to the gate simultaneously and independently from the DC component, V_G. However, combining AC and DC signals is not a trivial task: the presence of attenuators in the RF_G line (where the inner conductor is connected to ground) disables the possibility of connecting together the RF and the DC lines at room temperature. A capacitor allowing the transmission of the AC signal but blocking the DC component traveling into the RF line can be used, restricting the DC-AC signal coupling to the RF line extremity at the sample stage (after the thermalizing attenuators). An initial approach, tested by the previous student, *David van Zanten* [37], consist on fabricating an on-chip capacitor at the gate electrode using electron beam lithography. However, under this configuration, it was observed that the V_G^{AC} signal gets transmitted into the V_G DC line, creating undesired cross-talks with other DC lines, as they are not shielded from each other neither at the base temperature cavities, nor inside the three capillar coax shields. Such cross-talks induced a non-negligible oscillation of other DC voltages being applied simultaneously (like the biasing voltage across the junction) making extremely difficult to carry out precise turnstile measurements. This can be solved by adding an inductor to the V_G DC line that blocks the V_G^{AC} transmission, constituting, together with the capacitor, an ensemble called bias-tee.

During my thesis, we work on the integration of home-made lumped-element bias-tees on the sample-holders, allowing the coupling of the V_G and V_G^{AC} signals at a single bonding pad on the sample-holder (V_G^{AC+DC}), micro-bonded to the gate of the chip containing the electromigration junctions. Our sample-holders consist on a circular PCB plate with both flat surfaces metallized in aluminum with a gold coating, forming a bonding-pad pattern according to the receptacle of our Sionludis. The 27 spring connectors at the cryostat receptacle are pushed down when inserting the sample-holder, providing electrical contact with the DC bonding pads at the bottom side of the holder (Fig. 3.5b). A solid fixation of the holder to the cryostat, including its thermalization at base

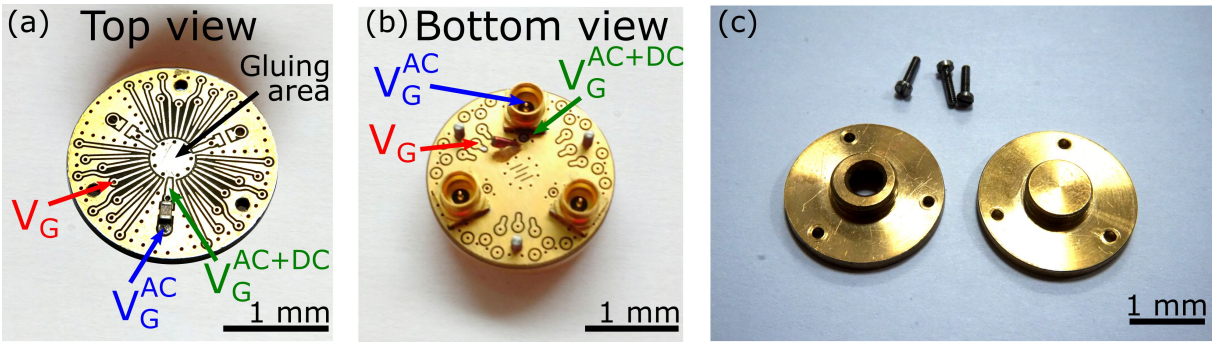

Fig. 3.5: (a) Top-side of the sample-holder, showing the 27 DC pads and the three RF pads. A capacitor connects the RF_G line pad (V_G^{AC}, blue arrow) with the common gate pad (V_G^{AC+DC}, green arrow). (b) Bottom-side of the sample-holder, showing the 27 pads for the DC lines and the three SMP connectors. The bias-tee conical inductor has been soldered between the DC V_G line (red arrow) and the common gate pad (V_G^{AC+DC}, green arrow). (c) Metallic caps and M1.4 screws. A hole could be drilled in the central part (left) to perform in-situ molecule evaporations.

temperature and electrical ground share, is achieved thanks to the three SMP connectors manually soldered on the bottom side of the sample-holders. The SMP connectors can be plugged to the cryostat SMP receptacles through SMP jack-to-jack adapters, allowing, as well, the transmission of RF signals to the sample-holder pads. The 27 DC signals and the electrical ground are brought to the top side through metallized holes in the PCB plate, and once on the top, each pad brings its signal to the center of the plate (Fig. 3.5a), where chips were glued individually using conductor paste model 4929N, then micro-bonded to the holder's pads using gold wires. The common gate electrode is connected to the RF_G line through a capacitor soldered on the holder's top side, and to the DC line providing the V_G signal through an inductor in the holder's bottom (Figs. 3.5a and b). Several sample-holders were prepared and equipped with bias-tees, using capacitors with nominal values between 100–250 nF and broadband tapered inductors with nominal values of 1.2 and 2.35 μH. The inductors' conical shape effectively changes the inductance along its length, permitting it to block AC signals over a considerably larger frequency range than usual cylindrical inductors.

Although the cryostat sample cavity provides an electromagnetic shield versus thermal radiation of hotter stages, the presence of predominant lengths associated to the cavity size can enhance the excitation of the corresponding electromagnetic modes, which may lead to undesired effects such as photon-assisted tunneling or non-white noise. Specifically designed brass pieces were ordered, in the shape of a cap (Fig. 3.5c) which can be screwed to the top face of the sample-holder where an individual chip is eventually glued and bonded, providing an additional small cavity at the sample-holder stage. Although it can be detrimental in terms of radiation shielding, a whole was drilled in several metallic caps (Fig. 3.5c, left), in order to expose the sample surface to the home-made evaporator presented in the next section.

3.1.5 In-situ molecule evaporator

A Joule-heating molecule evaporator unit compatible with the sample stage of our Sionludi cryostats was designed and fabricated to try out the possibility of obtaining QD junctions by performing consecutive in-situ molecule depositions on the electromigration constrictions at 4 K. Our molecule evaporator is based on a commercial Pt ohmic resistor (commonly used for thermometry, indicated by a red arrow in Fig. 3.6a), owning a well-known linear temperature dependence that allowed us to calibrate and control the evaporation process (explained in detail in Annex E). Normally, thermometers employing Pt-lumped-element resistors are implemented in a 4-probe configuration, which allows the precise measurement of its resistance to determine the temperature while applying small biasing currents. Nevertheless, as a high-precision temperature measurement is not necessary in our evaporator, we

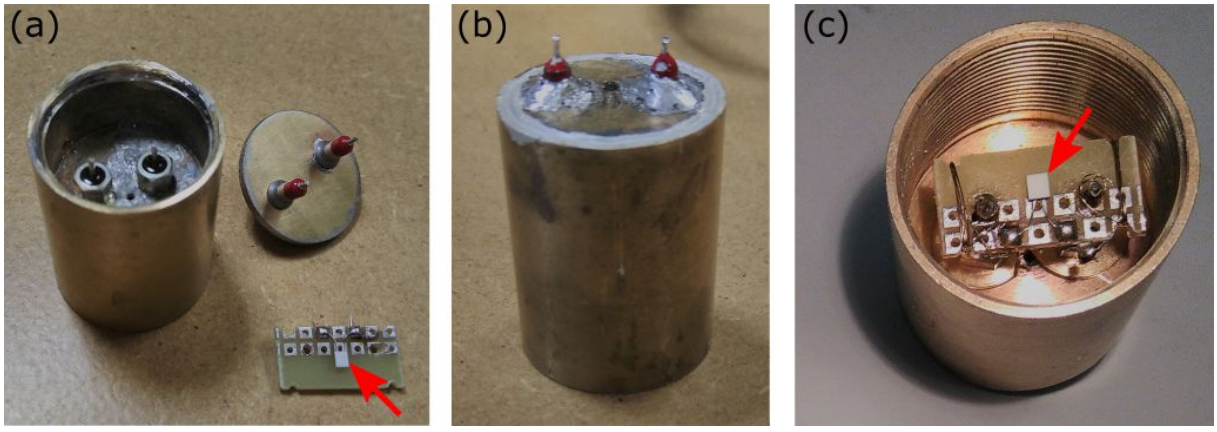

Fig. 3.6: (a) Picture showing the molecule evaporator unit elements. Two screwing-feedthru filters are visible inside the open cavity. On the side, the closing lid (where two π-filters have been soldered) and the PCB plate with the Pt resistor (red arrow). (b) The molecule evaporator is shown after assembly and soldering of the top lid (c) Bottom-view of the evaporator, noticing the PCB plate in place and the Pt resistor (red arrow) already wired.

opted for a 2-probe configuration that greatly simplifies its fabrication and installation in the cryostat. Like this, the Pt resistor heats up due to Joule effect by the current generated when voltage biasing its two terminals at the room temperature shield. Droplets of molecular colloidal solutions were drop-casted on the Pt resistor before closing and cooling down the cryostat, for a later deposition of molecules in-situ (at a temperature of 4 K and under high vacuum), eventually taking place as the temperature of the resistor is increased and the molecules desorb.

The molecule evaporator consists of a cylindrical piece of brass with an inner thread that can be screwed on top of the cryostat sample stage (Figs. 3.6). From this position the Pt resistor faces the sample, enabling the molecular deposition on the sample surface. Similarly to the initial electromagnetic-impermeable cavity present in the base temperature stage of the cryostat for thermalization and noise filtering of the DC measurements lines before they reach the sample cavity, our molecule evaporator includes an initial cavity on its upper side, employed for the same purpose (shown in Fig. 3.6a). Two π-filters, soldered in the metallic top lid, act as a base temperature thermalization and feedthrough of the evaporator lines into the cavity. Ideally, a couple of short ThermoCoax cables can be employed to connect the π-filters on the top lid with the two screwing-feedthru filters that bring the signal into the sample cavity. Then, Mn wires (owning a very low thermal conductivity) were used to connect the filters electrodes with leads on a PCB plate where the Pt resistor is already fixed and soldered (Fig. 3.6c). Although the general layout remained the same, certain elements and aspects of the evaporator evolved during my experiments period. All these evaporator versions were wired, installed and tested (with the help of other students: Danial Majidi, Naveen Shetty, Jacob Adamczyk and Gabriel Hofferman), finally arriving to the version presented here.

3.2 Measurement instruments centralization and procedures

For electromigration to be conveyed in a controlled manner, a real-time measurement system with a fast enough feedback loop is required. After the breaking procedure, the characterization of QD-SET devices need the simultaneous application of the bias and gate voltage signals (V_G and V_B). Both tasks can be carried out by an ADwin Gold II instrument, as well as the data acquisition of the current flowing through the sample (I) by including an I-V converter/amplifier device in the circuit. The NanoQt open-source software developed locally at Institute Néel allows to control the internal processor of our ADwin system in general. This program includes a Graphical User Interface (GUI) specialized in the measurement of QD transistors (including an electromigration feedback loop with variable parameters and accomplishing basic characterization functionalities like sweeping single voltage channels or include a lock-in excitation). Furthermore, NanoQt provides a development environment, where sequential measurements can be encoded and sent to any measuring instrument interfaced in the measurement PC, enabling to synchronize the application of V_G and V_B, and measurement of I, with the variation of other experimental parameters like the V_G^{AC} signal characteristics or a magnetic field. Besides this, the operation of Sionludi cryostats is tracked down with a real-time controller that allows real-time visualization of thermometers and remote control of the electronic apparatuses and valves in the cryogenic circuits and a heater present at the sample stage. By establishing a data connection (physical or virtual) between the measurement and the cryostat PCs, NanoQt can also communicate with the controller, reading out the temperatures and setting the sample stage heater.

Along my thesis, we established a centralized setup at the measurement PC, interfacing all our measuring instruments. Script codes for performing systematic and sequential measurements with NanoQt were written, tested and launched in real samples for an efficient use of the cryostat cool-down time. In this section, we briefly present the parameters input at electromigration feedback loop carried out by the ADwin system (3.2.1), and the measuring routine systematically followed to detect QD conduction after electromigration of each constriction in every single chip cooled down (3.2.1).

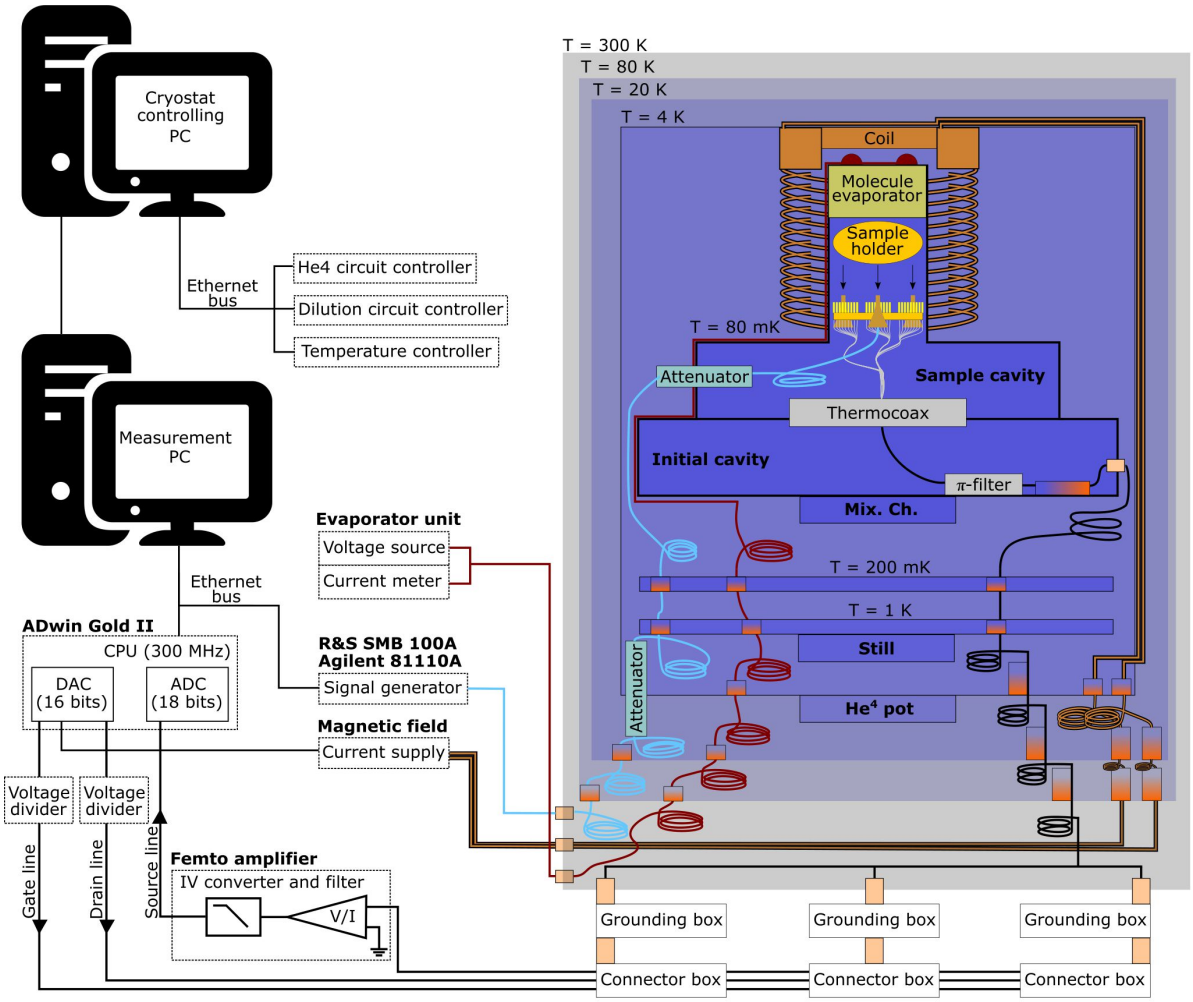

Fig. 3.7: Schematic of the usual measurement setup, showing the cryostat inner structure and elements (coil, evaporator, sample stage) including the respective wiring. A lock-in amplifier was introduced in the circuit for performing direct differential conductance measurements.

3.2.1 Fast-response system

The ADwin system counts with a 300 MHz digital signal processor, that can be programmed for real-time analysis of the input (ADC) and control of the output (DAC) voltage signals. The total voltage range of 20 V (-10 to +10 V) leads to a minimum resolution of $20/2^{14} \approx 1.2$ mV of the 14-bit ADC card and $20/2^{16} \approx 300\ \mu$V of the 16-bit DAC card, improved by connecting the corresponding channels to Femto amplifiers or voltage dividers, respectively. The electromigration feedback algorithm in the GUI of NanoQt takes advantage of ADwin's real-time signal processor (10^5 Hz) for a fast response stopping the breaking process. The biasing voltage can be ramped up at an specified speed and sampling rate (often set to 1–50 mV/s and 40 data points/s), while measuring the current flowing through the junction and calculating the resistance on real time. When the resistance is higher than a preselected target value (set to 12.9 kΩ for our constrictions), the biasing voltage ramp is suddenly stopped and brought back to zero (typical electromigration curves can be seen in section 2.4.2). While the ADwin processor owns a response time of 10 μs, by zooming it at the maximum of the $I - V_B$ curves it can be observed that the onset of electromigration takes place around ~50 μs before the current drops and the voltage ramp is stopped, indicating a characteristic electromigration time much higher than the response time. While more recent versions of ADwin systems include ADC cards of higher resolution (18 bit), a lower sampling (given by our 14 bit card) is advisable for an aggressive breaking procedure that allow to create sufficiently large gaps where few-nm nanoparticles can fit.

3.2.2 Electromigration routine

The fragility of our Al constrictions (after all, they are conceived to be easy to break) makes them extremely sensitive to static electricity discharges, which can easily explode them if special care is not taken along the single-chip manipulation. A systematic procedure must be followed scrupulously to ensure the survival of the constrictions during the nanoparticle deposition, gluing and micro-bonding to the sample-holder until the electromigration step, being necessary to test the sample after each step. At the insertion of the sample-holder in the cryostat, the measurement lines must be connected to ground (through the grounding boxes seen in Fig. 3.7) and the state of the constrictions is tested once more. If the constrictions display the usual resistance values, the lines are grounded again and we proceed to closing and pumping the cryostat, then start the cool down process to 4 K. Before ungrounding the lines, the circuit involving all instruments required for the specific measurement need to be fully connected as even the action of plugging/unplugging cables blows up the junctions (even after electromigration). The in-situ procedure employed to characterize and break a constriction consist of the following steps:

1. Measure the characteristic $I - V_B$ curve at low voltages (by applying a certain drain division), obtaining the constriction resistance R_T.
2. Launch the electromigration procedure with target resistances of 12.9 kΩ (making sure that the drain voltage division is set to 1 and the amplifier is set to full-bandwidth mode).
3. Measure the characteristic $I - V_B$ curve at low voltages (by applying a certain drain division), determining the tunnel junction shunt resistance R_{sh}.
4. Progressively measure the gate-dependence of the current ($I - V_G$ trace) at low biasing voltages of $V = 3 - 5$ mV.
5. If QD behavior is identified in the $I - V_G$ trace, the mixture condensation is started, cooling down the sample to the base temperature (50–80 mK) and further measurements are done. If not, we repeat the process on the next constriction.

The typical $I - V_G$ trace of a QD junction will show an increase of current over a certain range V_G range, often short, resulting in a spiky shape (Fig. 3.8a), indicating the gate position of the degeneracy point. The current peak must increase/decrease for higher/lower V_B, reverting its polarization when the sign of V_B is reversed (Fig. 3.8b and c).

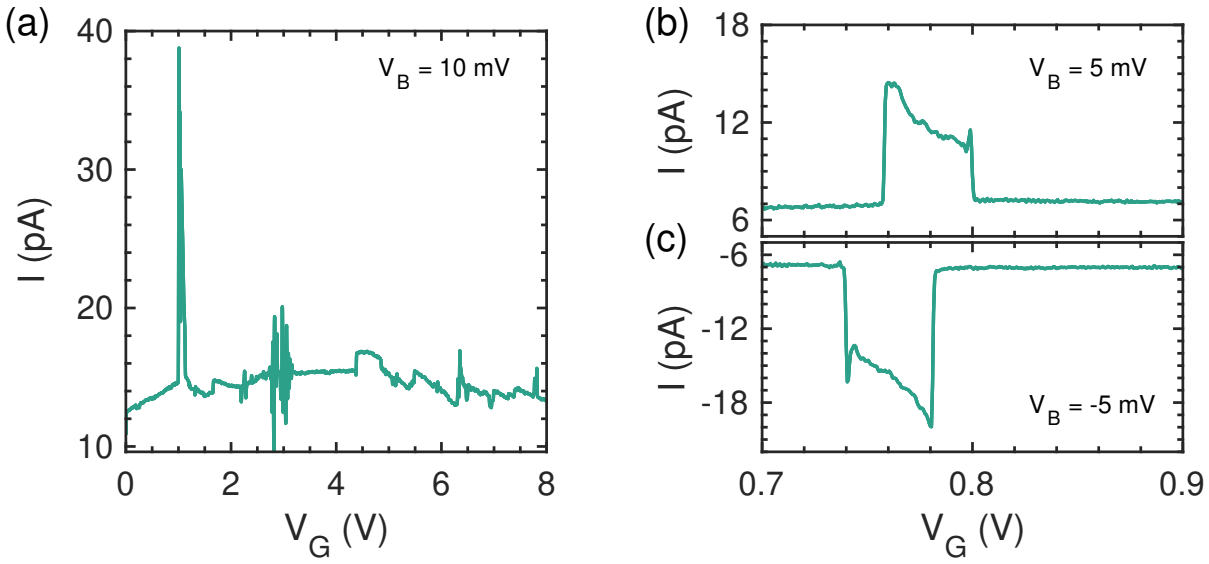

Fig. 3.8: (a) $I - V_G$ trace of a tunnel junction after electromigration of the constriction, measured at 4 K in device $\mathcal{S}_1$. The presence of a QD is signaled by the current peak, displaying a degeneracy point around $V_G = 1$ V. (b,c) Zoom-in at the current peak for positive and negative V_B, noticing the change in the sign of the current (measured at 80 mK).

4 Yu-Shiba-Rusinov states in superconductor-quantum dot transistors

The large charging energy and small gate couplings typically displayed by electromigration transistors, resulting from the small size of the colloidal quantum dots employed, restricts the access to different charge states in these devices to a single degeneracy point. On one hand, an elaborated analysis is generally required to extract the full set of the physical parameters and energy scales characterizing the system. On the other hand, a considerably large gate resolution is consequently obtained which, combined with the enhanced spectroscopic resolution commonly displayed by our all-aluminum devices, allows for precise studies of the transport features.
Superconductor-quantum dot transistors presenting a large asymmetry in the tunnel coupling to both leads often display signatures indicating the development of Kondo correlations at the strongly coupled one. For the normal state of the leads, the combination of Coulomb blockade and Kondo effect exerts an important influence on the sequential current, giving raise to significant deviations from the orthodox picture. For the superconducting state of the leads, the arising Yu-Shiba-Rusinov spectrum and its response against external parameters like magnetic field or temperature can be characterized with a substantial accuracy, revealing intriguing small-scale behaviors.

Contents

4.1 Overview of superconductor-quantum dot transistors

To study the competition of superconductivity and Kondo effect that gives raise to YSR states appearing well inside the energy gap of the electronic spectrum of a SC-QD junctions, certain conditions must be achieved. First of all, the system should display a significant charging energy, E_U, permitting to stabilize a single electron (spin) at the dot. Secondly, the tunnel coupling, γ, must be large enough to allow for a significant probability of higher-order processes involving the double occupation of the QD is required, promoting the SC proximization and Kondo cotunneling. Thirdly, a similar magnitude of the energy scales characterizing both effects, i.e., the SC gap, Δ and the Kondo temperature, $k_B T_K$, is necessary for a balanced interplay enabling their simultaneous manifestation in the electronic properties of the system. Finally, a probing electrode (in the weak coupling regime, characterized by a relatively small coupling scale γ_W) can be used for measuring the electronic spectrum without perturbing it. Nevertheless, these requisites have certain degree of flexibility, which have facilitated the observation of YSR spectra and their characterization in nanoscale systems displaying large disparities in their experimental configuration, such as SC junctions contacting NWs, CNTs or self-assembled QDs, as well as molecular adsorbates in a SC substrate explored with an STM. In all cases, the resulting SC-QD-probe junctions display a large asymmetry in the coupling that allows them to reach a spectroscopic regime where YSR states can be probed.

The arbitrary fixation of the tunnel couplings in SC-QD-SC junctions made by electromigration, together with the fast oxidation rate of most SC materials present (spoiling the tunnel barriers created during the breaking procedure) introduces additional difficulties that makes the study of this interplay rather challenging in electromigration systems. Thanks to our electromigration-compatible cryogenic setups, that enabled us to carry out the breaking procedure in-situ on a large number of constrictions, we managed to obtain a few asymmetrically coupled SC-QD-SC transistors reaching such spectroscopic regime. This section focuses on introducing the transport maps of five SC-QC-SC transistors displaying different couplings, discussing the typical phenomenology characterizing each regime and showing how relevant information and physical parameters can be extracted from the measurement (4.1.1). After that, we briefly comment on the main limitations commonly present in these systems (4.1.2).

4.1.1 Superconductor-quantum dot transistors at different coupling regimes

Several single chips were cooled down in cryostat B and ~ 100 constrictions were successfully electromigrated in-situ, at a temperature of 4 K and under high vacuum conditions. In all cases, a certain tunneling current could be measured after the breaking procedure, indicating the opening of a nanogap at the constriction, not necessarily caused by a QD bridging the junction but by direct tunneling between both electrodes, as commonly observed in EMBJs. Most of the constrictions presented shunt resistances of R_{sh} ~10 kΩ–10 GΩ, corresponding to such direct tunneling. Right before the cooldown of each chip, a deposition of 5-nm diameter Au nanoparticles was carried out on its surface, by following the drop-casting method described in section 2.5.1. Whereas the tunneling current in more than 50% of the junctions present a significant dependence on V_G, clear signatures of QD conduction could only be confirmed in five of them, further investigated at base temperature (around 80 mK). Among the characterization of these five QD transistors, we identified two prevalent coupling regimes. One device, called $\mathcal{S}_1$, was found to be in a strictly weak-coupling regime, displaying rather symmetric coupling parameters, $\gamma_{S,D}$, constituting the smaller energy scales of the system. The other four devices, $\mathcal{A}_1, \mathcal{A}_2, \mathcal{A}_3$ and $\mathcal{A}_4$, presented extremely asymmetric couplings, in the Kondo regime with one of the leads (γ), and in the weak-coupling regime at the other one (γ_W). In the following, we present the differential conductance[1] measured in the transport map of these five samples, and perform a standard analysis from the perspective of the orthodox theory of Coulomb blockade for discrete-spectrum QDs.

[1] A basic data treatment consisting of a standard local-regression smoothing (for parameters individually adapted) and offset removal (adjusting symmetric-V_B features and a zero-current at the bottom of the SC gap, typically $\lesssim 10$ μV in V_B and $\lesssim 0.1$ pA in I) has been systematically carried out for all the measurements shown in this chapter.

ANALYSIS OF THE WEAKLY COUPLED DEVICE

The orthodox model can provide an accurate description of QD transistors at a purely weak coupling regime, allowing for the extraction of the full set of parameters characterizing the device directly from its transport map (Fig. 4.1a). This analysis sets a reference for the interpretation of the conductance features displayed by asymmetrically coupled samples. The characteristic diamond-like structure stemming from the charge quantization imposed by Coulomb blockade can be clearly observed, setting the zero-bias degeneracy point separating two consecutive charge states at a gate value of $V_G^0 = 0.512$ V. From the diamond slopes of $\beta^+ = 0.175$ and $\beta^- = 0.345$, we derive a capacitive asymmetry of $C_D/C_S = 1.63$ between the QD and both transport electrodes, together with an unusually large gate coupling of $\alpha_G = 0.116 = 11.6$ % (employing Eqs. 1.2.26). Direct tunneling between both electrodes originates a certain conductance background, resembling the characteristic conductance curve of SC-SC tunnel junctions and displaying a negligible V_G-dependence. From a linear fit of the corresponding current (measured well inside a blocked diamond to avoid any QD-related contribution to the current), we extract a shunt resistance of $R_{sh} = 7.7$ GΩ characterizing this junction, resulting in a constant conductance background of $G_{\text{Bgnd}} = 2 \times 10^{-5}(2e^2/h)$. By averaging several of these dI/dV_B-V_B curves measured at the blocked regions (identical within the measurement noise), we obtain the current flowing solely through the QD (Fig. 4.1b).

As it can be observed in Fig. 4.1b, the current increase at the positive-slope diamond edge (DE^+) replicates the coherence peak of the SC-DOS, originating a white band of negative differential conductance in Fig. 4.1a. In contrast, the negative-slope diamond edge (DE^-) appears as a simple current step. The DE^+ corresponds to the alignment of the chemical potential of the energy level at conduction (ϵ_0) with E_F of the S electrode. The finer spectroscopic resolution displayed by the sequential current at this edge is a consequence of a lower tunnel coupling at this lead, resulting in a smaller lifetime broadening. In this way, the different spectroscopic resolution displayed by both DEs indicates that a certain coupling asymmetry, such that $\gamma_D > \gamma_S$ is nevertheless present in this sample which, in good agreement with capacitance asymmetry of $C_D/C_S = 1.63$ previously obtained from the slopes of the DEs. Electronic and vibrational excitations of the QD, generally manifesting as

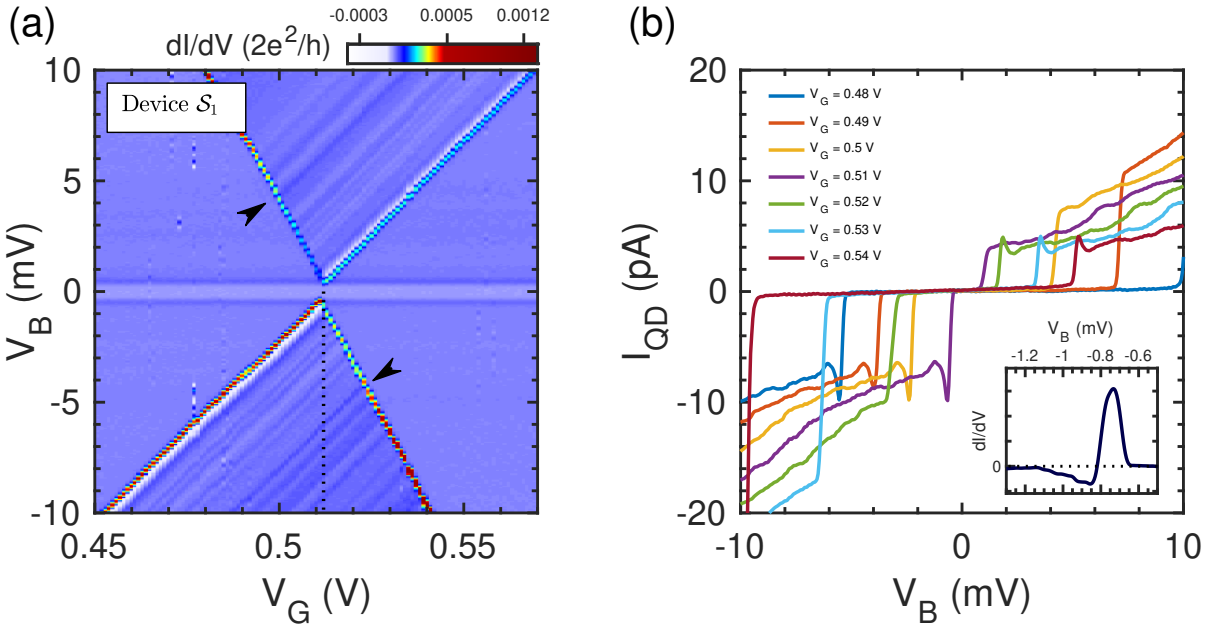

Fig. 4.1: (a) dI/dV_B transport map measured at 80 mK, showing the single degeneracy point at $V_G^0 \approx 0.512$ V (black dashed arrow) of device $\mathcal{S}_1$ that could be accessed. The slightly stronger resonance inside the on-state diamonds (black arrows) is identified with the addition of a subsequent QD energy level inside the V_B-window. (b) I-V_B curves showing the current flowing solely through the QD at different V_G values. Inset: dI/dV_B versus V_B for $V_G = 0.51$ V, zooming at the DE^+ peak (with a FWHM≈ 88 μeV).

additional lines inside the on-state diamonds, are probed at a higher resolution by the S lead, therefore appearing only parallel to this diamond edge. The slight coupling asymmetry is also evidenced by the current asymmetry displayed by the two on-state diamonds at $\pm V_B$ around the single-level conduction regime ($2\Delta < |eV_B| < E_\delta + 2\Delta$). The corresponding sequential currents at different bias polarities varies over a range of $I^+_{QD} \approx 4$ to 6 pA and $I^-_{QD} \approx -7$ to -10 pA (Fig. 4.1b). We proceed now with the identification of the energy scales:

- **The charging energy**: It is only possible to give a lower limit for the value E_U, as a single degeneracy point is accessible in our gate voltage range of ± 10 V. While it is tempting to consider that the QD's level depth, ϵ_0, increases uniformly with V_G along such whole range, gate offset switches can introduce discontinuities in the $\epsilon_0(V_G)$ dependence (discussed in the following section). Sudden changes in the current background were observed at relative distances of 1.5 and 0.6 V from V^0_G. By assuming a constant charging energy and gate coupling parameter, we obtain a minimum value of $E_U \geq 1.5 \times \alpha_G = 174$ meV.
- **The level spacing**: Although many excitations are present in this device, that one intersecting the diamond edges around $V_B = \pm 5$ mV display a stronger intensity (marked with black arrows in Fig. 4.1a). According to the expression derived in Ref. [1], a level spacing of $E_\delta \sim \frac{2\pi^2\hbar^2}{mk_F V} = 5$ meV corresponds to a Au particle with a radius of about 3 nm. While this expression is only qualitatively correct, the order-of-magnitude agrees with the 5 nm of average size of the Au particles in the commercial solution deposited in the samples.
- **The SC order parameter**: The SC gap present in both leads generates a SC-induced spectroscopic gap of magnitude $\Omega_{SC} = 2\Delta_S + 2\Delta_D$ appearing around zero-bias in the characteristic curves of the SC-QD-SC transistor, along the entire V_G range of the transport map. Such spectroscopic gap present an homogeneous value $\Omega_{SC} = 1.00$ meV in the device $\mathcal{S}_1$. However the SC gap of each lead cannot be extracted individually.
- **The thermal energy**: A thermal energy of $k_B T = 7$ μeV corresponds to the sample temperature of 80 mK at which these measurements were acquired. The conductance peak integrating the DE$^+$ displays a FWHM of 88 μeV (see inset in Fig. 4.1b).
- **The tunnel couplings**: From the direction of the coupling asymmetry ($\gamma_D > \gamma_S$) together with the asymmetry of the sequential current at the single-level conduction regime ($|I^-_{QD}| > |I^+_{QD}|$), this degeneracy point would be ideally expected to be described by Eqs. 1.2.34, leading to a coupling asymmetry on the order of $\gamma_D \sim 10\gamma_S$. However, the presence of such many excitations, together with the SC state of the leads, can introduce dramatic deviations from the simple sequential model. In general, the Green-function cotunneling model is required for a precise determination of the couplings from measurements in the SC state of the junction [38].

TRANSPORT MAPS OF ASYMMETRICALLY COUPLED DEVICES

The pair of YSR resonances emerging inside the spectroscopic gap, Ω_{SC} at one side of the degeneracy point shown in the transport map of devices $\mathcal{A}_1, \mathcal{A}_2, \mathcal{A}_3$ and $\mathcal{A}_4$ (Fig. 4.2) reveals a strong coupling asymmetry present in these junctions. The parity of the QD occupancy at both sides of the degeneracy point (respectively located at $V^{deg}_G = 0.4, 2.2, -0.8$ and 4.12 V, indicated by black dotted lines) can be determined straight away, as YSR resonances are caused by the competition between superconductivity and Kondo effect, the latter exclusively manifesting at odd charge states. The conductance background measured well inside the even blocked diamond is respectively found to be respectively being $G_{\text{Bgnd}} = 6.5, 8.6, 0.4$ and 1.1 in units of $(2e^2/h) \times 10^{-4}$, corresponding to $R_{sh} \approx 20, 15, 300$ and 120 MΩ. The enhancement of cotunneling processes caused by Kondo effect at the odd blocked-diamond originates a conductance background with a slight dependence on V_B and V_G at the odd-parity side of V^{deg}_G. While Ω_{SC} is clearly identifiable along the entire V_G-range, the characteristic diamond structure appears blurred (clearly visible only in devices $\mathcal{A}_1$ and $\mathcal{A}_4$) and the four DEs that integrate it display a strong asymmetry, being one of them much more intense than

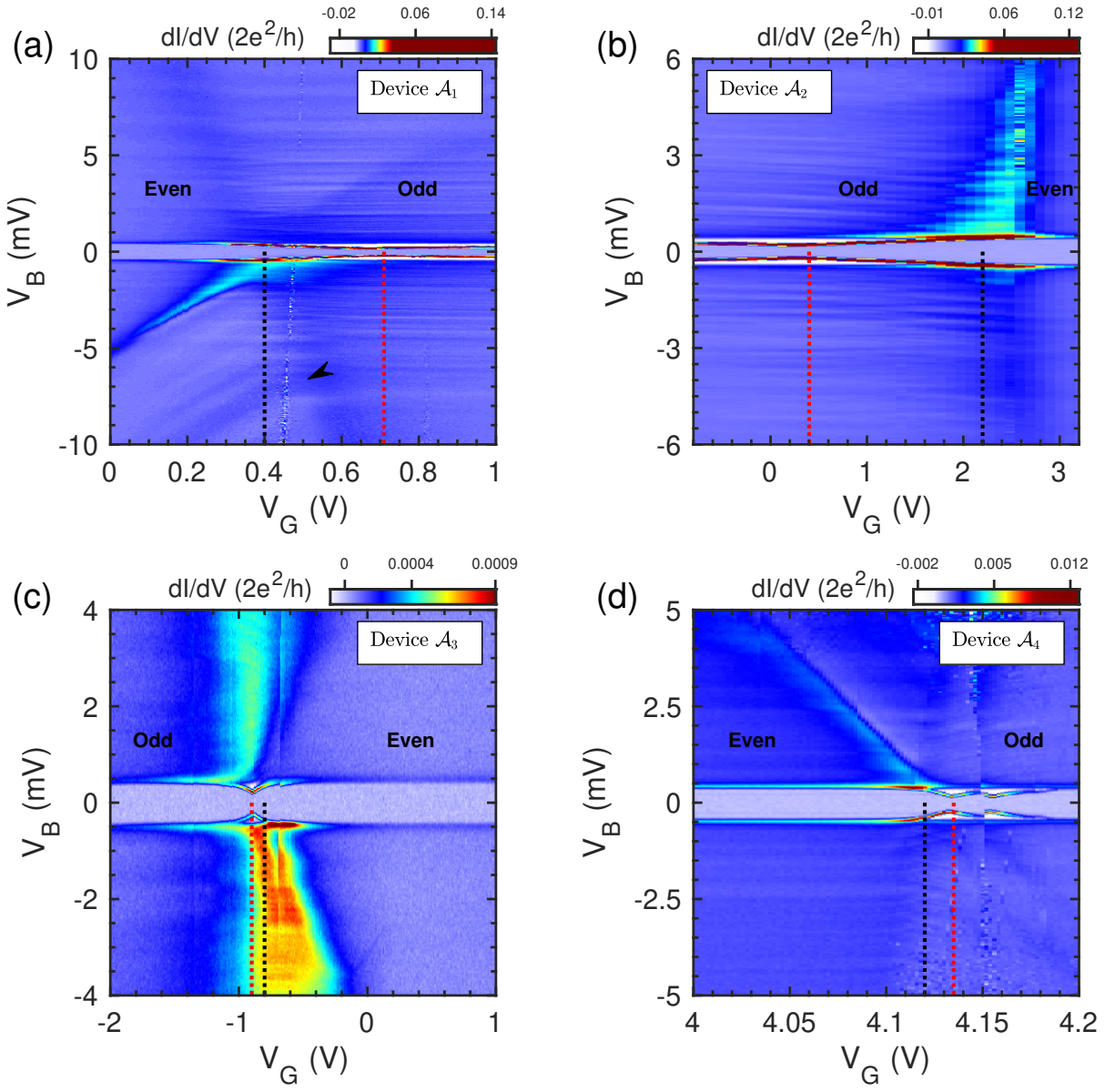

Fig. 4.2: dI/dV_B maps as a function of V_G and V_B, measured in devices $\mathcal{A}_1$ (a), $\mathcal{A}_2$ (b), $\mathcal{A}_3$ (c) and $\mathcal{A}_4$ (d) at 80 mK, using the lock-in technique. A strong asymmetry in the coupling leads to the emergence of a pair of YSR resonances, which develop only at one side of the degeneracy points, V_G^{deg} (black dashed line), indicating the odd parity of the corresponding charge state. In all cases, the YSR display a crossing, signaling the gate position of the singlet⇄doublet transition, V_G^{QPT} (red dashed line).

the others. In fact, it can be noticed that this enhanced DE appears always at the even charge state, either for positive ($\mathcal{A}_2$ and $\mathcal{A}_4$) or negative V_B ($\mathcal{A}_1$ and $\mathcal{A}_3$). The origin of such asymmetries of the DEs is discussed in detail in section 4.2.1.

The YSR states stick out as the most intense feature in the dI/dV_B map of the four devices. The bias position of the resonances display a certain gate dependence, in all cases making a kink identifying the gate position of the singlet⇄doublet phase transition, or QPT (respectively located at $V_G^{QPT} = 0.71, 0.4, -0.9$ and 4.135 V, indicated by the red dotted lines). While the YSR resonances surpass the gap edge, merging into the continuum DOS in samples $\mathcal{A}_3$ and $\mathcal{A}_4$, they remain below the SC gap in samples $\mathcal{A}_1$ and $\mathcal{A}_2$. Such distinct behavior can be linked to different relative values of the energy scales involved in the interplay between Kondo effect and superconductivity (E_U, Δ and γ), determining the location of the QPT boundary (illustrated in Fig. 1.23). As equivalent aluminum constriction and metallic nanoparticles were employed in the fabrication of all the devices presented

in this chapter, we expect similar values of E_U and Δ. Nevertheless, electromigration can introduce large disparities in the coupling parameters from one sample to the other. Large E_U/γ and Δ/γ ratios lead to the predominance of the doublet-GS phase, reducing the effective gate range of singlet-GS phase (between V_G^{deg} and V_G^{QPT}) and causing the YSR states to reach larger energies at the center of the odd charge state, eventually surpassing the edges of the SC gap. A lower value of γ can then be attributed to devices $\mathcal{A}_3$ and $\mathcal{A}_4$, in comparison with devices $\mathcal{A}_1$ and $\mathcal{A}_2$, in good agreement with the larger magnitude that the conductance features present in the two latter samples (see color scales in Fig. 4.2). The faintness of the diamond structure caused by the enhancement of higher-order process hinders the extraction of capacitive parameters and energy scales in asymmetrically coupled samples. A relatively clear diamond structure is only present in device $\mathcal{A}_1$, allowing to identify the subsequent electronic excitation (black arrow in Fig. 4.2a) of $E_\delta \approx 6-7$ meV, similarly to device $\mathcal{S}_1$. The following sections are devoted to explain the methods employed to extract the energy scales of such asymmetrical Kondo-weakly coupled samples from the transport measurements.

4.1.2 Electrostatic gate-offset switches

The apparison of stochastic charge-offset switches in QD junctions introduce random variations of μ_{QD}, that result detrimental for the performance of the devices. Such switches are specially present in chemically-bounded molecular junctions, generally manifesting as stochastic jumps between different charge states during the application of a relatively high V_B. Several works have studied the subject in detail, identifying restructurations of the molecule-metal interface as responsible for the switching mechanisms [252]. While our samples are thought to be immune to such effects (as the QDs employed are not chemically linked to the electrodes but rather suspended in between them), a different kind of charge-offset switches, displaying a distinct behavior, appear commonly in QD transistors [253]. Gate switches constitute one of our main limitations for the accessible V_G-range and the sample-stability over a measurement.

The equilibrium charge state of a QD transistor is determined by the number of electrons, N, present at the dot for V_B and V_G being set to zero. A certain offset, N_{offset}, smaller than unity ($0 < N_{\text{offset}} < 1$, appearing in Eq. 1.2.13) is typically present in actual devices, shifting the apparison of a degeneracy point for a V_G value different from zero. While such offset has been neglected in the derivation done in chapter 1, it can be accounted for by simply including a voltage-independent term of the form $e^2 N_{\text{offset}}/C$ in Eq. 1.2.28. In our devices, we observe sudden variations of N_{offset}, altering the relative position of μ_{QD} in the V_G coordinate, being highly recommended to keep V_G stable, only varying it slowly in between the acquirement of the I-V_B curves for the measurement of a transport map. Different manifestations of such gate switches show up in our devices, categorized as:

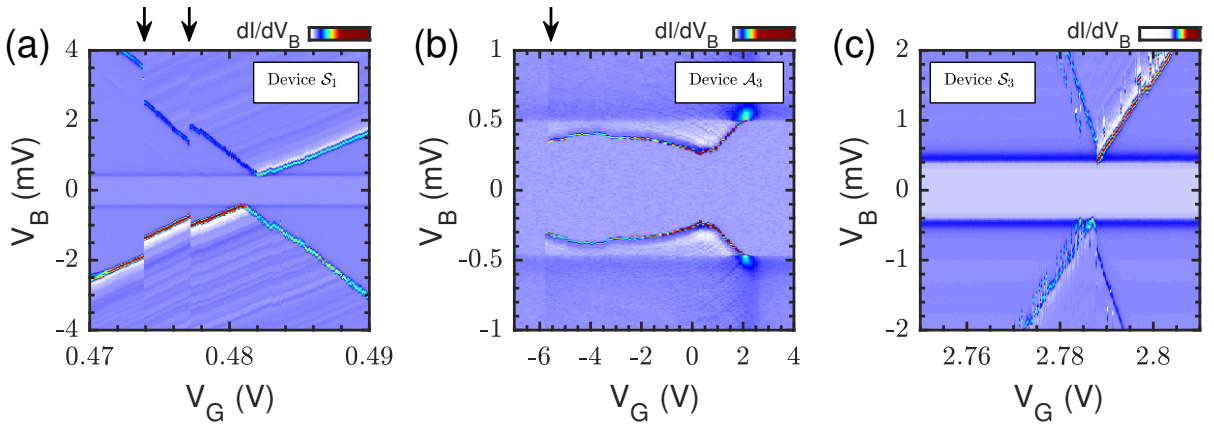

Fig. 4.3: Gate switches may manifest in the transport maps of our devices as purely stochastic (black arrows in a), occuring consistently at a certain V_G value (black arrow in b), or a persistently over a measurement (c, device $\mathcal{S}_3$ was measured in cryostat A and will be presented in Annex A).

- **Stochastic gate switches**: Appear randomly during measurements and introduce a certain μ_{QD}-shift, as shown in Fig. 4.3a. They are attributed to charge trapped in the oxide layer covering the gate electrode, occasionally refraining after keeping the sample cold for long enough (one or two weeks). This behavior was consistently present in devices $\mathcal{A}_3$ and $\mathcal{A}_4$ (apparent in Fig. 4.2c and d) making their characterization impossible in a reasonable time.
- **Permanent gate switches**: Appearing consistently at a particular V_G value, they are attributed to additional QDs around the nano-gap that change their charge state, modifying the electrostatic environment of the conducting QD (Fig. 4.3b). These switches preclude measurements above/below the specific V_G value, being the main reason that impede us to observe consecutive degeneracy points in devices owning a large gate coupling.
- **Persistent gate switching**: Involving typical times of a few seconds, they show up continuously over a measurement, typically inducing a switch in μ_{QD} between two close-by values (Fig. 4.3b). We ascribe this behavior to resist residues left over the sample surface, as it was found more often in devices kept under the protective resist layer for over a month or more.

4.2 Normal state characterization

The operation of Sionludi cryogenic setups allow to stabilize the sample environment either around 4 K, or at the base temperature (80 mK for cryostat B). Although the N-state of our devices can be accessed at 4 K, a great loss of the spectroscopic resolution, together with an increase of the background and noise, drastically reduces the measurement quality. To obtain well-resolved N-state transport maps at base temperature, we applied a perpendicular magnetic field (B) observing that, while certain SC-like features remain clearly visible for fields up to 40 mT (above the critical value for bulk Al of 10 mT, as expected for thin films), superconductivity was totally suppressed at 60 mT. Consequently, the YSR excitations present at the odd charge state of devices $\mathcal{A}_1, \mathcal{A}_2$ and $\mathcal{A}_3$ (Fig. 4.4a, b and c) turn into the characteristic Kondo resonance at zero-V_B, appearing unperturbed at such low B values (Fig. 4.4d, e and f). While device $\mathcal{A}_3$ exhibits a faint resonance, stemming from the relatively small value of γ in this sample, the prominent Kondo ridge arising in $\mathcal{A}_1$ and $\mathcal{A}_2$ allows for an exhaustive characterization of the Kondo phenomenon present in these devices. Sample $\mathcal{A}_1$ has been the subject of a more complete study, while we also include the analysis performed in device $\mathcal{A}_2$ for comparison. The Kondo spectrum in these two samples is examined together with the asymmetries arising at the diamond edges, at the first part of this section (4.2.1). Then, we compare the conductance measurements of device $\mathcal{A}_1$ with NRG simulations that reproduced qualitatively the finite-bias asymmetries (4.2.3). Finally, we present the method followed for the extraction of $k_B T_K$, determining its gate modulation (4.2.4).

4.2.1 Kondo spectrum analysis

The usual spectrum characterizing the Kondo effect appearing in a system composed by a magnetic QD tunnel-coupled to a N-state lead consist in a resonance at $V_B = 0$, as described by Anderson's model. The combination of Kondo effect with sequential tunneling originates strong asymmetries in the intensity and width of the two DEs (DE$^{\pm}$ for $\pm V_B$) displayed in the I-V_B or dI/dV_B-V_B curve at an even charge state. Actually, such asymmetries are present in the conductance maps of many works in the literature measuring different kinds of asymmetrically coupled QD junctions (like devices contacting CNTs [14, 25, 43], NWs [42], molecules [107, 105] or semiconducting QDs [31]). However very few of these studies focus on this aspect. Such asymmetries are specially remarkable in our samples: out of the four edges conforming the diamond structure (DE$^+$ and DE$^-$ both at the even and odd side of charge degeneracy) only DE$^-$ at the even side constitute a well developed peak of conductance in the N-state map of device $\mathcal{A}_1$ (Fig. 4.4d). Differently, both DEs at the even side of device $\mathcal{A}_2$ emerge as widely broadened peaks (Fig. 4.4e), hiding the odd-side DEs and surpassing the conductance of the zero-V_B Kondo resonance.

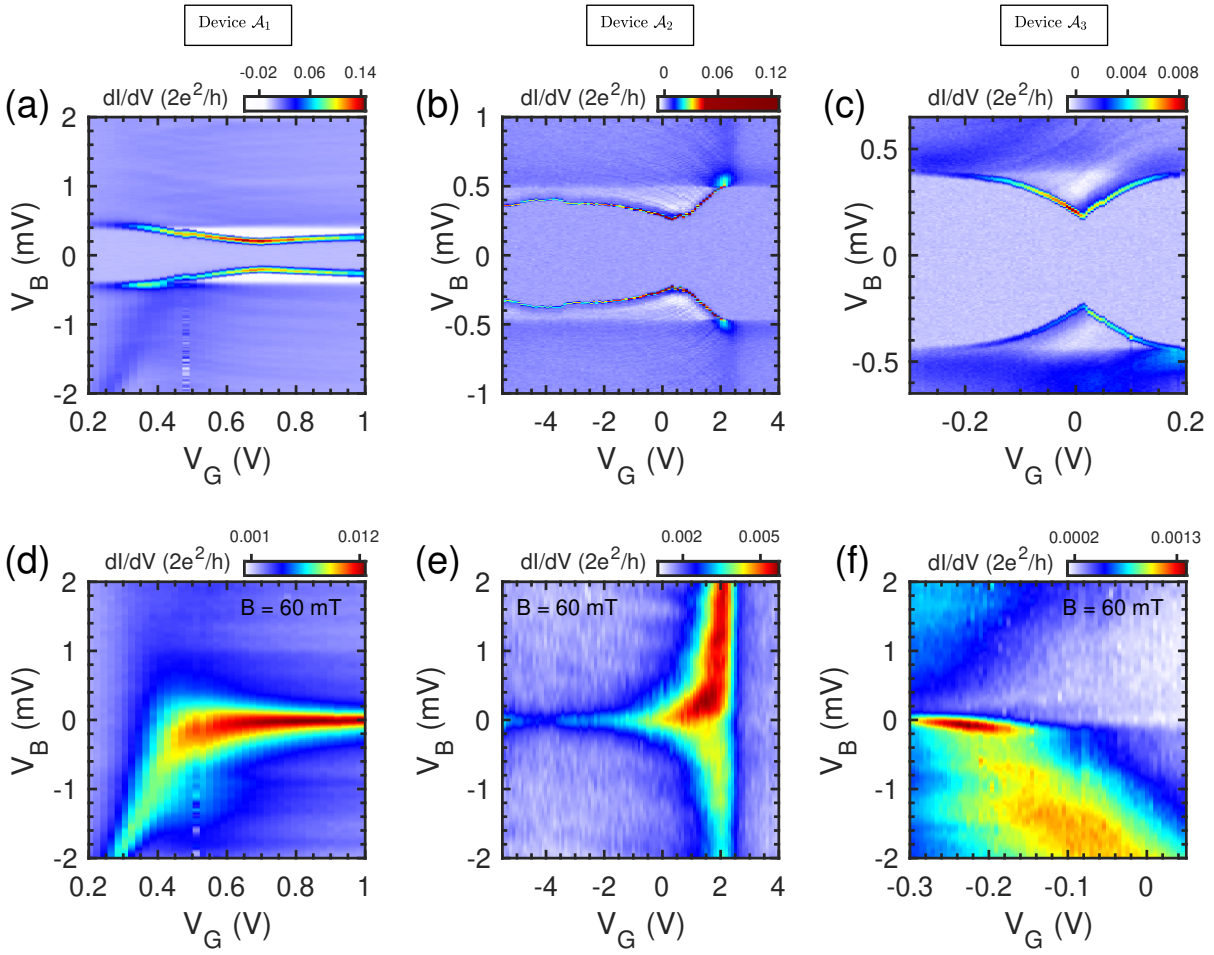

Fig. 4.4: dI/dV_B maps of devices $\mathcal{A}_1, \mathcal{A}_2$ and $\mathcal{A}_3$ acquired at base temperature in the normal (respectively a, b and c, obtained by applying a perpendicular B-field of 60 mT) and superconducting state (respectively d, e and f).

A different view illustrating this behavior is provided by slicing the transport maps into dI/dV_B-V_B curves at the different V_G values (Fig. 4.5a). We proceed to characterize the resonance's features (the maximum value of the conductance peak, G_{max}, and its full-width at half-maximum, FWHM) along its evolution from its appearance at zero-V_B inside the odd diamond into the enhanced-DE at the even diamond[2]. As shown in Fig. 4.5b and c, the zero-V_B resonance reaches stable line-shape well inside the odd diamond at both samples, where G_{max} and the FWHM saturate, indicating the V_G-range of the Kondo regime. While the G_{max} of the zero-V_B resonance (referred to as G_0) is expected to reach values similar to the quantum of conductance, $2e^2/h$, for symmetrical couplings, a strong renormalization of the conductance maximum is caused by the weakly-coupled lead. The corresponding expression for the maximum conductance of the zero-V_B resonance derived in Anderson's model (Eq. 1.2.48) can be approximated in the asymmetric-coupling limit ($\gamma \gg \gamma_W$) as:

$$G_0 = \frac{2e^2}{h}\frac{4\gamma_S\gamma_D}{(\gamma_S+\gamma_D)^2} \approx \frac{8e^2}{h}\frac{\gamma_W}{\gamma}. \tag{4.2.1}$$

A relation between the coupling parameters can be obtained by plugging the saturation value of G_{max} at the Kondo regime, corresponding to $G_0 = 0.0125$ for device $\mathcal{A}_1$ and $G_0 = 0.0015$ for $\mathcal{A}_2$ (measured in units of $2e^2/h$), as seen in Fig. 4.5b and c. The respective relations obtained for both samples, $\gamma \approx 300\gamma_W$ and $\gamma \approx 2700\gamma_W$.

[2] A constant conductance background of $G_{\text{Bgnd}} = 1.4 \times 10^{-3}(2e^2/h)$ was subtracted from the spectra of device $\mathcal{A}_2$, corresponding to the conductance baseline at the even diamond. The background is negligible for device $\mathcal{A}_1$.

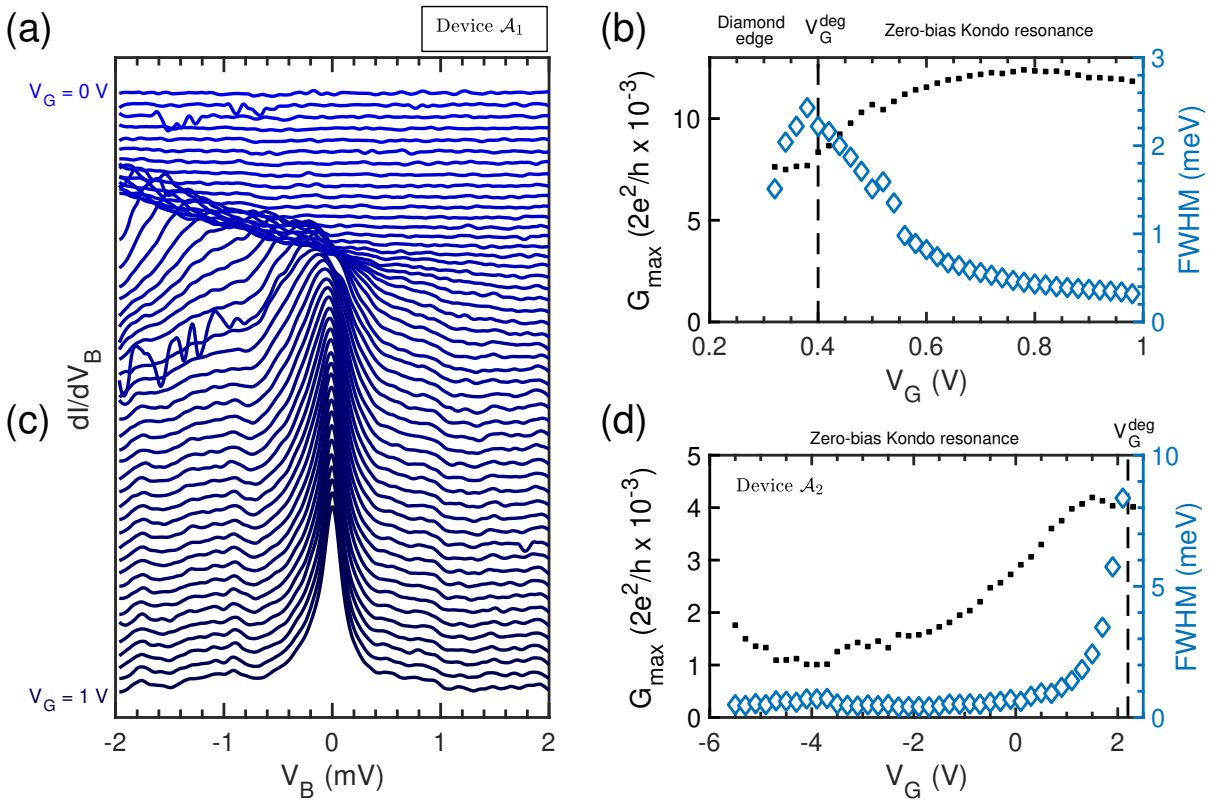

Fig. 4.5: (a) dI/dV_B spectra at different V_G for device $\mathcal{A}_1$ allowing for the extraction of the (b) gate-dependence of the corresponding resonance peak maximum and FWHM. (c) The same extraction performed in device $\mathcal{A}_2$. Vertical dashed lines indicate the position of charge degeneracy, V_G^{deg}, separating even and odd charge states.

4.2.2 Coulomb diamond analysis in the normal state

While most of the studies focus on the Kondo regime, deep inside the odd charge state, a reduced attention has been paid to the MV regime, around V_G^{deg}, and to the characteristics of the Coulomb-diamond conductance structure. By taking into consideration the usual asymmetric-biasing configuration arranged in experiments (applying V_B to the source lead, S, while keeping grounded the drain lead, D) together with asymmetric tunnel and capacitive couplings, *Aligia et al* demonstrated different characteristics (G_{max}, FWHM and V_B location) are expected for the four DEs around a degeneracy point [254] (DE$^+$ and DE$^-$, appearing both at the even and odd side of V_G^{deg}). In their study, they consider a QD Kondo-coupled to D and weakly-coupled to S, described from the perspective of Anderson's model. While the application of a voltage is considered to induce a positive displacement in the corresponding chemical potential at their work, we adopt the opposite convention here, taking $\mu_S = -eV_B$ and $\mu_D = 0$, allowing for a direct comparison with experiments. The chemical potential of the QD, defined as the level depth with respect to the first degeneracy point of an unoccupied orbital in the QD (see section 1.2.4) can be expressed as

$$\epsilon_0(V_B, V_G) = \mu_{QD}(V_B, V_G - V_G^0) = -e\alpha_G(V_G - V_G^0) - e\alpha_B V_B = \epsilon_0^G(V_G) + \epsilon_0^B(V_B), \qquad (4.2.2)$$

separating its bias and gate components. As it is useful for understanding the following sections, we remind here the relation between the level depth and the distinct charge states of the QD, which is simplified as a single spin-degenerated orbital in Anderson's model: the first even diamond extends over $E_U > \epsilon_0 > 0$ (corresponding to an empty orbital), the following odd diamond appears between $0 > \epsilon_0 > -E_U$ (corresponding to the half-filled orbital at which magnetic character arises), and the next even diamond extends between $-E_U > \epsilon_0 > -2E_U$ (where the double orbital occupancy is reached). These three charge states are consecutively separated by two degeneracy points, respectively called V_G^0 and V_G^1 and signaling the transitions empty→half-filled and half-filled→doubly-occupied.

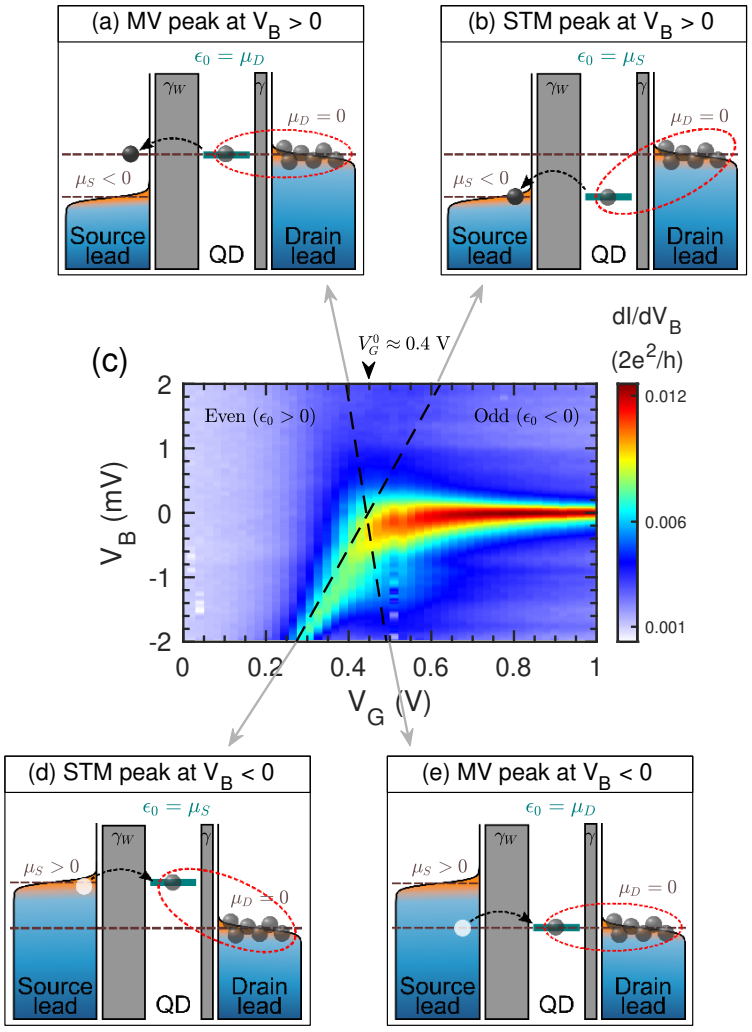

Fig. 4.6: Energy diagrams showing the energy-configuration of the chemical potentials at the four edges that integrate the diamond structure of device $\mathcal{A}_1$ (indicated by black dashed lines in c, obtained by the fits of the SC-state data shown in section 4.3.1). The degeneracy point, at $V_G^0 \approx 0.4$ V, corresponds to a transition of the QD occupancy from empty to half-filled, implying a level depth variation from $\epsilon_0 > 0$ to $\epsilon_0 < 0$. It can be deduced that the QD is strongly coupled to D, as a DE of stronger intensity appears for $V_B < 0$ at the even side of V_G^0, identified with the STM peak described in Ref. [254]. Following this conclusion, it is possible to assign the MV peak, defined at the alignment of the QD level with the Fermi level of the Kondo-coupled lead at μ_D (a and d), as the diamond edge of negative slope (DE^-), and the STM peak, which develops for the alignment of ϵ_0 with the Fermi level of the probing lead at μ_S (b and e), as the diamond edge of positive slop (DE^+).

The above expression (Eq. 4.2.2) allows for the implementation the effect of a bias lever arm, α_B, (as considered in the orthodox theory) into Anderson's model. While at zero bias, the level depth is fixed at ϵ_0^G by V_G, the application of a finite V_B across the junction induces both a change in μ_S and a variation in ϵ_0 with respect to its zero-bias value, of magnitude equal to ϵ_0^B, proportional to $\alpha_B = C_S/(C_S + C_D + C_G)$ (ranging between $0 < \alpha_B < 1$, acquiring values around 0.5 for ideally symmetric capacitive couplings $C_S \approx C_D \gg C_G$). Along the measurement of the characteristic curves of the devices, ϵ_0 is not fixed but changes linearly with V_B. The conductance peaks integrating the DEs (black dashed lines in Fig. 4.6c) appear when such floating level of the QD is aligned with μ at one of the leads. Due to the coupling asymmetry, different kinds of tunneling processes appear between the QD and each lead, being necessary to distinguish between the DE at which ϵ_0 is aligned with μ of the strongly coupled lead (called MV peak, Fig. 4.6a and e) and the weakly coupled lead (called STM peak, Fig. 4.6b and d). The following expressions for the width and maximum value of these two peaks at particular V_B values were obtained in Ref. [254] at the even diamond of a V_G^0-like charge degeneracy, explicitly showing the different dependences of both peaks' features on α_B:

$$\text{MV peak at } V_B = +e\alpha_G\widetilde{V}_G/\alpha_B e \begin{cases} \text{FWHM} = 2\gamma_T/\alpha_B e, \\ G_{max} = \alpha_B e C_T/\gamma_T, \end{cases} \tag{4.2.3}$$

$$\text{STM peak at } V_B = -e\alpha_G\widetilde{V}_G/(1-\alpha_B)e \begin{cases} \text{FWHM} = 2\gamma_T/(1-\alpha_B)e, \\ G_{max} = (1-\alpha_B) e C_T/\gamma_T, \end{cases} \tag{4.2.4}$$

where $\gamma_T = \gamma + \gamma_W$ and $C_T = C_S + C_D + C_G$.

These theoretical results are obtained by considering a weak coupling of the QD to S and a strong coupling to D, leading to $\alpha_B < 0.5$, at the even diamond on one side of the V_G^0-like degeneracy point. For such conditions, a higher and narrower STM peak was found to emerge at the even side of V_G^0 for $V_B < 0$[3]. The degeneracy point in device $\mathcal{A}_1$ is also V_G^0-like, as the magnetic behavior appears for higher V_G values (burying the unoccupied level below μ_D, becoming half-filled). At the even side, DE$^-$ displays a much larger intensity and smaller width, emulating the theoretical results. Thus, we can assign the strong coupling to the D lead in device $\mathcal{A}_1$, where S is the probing electrode. While concluding that the more intense DE corresponds to the alignment of ϵ_0 with μ of the weakly-coupled lead is rather counter-intuitive, the same kind of behavior is actually observed in device $\mathcal{S}_1$ found at the well-understood weak-coupling regime (Fig. 4.1). The higher spectroscopic resolution stemming from a weaker coupling (implying a smaller life-time broadening) results in a replication of higher intensity of the divergent coherence peak at the weakly-coupled lead along DE$^+$ (hence corresponding to the S lead also in this case), whereas the opposite DE$^-$ appears as a simple current step (revealed in the transport map by the lack of a band of negative differential conductance), as a consequence of a stronger coupling to D that broadens the level too much to resolve the line-shape of its coherence peaks.

At the subsequent degeneracy point of V_G^1, the STM and MV peaks still corresponds to DE$^+$ and DE$^-$ respectively , as it can be inferred from the work in Ref. [254]. Nevertheless, at the even side of V_G^1, the STM peak appears at $V_B > 0$ and the MV peak at $V_B < 0$. In fact, the transport map of sample $\mathcal{A}_2$ (Fig. 4.4d) shows that the QD occupancy transits from odd to even behavior as V_G is increased, identifying it as a change from half-filling to double occupancy of the resonant level and, therefore, recognizing the degeneracy point in this device as V_G^1-like. As the most intense DE at the even side of V_G^1 appears for $V_B > 0$, we can conclude that the QD is, once more, strongly coupled to D and weakly-coupled to S in device $\mathcal{A}_2$. A strong coupling to S is found in devices $\mathcal{A}_3$ and $\mathcal{A}_4$ as it can be obtained by deducing the nature of the degeneracy point (respectively V_G^1 and V_G^0) and observing the bias polarity at which the Kondo-enhance DE appears (Fig. 4.2c and d).

4.2.3 Comparison with NRG simulations

The Kondo model only provides an accurate description of the correlated QD-lead system around the Kondo regime of the odd magnetic charge state, defined as $-\gamma > \epsilon_0 > -(\gamma + E_U)$, but fails to describe it around the MV regime (close to V_G^0 and V_G^1) and at the even occupation diamonds. Alternatively, the DOS of the system can be obtained from simulations based on the NRG method along the full level-depth range, from empty to double occupancy (between $\epsilon_0 > 0$ and $\epsilon_0 < -E_U$). In addition, the conductance of a Kondo-weakly coupled junction system can be computed as well, following different approaches. In a close collaboration with our research group, *S. Florens* carried out several NRG simulations, obtaining the spectrum of the QD-lead correlated system, as well as calculations of the corresponding conductance measured by a weakly-coupled electrode following the model developed in Ref. [254]. Numerical results showed an accurate reproduction of the zero-bias experimental data of device $\mathcal{A}_1$, allowing for a more precise determination of the E_U/γ ratio present in this sample, while a qualitative agreement was obtained at finite-bias for the consideration of a bias lever-arm parameter.

The NRG simulation maps the DOS of the QD-lead hybrid along the entire range of level positions and energies for a relative scale of $E_U/\gamma = 6$ (Fig 4.7b). The spectrum of the QD-lead system is obtained at each level-depth value, considering a fixed level position at $\epsilon_0 = \epsilon_0^G$. The corresponding conductance map (Fig 4.8a) was calculated by considering a probing lead at a biasing voltage, V_B. In contrast to the fixed level positions in the DOS-map, the conductance calculation accounts for the flotation of the QD level, as described in Eq. 4.2.2, imposing a bias lever arm of $\alpha_B = 0.3$. In this sense, the quantity, ϵ_0^G, in the horizontal axis of Fig 4.7a indicates the QD level position at

[3] The STM peak appears at positive V_B in Ref. [254] due to the opposite sign of the chemical potential shift caused by the biasing voltage, defining the level depth as $\epsilon_0 = +e\alpha_G\widetilde{V}_G + e\alpha_B V_B$.

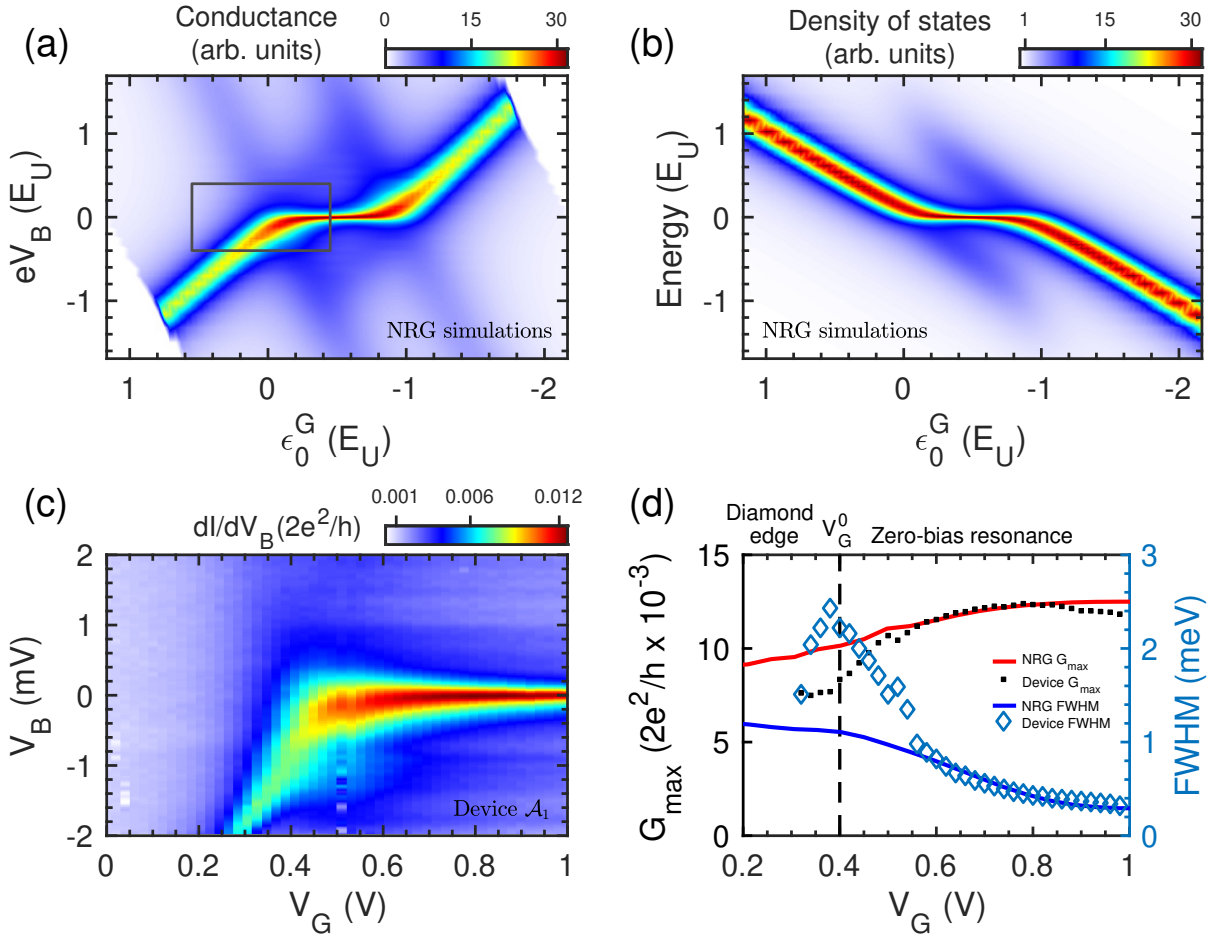

Fig. 4.7: (a,b) NRG maps of the DOS and conductance (G) of a QD Kondo-coupled to a N-state lead, obtained for a relative energy scale of $E_U/\gamma = 6$. A bias coupling parameter of $\alpha_B = 0.3$ was imposed for the calculation of the latter one. The region around V_G^0 at the G-map (highlighted with a square) corresponds to the experimentally accessible range of device $\mathcal{A}_1$ (c). (d) The G_{max} and FWHM values of the conductance resonance in the simulations is compared with the experimental data, showing significant deviations around V_G^0 (black dashed line) that sharpen at the DE.

$V_B = 0$. In contrast, finite biases induce a linear deviation of ϵ_0^B in the level depth with respect to ϵ_0^G, tilting the map with a slope determined by α_B with respect to the NRG-DOS map (the bottom-left and top-right corners lying out of the DOS-data range). For a direct comparison with experiments, the level-depth axis is reversed in both graphs, corresponding to increasing values of V_G (as $\epsilon_0^G = -e\alpha_G(V_G - V_G^0)$). By comparing both numerical maps, it can be observed that the conductance replicates the zero-V_B Kondo resonance in the NRG-DOS data at the odd charge state ($0 > \epsilon_0 > -E_U$), signaling the probing range of the asymmetrical QD junction. As the degeneracy points, at $\epsilon_0^G = 0$ (V_G^0) and $\epsilon_0^G = -1$ (V_G^1) are approached, the line-shape of the conductance resonance starts to deviate from the DOS spectrum as sequential transport comes into play. At the even charge states ($\epsilon_0 > 0$ and $\epsilon_0 < -E_U$) the resonance in the G-map evolves into a Kondo-enhanced diamond edge (corresponding to the STM peak of Fig. 4.6d), appearing at approximately opposite energies than the Kondo resonance at the DOS (identified, in a junction configuration, with the MV peak of Fig. 4.6a), reproducing the behavior displayed by our samples. In fact, the conductance calculation is performed by considering a voltage, V_B, applied to the weakly-coupled electrode (acting as S) while the QD is strongly coupled to the reference lead, D, emulating the configuration of device $\mathcal{A}_1$, and replicating its STM peak.

A substantial agreement with the experimental data (Fig 4.7c) is found at the corresponding range of numerical parameters, indicated by a gray square in Fig 4.7a. Both data sets can be compared by adjusting the renormalization factor of the numerical conductance with the experimental height of

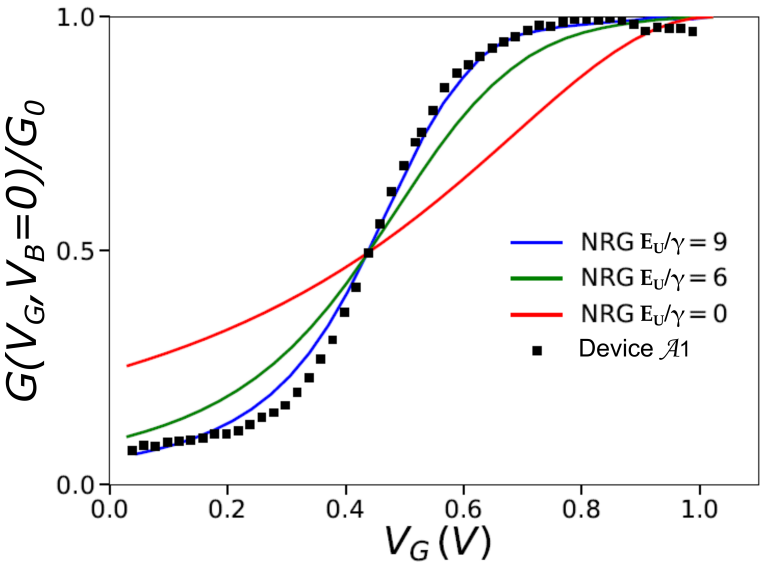

Fig. 4.8: (a) G-V_G traces at $V_B = 0$, obtained from NRG simulations for different values of the relative scale E_U/γ, are compared to the zero-bias conductance measured in device $\mathcal{A}_1$ (renormalized with the maximum conductance of the zero-V_B resonance, $G_0 = 0.0125 \times (2e^2/h)$). The reference points chose for adjusting the gate coupling are the center of the odd-diamond (extracted at $V_G = 1.08$ V from the k_BT_K fit shown in section 4.2.4) and the interception of the NRG curves with the experimental data at the midpoint of the Kondo ridge, $G_0/2$.

the zero-V_B resonance, as well as the adaptation of the horizontal axis by employing an experimental gate lever arm of $\alpha_G = 0.0089$ and locating the degeneracy point at $V_G^0 = 0.40$ V, as experimentally extracted in section 4.3.1. While the saturation of $G_{max} \to G_0$ and of the FWHM at the Kondo regime is well-reproduced by the numerical conductance (Fig 4.7d), significant deviations appear between the experimental data and the simulations when approaching the degeneracy point, growing larger as the even charge state is entered. This discrepancy is attributed to a certain disagreement between energy scale and bias coupling considered ($E_U/\gamma = 6$ and $\alpha_B = 0.3$) and the actual parameters in the device. Further NRG simulations were done for different E_U/γ values. To avoid additional inaccuracies induced by a differing bias coupling, we restrict the fitting range to the conductance trace at zero-V_B (Fig. 4.8). The steepness displayed by the Kondo ridge formation in the sample is missed by the NRG curve for $E_U/\gamma = 6$. However the trace obtained for $E_U/\gamma = 9$ captures these features, showing a quantitative agreement with the experimental data, fixing the energy-scale ratio for device $\mathcal{A}_1$. A slight overestimate of the conductance at the center of the diamond stems from the finite temperature of 80 mK at which the N-state map were acquired (just one order of magnitude below k_BT_K), as NRG simulations were done at the zero-temperature limit.

4.2.4 Extraction of the Kondo temperature scale

Changes in the line-shape of the zero-V_B resonance at different V_G indicates the variation of the Kondo energy scale, which characterizes the amplitude of the Kondo correlations. Such gate modulation of k_BT_K can be understood from its dependence on, $\epsilon_0(V_G, V_B)$, appearing explicitly in the expression derived by Haldane:

$$k_BT_K = \mathcal{C}\sqrt{\frac{\gamma E_U}{2}}\, e^{\pi\epsilon_0(\epsilon_0+E_U)/2\gamma E_U}, \tag{4.2.5}$$

The precise value of the prefactor $\mathcal{C}$ depends on the relative scale of E_U/γ and on the level depth, being well-defined ($\mathcal{C} = 0.182$) only for $E_U \gg \gamma$ and at the center of the odd charge state (for $\epsilon_0 = -E_U/2$), where the system reaches the particle-hole symmetry. Actually, its value also changes if the spin correlations extend over both leads of the QD junction (in which case Kondo effect is brought out of equilibrium when applying a finite V_B), or only one lead (configuration at which spectroscopy is performed). As these microscopic scales may not be easy to extract from measurements, numerous experimental works studying asymmetrically-coupled QD junctions at such spectroscopic configuration take k_BT_K as the FWHM of the zero-V_B resonance, sometimes multiplied by a prefactor smaller than unity (generally equal to 1/2). Alternatively, a more concrete criterion for the experimental extraction of k_BT_K, regardless of the energy hierarchy present in the sample, lies in the study of the temperature evolution of the zero-V_B resonance maximum, G_{max}.

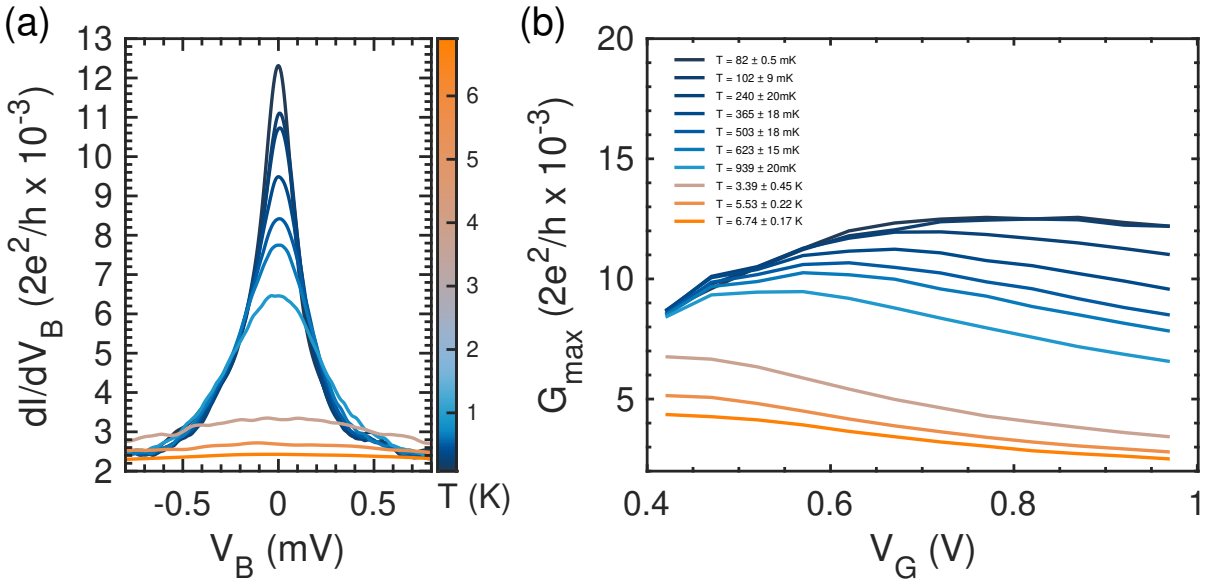

Fig. 4.9: (a) dI/dV_B-V_B curves taken at different temperatures for a gate value of $V_G = 0.97$ V. A non-uniform decay of the Kondo resonance with increasing temperature can be observed. (b) G_{max} values forming the zero-bias Kondo ridge along the V_G range of the odd charge state, measured at different temperatures.

Exposing the strongly coupled lead to an external parameter favoring an specific electronic distribution (like voltage differences, magnetic fields, temperature) have a disruptive effect on the Kondo correlations induced by the QD. While our samples $\mathcal{A}_1$ and $\mathcal{A}_2$ have both been subjected to a bias voltage and a magnetic field for the acquirement of the N-state transport maps, these parameters are not expected to disturb the formation of the Kondo cloud. On one hand, the V_B applied does not generate a current through the strongly coupled lead that can perturb the Kondo effect, but the entire voltage difference essentially drops at the tunnel junction, keeping both leads a constant electrostatic potential. On the other hand, the low B values between $60-75$ mT applied to quench away SC at the leads originates Zeeman splittings of energies $E_Z = g\mu_B B \sim 1$ μeV, in the same order of magnitude as the thermal energy at the base temperature of the cryostat ($k_B T \approx 7$ μeV), both of them been several orders below the actual Kondo energy of devices $\mathcal{A}_1$ and $\mathcal{A}_2$. Therefore, we can claim that Kondo effect in these two samples is at equilibrium. However, for increasing sample temperatures, the growing of electronic scattering rates in the metallic lead ($\sim T^2$) disturbs the screening cloud, eventually dissolving it for $T \gg T_K$. This effect manifest as a decline in the intensity of the zero-V_B resonance in device $\mathcal{A}_1$ (Fig. 4.9a). In fact, we observe that such decay does not take over the Kondo resonance uniformly as the temperature is increased, limiting to a reduction of G_{max} between 0.08-1.5 K, and making the resonance to completely vanish above 2 K. Furthermore, the zero-V_B resonance exhibits a distinct reduction at different V_G values along the odd diamond. The entire Kondo ridge measured at different temperatures is shown in (Fig. 4.9b). This data has been selected from a set of transport maps, measured at constant temperatures ranging from 80 mK to 6K while applying a constant magnetic field of 72 mT (see Fig.F.2 in Annex F).

The NRG simulations carried out by *Costi et al* [92], allowed them to demonstrate that the conductance decay caused in the zero-V_B resonance caused by a certain disruptive effect characterized by an energy scale, E_x, depends exclusively on the ratio between this energy and $k_B T_K$. This constitutes the main reason why $k_B T_K$ is called an "universal" energy scale. Generic expressions of the form $G_{max}(E_x) = G_0\ F(E_x/k_B T_K)$ characterize the evolution of G_{max}, where the function, F, depends on the nature of the particular perturbation. Years later, *Goldhaber-Gordon et al* found an empirical formula systematically fitting the evolution $G_{max}(T)$ in NRG simulations [100, 101], expressed as

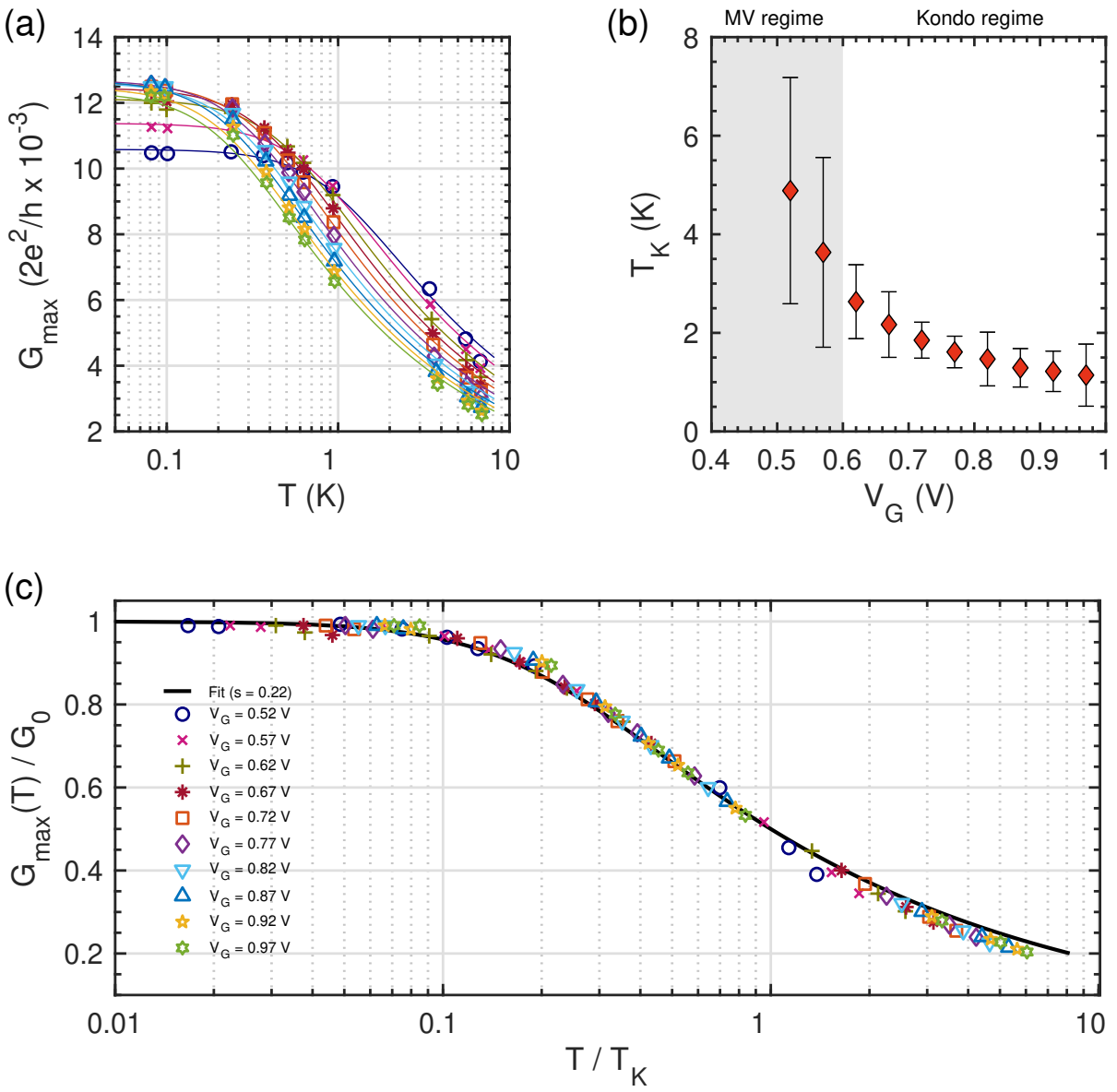

Fig. 4.10: (a) Linear square fits of the temperature evolution of G_{max} at different gate values are fitted to Eq. 4.2.6 using the least squares method. The colors identify the respective gate value. (b) Gate modulation of the Kondo scale obtained from the fits. The accuracy of the fitting formula is reduced at the MV regime, increasing significantly the error of the fit. (c) The data in panel a, collapse onto a single curve after proper rescaling, coinciding with Eq. 4.2.6 (black curve), indicating the nearness to the universal limit.

$$G_{max}(T) = G_0 \left(\frac{T^2}{T_K^2} \left(2^{1/s} - 1\right) + 1 \right)^{-s}, \tag{4.2.6}$$

obtaining best fittings for a phenomenological parameter value of $s = 0.22$ (if the QD spin is equal to 1/2). For $G_0 = 0.0125 \times (2e^2/h)$, we employed this formula to perform a fit of the experimental $G_{max}(T)$ at each V_G value, adjusting the free-parameter, T_K, by using the least-squares method (Fig. 4.10a). The resulting Kondo temperature of device $\mathcal{A}_1$ is found to vary between 1-5 K, well inside the V_G-range of the odd diamond (Fig. 4.10b). A considerable error is obtained at the MV regime, as Eq. 4.2.6 is not strictly valid at such range, while the error bars inside the Kondo regime mainly stem from the measurement at a highest temperature. After adequate rescaling, the experimental data collapse on a single curve (Fig. 4.10c), which actually coincides with the theoretical black curve (Eq. 4.2.6). These facts demonstrate that the Kondo effect developing in device $\mathcal{A}_1$ approaches the universal regime and is in virtual agreement with NRG simulations, implying a standard Kondo effect.

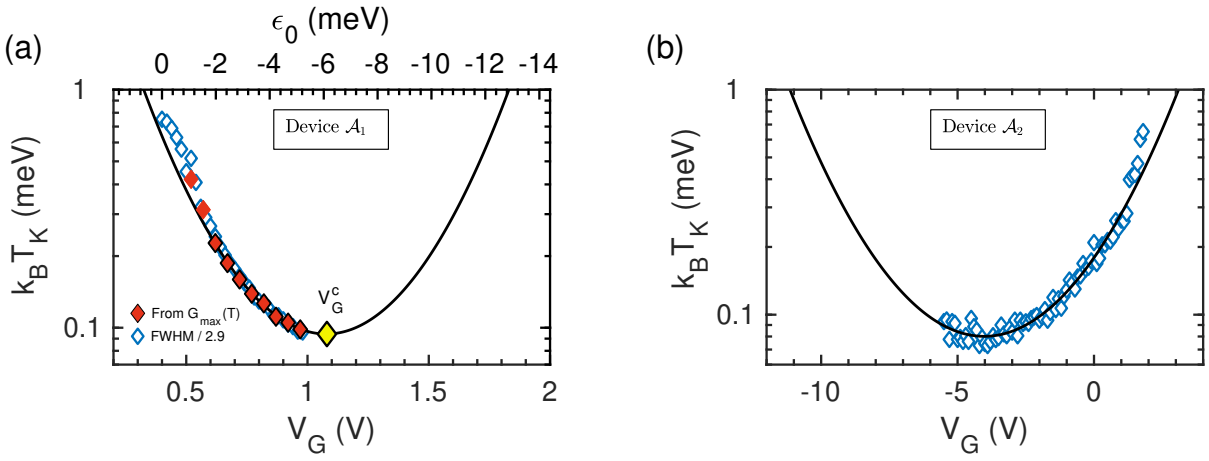

Fig. 4.11: (a) The FWHM of the zero-V_B resonance measured in device $\mathcal{A}_1$ at base temperature displays an identical V_G-dependence as k_BT_K extracted from the fits of $G_{max}(T)$. A parabolic fit of $G_{max}(T)$ (excluding the unframed markers lying at the MV regime) indicates the center of the odd diamond, at V_G^c (yellow marker). The precise relation between the level depth, ϵ_0 (horizontal scale at the top of the graph) and V_G could be established, for this sample, from the extraction of the gate coupling $\alpha_G = 0.0089$ and the degeneracy point $V_G^0 = 0.40$ V in section 4.3.1. (b) An identical fit was performed on the FWHM/2.9 data of device $\mathcal{A}_2$.

Contrarily to its usual application (the extraction of k_BT_K from the other microscopic scales obtained via NRG), we considered to employ Haldane's formula (Eq. 4.2.5) to fit the Kondo scale obtained from $G_{max}(T)$, as a method to estimate independently E_U and γ. While the gate modulation of k_BT_K in Fig. 4.10b is not expected to follow rigorously this expression as its derivation is done for a strict universal limit, the agreement of the experimental data with Eq. 4.2.6 indicate the nearness of device $\mathcal{A}_1$ to this regime. Such fit can provide us additional information on the extension of the odd charge state, as Kondo effect displays an identical behavior between its center (at V_G^c) and each of both degeneracy points (V_G^0 and V_G^1). We first extract the natural logarithm of Eq. 4.2.5, putting into manifestation the parabolic dependence of k_BT_K on the level depth:

$$\ln(k_BT_K) \sim \left(\frac{\pi}{2\gamma E_U}\right)\epsilon_0^2 + \left(\frac{\pi}{2\gamma}\right)\epsilon_0 + \ln(\text{const}). \tag{4.2.7}$$

The bias term of the level depth is not taken into consideration, as $G_{max}(T)$ is measured at $V_B = 0$, expressing it as $\epsilon_0 = \epsilon_0^G = -e\alpha_G(V_G - V_G^0)$. The gate coupling factor, $\alpha_G = 0.0089$, and the degeneracy point, $V_G^0 = 0.40$ V, are extracted independently in section 4.3.1. By restricting the fitted $G_{max}(T)$ data to the Kondo regime (black-framed orange markers in Fig. 4.11a) a parabolic fit of $\ln(k_BT_K)$ was performed using the least squares method, obtaining values of $E_U \approx 12$ meV and $\gamma \approx 2$ meV. In addition, the minimum of the fitting parabola signals the gate position of the center of the odd-charge state, located at $V_G^c \approx 1.08$ V (yellow square in Fig. 4.11a).

Actually, we found that the FWHM of the Kondo resonance measured at base temperature follows an identical V_G-dependence than k_BT_K, both data sets overlapping for a multiplicative factor of $k_BT_K = \text{FWHM}/2.9$, indicating a variation of k_BT_K between 90-750 μeV (1-8 K), together with the equivalence of both quantities close to the universal regime. The same multiplicative factor was employed to extract the Kondo scale of device $\mathcal{A}_2$ from the V_G-dependence of its FWHM, obtaining a k_BT_K covering a range of 80-500 μeV (1-6 K), slightly below sample $\mathcal{A}_1$. An identical parabolic fit was also performed, leaving α_G as a fitting parameter, as it could not be determined independently for this sample. Energy scales of $E_U \approx 11$ meV and $\gamma \approx 1$ meV, and a much smaller gate lever arm of $\alpha_G \approx 0.0009$ were obtained from the fit, as well as the odd-diamond center, located at a gate value $V_G^c \approx -4.0$ V.

4.3 Superconducting state characterization

The pairing order established in the leads in the presence of superconductivity oppose to the formation of the Kondo cloud, caused by Kondo effect for an even parity of the QD occupations. The singlet and doublet possible states of the QD-SC system conform its ground state (GS) and lowest excited state (LES), depending on the predominance of Kondo effect or superconductivity. The gate dependence of the magnitude of the Kondo effect (via the level depth) makes possible to tune the system through the transition (QPT) from the singlet-GS phase to the doublet-GS phase, manifesting in the spectrum as a crossing of the YSR resonances at zero-energy. We start this section by performing a fit of the Coulomb diamond edges of device $\mathcal{A}_1$, enhanced for the SC state of the leads (4.3.1). After that, we analyze the YSR spectrum and the evolution of its features for different gate voltages (4.3.2). Both studies, together with the analysis of the N-state data performed in the previous section enabled for the determination of the ensemble of capacitances, relevant gate positions and energy scales in samples $\mathcal{A}_1$ and $\mathcal{A}_2$. Then, we study the response of the YSR spectrum in device $\mathcal{A}_1$ for increasing magnetic B-field (4.3.3) and temperatures (4.3.4).

4.3.1 Coulomb diamond analysis in the superconducting state

The strong variation of the SC-DOS on energy around the Fermi level introduce several changes in the diamond structure appearing in the transport map for the SC state of the leads, as explained in section 1.3.2. On one hand, shifts in the position of the DEs are caused by to the opening of a spectroscopic gap with an extension of $\Omega_{SC} = 2(\Delta + \Delta_W)$ around zero-bias. In fact, the presence of an energy gap at the SC leads makes possible to get rid of thermal broadening effects, as the amount of quasiparticles above the gap vanish exponentially for a sample temperature such that $k_B T \ll \Delta$. On the other hand, the sequential current reproduces the divergences of the SC-DOS at the DEs, for the alignment of a discrete energy level in the QD with one the coherence peaks at one of the leads (Fig. 4.1). Not only thermal broadening is avoided, but spectroscopies are further sharpened due to such divergences, enhancing even more the resolution [38]. In good agreement with the above discussion, we systematically observe a considerable enhancement of the DEs intensities for the SC state of the leads, with respect to those appearing in N-state measurements. Indeed, while the DEs were barely noticeable in the N-state data of device $\mathcal{A}_1$, they emerge clearly as local conductance maxima in the transport map at the SC state, allowing to extract their location and obtain precisely the gate value of V_G^0 and some capacitive parameters of the junction from their slopes.

A peak-detection algorithm was employed to extract the local conductance maxima in the transport map of device $\mathcal{A}_1$ in the SC state, at the sectors of the four DEs (black dots in Fig. 4.12a). Linear fits (dashed lines) allowed to obtain the precise location of the DEs, revealing the complete diamond structure. By plugging the resulting slopes, of $\beta^+ = 0.0410$ and $\beta^- = 0.0115$, in Eqs. 1.2.26, we obtain a gate coupling parameter of $\alpha_G \approx 0.0089 \pm 0.0001 \approx 0.9\%$, and a coupling asymmetry to the transport electrodes of $C_D/C_S \approx 3.5 \pm 0.2$, indicating a stronger capacitive coupling to D in agreement with our previous analysis showing a stronger tunnel coupling this lead. By zooming at the degeneracy point area (Fig. 4.12b), it can be observed that the linear fits of the DEs at $V_B > 0$ (dashed lines) and $V_B < 0$ (dotted lines) respectively intersect at different gate values of $V_G = 0.396 \pm 0.001$ and $V_G = 0.406 \pm 0.001$ V. Such shift arises from the combination of the bias lever arm effect with the asymmetrical-biasing experimental configuration, explained in section 1.3.2, establishing the location of charge degeneracy at the midpoint: $V_G^0 \approx 0.401$ V (indicated by a red cross). Considering now the position of the odd diamond center at $V_G^c \approx 1.08$ V, taken as the minimum value of the parabolic fit of $\ln(k_B T_K)$ (indicated by a yellow diamond in Fig. 4.11a), the subsequent degeneracy point is expected to be found at $V_G^1 = V_G^0 + 2(V_G^c - V_G^0) \approx 1.76$ V. The entire odd-diamond structure can be reconstructed by duplicating the DEs' lines at V_G^1. Furthermore, by subtracting half the total gap $\Omega_{SC}/2$ from the bias component of each fit, the two lines of equal slope at each degeneracy point collapse into a single one that signals the DE appearing for the N state of the leads (illustrated in Fig. 4.12c and included in the N-state transport map shown in Fig. 4.6c). The resulting charging energy,

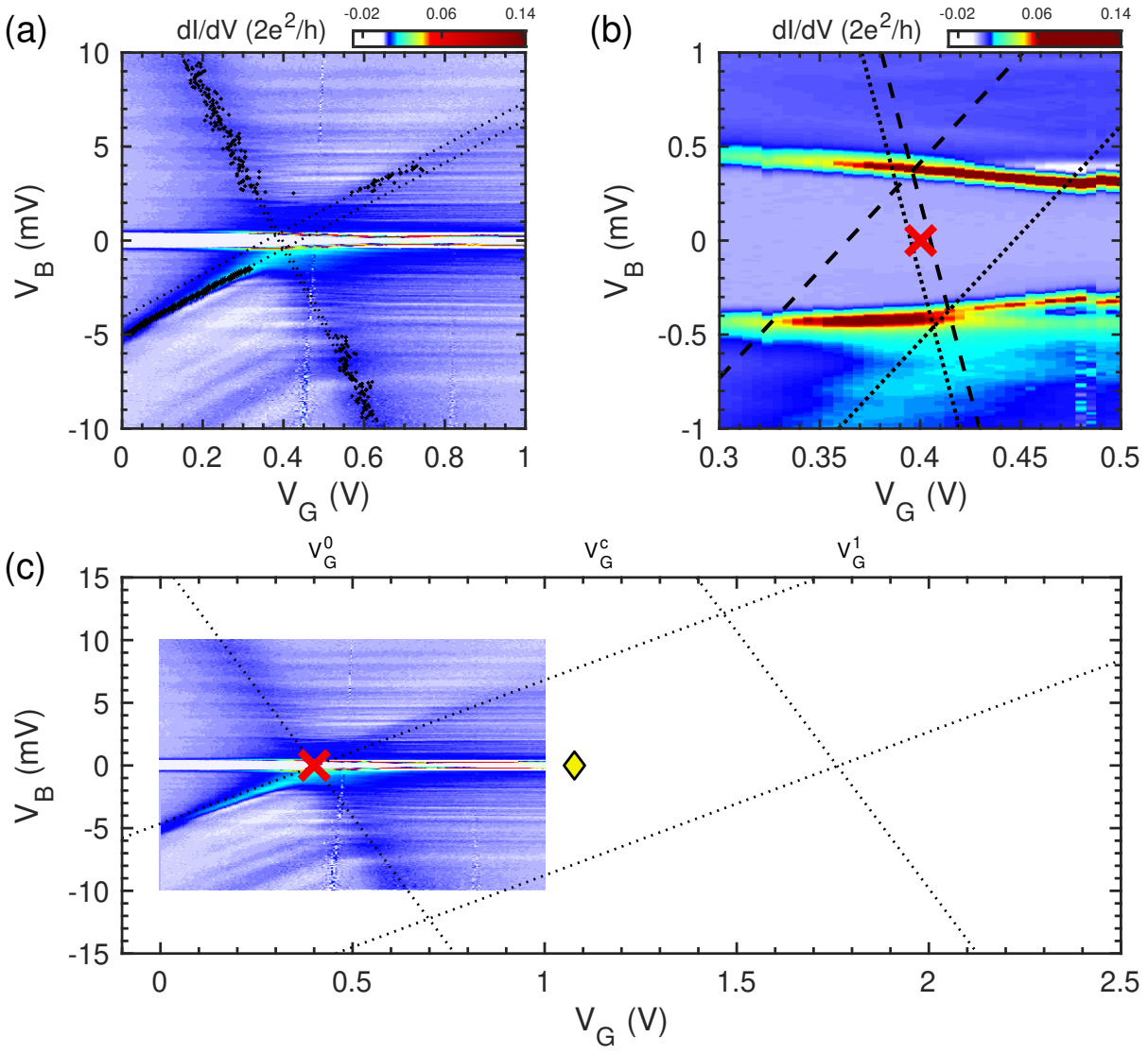

Fig. 4.12: (a) dI/dV_B map of device $\mathcal{A}_1$ in the SC state, acquired at base temperature at zero B-field. Linear fits (dotted lines) of the extracted local conductance maxima (black dots) indicate the location of the DEs. (b) Zoom-in at the degeneracy-point area, showing the intersection of the linear fits of the DEs at $V_B > 0$ (dashed lines) and $V_B < 0$ (dotted lines) with the SC gap edges at $V_G = 0.396$ V and $V_G = 0.406$ V, respectively, allowing to extract precisely the position of V_G^0 as the mid point at $V_G = 0.401$ V (red cross). (c) Taking as a reference the center of the odd diamond at $V_G^c \approx 1.1$ V (indicated with the yellow marker, as in Fig. 4.11a), the position of V_G^1 is extrapolated at $V_G \approx 1.76$ V. The entire odd diamond can be reconstructed by duplicating the linear fits at V_G^1 (here, $\Omega_{SC}/2$ has been subtracted from the vertical component of each fit, collapsing the four lines at the two DEs measured in the N state).

extracted either from the gate distance between both degeneracies as $E_U = -e\alpha_G(V_G^0 - V_G^1)$, or from the half-height of the diamond, collapse to a value of $E_U = 12.2 \pm 0.2$ meV. By combining its definition, $E_U = e^2/(C_S + C_D + C_G)$ (Eq. 1.2.18), with the expressions for the diamond slopes, it is then possible to extract values for the particular capacitive couplings: $C_D \approx 3.5\ C_S \approx 85.6\ C_G \approx 1.01 \times 10^{-17}$ F, and the bias coupling parameter: $\alpha_B = C_S/(C_S + C_D + C_G) \approx 0.22$. From the relative scale of $E_U/\gamma \approx 9$ obtained from the comparison of the N-state data with NRG simulations, we derive a strong coupling between the QD and the Kondo-coupled electrode of $\gamma \approx 1.4$ meV. Finally, the coupling ratio given by the renormalization of the zero-V_B Kondo resonance (Eq. 4.2.1) results in a weak coupling of $\gamma_W = \gamma/300 \approx 5\ \mu$eV.

While the characterization of the Kondo resonance and the derivation of the gate modulation of $k_B T_K$ could be also performed in device $\mathcal{A}_2$, the DEs at the odd side of the degeneracy point accessed in this device are completely buried, making impossible to repeat the linear fits in this sample.

Device	α_G	α_B	C_G (F)	C_S (F)	C_D (F)	V_G^0 (V)	V_G^c (V)	V_G^1 (V)
$\mathcal{A}_1$	0.0089	0.22	1.18×10^{-19}	2.88×10^{-18}	1.01×10^{-17}	0.401	1.08	1.76
$\mathcal{A}_2$	~ 0.0009	-	-	-	-	-10.2	-4	2.2

Tab. 4.1: Experimentally extracted capacitive parameters and particular gate voltages.

The demanding NRG simulations (in terms of computational power) were restricted to the specific parameter range of device $\mathcal{A}_1$. Nevertheless, a similar E_U/γ ratio was attributed to sample $\mathcal{A}_2$, stemming from the resemblance of the energy dispersion of the YSR resonances (Fig. 4.2a and b), and in agreement with the parabolic fit of $\ln(k_B T_K)$ leading to $E_U \approx 11$ meV, $\gamma \approx 1$ meV and $\alpha_G \approx 0.0009$ and $V_G^c \approx -4.0$ V for this device. Based on such gate coupling and diamond center position, together with the position of the accessible degeneracy point in this device ($V_G^1 \approx 2.2$ V), we can estimate the location of the out-of-range degeneracy point as $V_G^0 = V_G^1 - 2(V_G^1 - V_G^c) \approx 10.2$ V, which fulfills the relation of $E_U = e\alpha_G |V_G^1 - V_G^0|$ for the estimated values of E_U and α_G. All the extracted capacitive parameters and energy scales are respectively summarized in Tabs. 4.1 and 4.2.

4.3.2 Yu-Shiba-Rusinov spectrum analysis

We center our attention now on the characterization of the YSR resonances, measured at base temperature (around 80 mK) and in the absence of an external B field. As V_G is tuned inside the odd diamond, the YSR resonances detach from the edge of the total spectroscopic gap, Ω_{SC}, appearing at almost perfectly symmetric bias positions (V_B^{YSR}). While the conduction is completely suppressed below the resonances, for $|V_B^{YSR}| > |V_B| \geq 0$, a band of negative differential conductance appears between the YSR resonances and the total spectroscopic gap, for $\Omega_{SC}/2e > |V_B| > |V_B^{YSR}|$, as a consequence of the SC-DOS at the probing lead (clearly observed in Fig. 4.13a). The value of the total spectroscopic gap, $\Omega_{SC} = 2(\Delta + \Delta_W)$, appears around zero bias at the "even side" of charge degeneracy, where the entire SC spectral function is accumulated at the coherence peaks. In contrast, the YSR emerging at the "odd side" absorb most of this spectral function, greatly reducing the sharpness and intensity at the edges of Ω_{SC}. Extremely sharpened YSR resonances[4] arise in

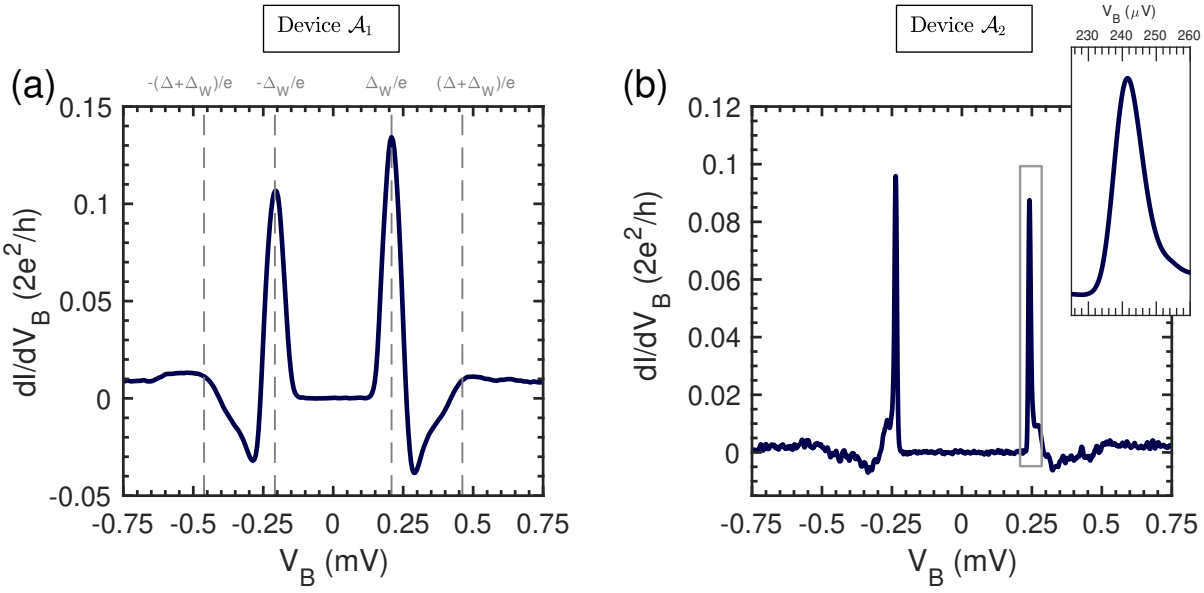

Fig. 4.13: (a,b) dI/dV_B-V_B curves of devices $\mathcal{A}_1$ and $\mathcal{A}_2$ acquired at the corresponding QPT gate positions of $V_G^{QPT} = 0.71$ and $V_G^{QPT} = 0.4$ V. The vertical, gray, dashed lines in (a) indicate the extraction of Δ and Δ_W from the peak-to-peak distances. The inset zooms into the YSR resonance delimited by the gray rectangle in (b).

[4] Reliable measurements of the YSR resonance heights required a reduced V_B sweeping speed of 1 μV/s

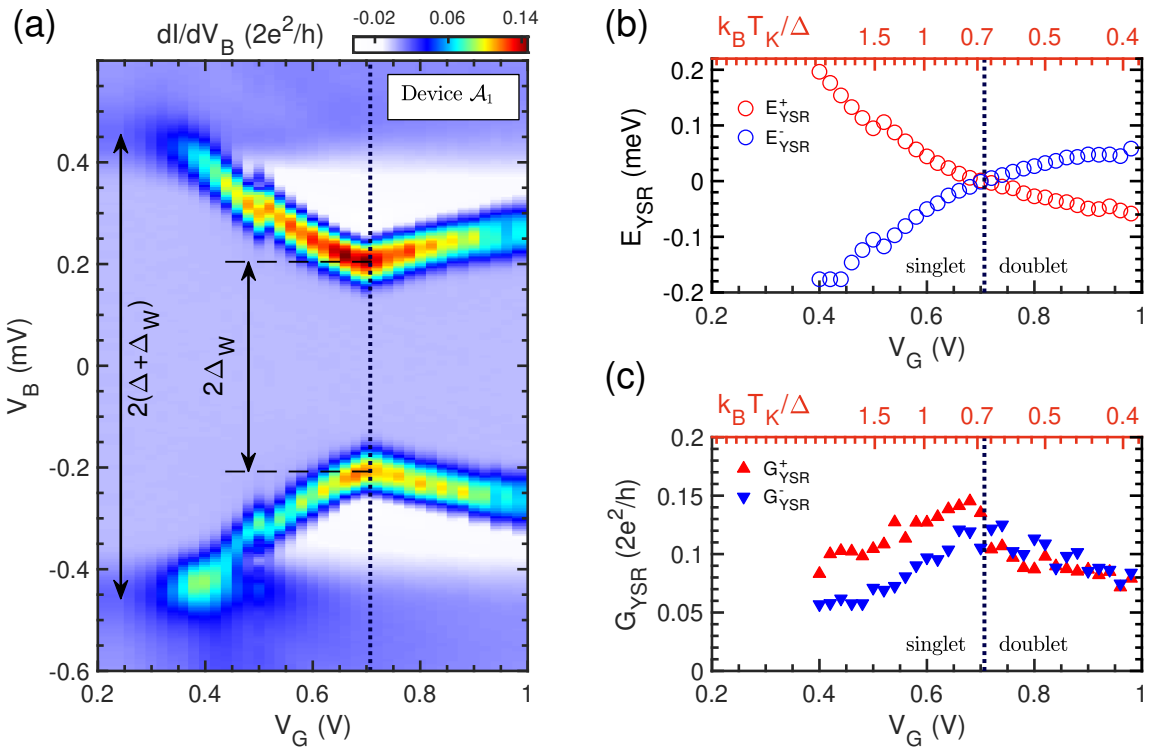

Fig. 4.14: (a) dI/dV_B map of device $\mathcal{A}_1$ zooming at the YSR resonances, allowing to extract their energy dispersion (b) and evolution of their peak intensity (c) as a function of gate voltage, or equivalently, k_BT_K scale. The vertical dashed line indicates the position of V_G^{QPT}, corresponding to the characteristic curve shown in Fig. 4.13a.

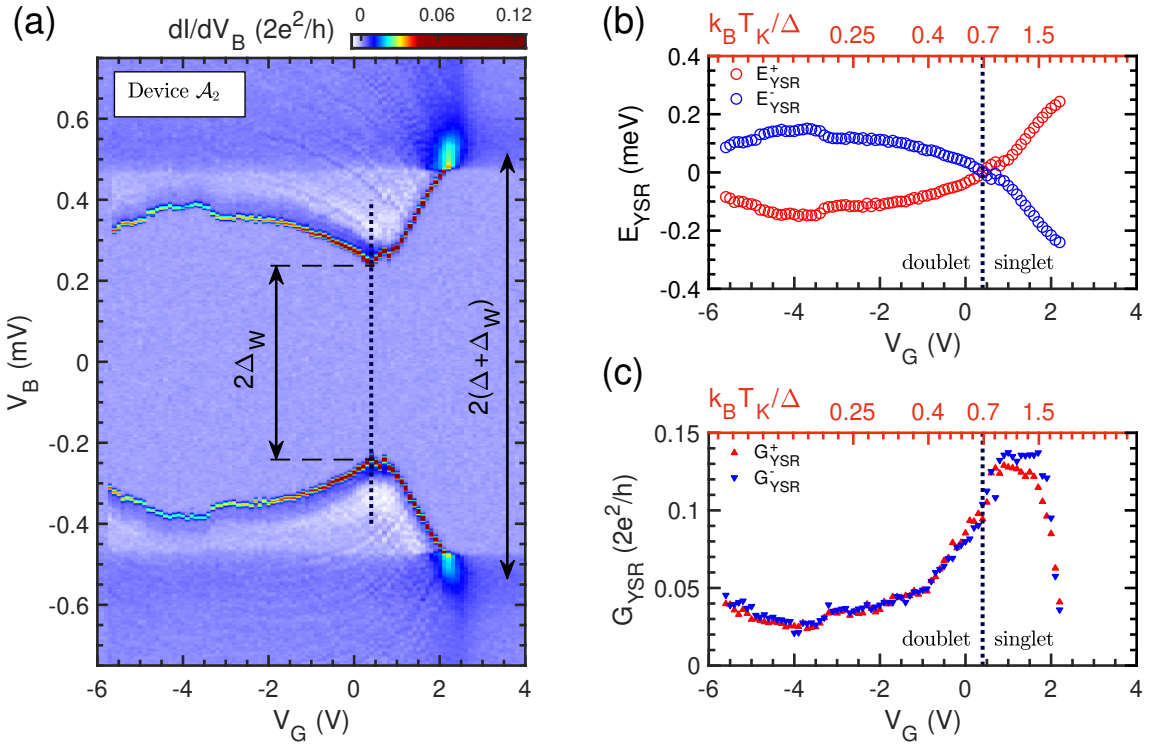

Fig. 4.15: (a) dI/dV_B map of device $\mathcal{A}_2$ zooming at the YSR resonances, allowing to extract their energy dispersion (b) and evolution of their peak intensity (c) as a function of gate voltage, or equivalently, k_BT_K scale. The vertical dashed line indicates the position of V_G^{QPT}, corresponding to the characteristic curve shown in Fig. 4.13b.

Device	E_U (meV)	E_δ (meV)	k_BT_K (μeV)	Δ (μeV)	Δ_W (μeV)	γ (μeV)	γ_W (μeV)
$\mathcal{A}_1$	12.2	5-7	90-750	248	203	1400	5
$\mathcal{A}_2$	~ 11	-	80-500	327	238	~ 1000	~ 0.4

Tab. 4.2: Experimentally extracted energy scales.

device $\mathcal{A}_2$ which has a lower value of γ_W with respect to device $\mathcal{A}_1$, displaying a FWHM between 8-9 μeV (Fig. 4.13b). Such reduced line-width demonstrate the spectroscopic power of all-aluminum electromigration junctions contacting metallic nanoparticles, allowing us to probe the YSR spectrum with an unprecedented resolution.

YU-SHIBA-RUSINOV SPECTRUM DEPENDENCE ON THE GATE VOLTAGE

The dependence of the YSR resonances on V_G can be appreciated in transport maps of devices $\mathcal{A}_1$ and $\mathcal{A}_2$ zooming at a low-V_B range (Figs. 4.14a and 4.15a, respectively). The bias position, $V_B^{\pm YSR}$, and the maximum conductance of both resonances were extracted along the accessible range by employing a peak-detection homemade algorithm. The crossing of the YSR states at zero-energy does not manifest as a crossing at zero-bias of the resonances due to the gapped SC-DOS at the probing electrode. Instead, $|V_B^{\pm YSR}|$ decreases when V_G is swept from the degeneracy point into the odd charge state, until it makes a kink at a minimum V_B. This feature identifies the gate location of the QPT, V_G^{QPT}, where the singlet$\rightleftarrows$doublet GS transition takes place, obtaining $V_G^{QPT} \approx 0.7$ for device $\mathcal{A}_1$ and $V_G^{QPT} \approx 0.4$ for device $\mathcal{A}_2$ (vertical dashed lines). Furthermore, the value of the SC gap in the probing lead, Δ_W, can be determined independently from the peak-to-peak distance of the YSR resonances in the spectrum acquired at V_G^{QPT} (Fig. 4.13a). The extraction of Δ_W at the crossing point also allows to determine the SC gap of the correlated lead, Δ, from the measurement of the total spectroscopic gap Ω_{SC}. The values of Δ and Δ_W obtained (indicated by vertical dashed lines in Fig. 4.13a) are given in Tab. 4.2, together with the other energy scales extracted in previous sections. Like this, the energies of the YSR states, $E_{YSR}^{\pm}$, can be extracted by subtracting Δ_W from $V_B^{\pm YSR}$, taking into account the sign inversion at the transition[5] (Figs. 4.14b and 4.15b). Minute deviations of $E_{YSR}^{\pm}$ occurring at certain gate voltages (at $V_G \approx 0.5$ and 0.92 V for device $\mathcal{A}_1$ and $V_G \approx 0.8$ and -3.4 V for device $\mathcal{A}_2$), were systematically present in all measurements acquired and are attributed to slight but persistent gate switches. Then we associate the conductance maxima extracted, to the corresponding YSR state at $E_{YSR}^{\pm}$, obtaining the gate-dependence of their peak intensities, $G_{YSR}^{\pm}$ (Figs. 4.14c and 4.15c). These peak intensities correspond to the spectral weights of the YSR states, $w^{\pm}$, renormalized by the tunnel coupling of the probing lead, γ_W. As in our case, the probing lead is in the SC state, the divergences at the coherence peaks enhance the intensity of such spectral features in the conductance measurement with respect to the rest of the spectra. It is therefore necessary to deconvolute the SC-DOS of the probe for obtaining precise values of $w^{\pm}$. However, we lack the tools for performing such treatment.

Keeping in mind that the Kondo energy scale is only approximately the parameter driving this transition, the correspondence between k_BT_K and V_G (Fig 4.11) is employed to derive the critical value of k_BT_K/Δ in devices $\mathcal{A}_1$ and $\mathcal{A}_2$ (orange axis in Figs. 4.14 and 4.15) found at $(k_BT_K/\Delta)_c \approx 0.67$ and 0.69, fairly coinciding for both samples (given the similarities in E_U, γ and Δ) and consistent with experiments on self-assembled QDs [12] (that also extract k_BT_K from the temperature dependence of the zero-bias Kondo conductance). By taking the Kondo scale as the FWHM/2 of the Kondo resonance, the YSR crossing point would be displayed around $(\text{FWHM}/2\Delta)_c \approx 0.97$ and 1.00, in good agreement with STM studies of magnetic molecules on SC substrates [10, 165, 147], as the SC-QD-SC systems in these works are very similar to those we obtained with our electromigration junctions (characterized by a large charging energy and an intermediate-coupling regime). The data

[5] Note that at the singlet phase, $E_{YSR}^{\pm} = eV_B^{\pm YSR} \mp \Delta_W$, whereas at the doublet phase, $E_{YSR}^{\pm} = eV_B^{\mp YSR} \pm \Delta_W$, relating each YSR state with the resonance of opposite bias sign due to their crossing at the QPT.

can also be rescaled to the theoretical definition of the Kondo energy (Eq. 4.2.5, using a constant prefactor of $\mathcal{C} = 0.182$ for the entire odd-diamond range), which leads to $(k_B T_K/\Delta)_c^{theo} \approx 0.26$. While predictions based on NRG simulations that implement such definition obtain a critical value around $0.3 - 0.4$ [113, 164, 158], the discrepancy is attributed to the reduced value of E_U/γ in our devices, constituting a regime where Eq. 4.2.5 is not strictly applicable.

Notably, multiple fainting replicas of the YSR states appearing for $|V_B| > |V_B^{YSR}|$ can be observed in the conductance map of device $\mathcal{A}_2$ (Fig. 4.15a). As mentioned at the end of section 1.3.1 structural disorder can lead to the apparison of spiky features at the DOS in the bands of aluminum, in principle, remaining at the SC state and appearing at energies above the gap in the quasiparticle DOS. Such irregular DOS can explain these additional features, relating them with a measurement artifact of the probe and emerging above the conductance baseline due to the high spectroscopic resolution of this sample.

PRECISE EXTRACTION OF THE GATE POSITION AT THE TRANSITION

For a precise extraction of the energies of the YSR states and the gate location of their crossing at the QPT, it is necessary to take into consideration the gating effect of the probing lead. The finite energy of the YSR states, $E_{YSR}^{\pm}$, requires the application of a finite bias, $V_B^{\pm YSR}$, to observe the corresponding resonances. By applying such V_B the level depth, ϵ_0, is displaced from its zero-bias value fixed by V_G at $\epsilon_0^G = -e\alpha_G(V_G - V_G^0)$, by an amount equal to $\epsilon_0^B = -e\alpha_B V_B^{\pm YSR}$ (Eq. 4.2.2). Consequently, the level depth is slightly different for the two YSR resonances measured at V_B^{+YSR} and V_B^{-YSR} in the characteristic dI/dV_B-V_B curve acquired at a constant V_G. In fact, the absolute values of V_B^{+YSR} and V_B^{-YSR} measured in sample $\mathcal{A}_1$, do not overlap completely (Fig. 4.16a) due to such flotation of the QD's energy level. For correcting the shear caused in the measurements by the bias lever arm, the V_G coordinate of each data points is to be replaced by the value of the bias-dependent level depth, as $e\alpha_G(V_G - V_G^0) + \alpha_B V_B^{\pm YSR}$, transforming the horizontal axis into $-\epsilon_0$. By employing the value of $\alpha_B \approx 0.22$ previously derived for device $\mathcal{A}_1$, we can correct the shear effect of such bias coupling, leading to the collapse of the energies of both YSR states into a single curve (Fig. 4.16b). Such treatment allows for a more accurate extraction of Δ_W and Δ in this device, and for the fitting of $E_{YSR}^{\pm}$ with calculations based on the renormalized YSR theory developed in Ref. [162] (see the supplemental material on Ref. [44] for further information). The previously obtained energy scales of sample $\mathcal{A}_1$ were employed in these calculations, carried out by S. Florens in a close collaboration with our research group, showing a very good agreement with the experimental data (black line in Fig. 4.16c). The theoretical curves, adjusted by taking the references set by the particular gate values

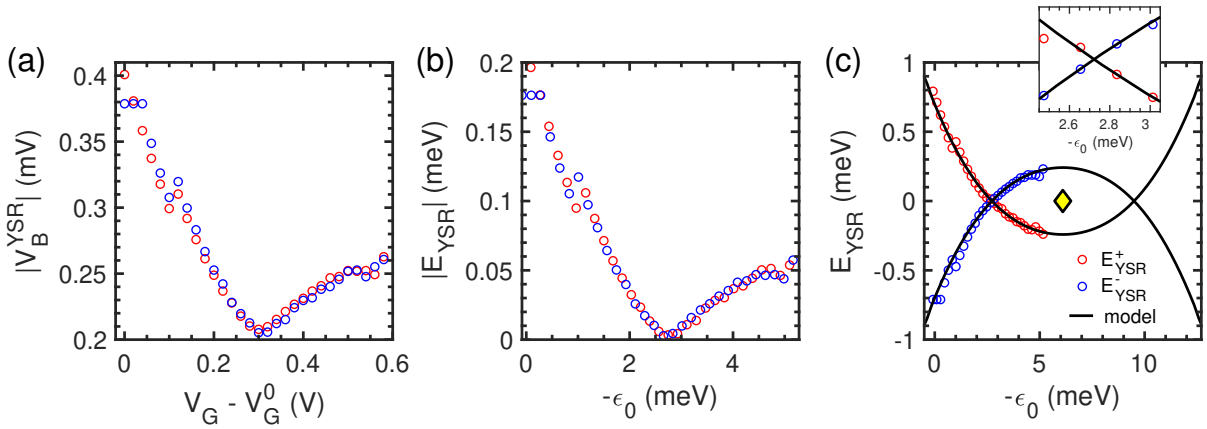

Fig. 4.16: (a) Absolute bias positions of the YSR resonances versus gate voltage. The two curves are not overlapping as a consequence of the shear induced in the measurement by the bias lever arm. (b) The separation between the two curves disappears when plotted against the level depth, correspondingly calculated by taking into account the finite bias at which each data point was measured. (c) The YSR energies are well fitted by the model developed in Ref. [162].

of the degeneracy point, $V_G^0 = 0.401$ V, and the center of the odd diamond, $V_G^c = 1.08$ V (yellow marker), reproduce the experimental data within a small error, enabling us to increase the precision of the QPT gate value, roughly obtained to be around 0.7 V in the previous analysis. The model displays the zero-energy crossing point taking place in a range of $-\epsilon_0^{QPT} \approx 2.7 - 2.75$ (see inset in Fig. 4.16c), or equivalently, $V_G^{QPT} = -e\alpha_G\epsilon_0^{QPT} \approx 0.705 - 0.71$ V.

4.3.3 Magnetic field dependence of the YSR spectrum

Once the transport characteristics of the Kondo-weakly coupled devices have been analyzed and understood, we move towards studying the effect that the external magnetic field exerts on the YSR spectrum. This study was conveniently restricted to device $\mathcal{A}_1$, as more complete and precise set of energy scales and physical parameters could be extracted for this sample. We start this examination by measuring the V_G-V_B transport map of this sample at several constant B-fields (the raw data is shown in Fig.F.3 in Annex F), allowing us to extract the gate dependence of the energy of the YSR states and intensities of both conductance resonances for each B-field value (Fig. 4.17a and b, respectively). Equivalently to the analysis performed at zero-field in the previous section, we start by extracting the values of Δ_W and Δ, respectively from the resonances' crossing point at the QPT, and the total spectroscopic gap ($\Omega_{SC} = 2\Delta + 2\Delta_W$) measured at the even side of V_G^0 (Fig. 4.17c). The SC energy gaps at both leads remain stable for low B-field values (presenting a tiny increase, attributed to the SC-DOS broadening induced by the B field [255]), starting to decay above 20 mT. The energies of the YSR states were equivalently obtained by subtracting Δ_W from the experimental data. As the effect of a magnetic field was not implemented in the calculations previously employed to fit the gate dependence of $E_{YSR}^{\pm}$ at zero field (shown in Fig. 4.16c), spline interpolations on $E_{YSR}^{\pm}(V_G)$ were performed (solid lines in Fig. 4.17a), improving the precision of the limited gate resolution of the measurements for the extraction of V_G^{QPT} (vertical black lines). The evolution of V_G^{QPT} with B field (Fig. 4.17d) is caused, in first instance by the gradual suppression of superconductivity, which reduces the effective pairing energy, Δ, and consequently, the value of k_BT_K at which the transition takes place, as the critical value of the relative scale k_BT_K/Δ (found to be about 0.67 for sample $\mathcal{A}_1$) is expected to remain constant. In fact, the reduction of Δ above 20 mT effectively drives the QPT to higher values of V_G (or lower values of k_BT_K) towards the center of the odd diamond. However, it can be observed that, at low B fields, V_G^{QPT} moves towards the opposite direction, tracing a slight but clear upturn that crosses with the zero-field value around 14 mT. Such effect arises as a consequence of the Zeeman splitting of the doublet state.

With the application of an external magnetic field, the two spin projections of the doublet state are Zeeman-split into at energies of $E_Z = \pm g\mu_B B/2$ (where μ_B is Bohr's magneton and g is the Landé factor). If the SC-QD system is tuned into the doublet-GS phase and subjected to an external B field, the spin at the QD lies in the spin configuration of lowest energy (at equilibrium and low temperatures such that $k_BT \ll E_Z$). As the excitation of the system with the probing lead (reaching the corresponding YSR resonance by applying a certain bias) involves the injection/extraction of an electron from the QD, the fermionic parity of the system changes, and only the singlet-like LES can be accessed but not the higher-energy spin projection of the doublet. In contrast, at the singlet-GS phase, both spin projections can be reached by exciting the system with a N-state probe at $|eV_B| = E_{YSR}^{\pm} \pm E_Z$. Consequently, the conductance resonances can appear split, for a strong enough Zeeman effect and a sufficiently fine spectroscopic resolution. This has been previously demonstrated in SC-QD systems made by contacting semiconducting NWs [29, 41, 42], thanks to the large Landé factor ($g \sim 20$). While the SC materials employed in these studies was rather robust against the external magnetic field necessary to observe well-split resonances, superconductivity rapidly vanishes in our aluminum junctions. Moreover, several studies on QD junctions contacting metallic nanoparticles of different materials and sizes in the range of a few nanometers present a certain variability in the g factors, in general being always lower than 2 [2, 256, 76]. In fact, previous experiments carried out within our group [38] obtained a Landé factor of $g \sim 1.7$ for devices made with the same gold nanoparticles employed here. Therefore, the combination of such reduced values

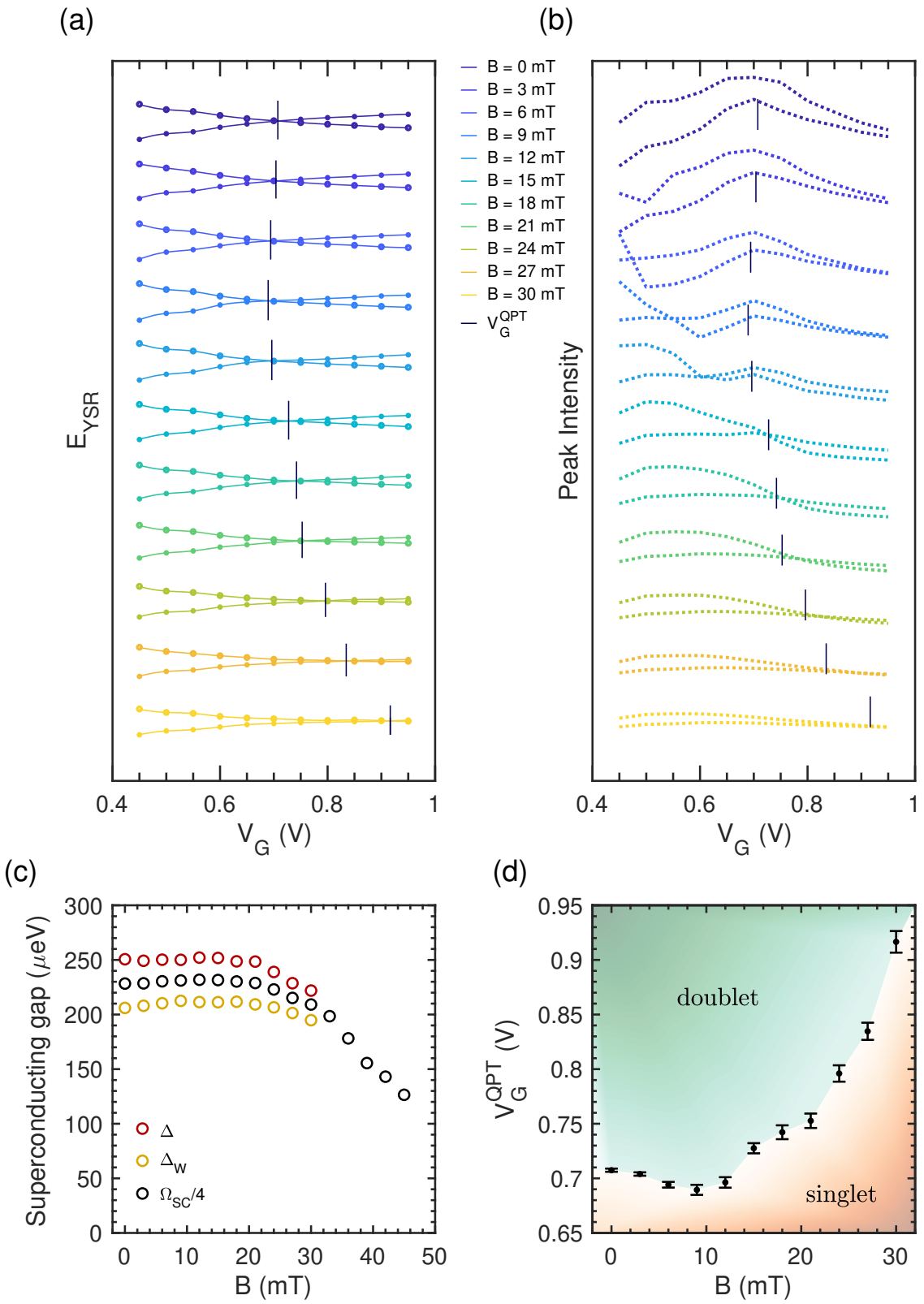

Fig. 4.17: (a) Gate-dependence of the energies of the YSR states and intensities of the corresponding resonances at different B fields. Precise values of V_G^{QPT} (vertical black lines) are extracted from the crossing point of spline interpolations (solid lines) of the experimental data (dots). A vertical displacement of the curves has been artificially introduced for clarity. (c) Closening of the SC gaps in the weakly- (Δ_W) and strongly-coupled (Δ) electrodes, as well as the total spectroscopic gap measured at the even diamond gate range (Ω_{SC}). (d) The gate location of the QPT at different B-fields, delimits the boundary in the phase diagram.

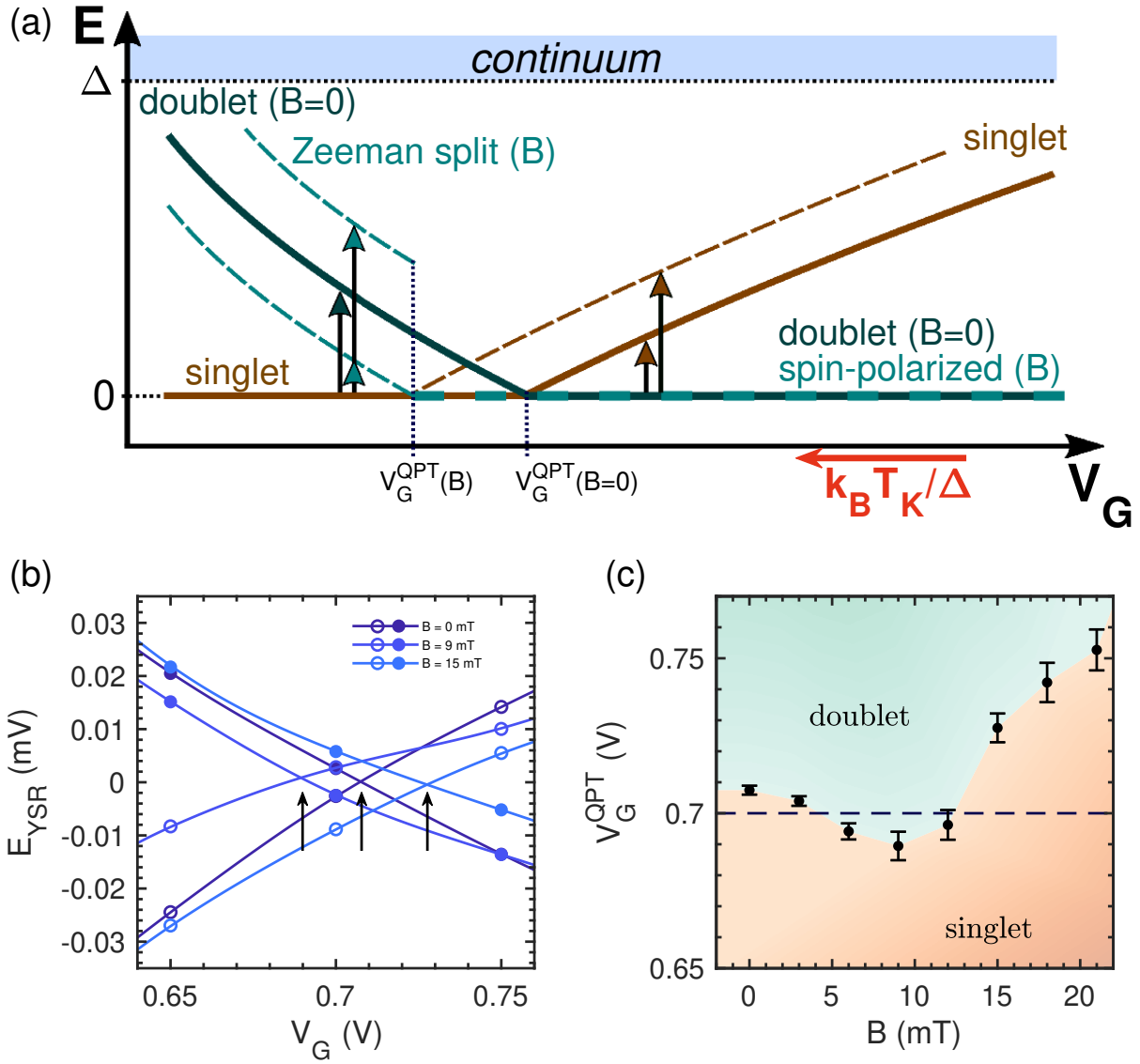

Fig. 4.18: (a) Sketch of level structure of YSR states at zero magnetic field (continuous lines) and finite (dashed lines) magnetic field, in vicinity of the ground-state transition. (b) Zoom in at low energies of $E^{\pm}_{YSR}$ at three different values of B field, evidencing the oscillation of V_G^{QPT} (indicated by black arrows) moving from one side of its zero-field value to the other. (c) Zoom in at a low B field range of the phase diagram shown in Fig. 4.17d. The horizontal dashed line corresponds to the gate position of the measurements shown in Figs. 4.19 and 4.20, traversing the phase boundary twice at fields around 4 and 12 mT.

of g with the relatively small B field that our SC leads can tolerate makes difficult to detect the splitting of the YSR resonance peaks. However, the upturn delineate by the critical gate voltage, $V_G^{QPT}(B)$, can be understood from this perspective. Indeed, because one of the spin projections of the doublet LES has a lower energy, the singlet-GS phase gradually shrinks, translated into a critical value of V_G moving to lower values (Fig. 4.18a and b). Such tendency can be clearly observed by zooming at the low-field range of the phase-diagram of Fig. 4.17d (shown in Fig. 4.18c). As the magnetic field is further increased, the reduction of the superconducting gap comes into play, with a quadratic-on-B dependence [255], overcoming the linear behavior of the Zeeman splitting and resulting in an increasing tendency of V_G^{QPT} at higher fields.

The magnetic-field-induced oscillation of the phase boundary can, hence, be qualitatively explained as a result of the complex competition between the the gap reduction and the Zeeman splitting of the doublet state [44]. Nevertheless, the underlying physics of our particular system appear to be more complex. On one hand, it might seem reasonable to simplify the B-field effect as inducing a

variation on a single microscopic scale of the system, equating E_Z at 10 mT with the level-depth variation corresponding to the displacement of V_G^{QPT} from its zero-field value (around 0.707 V) to its value at the lowest point of the upturn (around 0.690 V). However, this calculation leads to ridiculously large values of g, implying that the effect that the B-field exerts on the system goes beyond the mere splitting of the energy level in the dot. On the other hand, intriguing behaviors are observed at the singlet-GS phase, where an important increase of the conductance maximum of the YSR resonance appearing at negative bias, V_B^{-YSR}, gradually takes place as the B field is increased, while the resonance at V_B^{+YSR} remains almost unchanged (as it can be appreciated in Fig. 4.17b). A manifest inversion of the relative intensity of V_B^{+YSR} and V_B^{-YSR} occurs at the degeneracy point for B $\approx$ 6 mT, advancing towards the center of the odd diamond as B is increased and becoming the distinctive feature indicating the vicinity of the QPT. Similar inversions of the relative spectral weight have been previously observed as a function of the impurity distance in STM measurements, linked to distance-dependent asymmetries in the particle and hole-like components of the YSR wavefunction. Unfortunately, no time was left over my thesis project to perform a more detailed analysis of these aspects.

STUDY OF THE RE-ENTRANT PHASE BOUNDARY

To further examine the particular upturn traced by $V_G^{QPT}(B)$, we tuned the system into the singlet-GS phase at $V_G = 0$ V, very close to $V_G^{QPT}(B=0) \approx 0.705 - 0.71$ V, and measured its characteristic conductance at B fields from 0 up to 60 mT (Fig. 4.19), following the horizontal dashed line in Fig. 4.18c. The resulting dI/dV_B-B map shows the continuous evolution of the spectrum from the SC to the N state of the leads, reached for B > 55 mT. The total spectroscopic gap is progressively reduced, as superconductivity in the leads vanishes, diminishing the values of Δ and Δ_W, and broadening the SC-DOS profile. The YSR resonances decrease in amplitude and widen, showing a clear reduction of E_{YSR} above 40 mT until they collapse into the much less intense Kondo resonance at zero-bias, right below 60 mT.

At first sight, the position of the YSR resonances, appearing at positive and negative bias (respectively labeled as V_B^{+YSR} and V_B^{-YSR}), is rather symmetric with respect to zero, despite small deviations caused by the bias lever arm. However a closer inspection of the two conductance peaks reveals that, while V_B^{+YSR} remains almost invariant for low B fields showing a slight increase that

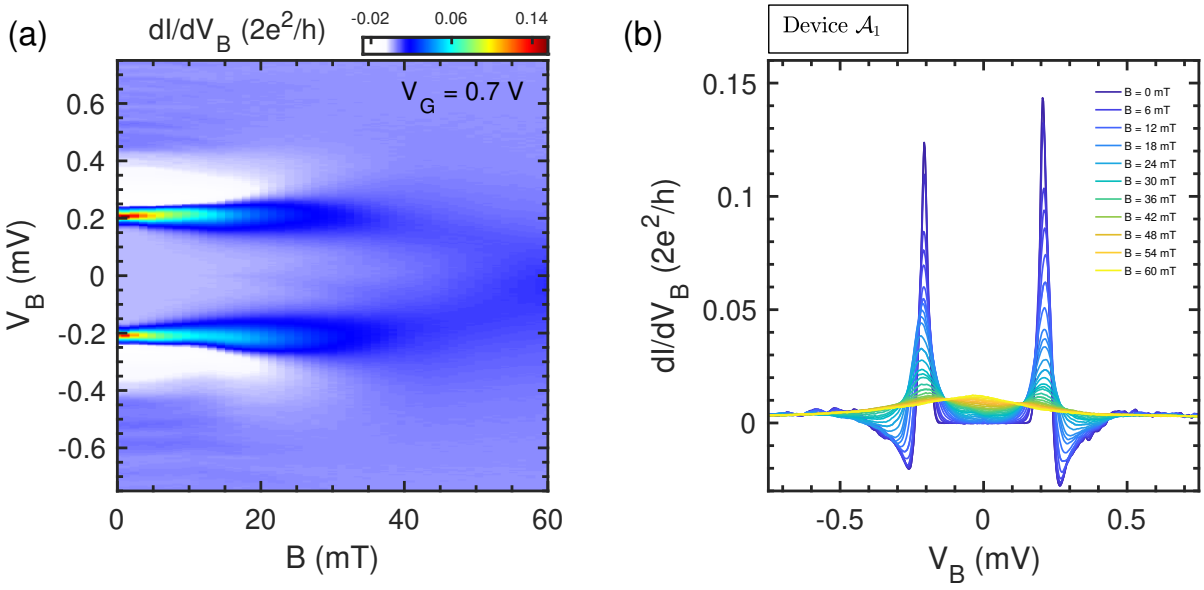

Fig. 4.19: (a) dI/dV_B map of device $\mathcal{A}_1$ for different B fields, taken at $V_G = 0.7$ V and showing the evolution of the YSR spectrum into the Kondo spectrum as the leads transit from the SC to the N state. (b) dI/dV_B-V_B curves at different B fields corresponding to the measurement shown in (a).

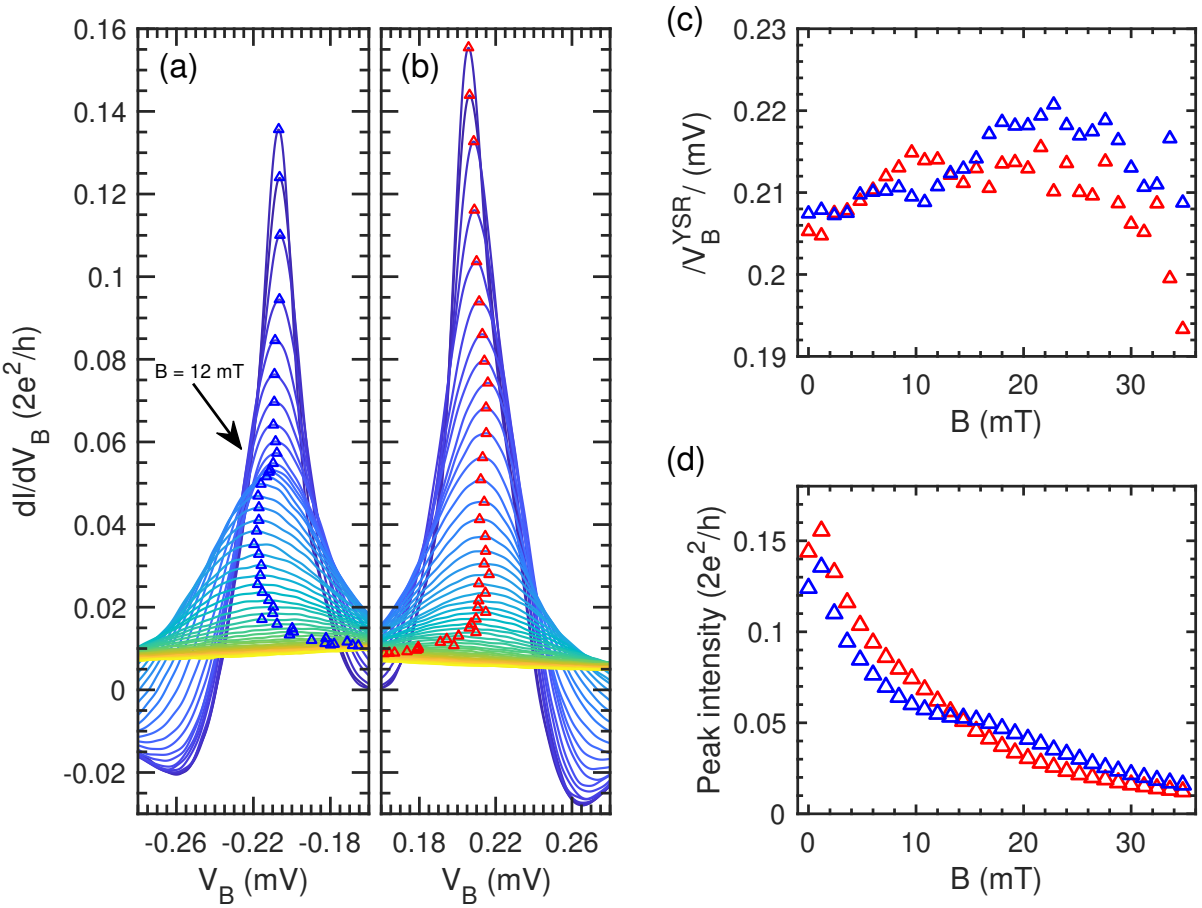

Fig. 4.20: Zoom-in at the YSR resonances appearing in the dI/dV_B-V_B curves of Fig. 4.19a at negative and positive bias (respectively called V_B^{-YSR} and V_B^{+YSR}, shown in panels a and b). (c) B-field dependence of the extracted bias position of V_B^{-YSR} and V_B^{+YSR}, crossing twice at a field around 4 mT and 14 mT. (d) B-field dependence of the top-conductance of both resonances (V_B^{-YSR} and V_B^{+YSR}), displaying a kink at 2 mT and crossing around 14 mT.

results from the SC-DOS broadening (Fig. 4.20b), the resonance at V_B^{-YSR} starts a shifting tendency towards more negative values starting at B = 10 mT until it levels off slightly below B = 20 mT (Fig. 4.20a). Nevertheless, shifts induced by the bias coupling characterized in the previous section can be employed in this case, as they indicate a mismatch between V_B^{+YSR} and V_B^{-YSR} of around 3 μV at $V_G = 0.7$ V. The rough offset correction performed by imposing the faint spectroscopic gap edges at symmetric bias positions was further adjusted by imposing such offset of 3 μV between V_B^{+YSR} and V_B^{-YSR} at zero-field (considering that the offset remains constant as B is increased). After carrying out this calibration (Fig. 4.20c), we found that V_B^{+YSR} and V_B^{-YSR} display a crossing between 2 and 6 mT, crossing again later around 14 mT, in good agreement with the previously obtained interceptions of the phase boundary re-entrance with a measurement at constant $V_G = 0.7$ V (Fig. 4.18c). Finally, we comment on the B-field dependence of the resonances' top-conductance (Fig. 4.20d). The characteristic kink, which signals the imminence of a transition at low B fields, shows up at 2 mT, whereas a crossing of the resonances' intensities is observed to occur around 14 mT, indicating the second traversal of the transition, in good agreement with the exposed above.

4.3.4 Temperature dependence of the YSR spectrum

For completeness, an equivalent study of the features of the YSR resonances at different temperatures. The V_G-V_B transport map of device $\mathcal{A}_1$ was measured at several temperatures (the raw data is shown in Fig. F.1 in Annex F), extracting the gate dependence of $E_{YSR}^{\pm}$, and intensities of the resonances for each temperature value (Fig. 4.21a and b, respectively). In contrast with the upturn displayed

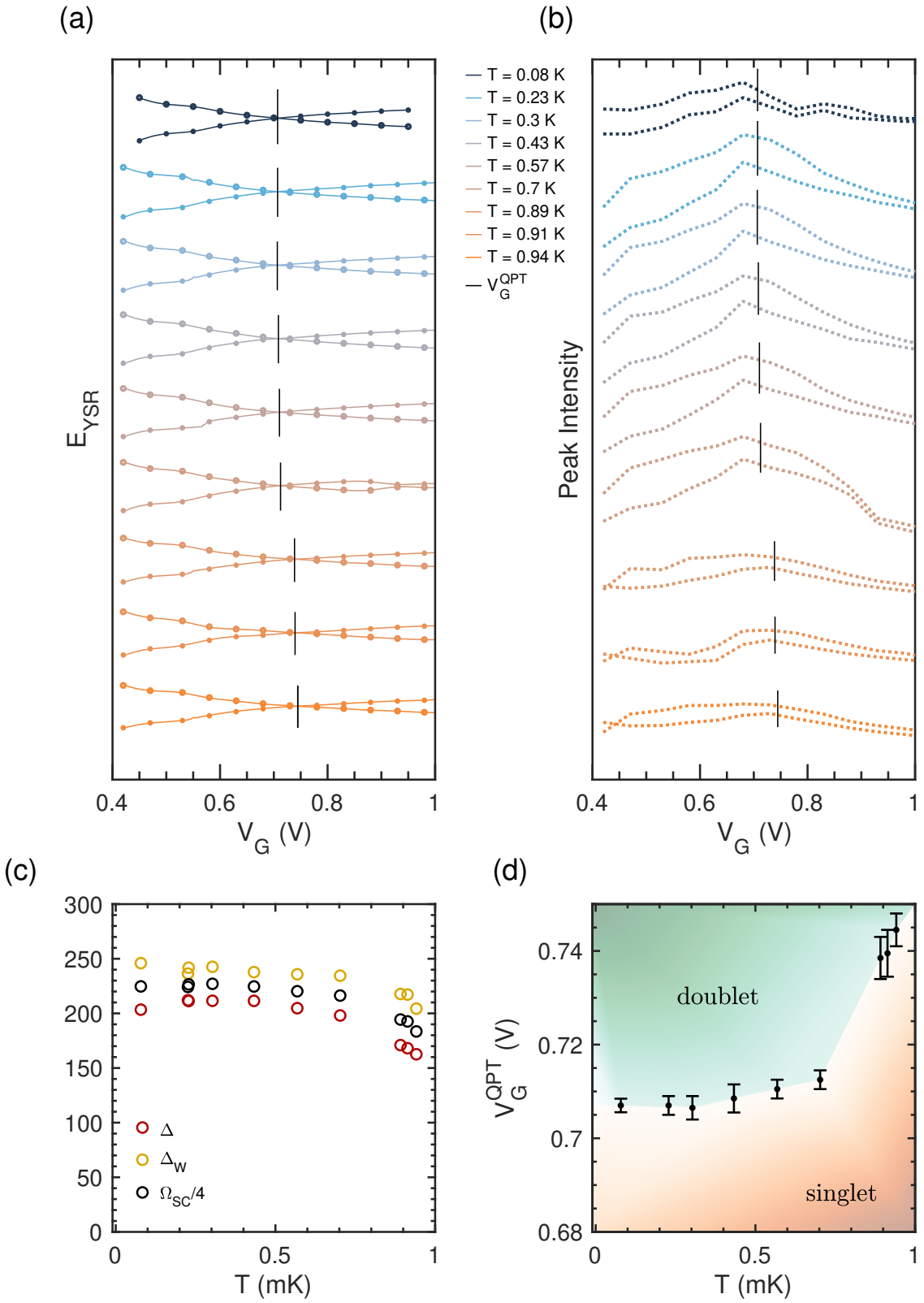

Fig. 4.21: (a) Gate-dependence of the energies of the YSR states and intensities of the corresponding resonances at different temperatures. Precise values of V_G^{QPT} (vertical black lines) are extracted from the crossing point of spline interpolations (solid lines) of the experimental data (dots). A vertical displacement of the curves has been artificially introduced for clarity. (c) Closening of the SC gaps in the weakly- (Δ_W) and strongly-coupled (Δ) electrodes, as well as the total spectroscopic gap measured at the even diamond gate range (Ω_{SC}). (d) The gate location of the QPT at different temperatures delimits the boundary in the phase diagram.

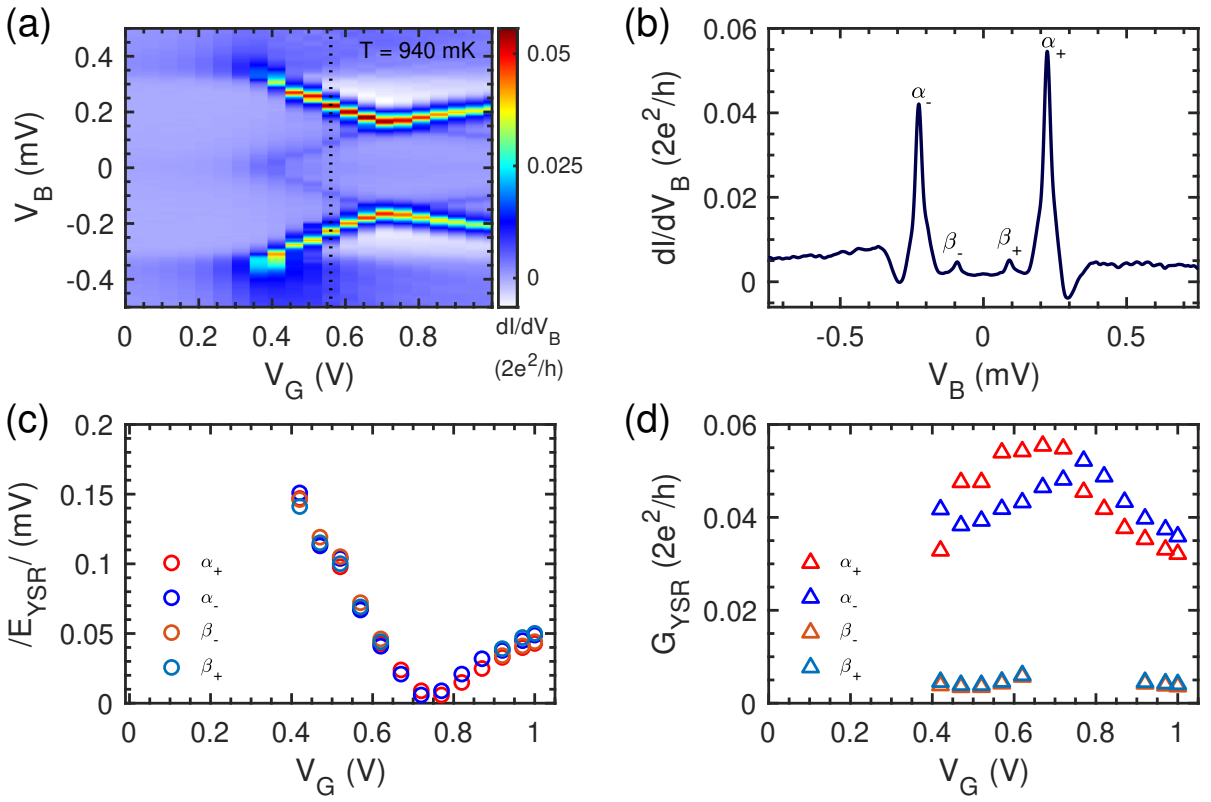

Fig. 4.22: (a) Transport map of device $\mathcal{A}_1$, measured at a temperature of 940 mK, showing the emergence of thermal replicas ($\beta_\pm$) of the main YSR resonances ($\alpha_\pm$). (b) Characteristic curve acquired at $V_G = 0.57$ V (dashed vertical line in a). A significant sub-gap conductance is caused both by the apparison of YSR thermal replicas as well as tunneling of thermal quasiparticles between the SC leads. (c,d) Extracted energies and top-conductances of the main YSR states and their thermal replicas.

by $V_G^{QPT}(B)$, the evolution of V_G^{QPT} with temperature (Fig. 4.17d) increases monotonically, as the narrowing of the SC gap reduces the effective Kondo temperature at which the transition takes place, driving the QPT slightly inside the odd diamond. In this case, the top-conductance of the two YSR resonances at $V_B^{\pm YSR}$ remains qualitatively equal to its low temperature value, up to $T = 0.89$ K, where the relative intensity of both resonances at V_G^0 is slightly disturbed due to thermally-excited quasiparticles that enhance first-order processes, increasing the conductance at the diamond apexes (Fig. 4.21b). Both resonances decrease in intensity and increase in width as the temperature is cranked up, due to the thermal broadening of the spectrum.

Remarkably, well-developed thermal replicas emerge in the YSR spectrum at temperatures above 900 mK, caused by the thermal excitation of the SC-QD system into its LES (Fig. 4.22a and b). Each thermal replica ($\beta^\mp$) appears at bias position of $|eV_B| = \Delta_W - E^\pm_{YSR}$, separated from its corresponding main resonance ($\alpha_\pm$) by an amount of $2\Delta_W$, resulting from the possibility of injecting electrons into the YSR state below E_F, or extracting them from the YSR state above E_F. Their energies can be equivalently extracted by subtracting Δ_W from their bias position, collapsing with the energies of the main YSR states (Fig. 4.22c, slight deviations are caused by the effect of the bias lever arm). Several works have observed and studied the characteristics of such thermal replicas before, either by STM [10, 257] or in devices contacting NWs [28, 40]. In such works, it has been observed that the relative values of the excitation/de-excitation rates of the SC-QD system with respect to the tunneling rate of the probing lead play a fundamental role in determining the intensities of the YSR resonances and their corresponding replicas. While the tunnel couplings are fixed in our case, we also observed a certain gate dependence of the intensities of the thermal replicas, imitating that one of the main peaks (Fig. 4.22d).

Conclusions and perspectives

In this thesis, we employed these all-aluminum electromigration constrictions to contact metallic nanoparticles and fullerenes. Most of the QD transistors obtained along my work presented a coupling asymmetry of a few orders of magnitude. YSR states are often present in these samples, emerging for odd fermionic occupancies and indicating the presence of significantly intense Kondo correlations between the QD and the strongly coupled lead. For a sufficiently weak coupling of the other lead, it can act as a tunneling probe that performs spectroscopies on the SC-QD correlated system at the other side of the junction, equivalently to an STM tip. Besides Kondo effect, the fundamental role that the bias lever arm play in these asymmetries, together with the asymmetric biasing configuration used for measuring the conduction, was put into manifestation. Only after accounting for these effects, the NRG simulations performed displayed a semi-quantitative agreement with the experimental data, demonstrating the importance of their consideration in the study of electromigration junctions.

Remarkably, the gate modulation of the Kondo scale, k_BT_K, could be extracted by fitting the evolution of the normal-state zero-bias conductance at different temperatures, demonstrating a behavior of the Kondo effect in one of our devices close to the universal regime. The resulting relation between gate voltage and Kondo temperature could be used to derive a critical value of the relative scale k_BT_K/Δ at which the phase transition between the two ground states of the SC-QD system, resulting from the interplay between superconductivity and Kondo effect, occurs. The obtained value of $(k_BT_K/\Delta)_c = 0.67-69$, consistently found in two devices displaying similar energy scales, is in good agreement with STM experiments and other devices contacting self-assembled QDs, as well as with theoretical works, if the differences between the Kondo scale definitions considered in each case are taken into account. One of these devices was further studied at different magnetic fields, showing the continuous evolution of the spectrum of the correlated spectrum from YSR at the SC state to Kondo in the N state. A notable shift of the QPT gate position towards opposite directions at different fields was characterized in detail, explained as being caused by the Zeeman splitting of the doublet excited state, effectively shrinking the gate range of the singlet ground-state phase. However, the progressive suppression of superconductivity as the magnetic field is cranked up, gradually reduces the value of Δ, displacing the critical gate voltage towards the opposite direction. The linear dependence of Zeeman effect governs the shift for low magnetic fields, while the quadratic dependence of the gap reduction dominates rapidly for increasing fields, being the upturn delineated by the critical gate voltage a consequence of the competition between these two effects. An equivalent study of the critical gate position was done for increasing sample temperatures, in this case obtaining a monotonic increase corresponding to the gradual closing of the superconducting gap. Such a precise study was possible thanks to the relatively high spectroscopic resolution achieved in our electromigration devices, in some cases displaying YSR resonances of conductance with a FWHM smaller than 10 μV, constituting the finest experimental spectroscopy of YSR states in the literature, to our knowledge.

Apart from the study of these competing quantum phenomena, it was of our interest to carry out charge pumping experiments and study the turnstile operation of our SC-QD-SC transistors, resulting from the application of a fast-oscillating AC voltage signal to the gate electrode. Previous experiments within our group showed a reduced frequency range of the turnstile operation of SC-QD-SC transistors, attributed to impedance mismatches. The main technical aspects of my work involved to improving the accuracy of the turnstile operation by getting rid of such undesired effects. For this, a coplanar waveguide electrode configuration was designed and successfully implemented in our fabrication recipe, gating the aluminum constrictions. Home-made bias-tees were also created in order to couple de AC and DC components of the gate signal at the sample-holder stage. An

installation of several radiofrequency cryogenic lines was carried out in a recently acquired cryogenic setup, devoted for these kind of experiments.

A Charge pumping experiments in superconductor-quantum dot transistors

A.1 Turnstile operation of a superconductor-quantum dot transistor

The current measured in the conduction diamonds of SET devices, consequence of sequential tunneling, stems from electrons traversing the device one by one. While the tunnel couplings determines the average rate at which single electrons tunnel in/out of the central electrode, the occurrence of these tunneling events is stochastic. An electron turnstile device, in contrast, is defined as a mesoscopic system that allows for restricting the time periods over which such individual tunneling events happen, allowing to gain control over the rate at which electrons flow through it. Like this, a turnstile current can be expressed as the charge of the individual particles (electrons in our case) times the frequency f of the acquisition-delivery cycle, usually driven with an AC signal:

$$I^* = \pm e f. \tag{A.1.1}$$

For such quantized currents to be measurable, turnstile devices must be operated at relatively high frequencies, generally in the order of the radio-frequency ($f \sim 1 - 1000$ MHz, leading to electron turnstile currents of $I^* \sim \pm 0.16 - 160$ pA). The quality and performance of a turnstile device, understood as a quantum current source, is given by the range and maximum f at which the measured current can maintain a certain accuracy ($|I - ef|$), and its stability is determined by the range over which other parameters (like temperature, biasing voltage, amplitude of the AC signal) can be varied without affecting I^*.

As summarized in the introductory chapter, several kinds of turnstile devices have been developed in the last decades, following distinct architectures and therefore achieving different performances, accuracies and stabilities. A rather simple conception, based on a SC-SET contacting a nanoisland, was demonstrated by *Pekola et al* either employing a SC island and N leads [46] or SC leads and a N island [47]. By combining the current suppression caused by the gapped SC-DOS and Coulomb Blockade single-electron charging effects, it is possible to lock one electron tunneling into the island from one lead (Fig. A.1b), and deliver it into the other one (Fig. A.1a), by moving the island's chemical potential across a charge degeneracy point with V_G, while keeping the biasing voltage below the gap: $0 < |eV_B| < 2\Delta$. As this process simply consist in a mere variation of V_G, it can be

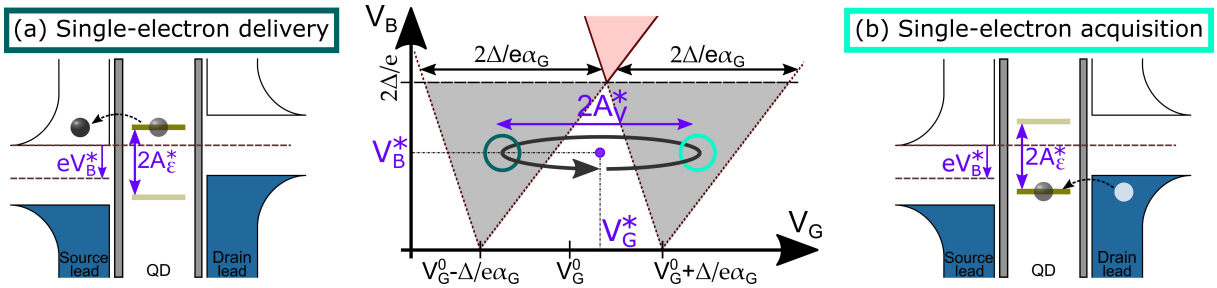

Fig. A.1: Illustrative schematic of an SC-QD-SC SET data map around a degeneracy point V_G^0 for positive-V_B. The extension of the diamond slopes into the SC gap down to their zero-V_B collapse at $V_G = V_G^0 \pm \Delta/e\alpha_G$ allows to determine the regions (colored in gray) for the acquisition (b) and delivery (a) of single electrons in the turnstile operation mode for a certain combination of V_B^*, V_G^* and A_v parameters.

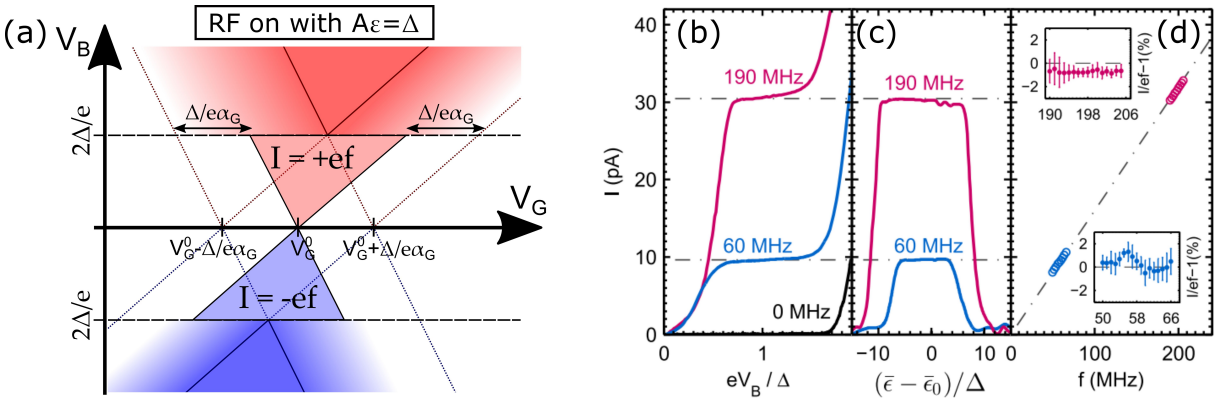

Fig. A.2: (a) Illustrative current map of a SC-QD-SC SET device, while an AC signal is applied to the gate electrode inducing a level depth oscillation of $\pm\Delta$, leading to the development of turnstile current plateaus around V_G^0 below the gap edge. Measurements performed in actual SC-QD-SC SET devices show the turnstile current plateaus as a function of (b) V_B (magenta, $A_\epsilon = 0.64\Delta$, and blue, $A_\epsilon = \Delta$) and (c) V_G (magenta, $V_B = 3\Delta/2e$, and blue, $V_B = \Delta/e$, both for $A_\epsilon = \Delta$). (d) The frequency-dependence of the plateaus shows a narrow working range around $50-66$ MHz, where the measured current displays an accuracy fluctuating at $\pm 1\%$ within the ideal value of ef (lower inset), and around $190-206$ MHz, where a systematic reduction of 0.7% is present, possibly due to missed tunneling events (upper inset). (extracted from [48]).

repeated iteratively at high frequencies by setting the DC gate voltage V_G close to charge degeneracy and applying an additional AC component V_G^{AC} to the gate electrode, for example, a sinusoidal signal:

$$V_G^{AC}(t) = A_v \sin(2\pi f t). \tag{A.1.2}$$

While the oscillation frequency of the signal determines the magnitude of I^*, the amplitude of the signal A_v determines the ranges of the DC voltages, V_B and V_G, at which the turnstile can operate (set-point). The well-defined hierarchy of energy scales present displayed our QD transistors, when obtained in a weak-coupling regime ($E_U \gg E_\delta \gg \Delta \gg k_B T \gg \gamma_T$), allows the same operation principle to be valid for the generation of a turnstile current. The level depth's oscillation, induced by the AC signal, as depicted in Fig. A.1, can be written as

$$\epsilon_0^{AC}(t) = -e\alpha_G^{AC} V_G^{AC}(t) = A_\epsilon \sin(2\pi f t), \tag{A.1.3}$$

where the proportionality between the level depth's oscillation amplitude $A_\epsilon = -e\alpha_G^{AC} A_v$ and the AC signal A_v is given by the AC gate coupling α_G^{AC}. The oscillation can be then included in the level depth expression, defined with respect to the zero-V_B degeneracy point V_G^0 (so that $\widetilde{V}_G = V_G - V_G^0$), as

$$\epsilon_0^*(V_B, \widetilde{V}_G, t) = \epsilon_0(V_B, \widetilde{V}_G) + \epsilon_0^{AC}(t) = -e\alpha_B V_B - e\alpha_G \widetilde{V}_G + A_\epsilon \sin(2\pi f t), \tag{A.1.4}$$

describing the system during turnstile operation and showing explicitly the experimental knobs ($V_B, \widetilde{V}_G$ and A_ϵ) over which the effective electron-pumping areas can be mapped.

It is possible to delimit the ranges for the turnstile set-point (defined by $V_B^*, \widetilde{V}_G^*$ and A_ϵ^*, highlighted in purple in Fig. A.1) and discriminate areas of optimal operation and of reduced functionality. For example, measuring the V_B, V_G current map while continuously applying a certain RF signal (A_v and f), turnstile current plateaus are expected to emerge below the SC gap, around charge degeneracy (Fig. A.2a). Charge-pumping experiments have already been carried out in our aluminum SC-QD-SC transistors with voltage signals of square profile rather than sinusoidal ones [48] (mathematically described with the sign function, replacing $\sin(2\pi f t) \to \mathrm{sgn}(\sin(2\pi f t))$ in Eqs. A.1.2, A.1.3 and A.1.4). The study of the SC-QD-SC turnstile properties revealed a limited working frequency range, around $50-66$ and $190-206$ MHz (Fig. A.2d), attributed to impedance mismatches along the RF line that impede a proper signal transmission at the rest of the frequencies. Nevertheless, well-developed current plateaus were observed for the operative values of f, traced across the V_B and V_G parameters, as shown in Fig. A.2b and c respectively, approaching the standard ef value (indicated

with grey dashed-dotted lines). In a theoretical way, the effect of those impedance mismatches can be included in the parameter α_G^{AC}, which expresses the transmissivity of the electrical line employed to send the RF signal through the cryogenic setup down to the QD transistor. A detailed analysis of the possible phenomena generating a frequency dependence of α_G^{AC} is given in annex B. In order to correct for those detrimental mismatches, we designed and implemented an impedance-matched gate electrode that could be combined with our all-aluminum electromigration junctions, as explain along chapter 2. Additionally, an entire RF circuit was installed in cryostat A, employing adapted coaxial wires, connectors, and attenuators, that improve the quality of the cryogenic RF line (explained in section 3.1.3). Finally, we also prepared home-made bias tees by soldering lumped elements to our sampleholders (explained in section 3.1.4). All these technical improvements were done envisioning an improvement of the turnstile operation of our SC-QD-SC transistors.

Apart from the technical limitations caused by impedance mismatches at the measurement RF line, several fundamental mechanisms can induce errors in the electron-pumping operation of island-like and dot-like SC-SETs, driving the current away from the ef metrological standard [258]. Attending to the nature of its origin, error sources can be categorized into four different groups, related with the pumping speed, thermal smearing, accumulation of quasiparticles and higher-order processes:

- **Missed tunneling events**: The driving frequency determines the effective tunneling time, $\tau^* \sim 1/f$, spent by $\mu_{Isl,QD}$ in the energy range to acquire/deliver an electron. This characteristic time must be $\tau^* \gg 1/\Gamma_{S,D}$ for the electrons to have enough time to tunnel during each cycle. Otherwise, missed tunneling events appear, in which the electron did not have enough time to tunnel into/out of the dot. The highest pumping f at which the turnstile can be operated, while keeping a maximum accuracy, is then limited by $\gamma_{S,D}$ (or $R_T^{S,D}$), which, at the same time, should be kept small to reduce the probability of higher-order processes. In any case, τ^* can be maximized by employing square waves (resulting in $\tau^* = 1/(2f) - \tau_{rise}$), where τ_{rise} is the rising time parameter of the wave generator), as done in the experiments shown in Fig. A.2b.
- **Thermal effects and backtunneling**: The oscillation amplitude, A_ϵ must be adapted for each V_B set-point, so that $\mu_{Isl,QD}$ surpasses only the gap edges of each corresponding lead in the delivering/acquiring semi-cycles, remaining below the edge of the other lead. The thermal smearing of the island's Fermi-distribution in SC-SETs results in high-energy electrons reaching the opposite gap edge already at $T \approx 300$ mK. Additional errors processes like the replacement of the electron tunneling out during the delivery semi-cycle (specially at high V_B close to 2Δ) or the electron delivery to the same lead from which it was acquired (baptized as backtunneling, more important for $V_B \approx 0$) are then introduced, being minimized at an optimal set-point of $V_B = \Delta$ [46, 47]. The large energy-discretization present in our SC-QD-SC transistors suppresses such thermal-related errors [48], being, in principle, possible to operate the turnstile at higher temperatures (up to $k_B T \approx E_\delta$) and for any V_B set-point ($0 < |eV_B| < 2\Delta$) provided that the amplitude is configured adequately ($\Delta - |eV_B|/2 < A_\epsilon < \Delta + |eV_B|/2$).
- **Quasiparticle accumulation**: More recently, the accumulation of quasiparticles in the SC leads (arising from residual electromagnetic radiation and/or as a consequence of the turnstile operation itself) has been identified as an important source of errors [138], which results in undesired tunneling events like the lost of an electron at the acquiring semi-cycles or vice versa. While the inclusion of on-chip ground planes has been proven efficient for reducing the radiation-induced quasiparticles in SC-SET devices [202], grounded metallic structures in contact with the SC leads (acting as quasiparticle traps) can be employed to reduce the quasiparticle overpopulation [259]. On the contrary, the lack of available states into which quasiparticles can tunnel, grants SC-QD-SC transistors immunity against this error source [48].
- **Higher-order tunneling**: Elastic cotunneling processes own negligible probabilities in systems owning SC leads and a N-state central electrode by the SC gap in the leads for $|eV_B| < 2\Delta$. However different kinds of inelastic higher-order processes, namely Andreev reflections (second-order) and CP-electron cotunneling (third-order, sometimes referred to as an Andreev reflection of successive order), may introduce non-negligible sub-gap leakage currents [260]. As

both Andreev-type processes requires the simultaneous occupation of the dot by, at least, two electrons for the transmission of a CP, its associated rate reduces for $E_U/\Delta \gg 1$ [261], as well as for weaker couplings γ. The former condition is greatly satisfied in our SC-QD-SC transistor, in contrast with SC-SETs. However, the coupling per energy level is much stronger in QD devices, overall resulting in similar rates for such higher order process in both systems (see the supplemental information of Ref. [48]). Residual electromagnetic radiation in the sample cavity can also promote the rate of these processes in turnstile devices [139].

In summary, single-electron charges are conveyed across the device by a single energy level in the SC-QD-SC transistor operated as a turnstile. The effect of several error sources, present in the SC-SET, are diminished or completely avoided thanks to the large energy-discretization in the QD. Injection of electrons at precise energies (within the lifetime broadening induced by the coupling) must be possible with this system, serving as a monochromatic single-electron source.

A.2 Overview of the devices

Several SC-QD-SC transistors were obtained by carrying out in-situ electromigration in cryostat A, at a temperature of 4 K and under high vacuum conditions, some of them presented here (Fig. A.3). Devices $\mathcal{S}_3$, $\mathcal{S}_4$, and $\mathcal{S}_5$ presented a well defined and relatively symmetric diamond structure, indicating a weak coupling regime and the predominance of Coulomb blockade. While the diamond structure in device $\mathcal{S}_6$ is also rather symmetric, classifying this sample as weakly-coupled, additional conductance features of uncertain origin arise around the degeneracy point. On the other hand, devices $\mathcal{A}_5$ and $\mathcal{A}_6$ display YSR-like sub-gap states, developing only at one side charge degeneracy and merging back into the continuum at the odd charge state. While charge pumping experiments were carried out in all of them, a complete characterization of the turnstile operation was not possible in any of the devices. We restrict this Annex to the most relevant results.

Notably, device $\mathcal{S}_4$ was obtained from one junctions employed to carry out the test of the in-situ evaporator unit, depositing of C_{60} molecules (see Annex E), constituting the only molecular junction characterized in this thesis. Gate switches continuously taking place in devices $\mathcal{S}_3$ and $\mathcal{A}_5$, impeded

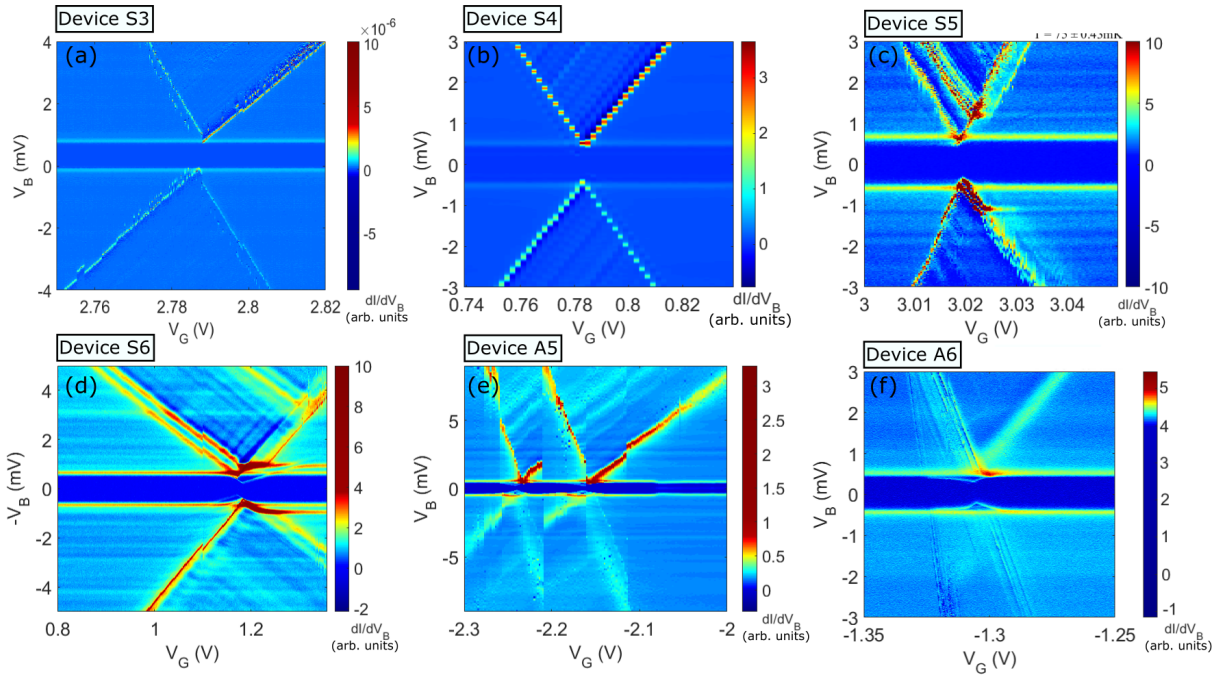

Fig. A.3: (a-f) dI/dV_B maps as a function of V_G and V_B, measured in QD transistors at 50 mK, using the lock-in technique.

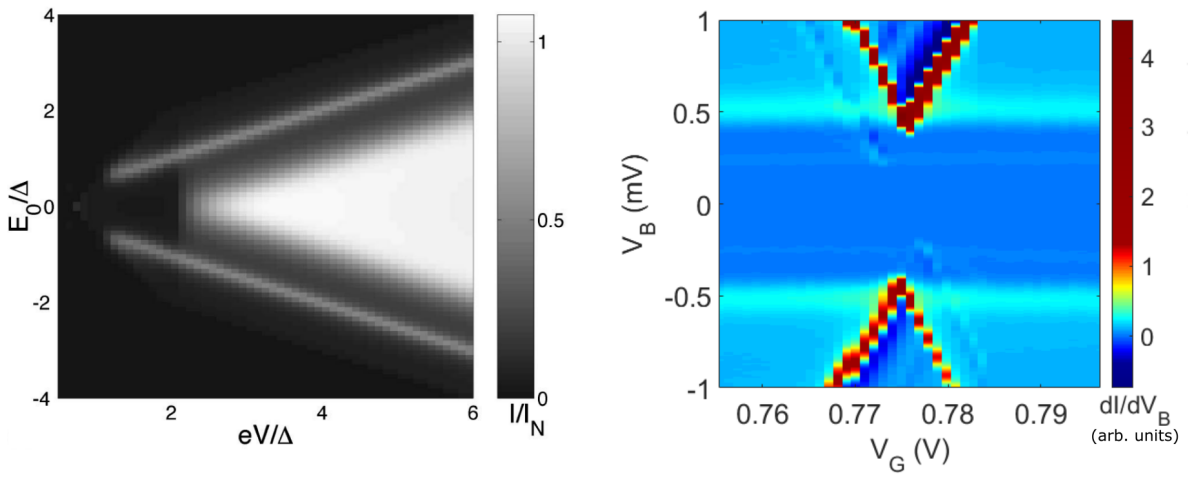

Fig. A.4: (a) Numerical transport map of a SC-QD-SC transistor showing the on-state conduction diamond and displaying CPE cotunneling (extracted from [262]). (b) dI/dV_B maps of device $\mathcal{S}_4$ zooming at the degeneracy point, where the conduction features of CPE can be clearly observed.

us to stabilize the chemical potential of the QD. The charge-pumping measurements that will be presented later, in section A.3, were carried out in device $\mathcal{S}_5$.

COOPER-PAIR ELECTRON COTUNNELING

Cooper pair electron cotunneling (CPE) consist in a second-order tunneling process appearing in SC-QD junctions, in which the two electrons forming a CP at one lead in the SC state tunnel through the QD, reaching the other lead of the junction as quasiparticles. For this process occurs for a finite bias such that $|eV_B| > \Delta$, becoming resonant for the alignment of an unnoccupied orbital at the QD with E_F of one of the SC leads, as well as with empty quasiparticle states at the other lead [262]. The resulting pair current emerges in the transport map of SC-QD-SC transistors on the sides of the on-state diamond, showing a conductance resonance that runs parallel to the diamond edge at a distance equal to Δ (Fig. A.4).

CPE cotunneling processes have been identified as of the main physical effects limiting the accuracy of the turnstile operation of SC-SET devices [47], as well as of QD transistors [48], since they introduce a sub-gap current around the degeneracy point, where the set-point of turnstile operation is located. Several of our weakly-coupled devices display such effects, although sometimes it is extremely faint. On the other hand, it is clearly visible in the transistor contacting a C_{60} molecule (device $\mathcal{S}_4$). By zooming at the degeneracy point, the transport map of this sample reveals the persistence of these conductance features at energies below the gap (Fig. A.4b). Remarkably, the CPE conductance resonances appear only along on diamond edge in device $\mathcal{S}_4$, which might be originated by an asymmetry in the coupling or by the specific parity of the QD occupation at this degeneracy point. Extremely faint sub-gap resonances of unknown origin also appear in the measurement, displaying a gate-independent behavior.

A.3 Charge pumping experiments

In this section, we briefly discuss charge-pumping experiments performed in device $\mathcal{S}_5$, by applying a sinusoidal RF signal to the gate electrode, resulting in an oscillation of ϵ_0, according to Eq. A.1.4. First of all, we characterize the DC transport properties of the SC-QD-SC transistor. The differential conductance map (Fig. A.5a) reveals a well developed diamond structure which, together with the absence of YSR resonances, indicates the weak coupling of the device. However, by taking a highly-amplified current map around the degeneracy point, we nevertheless observe that a certain sub-gap current of ~ 1 pA emerges (Fig. A.5b), attributed to CPE effects. In addition, charge offset switches

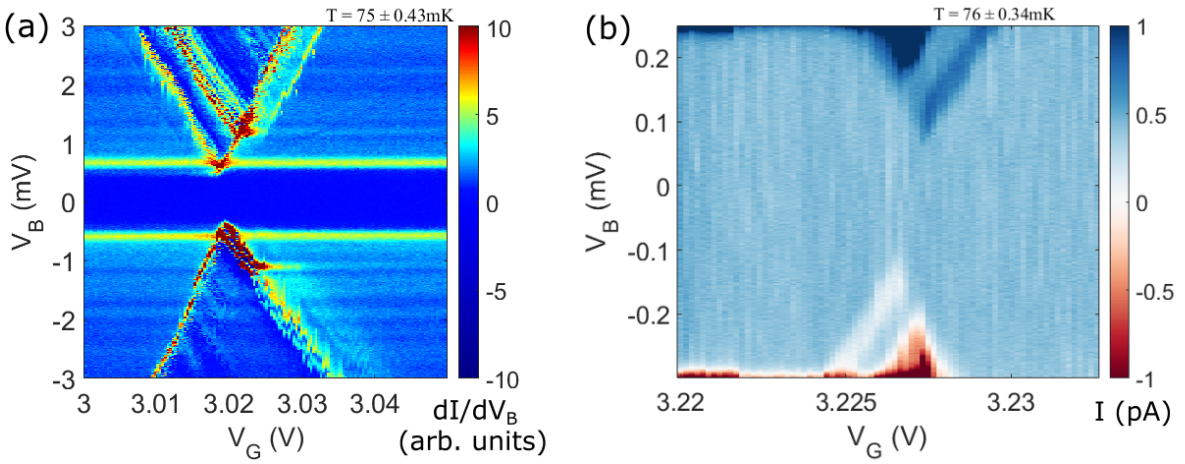

Fig. A.5: (a)) dI/dV_B map of device $\mathcal{S}_5$ acquired at base temperature with the lockin technique. (b) Current mat of the same device zooming at the gap region around the degeneracy point, acquired with a high amplification that enables to detect emerging sub-gap currents. A gate offset switch displaced the degeneracy point between measurements in (a) and (b).

also occur at this sample (note that the degeneracy point is located at different gate positions at both measurements shown in Fig. A.5). However, these switches are infrequent enough to acquire stable measurements in between them.

As a first characterization step, we record the current map of the device while applying a signal of $A_v = 10$ and 35 mV at the input of the cryogenic setup, oscillating at $f = 100$ MHz (Fig. A.6). At each experiment, we observe the emergence of two current plateaus at opposite V_B signs, emerging below the SC-induced spectroscopic gap around charge degeneracy, in agreement with our expectations. While both current plateaus at both measurements display a similar intensity, reaching values ranging between $(1.2 - 1.3) \times ef$ at the negative current plateaus of both measurements, and between $(1.02 - 1.1) \times ef$, for the positive ones. The independence of the current plateau level with the amplitude of the RF signal apply indicate a rather good turnstile behavior were capacitive crosstalks are not significant at these frequencies. On the other hand, the asymmetry of the current plateaus at different V_B sign can be explained by a certain asymmetry in the in the couplings. At last, the systematic overshoot of ef is attributed to a parasitic current contribution caused by CPE processes. The triangular shape of the current plateaus in Fig. A.6a, reaching zero-bias at the apexes,

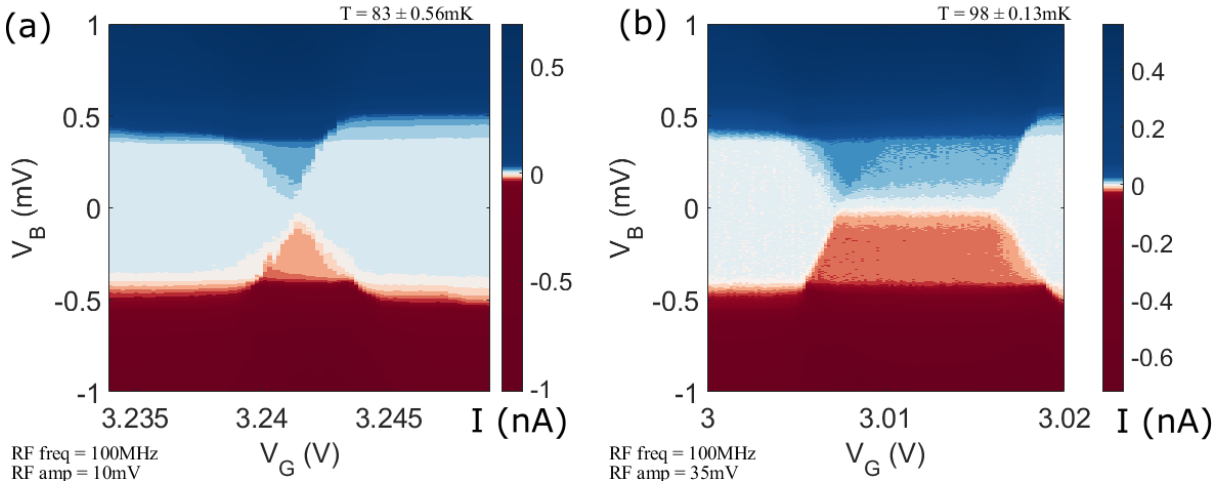

Fig. A.6: (a,b)) Current maps of device $\mathcal{S}_5$ acquired while applying a sinusoidal RF signal at the gate electrode of f = 100 MHz and respective amplitudes of 10 and 35 mV at the input of the cryostat.

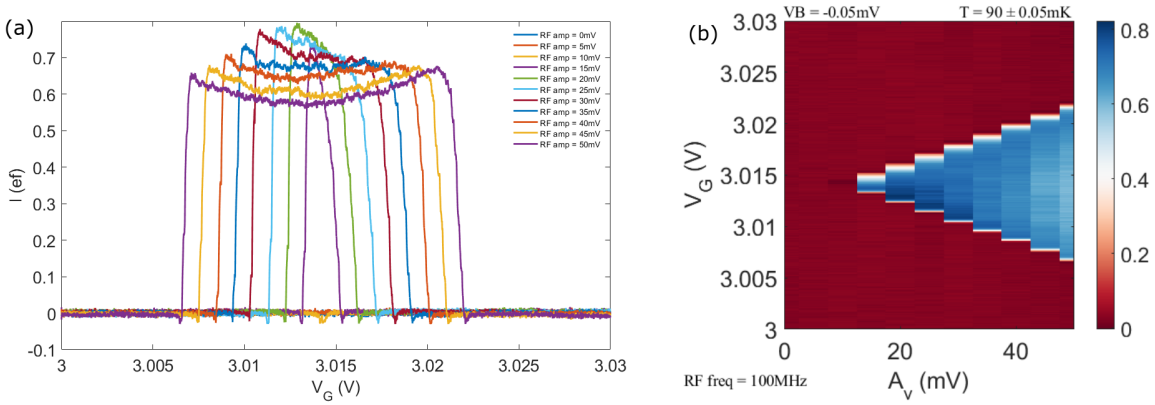

Fig. A.7: (a,b) I-V_G curves for different RF amplitudes and the corresponding map, acquired at $V_B = -0.05$ mV and for an oscillation frequency of $f = 100$ MHz. The current plateaus present a certain concave or tilted shape at their summit, and remain below ef.

indicates that the corresponding oscillation of ϵ_0 is $A_\epsilon \approx 2\Delta$, allowing the conveyance of electrons as soon as a finite V_B is applied. In contrast, the large extension of the current plateaus in Fig. A.6b indicates a large overshooting of the SC-gap in the acquisition and delivery semi-cycles. Remarkable, a slight backtunneling onset can be seen in Fig. A.6b, corresponding to the injection of electrons into the same lead from which the were acquired, above its SC-gap.

AMPLITUDE RESPONSE

When applying the RF signal to the gate electrode, the overall current of the junction increases. In order to ensure that the current plateaus are generated by a electron turnstile conveyed by a single orbital in the QD, it is necessary to demonstrate the linear dependence of the V_G-range of the plateau with the amplitude of the signal. In fact, as the amplitude of the signal A_v increases, so it does the oscillation of ϵ_0 in an actual SC-QD-SC turnstile, resulting in a larger effective gate range. To prove so, we tune the system at a V_B below the spectroscopic gap, and sweep V_G across the degeneracy point, while the RF signal is applied. For arbitrarily small values of A_v, the level-depth oscillation cannot surpass the SC gaps at the leads, and turnstile current cannot be conveyed. However, for increasing values of A_v, the SC gap edges are eventually reached, generating a turnstile current plateau that increases its V_G range as A_v is enlarged (Fig. A.7). The slope of such linear increase is given by α_G^{AC}. While such linear increased is displayed by device $\mathcal{S}_5$ (Fig. A.7), the reduced current values at the

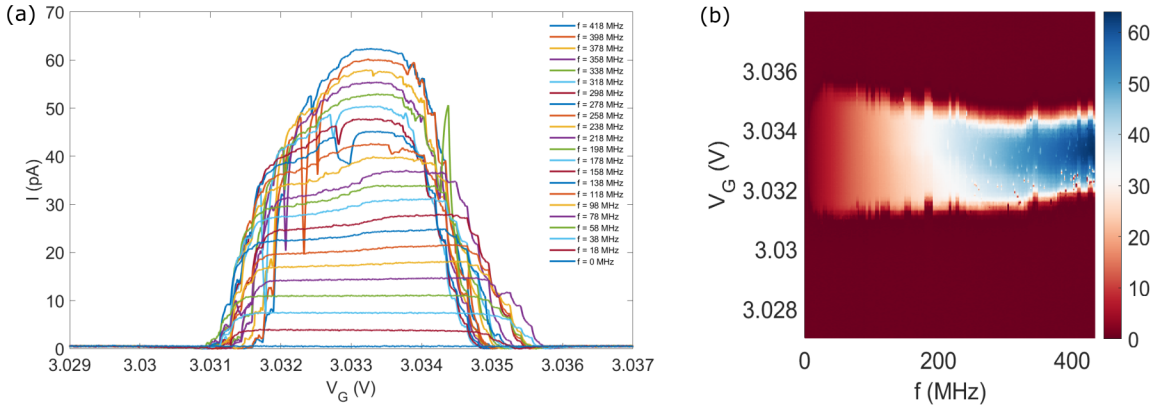

Fig. A.8: (a,b) I-V_G curves for different RF frequencies and the corresponding map, acquired at $V_B = -0.15$ mV and for an oscillation amplitude of $A_v = 30$ mV. The current plateaus present a certain convex or tilted shape at their summit, and approach ef.

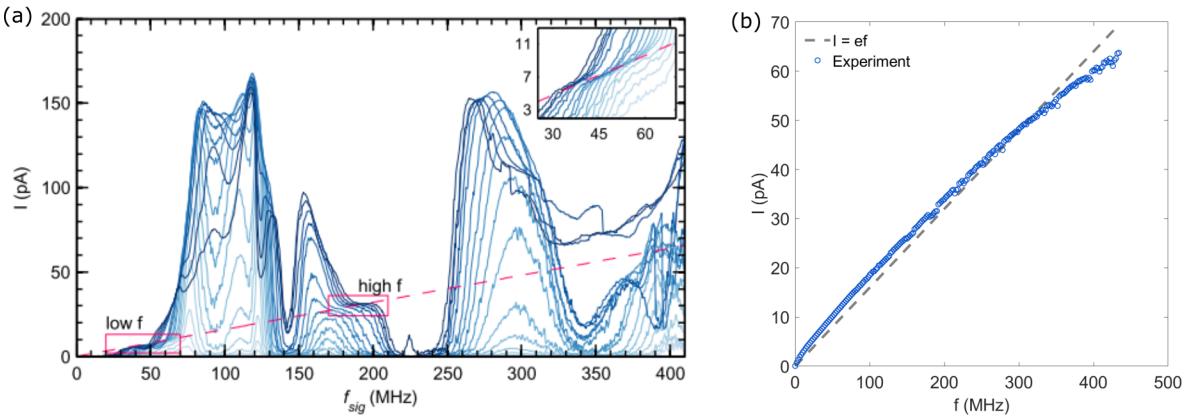

Fig. A.9: (a) Transmission of turnstile experiments carried out in a SC-QD-SC transistor by previous students. The current presents extremely large differences and drastic changes of tendencies at each frequency for varying amplitudes (color)). The turnstile regime is reached only at two small frequency windows around 60 and 200 MHz (extracted from [37]). (b) Measurements carried out in our SC-QD-SC transistors show a quasilinear dependence of the current at the turnstile plateaus with frequency. Values have been extracted from the measurement shown in Fig. A.8 averaging the current around the center of the plateau.

top of the plateaus are caused by the low bias at which this measurement is taken ($V_B = 50$ μeV).

FREQUENCY RESPONSE

Once demonstrated that our device actually behaves as a SC-QD-SC transistor at turnstile operation, we study the frequency response of the sample. Experiments carried out by previous students demonstrated a reduced frequency range of the turnstile operation of SC-QD-SC transistors. The range was limited between two narrow windows of $50 - 66$ and $190 - 206$ MHz. For the rest of the frequencies, currents showing enormous disparities with ef were observed (A.9a), attributed to the generation of standing waves along the cryogenic RF line because of the presence of impedance mismatches. As primary objective of my thesis project was to improve the turnstile operation range and accuracy, we implemented the combination of coplanar waveguide gate electrodes (matched at 50 Ω) with the electromigration constrictions, and carried out a careful installation of RF measurement lines in a new cryogenic setup (adapting as well the sampleholders). After all these improvements, the frequency response of SC-QD-SC transistors operated as turnstiles displayed a quasilinear and continuous dependence on f, carrying along an extraordinary increase of the frequency range of turnstile operation, ranging between $1 - 430$ MHz (A.9b). Extremely flat plateaus are observed at low frequencies (1-100 MHz), nevertheless showing a current value that surpass ef, attributed to the CPE processes observed in this sample (Fig. A.8). At higher frequencies (300-400 MHz) the current plateaus adopt a rather irregular shape at the summit, falling below ef. This behavior is in good agreement with missed tunneling events, becoming more common as the frequency is increased.

B Modeling the AC gate coupling

The turnstile operation of S-QD-S junctions requires a fast oscillation of the dot's chemical potential (ϵ_0), which can be induced by applying an AC signal to the gate electrode (as explained in Annex A). The amplitude of the ϵ_0 oscillation is denoted here by ϵ_{QD}^{AC} and is proportional to the oscillation amplitude selected in the wave signal generator of the laboratory (A_v),being the proportionality constant $\alpha_G^{AC} = \epsilon_0^{AC}/A_v$ denoted as the AC gate coupling parameter. In principle we assume that the change in ϵ_0 induced by a voltage applied to the gate is instantaneous, meaning that $\alpha_G^{AC} = \alpha_G$ were α_G is the DC gate coupling parameter that can be extracted from the stability diagram of a QD junction. For turnstile currents to be detectable, the AC oscillation must be in the radio-frequency (RF) range (typically $f = 0.1 - 10000$ MHz), which requires the installation of a transmission line in the cryogenic set-up (see Section 3.1.3). Different effects (arising from the transmission line materials, the location of the QD junction along the line, impedance mismatches...) can affect the propagation of RF signals in the line, modifying the oscillation amplitude reaching the gate electrode, for instance, diminishing the AC with respect to the DC gate couplings $\alpha_G^{AC} \leq \alpha_G$. Understanding how AC signals travel through the transmission line of our experimental set-up becomes fundamental for a correct interpretation of effects observed in turnstile operation. In this Annex we recall the theoretical description of the propagation of electromagnetic (EM) waves through a waveguide (transmission line), and particularize it to our system (antenna configuration) in an attempt to analyze the possible sources that can affect α_G^{AC} and reduce its effective value with respect to α_G.

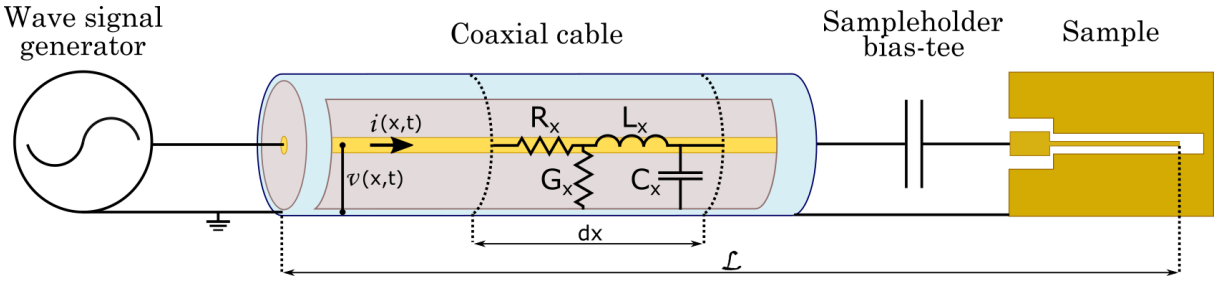

Fig. B.1: RF transmission line schematic. One end is connected to a wave signal generator, while the other side ends in the gate electrode edge. The line has been simplified as a single coaxial cable of length $\mathcal{L}$ divided into equivalent infinitesimal segments (dx), each of them modelled by the lumped elements R_x, G_x, C_x and L_x.

A transmission line is a circuit element that can propagate electromagnetic (EM) waves, where the voltage and current magnitude and phase oscillate in time and space, acting as a wave-guide. For this propagation to take place, two conductors are needed. Coaxial cables (with an inner conductor and a coaxial shield) or printed circuits with a CPW geometry (like our gate electrode) are different examples of the transmission line concept. To start with, we model our RF transmission line as divided into infinitesimal elements of length dx, as sketched in Fig. B.1, following the so-called lumped elements approximation [263]. Each of these elements is characterized by the following quantities:

- R_x is the series resistance per unit length of the inner conductor.
- G_x is the conductance per unit length between both conductors.
- L_x is the series inductance per unit length of the inner conductor.
- C_x is the capacitance per unit length between both conductors.

These four parameters define the characteristic impedance (Z_0) of the infinitesimal transmission line element, where L_x and C_x dictate the dynamic behavior (introducing phases in the signals), and R_x and G_x represent the power losses of the line (attenuating the signals amplitudes). Most of the transmission line in our set-up consist of on-series coaxial cables, connected through SMA connectors and attenuators, all of them with an specified characteristic impedance of $Z_0 = 50\ \Omega$. Also, our gate electrode GCPW design was done to ensure its impedance-matching at $50\ \Omega$ (see Chapter 2). However, the sample-holders RF bonding pads (including the home-made bias tee) and the micro-bonding wires are not impedance-matched. In this approximation we will consider R_x, G_x, C_x and L_x (and therefore Z_0) constant along the whole transmission line length for the analytical calculation, and impedance mismatching effects will be discussed at the end of the Annex. To finish with, the impedance at the extremes of the transmission line ($x = 0, \mathcal{L}$), defined by the boundary conditions, will impose the transmission characteristics of the line, as it will be shown later.

TELEGRAPHER'S EQUATIONS SOLUTION

Our starting point is the Telegrapher's equations system, obtained by applying Kirchhoff's laws to an infinitesimal transmission line element:

$$\begin{cases} \dfrac{\partial v(x,t)}{\partial x} = -R_x i(x,t) - L_x \dfrac{\partial i(x,t)}{\partial t}, & \text{(B.0.1a)} \\ \dfrac{\partial i(x,t)}{\partial x} = -G_x v(x,t) - C_x \dfrac{\partial v(x,t)}{\partial t}. & \text{(B.0.1b)} \end{cases}$$

The Telegrapher's equations give an expression for the voltage (v) and the current (i) in the transmission line as a function of position (x) and time (t). We shall consider solutions in the form of monochromatic waves, with a time-frequency oscillation ω, which can be written as $v(x,t) = V(x)e^{j\omega t}$ and $i(x,t) = I(x)e^{j\omega t}$ (j is the imaginary unit). If we insert these solutions in the Telegrapher's equations, the time-dependent part disappears:

$$\begin{cases} \dfrac{dV(x)}{dx} = -(R_x + j\omega L_x) I(x), & \text{(B.0.2a)} \\ \dfrac{dI(x)}{dx} = -(G_x + j\omega C_x) V(x). & \text{(B.0.2b)} \end{cases}$$

Now, by deriving and substituting the first order derivatives, we arrive to a system of two uncoupled second-order wave equations:

$$\begin{cases} \dfrac{d^2V(x)}{dx^2} - \nu^2 V(x) = 0, & \text{(B.0.3a)} \\ \dfrac{d^2I(x)}{dx^2} - \nu^2 I(x) = 0, & \text{(B.0.3b)} \end{cases}$$

where ν is a complex number, usually referred to as the propagation constant, whose real and imaginary parts (α and k) represent the line attenuation and the wave number:

$$\nu = \alpha + jk = \sqrt{(R_x + j\omega L_x)(G_x + j\omega C_x)}. \quad \text{(B.0.4)}$$

The particular solutions of this kind of wave equations are traveling waves propagating in opposite space directions. Therefore, the general solution is a linear combination of both of them:

$$\begin{aligned} v(x,t) &= V_0^+ e^{j\omega t} e^{-\nu x} + V_0^- e^{j\omega t} e^{+\nu x} \\ &= V_0^+ e^{j(\omega t - kx)} e^{-\alpha x} + V_0^- e^{j(\omega t + kx)} e^{+\alpha x}, \end{aligned} \quad \text{(B.0.5)}$$

$$\begin{aligned} i(x,t) &= I_0^+ e^{j\omega t} e^{-\nu x} + I_0^- e^{j\omega t} e^{+\nu x} \\ &= I_0^+ e^{j(\omega t - kx)} e^{-\alpha x} + I_0^- e^{j(\omega t + kx)} e^{+\alpha x}. \end{aligned} \quad \text{(B.0.6)}$$

The complex coefficients $V_0^{\pm}$ and $I_0^{\pm}$ represent the corresponding amplitudes and phases of each traveling wave. They are related by the characteristic impedance (Z_0), whose dependence on the transmission line parameters can be obtained by plugging these expressions for v and i in Eqs. (B.0.1):

$$Z_0 = \frac{V_0^+}{I_0^+} = -\frac{V_0^-}{I_0^-} = \sqrt{\frac{R_x + j\omega L_x}{G_x + j\omega C_x}}. \tag{B.0.7}$$

GENERATOR/OPEN-CIRCUIT BOUNDARY CONDITIONS

The complex coefficients $V_0^{\pm}$ and $I_0^{\pm}$ can be determined by specific boundary conditions of a particular problem. In the case of our interest, the transmission line is connected to a wave signal generator on one end ($x = 0$), that generates a voltage signal of frequency $f = \omega/2\pi$ and amplitude A_v. The voltage wave induces at the same time a current wave of amplitude A_i. This imposes the boundary conditions at this extreme of the line, leading to Eqs. (B.0.8a and b). It must be noted that both amplitudes are related by $A_v = Z_{in}A_i$, where Z_{in} is called the input impedance of the equivalent circuit seen by the wave signal generator. Hence, Z_{in} represents the total impedance of the whole transmission line and it will be calculated later. The output connectors of standard signal generators are matched at 50 Ω allowing us to neglect an internal impedance term.

At the opposite extreme ($x = \mathcal{L}$), the transmission line ends in the sample's gate electrode extremal edge, which displays a very large resistance to ground (~ 1 TΩ at base temperature). This dead end implies an open-circuit boundary condition that makes the characteristic impedance to diverge ($Z_{\mathcal{L}} \to \inf$). As the impedance becomes infinite, the current at $x = \mathcal{L}$ must vanish at all times which, combined with the first Telegrapher's equation, imposes that the derivative of the voltage is zero, leading to Eqs. (B.0.8c and d). Grouping the four boundary conditions, we have:

$$\begin{cases} v(0,t) = A_v e^{j\omega t}, & \text{(B.0.8a)} \\ i(0,t) = A_i e^{j\omega t}, & \text{(B.0.8b)} \\ \dfrac{\partial v(x,t)}{\partial x}\Big|_{x=\mathcal{L}} = 0, & \text{(B.0.8c)} \\ i(\mathcal{L},t) = 0. & \text{(B.0.8d)} \end{cases}$$

This situation corresponds to an antenna, where the transmitted waves (sent in by the generator) get totally reflected at the gate's extremity and the subsequent interference leads to the establishment of a standing wave along the whole transmission line for both voltage and current. Paradoxically, in the opposite case of a short-circuit at the end of the line ($Z_{\mathcal{L}} \to 0$), the corresponding boundary conditions for voltage and current appear interchanged, in the same way originating a total reflection that also results in the generation of whole-line standing waves.

By applying the corresponding boundary conditions into the expressions (B.0.5) and (B.0.6), we obtain an equations system that relates the four complex coefficients in terms of the characteristics of the transmission line (implicit in ν) and the signal sent by the wave signal generator (A_v and A_i):

$$\begin{cases} V_0^+ + V_0^- = A_v, & \text{(B.0.9a)} \\ I_0^+ + I_0^- = A_i, & \text{(B.0.9b)} \\ \dfrac{V_0^+}{V_0^-} = e^{2\nu\mathcal{L}}, & \text{(B.0.9c)} \\ \dfrac{I_0^+}{I_0^-} = -e^{2\nu\mathcal{L}}. & \text{(B.0.9d)} \end{cases}$$

If we solve the system, we obtain expressions for the traveling waves complex coefficients:

$$\begin{cases} V_0^+ = \dfrac{A_v}{1+e^{-2\nu\mathcal{L}}}, & \text{(B.0.10a)} \\ V_0^- = \dfrac{A_v}{1+e^{2\nu\mathcal{L}}}, & \text{(B.0.10b)} \\ I_0^+ = \dfrac{A_i}{1-e^{-2\nu\mathcal{L}}}, & \text{(B.0.10c)} \\ I_0^- = \dfrac{A_i}{1-e^{2\nu\mathcal{L}}}. & \text{(B.0.10d)} \end{cases}$$

Having found the values of the standing waves complex coefficients, the only remaining task to obtain a complete insight of the solution would be to extract the real part of the voltage and current waves in Eqs. (B.0.5) and (B.0.6). In order to simplify it, we will take a last theoretical approximation by considering a lossless transmission line.

LOSSLESS TRANSMISSION LINE APPROXIMATION

In the lossless transmission line approximation, the resistive components (and therefore the attenuation) are neglected ($R_x, G_x = 0 \rightarrow \alpha = 0$). As a consequence, the propagation constant becomes a pure imaginary number ($\nu = jk$), and Eq. (B.0.4) results in a linear dispersion relation $\omega = kv_p$, where the propagation speed (phase velocity) $v_p = 1/\sqrt{L_x C_x}$ is constant (independent of k). In this situation, waves propagate at the same speed along the line for any wave number k, and the characteristic impedance of the line is a real number ($Z_0 = \sqrt{L_x/C_x}$). Under these considerations, the expression for the complex coefficients in Eqs. (B.0.10) can be rewritten as:

$$\begin{cases} V_0^+ = \dfrac{A_v}{2\cos(k\mathcal{L})}e^{jk\mathcal{L}} = \dfrac{A_v}{2}\big[1 + j\tan(k\mathcal{L})\big], & \text{(B.0.11a)} \\ V_0^- = \dfrac{A_v}{2\cos(k\mathcal{L})}e^{-jk\mathcal{L}} = \dfrac{A_v}{2}\big[1 - j\tan(k\mathcal{L})\big], & \text{(B.0.11b)} \\ I_0^+ = -j\dfrac{A_i}{2\sin(k\mathcal{L})}e^{jk\mathcal{L}} = \dfrac{A_i}{2}\big[1 - j\cot(k\mathcal{L})\big], & \text{(B.0.11c)} \\ I_0^- = j\dfrac{A_i}{2\sin(k\mathcal{L})}e^{-jk\mathcal{L}} = \dfrac{A_i}{2}\big[1 + j\cot(k\mathcal{L})\big]. & \text{(B.0.11d)} \end{cases}$$

Although A_v is imposed by the wave signal generator and therefore it is a real number, in general A_i is a complex number. However, in an electromagnetic wave, Maxwell equations impose a phase of $\pi/2$ between the electric and the magnetic fields, or equivalently, between the voltage and the current of AC signals. Therefore, the amplitude A_i must be imaginary and it can be derived from Eq. (B.0.7), expressed in terms of A_v and the transmission line characteristic impedance per unit length which, in our case, is $Z_0 = 50\ \Omega$. In addition, it is possible to extract the equivalent input impedance of the whole transmission line circuit Z_{in}:

$$\begin{aligned} Z_0 = \frac{V_0^+}{I_0^+} = -\frac{V_0^-}{I_0^-} = j\frac{A_v}{A_i}\tan(k\mathcal{L}) \rightarrow \\ \rightarrow A_i = j\frac{A_v}{Z_0}\tan(k\mathcal{L}) = j\frac{A_v}{\sqrt{L_x/C_x}}\tan(k\mathcal{L})\,, & \text{(B.0.12)} \\ \rightarrow Z_{in} = \frac{A_v}{A_i} = \frac{Z_0}{j}\cot(k\mathcal{L}) = -j\sqrt{L_x/C_x}\cot(k\mathcal{L})\,. & \text{(B.0.13)} \end{aligned}$$

We recover the well-known results of lossless transmission lines in an antenna configuration (with an open-circuit condition, see [264, 265]). We can rewrite Eqs. (B.0.11c and d), so that all the

complex coefficients are expressed in real/imaginary and modulus/argument notation:

$$\begin{cases} V_0^+ = \dfrac{A_v}{2\cos(k\mathcal{L})} e^{jk\mathcal{L}} = \dfrac{A_v}{2}\big[1 + j\tan(k\mathcal{L})\big], & \text{(B.0.14a)} \\ V_0^- = \dfrac{A_v}{2\cos(k\mathcal{L})} e^{-jk\mathcal{L}} = \dfrac{A_v}{2}\big[1 - j\tan(k\mathcal{L})\big], & \text{(B.0.14b)} \\ I_0^+ = \dfrac{A_v}{2Z_0\cos(k\mathcal{L})} e^{jk\mathcal{L}} = \dfrac{A_v}{2Z_0}\big[1 + j\tan(k\mathcal{L})\big], & \text{(B.0.14c)} \\ I_0^- = \dfrac{A_v}{2Z_0\cos(k\mathcal{L})} e^{j(\pi - k\mathcal{L})} = \dfrac{A_v}{2Z_0}\big[-1 + j\tan(k\mathcal{L})\big]. & \text{(B.0.14d)} \end{cases}$$

By injecting these coefficients into Eqs. (B.0.5) and (B.0.6) and taking the real part, we obtain the final expressions for the voltage and the current:

$$\begin{aligned} v(x,t) &= \frac{A_v}{2\cos(k\mathcal{L})}\big[e^{j(\omega t - k(x-\mathcal{L}))} + e^{j(\omega t + k(x-\mathcal{L}))}\big] \rightarrow \\ &\rightarrow \mathrm{Re}(v) = \frac{A_v}{\cos(k\mathcal{L})}\cos(\omega t)\cos(k(\mathcal{L}-x)), \end{aligned} \tag{B.0.15}$$

$$\begin{aligned} i(x,t) &= \frac{A_v}{2Z_0\cos(k\mathcal{L})}\big[e^{j(\omega t - k(x-\mathcal{L}))} + e^{j(\omega t + k(x-\mathcal{L}) + \pi)}\big] \rightarrow \\ &\rightarrow \mathrm{Re}(i) = -\frac{A_i}{Z_0\cos(k\mathcal{L})}\sin(\omega t)\sin(k(\mathcal{L}-x)). \end{aligned} \tag{B.0.16}$$

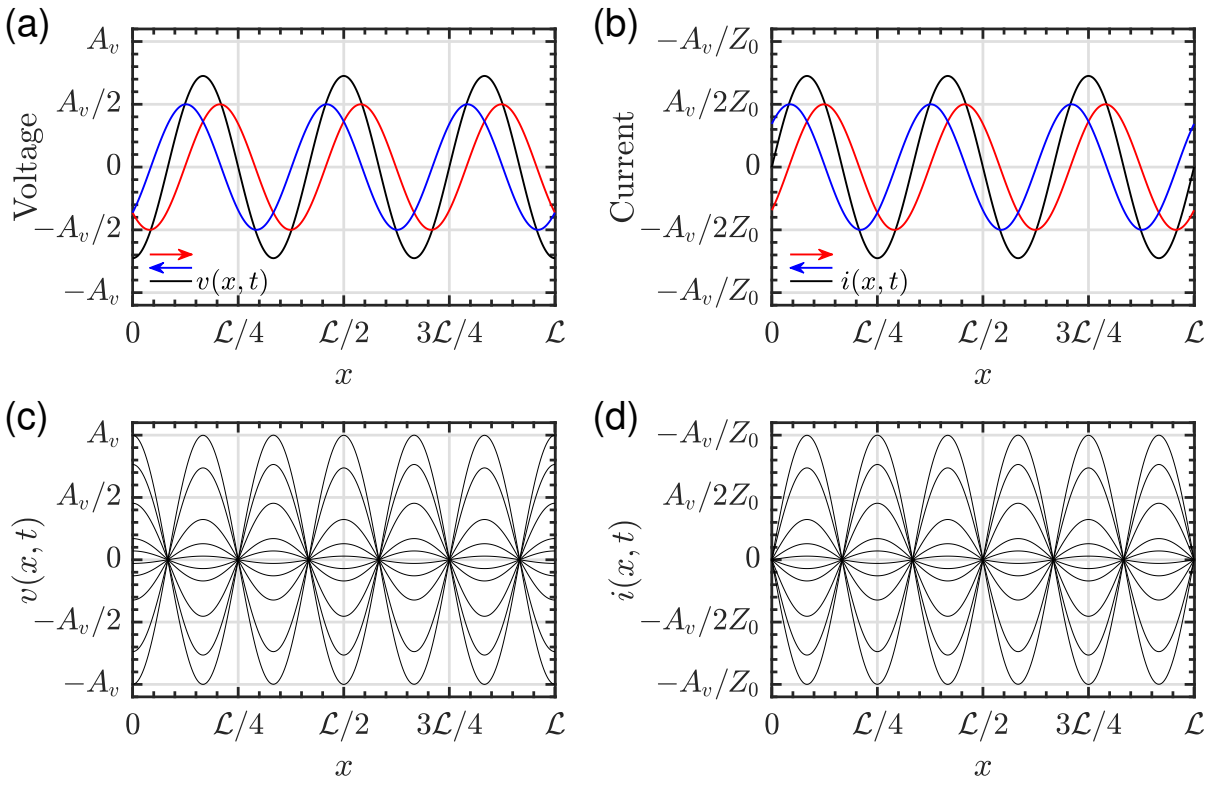

Fig. B.2: (a and b) The expressions obtained for the voltage (a) and current (b) stationary waves (Eqs. B.0.15 and B.0.16, colored in black) match with the sum of the real part of waves traveling to the right ($\cos(\omega t - kx)$, in red) and to the left ($\cos(\omega t + kx)$, in blue) multiplied by the corresponding coefficients ($V_0^{\pm}$ and $I_0^{\pm}$). The voltage (c) and current (d) stationary waves plotted at different times display the complete oscillation, showing the distribution of nodes and anti-nodes along the line. For graphic purposes we have chosen $\mathcal{L} = 3\lambda = 6\pi/k$.

By representing the opposite-direction traveling waves (accounting for the $\pi/2$-phase shift between voltage and current), we can observe that their sum corresponds to the voltage and current real part extracted in Eqs. B.0.15 and B.0.15 (Figs. B.2a and b respectively). The amplitude of the stationary waves changes (as it can be observed in Figs. B.2c and d) while a series of nodes and anti-nodes (where the oscillation is zero and maximum, respectively) are distributed along the line's length.

The variation of the oscillation amplitude introduces a dependence of the AC gate coupling parameter on the position of the QD junction (x_{QD}) on the gate electrode. If x_{QD} is placed at an anti-node, then the coupling is maximum and $\alpha_G^{AC} = \alpha_G$, whereas if it is placed at a node, the oscillation vanishes and $\alpha_G^{AC} = 0$, following a sinusoidal dependence in between. As imposed by the boundary conditions, we can see in Fig. B.2c that an anti-node of the voltage wave is present at the extreme of the gate electrode ($x_{anti} = \mathcal{L}$), while the closer node is at a distance of $\lambda/4$ from the edge, i.e., at $x_{node} = \mathcal{L} - \lambda/4$ (where $\lambda = 2\pi/k$ is the wavelength of the AC signal). The distribution of nodes and anti-nodes depends on k and, through the dispersion relation, on the selected oscillation frequency $\omega = kv_p$. The nominal value for the propagation speed of the coaxial wires installed in our measurement set-up (type UT85B-SS [251]) is $v_p = 0.7c = 2.1\ 10^8$ m/s, being c the speed of light in vacuum. In the turnstile experiments, we worked with signals of frequencies typically in the range of $\Delta f = (0.1 - 1000)$ MHz, or equivalently $\Delta\omega = 2\pi(0.1 - 1000)\ 10^6$ s^{-1}, leading to a wave number range of $\Delta k = 0.95\pi(0.001 - 10)$ m^{-1} (or equivalently a wavelength range of $\Delta\lambda = 2.1(0.1 - 1000)$ m). Therefore, the smaller wavelengths we use are $\lambda^{min} \approx 0.2$ m, meaning that the closer node distance to the gate end is $d_{node}^{min} = \mathcal{L} - x_{node} = \lambda^{min}/4 = 5$ cm. On the other hand, the electromigration junctions in our sample design extend over a length of 90 μm and they are at a distance of $d_{QD} = \mathcal{L} - x_{QD} = 150 - 240$ μm from the edge of the gate electrode. We observe that this distance is negligible compared with the closest node distance in our frequency range ($d_{QD} << d_{node}^{min}$), hence, we expect our junctions to be relatively close to the gate edge anti-node so that $\alpha_G^{AC} \approx \alpha_G$. However, the frequency dependence of the nodes/anti-nodes distribution ($\lambda = v_p/f$) may introduce detectable variations in α_G^{AC} for different values of the AC signal frequency $f = 2\pi\omega$. We can derive the following expression for α_G^{AC} in terms of f and d_{QD} from Eq. (B.0.15), corresponding to the spatial modulation of the stationary wave amplitude:

$$\alpha_G^{AC}(f) = \cos(kd_{QD})\ \alpha_G = \cos\left(\frac{2\pi f}{v_p} d_{QD}\right)\ \alpha_G \tag{B.0.17}$$

RESONANCE OF THE CIRCUIT

Surprisingly, the presence of a dividing term with the form $\cos(k\mathcal{L})$ in the stationary waves in Eqs. (B.0.15) and (B.0.16) leads to a divergence of the oscillation amplitudes for values of k such that $k\mathcal{L} = (2n-1)\pi/2$ with n being a natural number (note that away from the dissipationless ideal case, the divergence vanishes). For a transmission line length of $\mathcal{L} = 2$ m, the divergence wave numbers are $k_{res} = (2n-1)\pi/4 \approx 0.8, 2.4, 3.9, 5.5, ...$ m^{-1}, which correspond to $f_{res} = v_p k/2\pi = 2.1\ 10^8(2n-1)/8 \approx 25, 75, 125, 175, ...$ MHz. These values are just in the range of frequencies we use for turnstile experiments. Taking a look at the expression of the circuit input impedance Z_{in} (B.0.13), proportional to $\cot(k\mathcal{L})$, we observe that if $k = k_{res} \rightarrow Z_{in} = 0$ (Fig. B.3a). For values of the frequency such that $f = f_{res}$, the circuit impedance from the wave generator point's of view is zero, and therefore the amplitude of the voltage and current oscillation diverges ($A_v, A_i \rightarrow \infty$). In order to study the magnitude of this effect, we modified the RF circuit, connecting the gate electrode's end to another RF line that brings the signal out of the cryostat to a transmission readout (which conserves the open-circuit boundary condition), as depicted in Fig. B.3b. The transmission of the line follows a bumpy-like trace with a relatively flat region at the range of 400–800 MHz, and a spiky periodic structure is superimposed indicating the resonance frequencies f_{res} of the circuit (Fig. B.3c).

From the perspective of turnstile operation, the divergences of A_v will result in an tangent-function-like increase of the oscillation of ϵ_0 as f approaches f_{res}, being equivalent to an effective increase

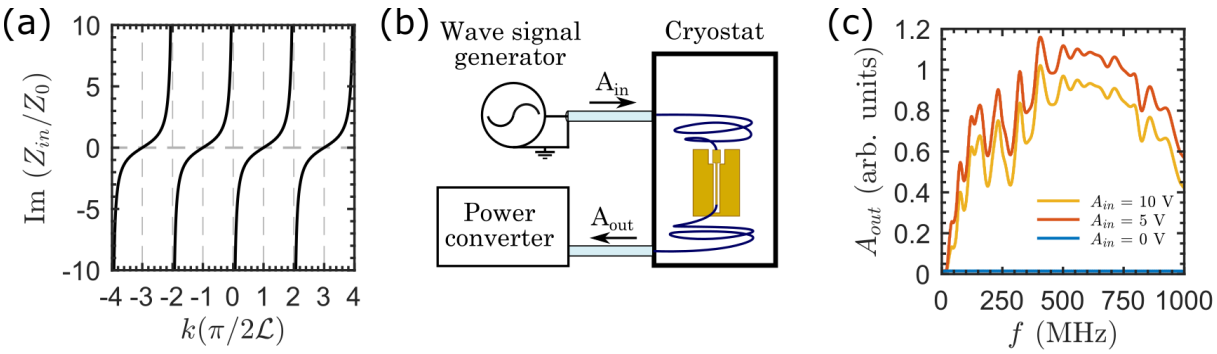

Fig. B.3: (a) Input impedance of a lossless transmission line in open-circuit configuration as a function of the wave number k. The impedance vanishes when k is an odd number of times $\pi/2\mathcal{L}$ leading to a divergence of the oscillation amplitudes. (b) Schematic of the transmission line testing circuit. The signal generator sends a wave of frequency f and amplitude A_{in} into the transmission line. The end of the gate electrode is connected to a secondary line that brings the signal out of the cryostat into a power detector (model ZX47-50LN-S+), that reads the output amplitude A_{out}. (c) A_{out} as a function of f for different A_{in}. Periodically-spaced peaks of A_{out} reveal at the resonance frequencies of the line.

of A_v. This increment of ϵ_0^{AC} may lead to a surpass of the turnstile V_B region (delimited by the superconducting gap Δ), effectively decreasing the net current below ef due to tunneling events of electrons in the QD to/from the wrong electrode. Taking these resonances into consideration, we shall introduce a diverging term in the previous expression for α_G^{AC} (B.0.17):

$$\alpha_G^{AC}(f) = \frac{\cos(kd_{QD})}{\cos(k\mathcal{L})}\,\alpha_G = \frac{\cos(2\pi f d_{QD}/v_p)}{\cos(2\pi f \mathcal{L}/v_p)}\,\alpha_G. \tag{B.0.18}$$

VOLTAGE STANDING WAVE RATIO

From our previous analysis we concluded that when a wave traveling in a transmission line of constant impedance Z_0 reaches a position x, where the impedance of the line changes (becoming Z_x), the mismatch induces a certain reflection of the incoming wave. This effect is typically quantified in terms of the voltage reflection coefficient, defined as:

$$\Upsilon_x = \frac{V_0^- e^{\nu x}}{V_0^+ e^{-\nu x}} = \frac{Z_x - Z_0}{Z_x + Z_0}. \tag{B.0.19}$$

The expression for the voltage wave (B.0.5) can be rewritten as:

$$\begin{aligned} v(x,t) &= V_0^+ e^{j\omega t} e^{-\nu x} + V_0^- e^{j\omega t} e^{+\nu x} \\ &= V_0^+ e^{j\omega t} e^{-\nu x}\big[1 + \Upsilon_x\big]. \end{aligned} \tag{B.0.20}$$

A perfectly impedance-matched transmission line with an open-circuit end, as we have considered so far, is an elementary case in which the line has a perfectly constant impedance per unit length Z_0 along its whole extension (leading to $\Upsilon_x = 0$), with exception of a load at its extremity $\mathcal{L}$, where $Z_\mathcal{L}$ diverges. By making $Z_\mathcal{L} \to \inf$, we that the reflection coefficient $\Upsilon_\mathcal{L} \to 1$ from Eq. (B.0.19), indicating the total reflection of the wave. However, actual transmission lines may have many different impedance mismatches $(Z_1, Z_2, Z_3, ...)$ distributed along their length (at positions $x_1, x_2, x_3, ...$), for example, originated by an excessive bending of the coaxial cable, which can induce some damage of the dielectric media. Commercial RF connectors and attenuators (present at different locations of the RF line as indicated in section 3.1.3) may also introduce a certain impedance mismatch. Different values of the reflection coefficient $(\Upsilon_1, \Upsilon_2, \Upsilon_3, ...)$ at each mismatch will partially reflect the wave and originate opposite traveling waves with an arbitrary phase, leading to a certain destructive interference

with the incoming wave, overall resulting in the generation of a standing waves distribution between the mismatches, with different maximum oscillation amplitudes ($A_{v1}, A_{v2}, A_{v3}, ... \leqslant A_v$). Impedance mismatches are often difficult to detect and evaluate in experimental set-ups, which makes extremely hard to extrapolate the values of Υ_x and $A_v(x)$ and each position along the line. Instead, an equivalent circuit perfectly matched (from its beginning at the wave signal generator to its extremity at the sample) is considered, where the equivalent impedance $Z_{\mathcal{L}} = Z_1 + Z_2 + Z_3 + ...$ is employed to estimate an equivalent reflection coefficient $\Upsilon_{\mathcal{L}}$. The voltage-standing-wave-ratio (VSWR) is then defined as the ratio between the maximum (A_v^{max}, generally equal to A_v for impedance-matched signal generators) and the minimum (A_v^{min}) standing-wave amplitudes:

$$\text{VSWR} = \frac{A_v^{min}}{A_v^{max}} = \frac{1 + |\Upsilon_{\mathcal{L}}|}{1 - |\Upsilon_{\mathcal{L}}|}. \tag{B.0.21}$$

In general, the quality of a transmission line is defined in terms of its VSWR, which ideally is equal to one (or equivalently, $\Upsilon_x = 0$ at all x positions), indicating a perfect transmission. In our experimental set-up, we intend to have a perfect transmission along the line except at the gate electrode end ($\Upsilon_{\mathcal{L}} = 0$). Per contra, our transmission line is not matched at the sample-holder stage (bias tee and micro-bonding wire), occasioning a VSWR < 1 that will induce certain reduction of the effective oscillation amplitude of the voltage wave that arrives to the gate electrode with respect to the generator's one. New technologies allowing to contact the lithography-defined electrodes to an RF line with an impendance-matched connection inside a cryogenic set-up are currently under development to replace the classical unmatched micro-bonding wires (explained in Annex C). We expect the micro-bonding wires connecting the sample and the sample-holder RF pads to induce a certain reflection, that will reduce even further the oscillation amplitude at the gate electrode, and consequently α_G^{AC}. Since the gate electrode is at the end of the circuit, reached by the voltage signal after traversing all possible mismatches, we assume the worst case scenario and take the oscillation at the gate as A_v^{min}. Taking this into account, the final expression for α_G^{AC} can be written simply like:

$$\alpha_G^{AC}(f) = \text{VSWR}(f)\, \frac{\cos(k d_{QD})}{\cos(k\mathcal{L})}\, \alpha_G = \text{VSWR}(f)\, \frac{\cos(2\pi f d_{QD}/v_p)}{\cos(2\pi f \mathcal{L}/v_p)}\, \alpha_G, \tag{B.0.22}$$

where the VSWR introduces an additional frequency dependence, dragged from the definition of Υ (B.0.19).

In conclusion, the AC coupling in our QD junction will generally depend on the frequency f of the RF signal, both for experimental reasons (impossibility of having a perfectly impedance-matched transmission line down to the gate electrode) and fundamental reasons (even if the electromigration junctions are placed precisely at the gate electrode end, the fact that the line has a finite length will originate divergences for certain frequencies). By patterning the electromigration constrictions close to the gate end in our sample design, we tried to maximize the coupling to the voltage oscillation of the anti-node in the gate's end. In any case, the AC gate coupling parameter must be calibrated independently in each different junction, using the turnstile current as tool to obtain information on the frequency response of the QD.

C Grounded coplanar waveguide simulations

In the previous Annex (B), we discuss the importance of having an impedance-matched transmission line to avoid the generation of standing waves due to partial reflections inducing destructive interference of radio-frequency (RF) signals. In experimental nano-electronics, samples are commonly glued to the sample-holder and their bonding pads are micro-bonded to the sample holder pads, which are connected to the cryostat electrical lines. Since micro-bonding wires are not coaxial or impedance-matched, often few micro-bonding wires are bonded between the sample's and the sample-holder's RF pad (instead of just a single wire, as it is done for DC lines). Microelectronics die-mounting techniques that allow an impedance-matched connection to an integrated planar circuit, like the chip-flip method [266, 267, 268] are currently under development for their adaptation to cryogenic set-ups and nano-circuit samples. However, transmission measurements performed with a vector network analyzer show that the transmittivity of sample-holder's RF pads connected by several micro-bonding wires do not decrease significantly with respect to unity up to 1 GHz (equivalently, VSWR ≈ 1).

In spite of proper transmission measured at the sample-holder connections, turnstile measurements in S-QD-S junctions with an unmatched gate electrode carried out in the past by previous students, revealed a strong frequency-dependence of the RF signal amplitude arriving at the gate electrode. These results enlightened the necessity of changing the sample design in order to match the impedance of the gate electrode to the rest of the RF cryogenic transmission line (50Ω), constituting the main objective of this project in terms of sample fabrication. The Grounded-CoPlanar-Waveguide (GCPW) geometry (Fig. C.1a), allows one to modify the impedance of a lithographically patterned electrode depending on specific sizes of its design (which can be adapted in the lithographic virtual masks) and the characteristics of the substrate (Fig. C.1b). We adopted this GCPW configuration for our gate electrode model. The size parameters (w_w,s_w) of our design were calculated by performing simulations for different available substrate materials (ε_R) and thicknesses (h_w), to match an impedance of 50Ω. In a GCPW configuration, the impedance of the transmission line Z_0 is given by;

$$Z_0 = \frac{60\pi}{\sqrt{\varepsilon_{eff}}} \frac{1}{\frac{K(k)}{K(k')} + \frac{K(kl)}{K(kl')}}, \tag{C.0.1}$$

where ε_{eff} represents an effective dielectric permittivity of the whole media, and K is the first kind elliptical integral ([269]). The effective dielectric permittivity (ε_{eff}) derives from an extrapolation of two semi-infinite media around the transmission line, one of them being vacuum (ε_0), and the other one a certain material with a certain relative dielectric permittivity, ε_R. The first kind elliptical integral K also appears in the definition of ε_{eff}:

$$\varepsilon_{eff} = \frac{1 + \varepsilon_R \frac{K(k')}{K(k)} \frac{K(kl)}{K(kl')}}{1 + \frac{K(k')}{K(k)} \frac{K(kl)}{K(kl')}}, \tag{C.0.2}$$

The four integration variables are related to the characteristic sizes of the design (w, s_w, h):

$$\begin{cases} k = w_w/s_w, & \text{(C.0.3a)} \\ k' = \sqrt{1-k^2}, & \text{(C.0.3b)} \\ kl = \dfrac{\tanh\left(\frac{w_w \pi}{4h_w}\right)}{\tanh\left(\frac{s_w \pi}{4h_w}\right)}, & \text{(C.0.3c)} \\ kl' = \sqrt{1-kl^2}. & \text{(C.0.3d)} \end{cases}$$

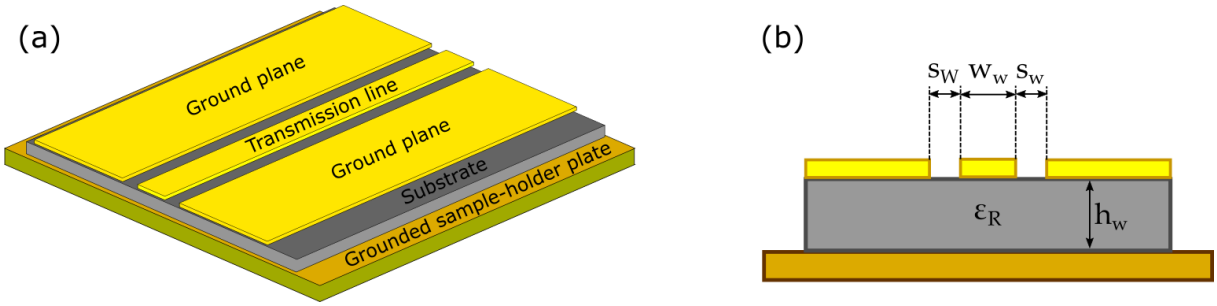

Fig. C.1: (a) 3D model of a printed circuit following the GCPW architecture. The central electrode (the gate in our case), usually called transmission line electrode, carries the RF signal and it is placed in between two metallic plates of the same thickness that are connected to the ground of the system (often called ground planes). The circuit has been printed on a semiconducting or insulating substrate, and has a thickness of h. The whole sample is placed (glued or grown) on a grounded metallic plate, which represents for us the sample-holder. (b) Cross-sectional view of (a), the parameters that define the impedance of the transmission line are its width (w), the spacing with respect to the ground planes (s_w), the relative dielectric permittivity of the substrate ε_R and its thickness h.

The method employed to evaluate the elliptical integrals consists in the iterative calculation of three parameters (a, b, c), with initial values depending on the GCPW sizes through the integration variables k, k', kl, kl':

$$\begin{cases} a_0 = 1, & \text{(C.0.4a)} \\ b_0 = \sqrt{1-k^2}, & \text{(C.0.4b)} \\ c_0 = k. & \text{(C.0.4c)} \end{cases}$$

In each iteration (N) of this method, the new parameters a, b and c depend on their values in the previous round $(N-1)$, and an approximated evaluation of the integral K is obtained. After each consecutive iteration, the precision of the value for K (given by c) increases.

$$\begin{cases} a_N = \dfrac{a_{N-1}+b_{N-1}}{2}, & \text{(C.0.5a)} \\ b_N = \sqrt{a_{N-1}b_{N-1}}, & \text{(C.0.5b)} \\ c_N = \dfrac{a_{N-1}-b_{N-1}}{2}, & \text{(C.0.5c)} \\ K(k) = \dfrac{\pi}{2a_N}, & \text{(C.0.5d)} \end{cases}$$

Turnstile current measurements (appearing in Annex A.3) carried out in one of our S-QD-S junctions and driven with an impedance-matched GCPW-gate electrode fabricated following the specifications of this model, illustrate that the induced oscillation in the QD's chemical potential is rather independent on the RF signal frequency. These results demonstrate the flat transmittance of our GCPW design up to frequencies of, at least, few hundred MHz, above which missed tunneling events introduce a decrease of the current due to the feeble coupling of this particular QD. The comparison between unmatched and matched gate electrodes shows a great improvement in the turnstile current of our samples at different frequencies, and the resounding success of the GCPW design implementation.

D Nano-fabrication recipe

This Annex is a compilation of all the adjusted fabrication parameters we employed in our sample fabrication. The substrate employed were 2-inch intrinsic silicon <110> wafers (with a resistivity around 8000 Ω cm and a thickness of 275 μm). A procedure based on three lithography steps and an oxide layer growth allow us to fabricate simultaneously few hundreds of individual chips. Each chip can be cooled down at a time and it contains 30 electromigration constrictions divided in two arrays.

In the first lithography (Tab. D.1), we clean the substrate and pattern the structures corresponding to the gate electrode, the ground planes and the alignment marks. It is important to align the structures with the crystalline axis of the substrate to avoid accidentally breaking the chips at the later wafer-dicing stage.

Gate electrode lithography			
Step	**Description**	**Equipment**	**Parameters**
0	Cleaning	Acetone, ethanol, IPA, N_2	Rinse and dry
1	RIE O_2 plasma	Plassys Ion milling	5 min with 20 W, 45 sccm, 0.07 mbars
2	Pre-Bake	Hotplate	4 min at $185°$C
3	Spincoat LOR3A	Spincoater Spin150	30 s at 6000 rpm
4	Bake LOR3A	Hotplate	2 min at $185°$C
5	Spincoat S1805	Spincoater Spin150	30 s at 6000 rpm
6	Bake S1805	Hotplate	1 min at $115°$C
7	Laser exposure	Heidelberg DWL 66	Dose of 68 mW/cm^2
8	Development	MF26A DI water and N_2	60 s rinse and dry
9	RIE O_2 plasma	Plassys Ion milling	5 s with 20 W, 45 sccm, 0.07 mbars
10	Metal evaporation	Plassys MEB550S	3 nm Ti (0.3 Å/s) 30 nm Au (0.3 Å/s)
11	Lift off	Acetone (pippeting) Sonication (optional) Remover PG	pippeting after 10 min 1 min at 40-60% power $\geq$ 1 hour at $80°$C
12	Cleaning	Acetone, ethanol, IPA, N_2	Rinse and dry
13	RIE O_2 plasma	Plassys Ion milling	5 min with 20 W, 45 sccm, 0.07 mbars

Tab. D.1: Detailed recipe for laser lithography with a LOR3A-S1805 bilayer resist.

The last step in the gate electrode lithography (RIE O_2 plasma) is not done directly after lift-off and cleaning but right before the oxide growth to ensure a clean surface, getting rid of any remaining resist residues. For the ALD growth of ZrO_2, we employed the standard TDMAZ precursor ($Zr(N(CH_3)_2)_4$)

sold by Sigma-Aldrich. All the measurements shown in this document were done in samples where 180 growth cycles as the one shown in Tab. D.2 were done (corresponding to an oxide layer of ≈ 18 nm). After the oxide layer is grown in the wafer, we restrict the duration of RIE O_2 plasma at 20 W for cleaning the sample surface to a maximum of 5 seconds.

Insulating oxide growth			
Fixed parameters	**Step**	**Operation**	**time(s)**
Precursor temperature: $90°$	1	TDMAZ injection	0.015
Tee temperature: $150°$	2	Waiting time	120
Chamber temperature: $100°$	3	H_2O injection	0.015
Bellow temperature: $150°$	4	Waiting time	120

Tab. D.2: Detailed recipe for the ALD growth of ZrO_2.

Although the virtual mask laser lithography machine (Heidelberg DWL 66) can be used for the insulation of the bonding lines lithography, we ordered a chromium hard mask to use a classical mask aligner due to its fast insulation speed (30 s) as it is shown in Tab. D.3. The minimum resolution of ≈ 1 μm does not pose a problem, since the structures patterned in this step have a minimum size of 5 μm. The hard-contact allows one to align the mask precisely but it can damage the ALD on some chips. Alignment and contact must be done extremely carefully in order not to induce any damage in the oxide.

Access lines lithography			
Step	**Description**	**Equipment**	**Parameters**
0	Cleaning	Acetone, ethanol, IPA, N_2	Rinse and dry
1	RIE O_2 plasma	Plassys Ion milling	5 s with 20 W, 45 sccm, 0.07 mbars
2	Spincoat LOR3A	Spincoater Spin150	30 s at 2000 rpm
3	Bake LOR3A	Hotplate	1 min at $170°$C
4	Spincoat UV3	Spincoater Spin150	30 s at 4000 rpm
5	Bake UV3	Hotplate	1 min at $130°$C
6	DUV exposure	Mask aligner MJB3	45 s with 0.5 mW/cm^2)
7	Development	MF26A DI water and N_2	45 s rinse and dry
8	RIE O_2 plasma	Plassys Ion milling	5 s with 20 W, 45 sccm, 0.07 mbars
9	Metal evaporation	Plassys MEB550S	3 nm Ti (0.3 Å/s) 50 nm Au (0.3 Å/s)
10	Lift off	Acetone (pippeting) Remover PG	10 min $\geq$ 1 hour at $80°$C
11	Cleaning	Acetone, ethanol, IPA, N_2	Rinse and dry

Tab. D.3: Detailed recipe for DUV lithography with a LOR3A-UV3 bilayer resist.

The last lithography step concerns the electromigration constrictions. Electron beam lithography (EBL) is necessary to precisely pattern the sharp bow-tie shaped structures of the junctions. Since the

aluminum-gold contact degrade with time, significantly affecting the electromigration quality after one month, it is recommended to dice the wafer into several pieces containing few chips and perform the EBL on single pieces, distributing them over measurement periods. We spincoated a protective resist layer of S1818 at 2000 rpm for 30 seconds to safeguard the structures from the cutting procedure. The wafer was then diced using a manual diamond micron-scriber (S100-4 model). The protective resist layer was removed and the EBL process (described in Tab. D.4) was carried out.

Electromigration constrictions lithography			
Step	**Description**	**Equipment**	**Parameters**
0	Cleaning	Acetone, ethanol, IPA, N_2	Rinse and dry
1	RIE O_2 plasma	Plassys Ion milling	5 s with 20 W, 45 sccm, 0.07 mbars
2	Spincoat PMMA/MMA 6%	Spincoater Spin150	30 s at 4000 rpm
3	Bake PMMA/MMA 6%	Hotplate	5 min at $200°$C
4	Spincoat PMMA 3%	Spincoater Spin150	30 s at 6000 rpm
5	Bake PMMA 3%	Hotplate	5 min at $180°$C
6	EBL exposure	NanoBeam nB5	8.5 C/m^2 (access lines) 11.05 C/m^2 (constrictions)
7	Development	MIBK/IPA (1/3) IPA and N_2	1 min 1 min and dry
8	RIE O_2 plasma	Plassys Ion milling	15 s with 10 W, 45 sccm, 0.07 mbars
9	Metal evaporation	Plassys MEB550S	14.5 nm Al ($-25°$ at 0.5 Å/s) 14.5 nm Al ($+25°$ at 0.5 Å/s) 80 nm Al ($0°$ at 10 Å/s)
10	Lift off	NMP solvent (pippeting)	$\geq$ 1 hour at $80°$C
11	Cleaning	Acetone, ethanol, IPA, N_2	Rinse and dry

Tab. D.4: Detailed recipe for electron beam lithography with a PMMA/MMA-PMMA bilayer resist.

After the last metal evaporation in a wafer piece, we proceed immediately to probe station tests of some of the single chips in the piece. If room temperature electromigration parameters matched the electrical characterization shown in section 2.4.2, we spincoated a protective resist layer of S1818 at 2000 rpm for 30 seconds to safeguard the structures and prevent oxidation of the Al constrictions. The silicon piece was diced into single chips using again the manual diamond micron-scriber. When the cryogenic set-up was available, the single-chip processing continued with the QDs deposition (after removing the protective resist), gluing and bonding to the sample-holder and inserted into the cryostat, where in-situ electromigration was carried out at a temperature of $T = 4$ K in high vacuum conditions. The final procedure of QD deposition and cooldown must be done within a few hours (a whole workday maximum) to avoid the oxidation of the thin Al constrictions.

E In-situ evaporator unit calibration and tests

Our molecule evaporator unit is based on the Joule heating of a Pt ohmic element, by the flow of an electrical current. It has been specifically designed to be compatible with the base temperature stage of our Sionludi cryostats, facing the sample in order to carry out in-situ depositions of molecules at cryogenic temperatures (also called quench condensation [234]). However, once Al electromigration is finished, holding the Sionludi inner stages at cryogenic temperatures is absolutely necessary to keep activated the cryosorption process and maintain the high-vacuum level ($\sim 10^{-8}$), avoiding the oxidation of the junction contact leads. Therefore, the objective is to verify if molecule evaporations can be carried out without inducing a significant heating, keeping the tunnel junctions resistance stable and evaluate its feasibility for the obtainment of QD junctions. In this Annex, we explain the calibration and tests done for the optimization of an evaporation procedure of C60 fullerenes on Al EMBJs.

As mentioned in section 3.1.5, the evaporator configuration evolved as tests were performed. The design shown here (Fig. E.1a) is the final version, containing all the improvements added by the end of my period of experiments. In this configuration, two π-filters, soldered to the lid, act as a feedthrough of the electrical lines into the evaporator cavity. Copper wires connects the π-filters to other two feedthrough filters that bring the signal into the sample cavity when the evaporator is plugged in the cryostat (ideally these copper wires can be replaced by lossy Thermocoax cables, which can filter out high-frequency noise). In the sample cavity side, Mn wires of 10 cm connect the feedthrough filters to the Pt resistor leads by soldering pads in a PCB plate as depicted in Fig. E.1b. While the filters help thermalizing of the evaporator lines at the sample stage temperature, the low thermal conductivity of Mn wires provide a certain thermal isolation of the Pt resistor, allowing to heat it up while reducing its impact in the sample stage temperature.

ROOM TEMPERATURE CALIBRATION OF THE EVAPORATOR UNIT

The Pt resistor lumped element (model PT100 class A) has a well-known linear dependence with temperature (shown in blue in Fig. E.1c), with a nominal value of $R_{Pt}(0\ °\text{C}) = 100\ \Omega$. When applying a voltage tension (V_{ev}) between the evaporator leads (π-filters electrodes), a certain current starts flowing through the circuit. Since the main resistive element is the Pt resistor ($R_{Pt}(T)$), its

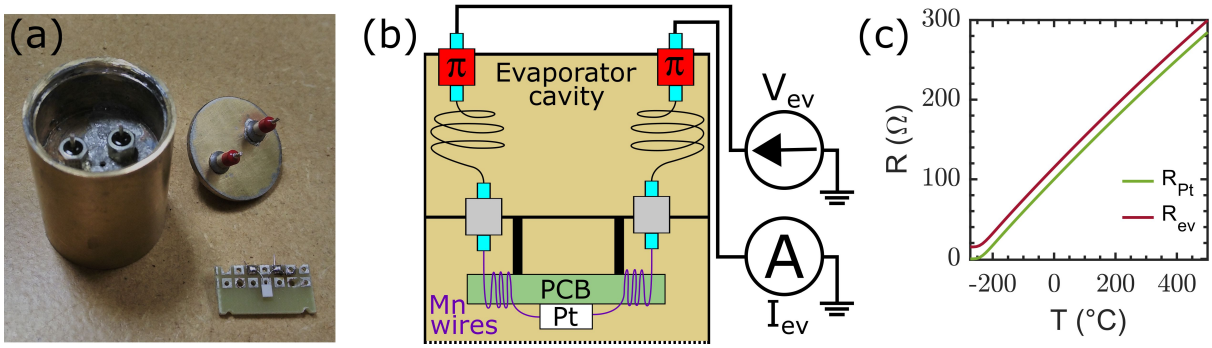

Fig. E.1: (a) Picture of the molecule evaporator unit prior to mounting and soldering. The evaporator cavity is open, showing the feedthrough filters. On the side we can see the metallic lid with two π-filters, and the Pt resistor soldered to the PCB plate. (b) Schematic showing the structure of the evaporator once mounted. (c) Temperature dependence of the Pt element resistance and the extrapolated resistance of the whole evaporator unit.

temperature will increase due to Joule effect heating, in turn increasing its resistance and altering the current flowing in the circuit. Like this, the system enters in a transient state, gradually reaching an stationary current (I_{ev}), corresponding to an stationary temperature (T_{Pt}) and resistance (R_{Pt}) of the Pt element, determining the stationary resistance of the evaporator circuit ($R_{ev} = V_{ev}/I_{ev}$). The total resistance of the circuit is equal to the sum of the Pt element resistance (R_{Pt}) plus the series resistance brought in by the wires and filters (R_{ev}^{ser}):

$$R_{ev}(T) = R_{Pt}(T) + R_{ev}^{ser}. \tag{E.0.1}$$

By performing a zero-bias measurement of the evaporator resistance at room temperature we observe $R_{ev}(25\ ^\circ\text{C}) = 125\Omega$. Since the corresponding value of $R_{Pt}(25\ ^\circ\text{C}) = 110\ \Omega$, we can extrapolate a series circuit resistance of $R_{ev}^{ser} = 15\ \Omega$. Considering the temperature dependence of R_{ev}^{ser} negligible, we can define a calibration curve for our evaporator unit by introducing R_{ev}^{ser} as an offset in the R_{Pt} temperature dependence (shown in magenta in Fig. E.1c). In this way, by applying a certain V_{ev}, we can extract R_{ev} by measuring the stationary current I_{ev}, determining the stationary temperature, T_{Pt}, of the Pt resistor.

ROOM TEMPERATURE FULLERENE EVAPORATION TESTS

From a theoretical point of view, the heating per unit mass (specific energy) is the relevant quantity that determines the rate at which a certain material evaporates at a given temperature. However, it is a difficult magnitude to determine experimentally, so that evaporation and desorption processes are commonly characterized by the evaporator temperature. This is a rather imprecise parameter that depends on the experimental set-up, since different evaporator configurations lead to rather non-uniform temperature distributions in the molecular media (crystal powders, colloidal solutions, polymers matrices, etc) and its definition is usually linked to specific deposition rates, that depends on the vacuum level. On top of that, the desorption temperature of molecules adsorbed in a surface (by Van-der-Waals electrostatic forces) can also depend on their chemical composition. Although the maximum desorption rates of fullerene molecules takes place at a rather large range of temperatures ($300 - 700\ ^\circ\text{C}$) that depends on the fullerene type [270, 271, 244] and the adsorption surface [272, 273, 274], in all these experiments it has been consistently found that the desorption of C_{60} molecules starts taking place at temperatures of $T_{C60} = 200 - 250\ ^\circ\text{C}$. In this way, in-situ quench condensation of C_{60}s has been already employed to obtain QD junctions from nano-spaced electrodes [243]. Based on these results, we employ a colloidal solution of C60 molecules (with a concentration of $\mathcal{C}_{C60} = 1$ μg/μL) to impregnate the Pt resistor prior to each evaporation test, by drop-casting a droplet (10 μL) of solution and let the toluene solvent evaporate, so that the molecules get adsorbed on the resistor surface.

A preliminary version of the evaporator was fabricated to be tested at room temperature in a provisional high-vacuum set-up. For this purpose, we employed bare Si−SiO_2 substrates, placed in front of the evaporator resistor. After casting the C60 solution on the Pt resistor and let it dry, the evaporator was mounted on the set-up and we started the vacuum pumping. When a high vacuum level ($\sim 10^-6$ mbars) was reached, few evaporation attempts were carried out by applying a certain V_{ev}, while measuring I_{ev}, for a duration of 5 minutes. After each evaporation, the testing substrate was extracted from the set-up and observed under an AFM microscope at different locations. We expected to observe indication of the C60 deposition for an evaporator temperature $T_{Pt} \geq T_{C60}$. While for a biasing voltage of $V_{ev} = 3.0$ V and an stationary current of $I_{ev} = 16.9$ mA (leading to a circuit resistance of $R_{ev} \approx 177\ \Omega$, indicating an evaporator temperature of $T_{Pt} \approx 160\ ^\circ\text{C}$) we did not observe any significant changes in the substrate, for $V_{ev} = 3.5$ V and $I_{ev} = 17.7$ mA (leading to a circuit resistance of $R_{ev} \approx 198\ \Omega$ and a evaporator temperature of $T_{Pt} \approx 215\ ^\circ\text{C}$) the AFM measurements showed the presence of multiple circular structures (of ~ 1 nm height) indicating the success of the evaporation at the expected temperature range (Fig. E.2).

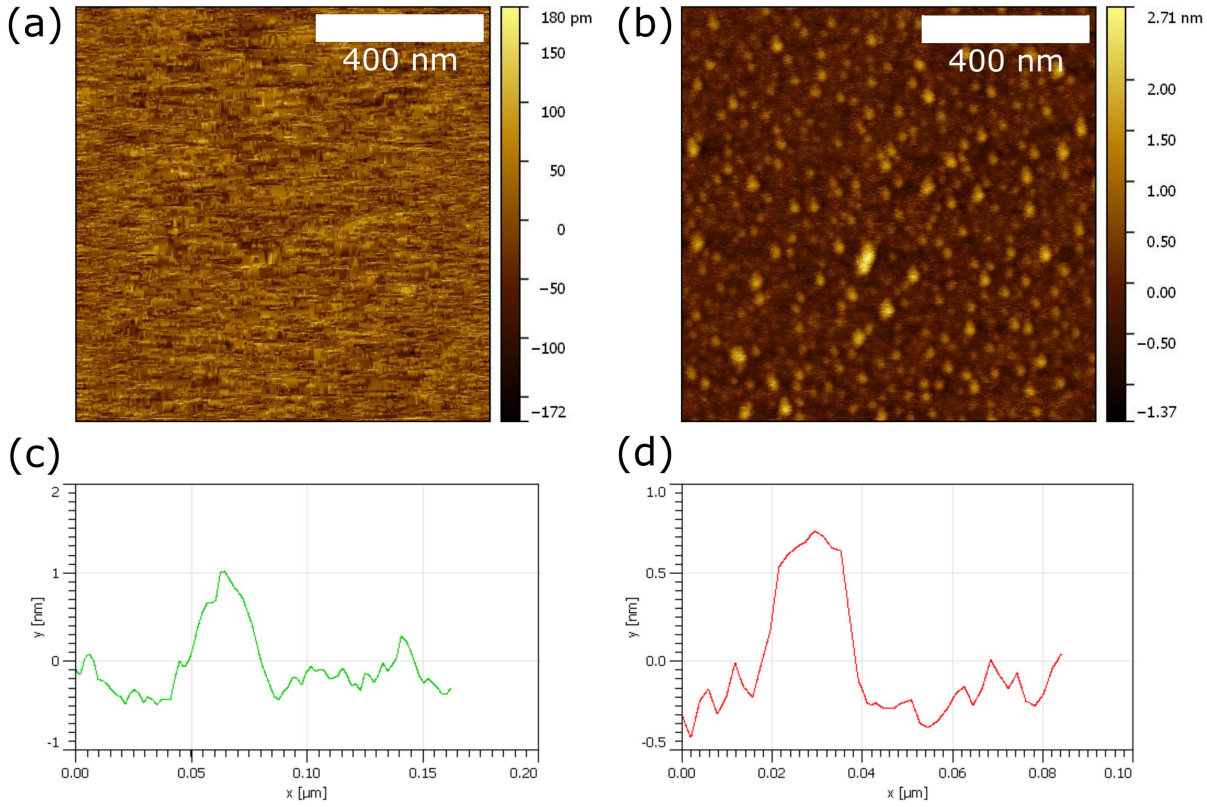

Fig. E.2: (a,b) AFM topographic images on 500 nm thermal oxide doped-Si substrates after evaporation tests at room temperature. (a) After an evaporation attempt at $T_{Pt} \approx 160$ °C for 5 minutes, no particle is observed and the surface presents a standard substrate roughness of 350 nm. (b) After an evaporation attempt at $T_{Pt} \approx 215$ °C for 5 minutes, the image shows a surface covered by nano-particles with different sizes, displaying a vertical roughness around 4 nm. (c,d) Profile scans taken across some isolated particles of the smaller lateral diameter reveal a height around 1 nm, indicating the presence of C60 molecules on the surface.

CALIBRATION OF THE EVAPORATOR CRYOGENIC CIRCUIT AT LOW TEMPERATURES

The satisfactory results of the C60 evaporation tests performed at room temperature motivated us to further test in-situ evaporations at low temperatures (see section 3.1.5). For this, two electrical lines connecting the evaporator leads at the sample stage, with terminals at the room temperature shield were installed in refrigerator A. Superconducting wires were soldered to the π-filters leads, and descend to the 4 K stage where they were soldered to thermalizing leads. Usual copper cables connect the 4 K stage leads to external terminals at room temperature. The superconducting wires are thermalized at the cold cryostat stages (temperatures of 1 K, 200 mK and 50 mK) employing copper/aluminum stripes on a film of kapton attached to the cold stages surfaces. At the warmer cryostat stages (80 K, 20 K and 4 K), the evaporator lines are thermalized using massive metallic leads. A simplified schematic is shown in Fig. E.3a.

Having the evaporator in place inside the cryostat, we measured the zero-bias total resistance of the whole circuit of $R_{ev}^{tot}(25\ °\text{C}) = 214\ \Omega$ at room temperature. In the same way as it was done for the calibration of the evaporator circuit, we divided the total resistance of the whole evaporator cryogenic circuit as a sum of resistances of individual parts:

$$R_{ev}^{tot}(T) = R_{Pt}(T) + R_{ev}^{ser} + R_{cryo}^{ser}. \tag{E.0.2}$$

Since the superconducting wires (with a critical temperature around 9 K) are in normal state, they add a significant resistance of about 40Ω each, which we expect to disappear at cryogenic temperatures of 4 K or below, vanishing the R_{cryo}^{ser} term so that the only temperature dependence is due to the Pt resistor.

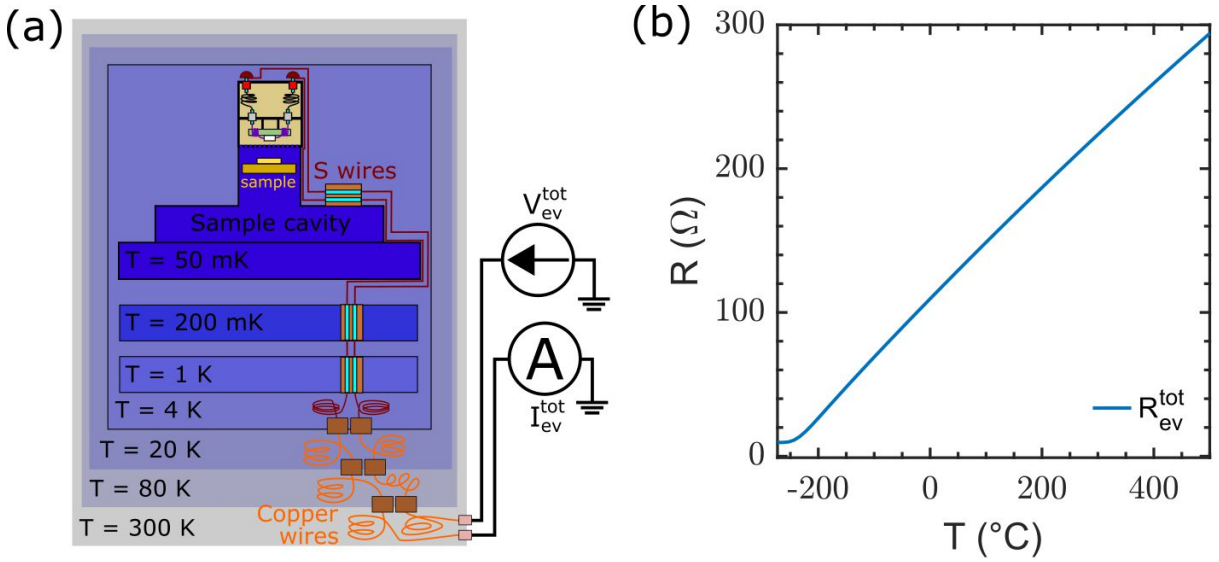

Fig. E.3: (a) Schematic showing the configuration of the evaporator circuit inside the cryostat, indicating the superconducting (S) wires with the thermalizations at the cold stages (aluminum/copper stripes on kapton films) and the copper cables at the warmer stages. (b) Temperature dependence of the cryogenic evaporator circuit, extrapolated by adding an offset of 9.5 Ω to the Pt calibration curve shown in magenta in Fig. E.1c.

Similarly to the electromigration routine (section 3.2.2), the cryostat is set into a stable operation mode during the evaporation process, so that all the colder stages and the 4 K stage are kept at a temperature around 4–5 K. Measuring the zero-bias resistance at 4 K, we obtain $R_{ev}^{tot}(-269\ °C) = 9.5\ \Omega$. Since the cryogenic copper lines have a negligible resistance and the cold stage wires are in superconducting state, and taking into account that the resistance of the Pt element is negligible at these temperatures, we attribute it to the evaporator filtering elements, so that $R_{ev}^{ser} = 9.5\ \Omega$. Therefore, we can proceed in the same way as in the room temperature tests, and trace the calibration line of the evaporator cryogenic circuit ($R_{ev}^{tot}(T)$) by adding an offset of 9.5 Ω to the Pt resistor temperature dependence (Fig. E.3b).

FULLERENE EVAPORATION TESTS AT LOW TEMPERATURES

The first tests of in-situ fullerene evaporations at low temperatures were done on two real samples containing Al electromigration constrictions, in two different cooldowns. After gluing and microbonding a chip to the sample-holder, we insert the ensemble in the receptacle at the sample stage, put the evaporator in place, close the cryostat, pump vacuum and cool down to 4 K. The objectives of these two primary exams were to check the compatibility of a high temperature evaporation while the cryostat is kept cold, and test if, indeed, a C60 deposition on the surface of the sample takes place, as well as trying electromigration after the evaporation. As usual, different voltage tensions, V_{ev}^{tot}, were applied at the external terminals of the evaporator circuit, and the current, I_{ev}^{tot}, flowing through the circuit was measured, allowing us to extract the total resistance of the circuit as $R_{ev}^{tot} = V_{ev}^{tot}/I_{ev}^{tot}$.

Our first observation was an increased stabilization time until the stationary current was reached, from few seconds up to few minutes, for increasing voltages. In the first try, we left the experiment evolve until current fluctuations were below below 0.01 mA while applying a constant voltage (the whole procedure took around 3 hours). In the second try we stop the voltage as soon as the current was fluctuating an amount below 0.2 mA (with an overall duration of 45 minutes). During the stabilization time, the sample stage thermometer indicated a temperature increase between 4-10 K. After reaching the stationary current for each V_{ev}^{tot} value, we let the system cool down again to 4 K before applying the next V_{ev}^{tot} step. In both cases we measured an identical I_{ev}^{tot}, indicating that the same R_{ev}^{tot} was reached (shown in Fig. E.4a). From the measurement of R_{ev}^{tot}, we extrapolated T_{Pt} from the calibration curve in Fig. E.3b, establishing the relation between V_{ev}^{tot} and the Pt resistor temperature shown in Fig. E.4b.

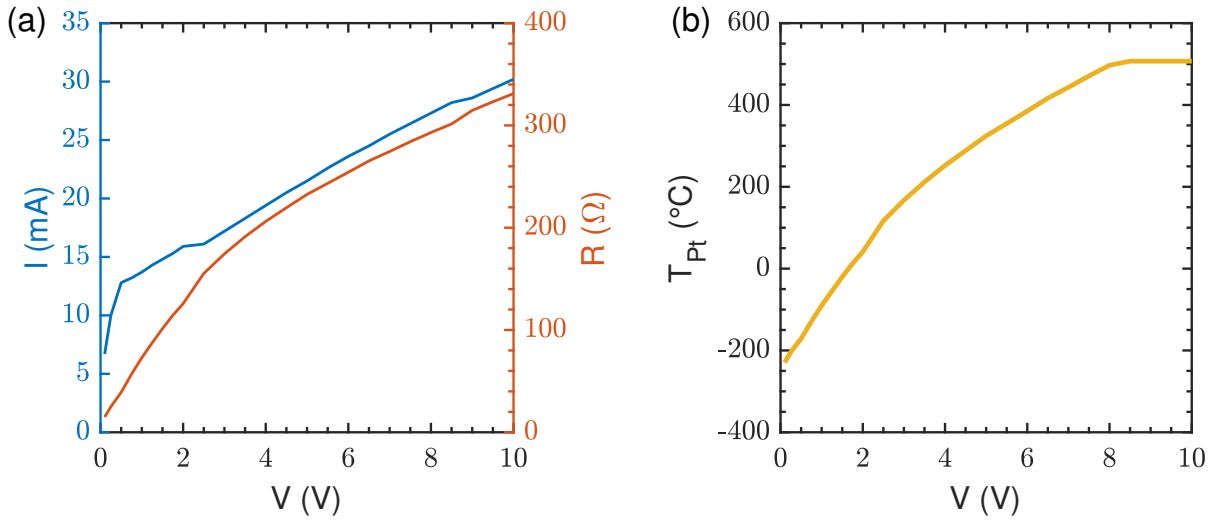

Fig. E.4: (a) Current measurement and resistance of the cryogenic evaporator circuit as a function of the bias voltage applied to the cryostat external connectors. The deviation from the general behavior at low voltages may indicate the transition into the normal state of part of the S wires due to the evaporator heating. (b) Temperature of the Pt resistor as a function of the voltage applied, extrapolated from the measured resistance by using the calibration curve in Fig. E.3b.

Although the sample stage thermometer (placed close to the mixing chamber, away from the sample and evaporator location) did not increase above 10 K during both tests, we observe in Fig. E.4 that the Pt resistor possibly reached temperatures above 550 °C for the highest values of V_{ev}^{tot} (8–10 V). In fact, after finishing the evaporator calibration on the first test, we observed that the constrictions resistance had increased one order of magnitude from its usual value (about 200–300 Ω, measured from the external connectors of the cryostat), and electromigration could not be carried out properly. Later observation of the sample in a SEM (Fig. E.5a and b) revealed small circular features appearing over the whole surface (similar to those shown in Fig. 2.11d and e). At the same time, we observed that the aluminum-gold interface (at the constrictions access lines on the chip) displayed degradation features identical to those shown in Fig. 2.11a and b, explaining the elevated resistance of the constrictions in this sample after the evaporation procedure. Both behaviors (bubbles below the ALD oxide and the formation of purple plague compounds) would be enhanced by the exposition of the sample at high temperatures over a long time, confirming our suspicion on the high temperatures reached, but at the same time, in good agreement with the calibration curve of Fig. E.4b. However, in this SEM pictures, the constriction structures appear blurrier than usual, in good agreement with molecular layer covering the sample surface, which may indicate the success of the fullerene evaporation.

To avoid these problems, the total time of the evaporation procedure was reduced to less than 45 minutes in the second test. Although, the constrictions showed resistances between 300–500 Ω, slightly higher than usual, electromigration was carried out successfully and a QD junction was obtained and characterized, shown in the main document of this thesis. Pictures of this sample (Fig. E.5c and d) taken with an SEM after warming up did not showed any of the problems found in the first test. These images show clearer indication that a non-uniform layer covers the whole surface, displaying wrinkles close to the structures edges.

OPTIMIZATION OF THE IN-SITU EVAPORATION PROCEDURE

The obtainment of a QD junction when electromigrating the constrictions right after the second calibration test reaffirmed the correct functioning of the evaporator unit and its success as an alternative method for performing QD depositions in EMBJ samples. After this, we focus on the establishment of an evaporation procedure for the deposition of molecular sub-mono layers (to minimize the occurrence of charge-offset gate switches), while studying the compatibility of performing subsequent evaporations with stable tunnel resistances of junctions already electromigrated.

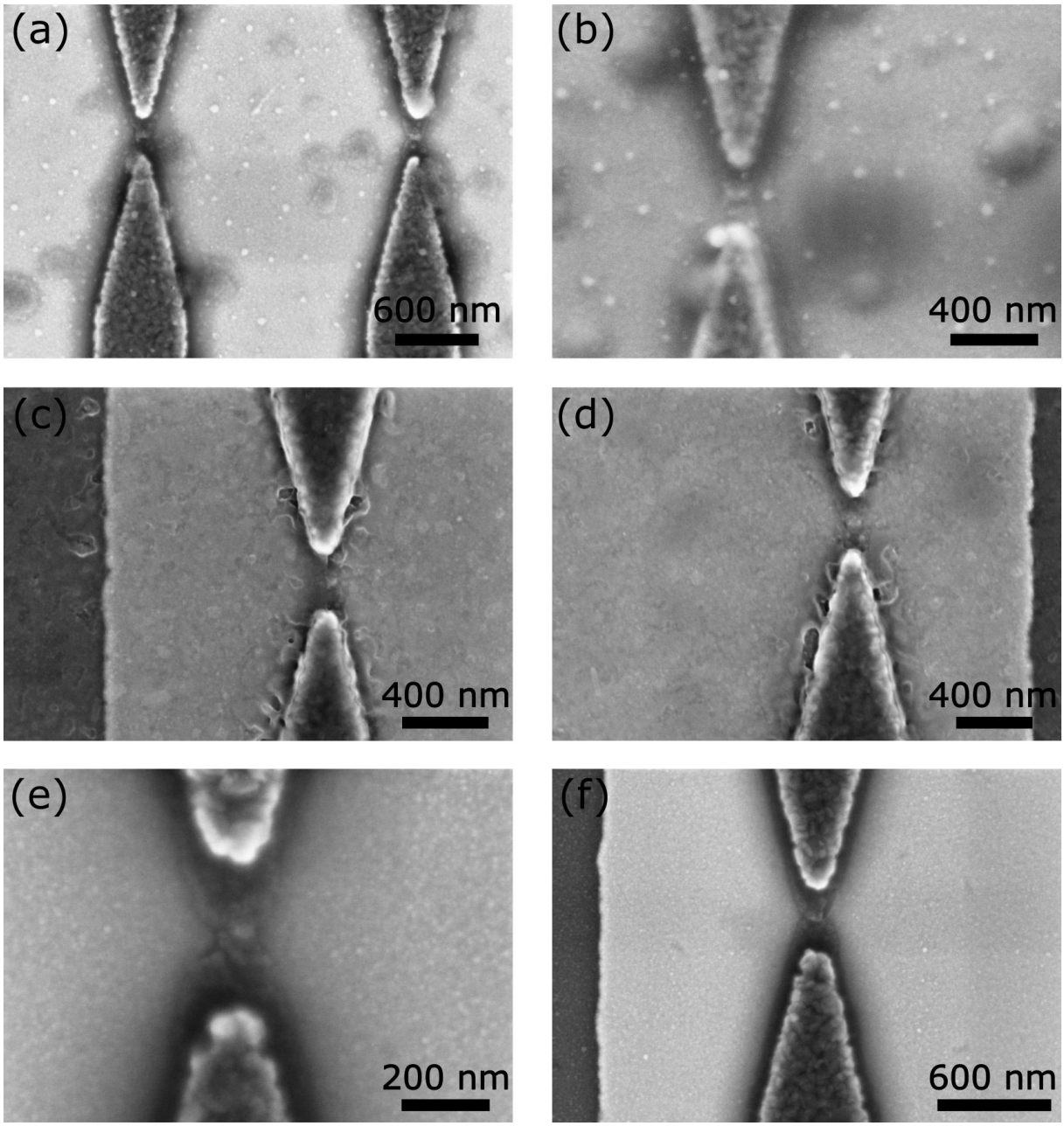

Fig. E.5: SEM images of constrictions electromigrated at 4 K, used for testing in-situ evaporations of fullerenes. (a,b) Bumps appeared all over the sample surface. Bright points about 50 nm diameter may be identified with C60 clusters. (c,d) An non-uniform layer seems to be covering the sample surface, making wrinkles around the Al structures. (e,f) Apart from an increased blurrier of the Al forming the constrictions, no indicative signs confirming the presence of molecules on the surface can be appreciated.

The deposition of molecules after breaking the Al constrictions can be dangerous for the bare aluminum electrodes at the nano-gap formed by electromigration, since the heating of the sample cavity (caused by the evaporator operation) can lead to the interruption of the cryosorption process at the sample cavity and degrade the standard vacuum level of the cryostat ($\sim 10^{-8}$). Actually, it has been shown that extremely low oxygen pressures ($\sim 10^{-7}$) can oxidize an exposed aluminum surface in a matter of 100 seconds ([223]). In contrast, our aluminum electrodes are partially shielded by the whole constriction structure, being only accessible from the nano-gap empty space, thus we expect a certain robustness of the tunnel resistance stability facing short evaporations that will not stop the cryosorption process notably. On top of that, a massive molecule evaporation (like those carried out on the first tests) after electromigration can possibly result in a detrimental overpopulation of QDs

at the junction. In order not to saturate the electromigration nano-gap, nor degrade the vacuum level significantly, we intend to perform flash evaporations of few seconds duration, ideally leading to depositions of a single sub-mono layers of molecules on the sample surface.

The low-temperature T_{Pt} calibration curve (Fig. E.4b) shows the reach of T_{C60} (around $200-250$ °C) at voltages around 3.5 V, in very good agreement with the room temperature tests, indicating the validity of the calibration. However, since the stationary state takes a significant time to stabilize, and we want to keep the evaporation time short, we aimed for higher temperatures of the Pt resistor, namely around $T_{Pt} \approx 450$ °C (corresponding to $V_{ev}^{tot} = 7$ V). We observed a typical stabilization time of 45 s at the end of which I_{ev}^{tot} oscillate less than 0.1 mA for $V_{ev}^{tot} = 7$ V. Since we are overshooting T_{C60}, there is no need to reach the steady state, so we established a flash evaporation duration between 30 and 60 s. Prior to electromigration and the consecutive flash evaporations, we performed a preliminary long evaporation at lower voltages ($V_{ev}^{tot} = 1-5$ V). This preliminary evaporation was intended to eliminate solvent residues in the Pt resistor, desorb the oxygen molecules from the heating parts of the evaporator (eventually getting cryosorpted in nearby cold surfaces) and provide a first QD evaporation prior to electromigration, that can also result in a QD junction, as we saw in the calibration tests. Two samples were electromigrated in separate cool downs, following an identical iterative evaporation procedure:

1. A preliminary evaporation was performed by applying a voltage of 5 V for 30 minutes, leading to an evaporator temperature of $T_{Pt} \approx 300$ °C.
2. All the constrictions were electromigrated and characterized.
3. Between one and three consecutive evaporations were performed later by applying three 7 V voltage flashes of 30 seconds (reaching $T_{Pt} = 450$ °C), letting the sample stage temperature relax to 4 K after each flash.
4. The electrical characteristics of the tunnel junctions were explored again.
5. If no stable QD junction was found, the procedure was repeated from step number 2.

The $I - V_B$ curves indicated an increased of the tunnel resistance of a 0.5–25 MΩ in around 50% of the junctions after each cycle of three consecutive evaporations (in the first chip cooled down), while after cycles of single evaporations the tunnel resistance remained approximately the same (in the second chip cooled down). The $I - V_G$ traces showed a completely different gate dependence of the tunnel junctions current in most cases in the first sample, whereas only in around 30% of the constrictions of the second sample. In the first sample, one QD junction was obtained directly after the preliminary evaporation, and a different junction showed clear QD conduction features after the first cycle of three consecutive evaporations. In contrast, no stable QD junction was found in the second sample. Additionally, most of the $I - V_B$ and $I - V_G$ measurements become extremely unstable after a couple of iterations of the evaporation procedure, possibly due to the high number of molecules around the junction, occasioning constant electrostatic switching noise. Posterior SEM images of both samples (Figs. 2.20e and f respectively) do not show any clear indication pointing towards the success of the evaporation, except for the aluminum structures appearing blurrier than usual.

In short, C60 evaporations were carried out on a total of 33 constrictions (electromigrated either prior of after the deposition), out of which we obtained one QD junction and signatures of QD conduction in other two. In spite of the reduced yield of success, we consider that insufficient samples were tested to be conclusive about this percentage. All these tests were done with different but equivalent versions of the evaporator unit. This evolution improved the evaporator integrity and reparation accessibility, allowing the next user to further optimize the process and electromigrate more constrictions for a finer tuning of the success rate.

F Conductance maps at different temperatures and magnetic fields

In this annex we present the raw data of some of the measurements performed in $\mathcal{A}_1$ on which we based the extensive studied performed in this sample and discussed in chapter 4. This measurements consist in V_B-V_G conductance maps at several temperatures (Figs. F.1 and F.2), both for the superconducting and normal state of the leads, as well as for different magnetic fields (Figs. F.3 and F.4). Apart from the conductance resonances caused by the emergence of YSR states, much fainter sub-gap resonances arise additionally in some of these measurements. At temperatures around 900 mK and above, these secondary resonances are identified as the well-known thermal replicas. The origin of secondary sub-gap resonances developing at base temperature, for intermediate B fields between 18 and 36 mT, are attributed to the apparison of a finite density of states induced by the B field below the superconducting gap of the leads, gradually reaching their Fermi level.

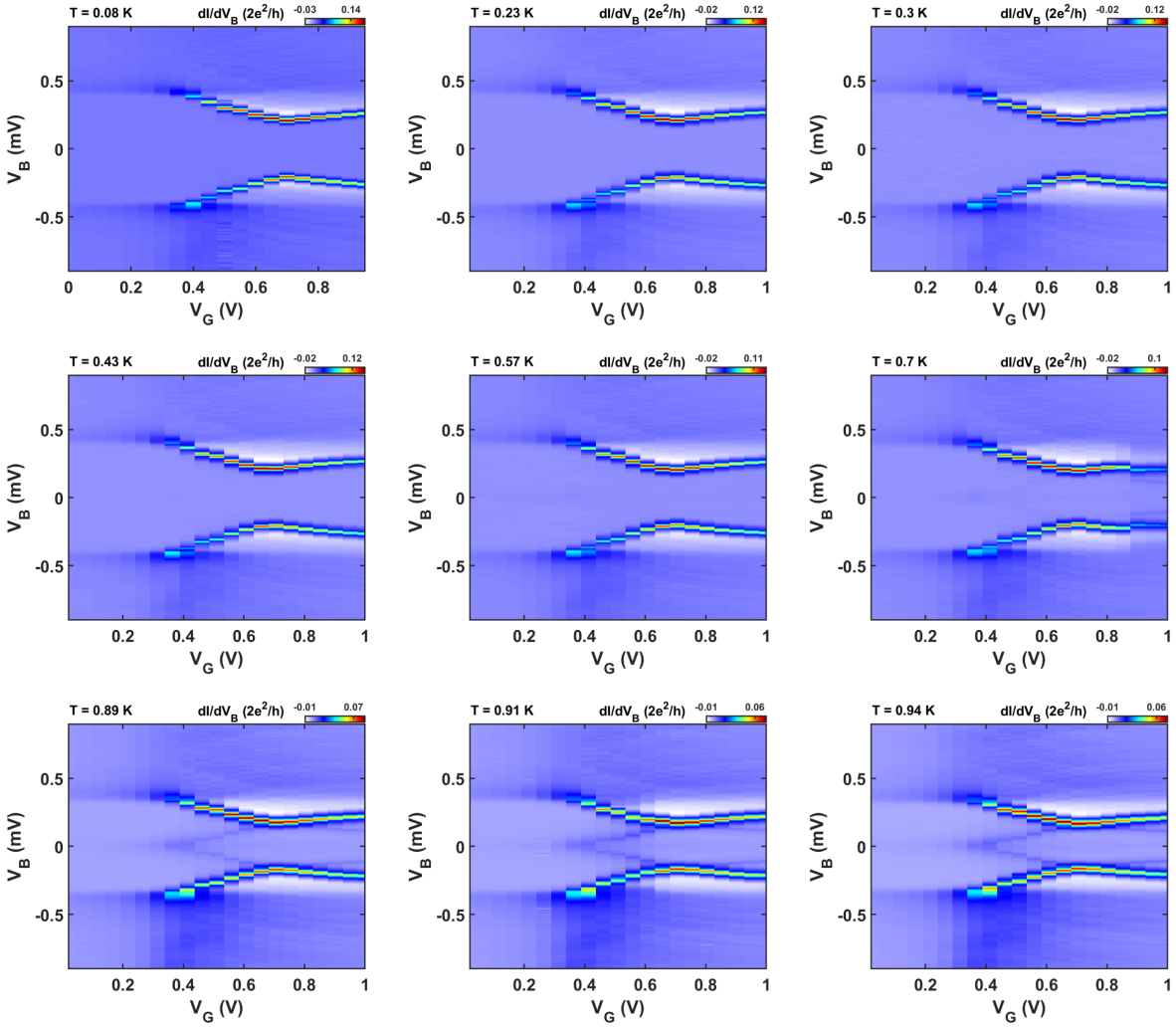

Fig. F.1: $dI - dV_B$ maps of device $\mathcal{A}_1$ as a function of V_G and V_B acquired at different temperatures and for zero magnetic field.

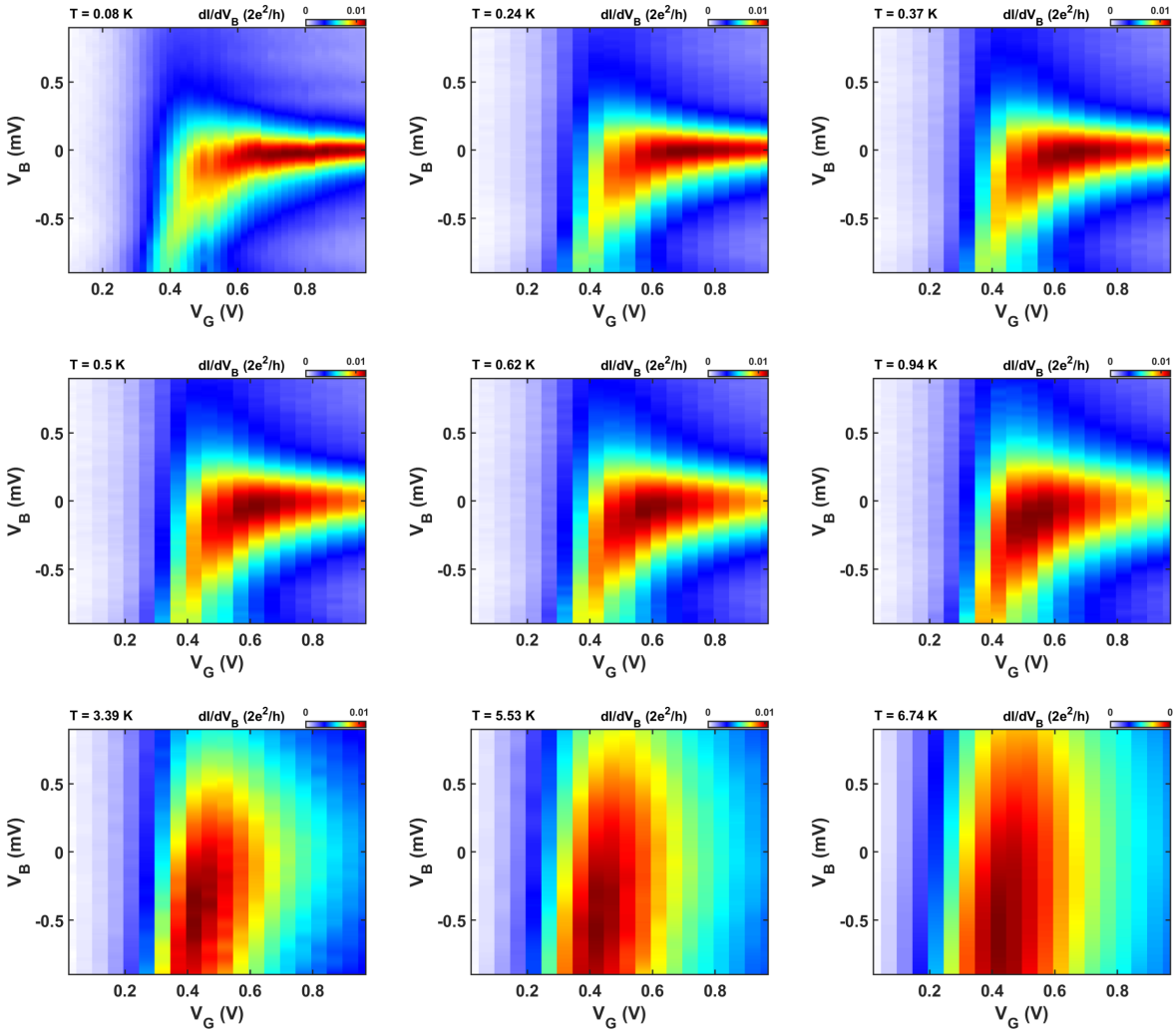

Fig. F.2: $dI - dV_B$ maps of device $\mathcal{A}_1$ as a function of V_G and V_B acquired at different temperatures and a constant magnetic field of 72 mT.

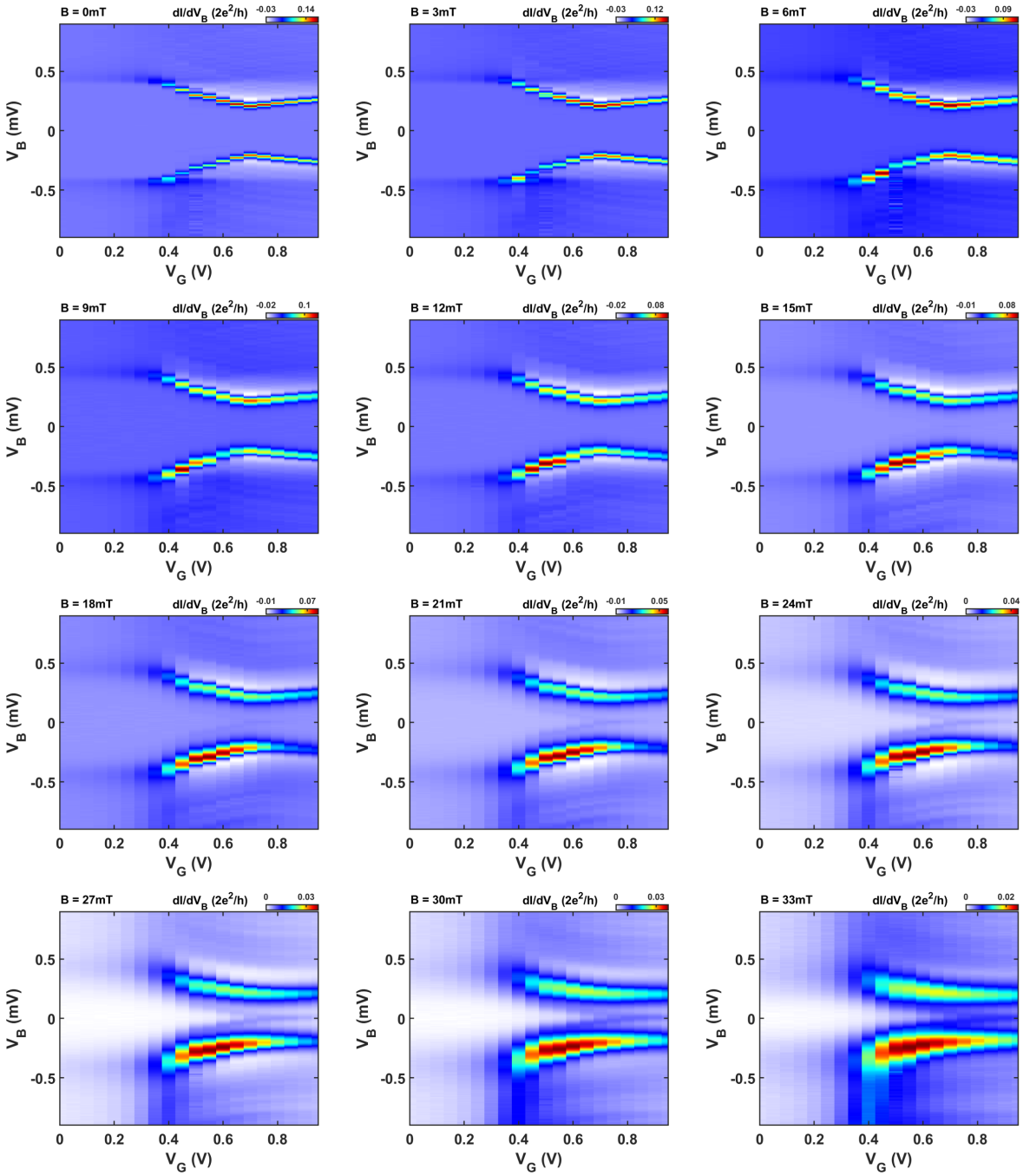

Fig. F.3: $dI - dV_B$ maps of device $\mathcal{A}_1$ as a function of V_G and V_B acquired at base temperature at magnetic fields ranging between 0 and 33 mT.

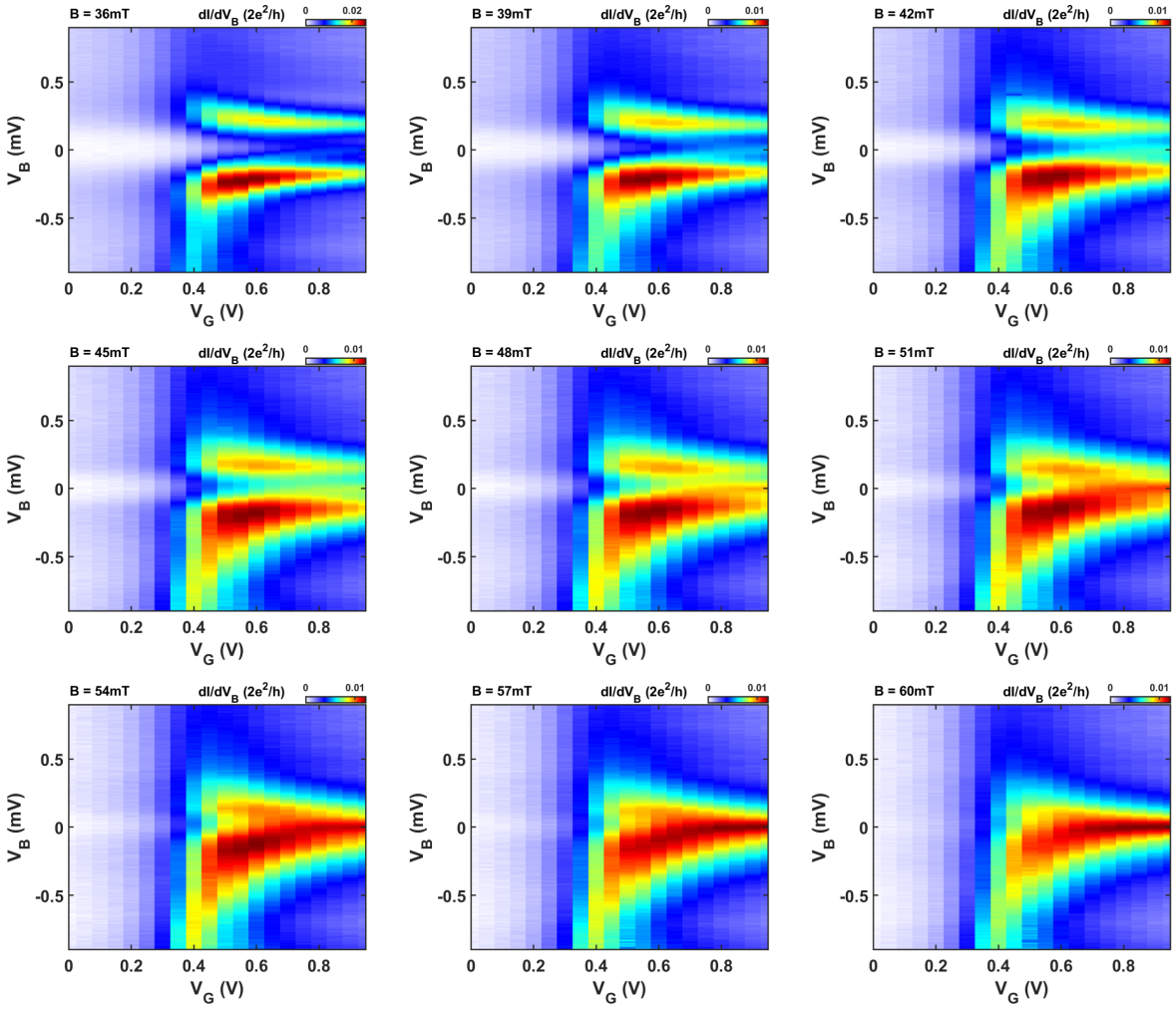

Fig. F.4: $dI - dV_B$ maps of device $\mathcal{A}_1$ as a function of V_G and V_B acquired at base temperature at magnetic fields ranging between 36 and 60 mT.

Bibliography

[1] D. Ralph, C. Black, and M. Tinkham, "Spectroscopic measurements of discrete electronic states in single metal particles," *Physical review letters*, vol. 74, no. 16, p. 3241, 1995.

[2] C. Black, D. Ralph, and M. Tinkham, "Spectroscopy of the superconducting gap in individual nanometer-scale aluminum particles," *Physical review letters*, vol. 76, no. 4, p. 688, 1996.

[3] D. Ralph, C. Black, and M. Tinkham, "Gate-voltage studies of discrete electronic states in aluminum nanoparticles," *Physical review letters*, vol. 78, no. 21, p. 4087, 1997.

[4] D. L. Klein, R. Roth, A. K. Lim, A. P. Alivisatos, and P. L. McEuen, "A single-electron transistor made from a cadmium selenide nanocrystal," *Nature*, vol. 389, no. 6652, p. 699, 1997.

[5] M. Buitelaar, T. Nussbaumer, and C. Schönenberger, "Quantum dot in the kondo regime coupled to superconductors," *Physical Review Letters*, vol. 89, no. 25, p. 256801, 2002.

[6] Y.-J. Doh, J. A. van Dam, A. L. Roest, E. P. Bakkers, L. P. Kouwenhoven, and S. De Franceschi, "Tunable supercurrent through semiconductor nanowires," *science*, vol. 309, no. 5732, pp. 272–275, 2005.

[7] P. Jarillo-Herrero, J. A. Van Dam, and L. P. Kouwenhoven, "Quantum supercurrent transistors in carbon nanotubes," *Nature*, vol. 439, no. 7079, pp. 953–956, 2006.

[8] H. I. Jørgensen, K. Grove-Rasmussen, T. Novotnỳ, K. Flensberg, and P. E. Lindelof, "Electron transport in single-wall carbon nanotube weak links in the fabry-perot regime," *Physical review letters*, vol. 96, no. 20, p. 207003, 2006.

[9] P. Joyez, P. Lafarge, A. Filipe, D. Esteve, and M. Devoret, "Observation of parity-induced suppression of josephson tunneling in the superconducting single electron transistor," *Physical review letters*, vol. 72, no. 15, p. 2458, 1994.

[10] K. Franke, G. Schulze, and J. Pascual, "Competition of superconducting phenomena and kondo screening at the nanoscale," *Science*, vol. 332, no. 6032, pp. 940–944, 2011.

[11] M. R. Buitelaar, W. Belzig, T. Nussbaumer, B. Babić, C. Bruder, and C. Schönenberger, "Multiple andreev reflections in a carbon nanotube quantum dot," *Physical review letters*, vol. 91, no. 5, p. 057005, 2003.

[12] C. Buizert, A. Oiwa, K. Shibata, K. Hirakawa, and S. Tarucha, "Kondo universal scaling for a quantum dot coupled to superconducting leads," *Physical review letters*, vol. 99, no. 13, p. 136806, 2007.

[13] T. Sand-Jespersen, J. Paaske, B. M. Andersen, K. Grove-Rasmussen, H. I. Jørgensen, M. Aagesen, C. Sørensen, P. E. Lindelof, K. Flensberg, and J. Nygård, "Kondo-enhanced andreev tunneling in inas nanowire quantum dots," *Physical review letters*, vol. 99, no. 12, p. 126603, 2007.

[14] A. Eichler, M. Weiss, S. Oberholzer, C. Schönenberger, A. L. Yeyati, J. Cuevas, and A. Martín-Rodero, "Even-odd effect in andreev transport through a carbon nanotube quantum dot," *Physical review letters*, vol. 99, no. 12, p. 126602, 2007.

[15] A. Eichler, R. Deblock, M. Weiss, C. Karrasch, V. Meden, C. Schönenberger, and H. Bouchiat, "Tuning the josephson current in carbon nanotubes with the kondo effect," *Physical Review B*, vol. 79, no. 16, p. 161407, 2009.

[16] J.-P. Cleuziou, W. Wernsdorfer, V. Bouchiat, T. Ondarçuhu, and M. Monthioux, "Carbon nanotube superconducting quantum interference device," *Nature nanotechnology*, vol. 1, no. 1, p. 53, 2006.

[17] J. A. Van Dam, Y. V. Nazarov, E. P. Bakkers, S. De Franceschi, and L. P. Kouwenhoven, "Supercurrent reversal in quantum dots," *Nature*, vol. 442, no. 7103, p. 667, 2006.

[18] H. I. Jørgensen, T. Novotnỳ, K. Grove-Rasmussen, K. Flensberg, and P. E. Lindelof, "Critical current 0- π transition in designed josephson quantum dot junctions," *Nano letters*, vol. 7, no. 8, pp. 2441–2445, 2007.

[19] S. De Franceschi, L. Kouwenhoven, C. Schönenberger, and W. Wernsdorfer, "Hybrid superconductor–quantum dot devices," *Nature nanotechnology*, vol. 5, no. 10, p. 703, 2010.

[20] R. Maurand, T. Meng, E. Bonet, S. Florens, L. Marty, and W. Wernsdorfer, "First-order 0- π quantum phase transition in the kondo regime of a superconducting carbon-nanotube quantum dot," *Physical Review X*, vol. 2, no. 1, p. 011009, 2012.

[21] M. Deng, S. Vaitiekėnas, E. B. Hansen, J. Danon, M. Leijnse, K. Flensberg, J. Nygård, P. Krogstrup, and C. M. Marcus, "Majorana bound state in a coupled quantum-dot hybrid-nanowire system," *Science*, vol. 354, no. 6319, pp. 1557–1562, 2016.

[22] M. Ruby, F. Pientka, Y. Peng, F. von Oppen, B. W. Heinrich, and K. J. Franke, "End states and subgap structure in proximity-coupled chains of magnetic adatoms," *Physical review letters*, vol. 115, no. 19, p. 197204, 2015.

[23] K. Grove-Rasmussen, H. I. Jørgensen, B. M. Andersen, J. Paaske, T. S. Jespersen, J. Nygård, K. Flensberg, and P. E. Lindelof, "Superconductivity-enhanced bias spectroscopy in carbon nanotube quantum dots," *Physical Review B*, vol. 79, no. 13, p. 134518, 2009.

[24] J. Pillet, C. Quay, P. Morfin, C. Bena, A. L. Yeyati, and P. Joyez, "Andreev bound states in supercurrent-carrying carbon nanotubes revealed," *Nature Physics*, vol. 6, no. 12, pp. 965–969, 2010.

[25] J.-D. Pillet, P. Joyez, M. Goffman, *et al.*, "Tunneling spectroscopy of a single quantum dot coupled to a superconductor: From kondo ridge to andreev bound states," *Physical Review B*, vol. 88, no. 4, p. 045101, 2013.

[26] B.-K. Kim, Y.-H. Ahn, J.-J. Kim, M.-S. Choi, M.-H. Bae, K. Kang, J. S. Lim, R. López, and N. Kim, "Transport measurement of andreev bound states in a kondo-correlated quantum dot," *Physical review letters*, vol. 110, no. 7, p. 076803, 2013.

[27] W. Chang, V. Manucharyan, T. S. Jespersen, J. Nygård, and C. M. Marcus, "Tunneling spectroscopy of quasiparticle bound states in a spinful josephson junction," *Physical review letters*, vol. 110, no. 21, p. 217005, 2013.

[28] E. J. Lee, X. Jiang, R. Aguado, G. Katsaros, C. M. Lieber, and S. De Franceschi, "Zero-bias anomaly in a nanowire quantum dot coupled to superconductors," *Physical review letters*, vol. 109, no. 18, p. 186802, 2012.

[29] E. J. Lee, X. Jiang, M. Houzet, R. Aguado, C. M. Lieber, and S. De Franceschi, "Spin-resolved andreev levels and parity crossings in hybrid superconductor–semiconductor nanostructures," *Nature nanotechnology*, vol. 9, no. 1, p. 79, 2014.

[30] E. J. Lee, X. Jiang, R. Aguado, C. M. Lieber, S. De Franceschi, *et al.*, "Scaling of subgap excitations in a superconductor-semiconductor nanowire quantum dot," *Physical Review B*, vol. 95, no. 18, p. 180502, 2017.

[31] R. Deacon, Y. Tanaka, A. Oiwa, R. Sakano, K. Yoshida, K. Shibata, K. Hirakawa, and S. Tarucha, "Tunneling spectroscopy of andreev energy levels in a quantum dot coupled to a superconductor," *Physical review letters*, vol. 104, no. 7, p. 076805, 2010.

[32] A. Yazdani, B. Jones, C. Lutz, M. Crommie, and D. Eigler, "Probing the local effects of magnetic impurities on superconductivity," *Science*, vol. 275, no. 5307, pp. 1767–1770, 1997.

[33] G. C. Ménard, S. Guissart, C. Brun, S. Pons, V. S. Stolyarov, F. Debontridder, M. V. Leclerc, E. Janod, L. Cario, D. Roditchev, *et al.*, "Coherent long-range magnetic bound states in a superconductor," *Nature Physics*, vol. 11, no. 12, pp. 1013–1016, 2015.

[34] N. Hatter, B. W. Heinrich, M. Ruby, J. I. Pascual, and K. J. Franke, "Magnetic anisotropy in shiba bound states across a quantum phase transition," *Nature communications*, vol. 6, no. 1, pp. 1–6, 2015.

[35] L. Farinacci, G. Ahmadi, G. Reecht, M. Ruby, N. Bogdanoff, O. Peters, B. W. Heinrich, F. von Oppen, and K. J. Franke, "Tuning the coupling of an individual magnetic impurity to a superconductor: quantum phase transition and transport," *Physical review letters*, vol. 121, no. 19, p. 196803, 2018.

[36] J. O. Island, R. Gaudenzi, J. de Bruijckere, E. Burzurí, C. Franco, M. Mas-Torrent, C. Rovira, J. Veciana, T. M. Klapwijk, R. Aguado, *et al.*, "Proximity-induced shiba states in a molecular junction," *Physical review letters*, vol. 118, no. 11, p. 117001, 2017.

[37] D. Van Zanten, *Quantum dynamics revealed in weakly coupled quantum dot-superconductor turnstiles*. PhD thesis, 2015.

[38] D. van Zanten, F. Balestro, H. Courtois, and C. Winkelmann, "Probing hybridization of a single energy level coupled to superconducting leads," *Physical Review B*, vol. 92, no. 18, p. 184501, 2015.

[39] C. B. Winkelmann, N. Roch, W. Wernsdorfer, V. Bouchiat, and F. Balestro, "Superconductivity in a single-c 60 transistor," *Nature Physics*, vol. 5, no. 12, p. 876, 2009.

[40] A. Kumar, M. Gaim, D. Steininger, A. L. Yeyati, A. Martín-Rodero, A. Hüttel, and C. Strunk, "Temperature dependence of andreev spectra in a superconducting carbon nanotube quantum dot," *Physical Review B*, vol. 89, no. 7, p. 075428, 2014.

[41] A. Jellinggaard, K. Grove-Rasmussen, M. H. Madsen, and J. Nygård, "Tuning yu-shiba-rusinov states in a quantum dot," *Physical Review B*, vol. 94, no. 6, p. 064520, 2016.

[42] S. Li, N. Kang, P. Caroff, and H. Xu, "0- π phase transition in hybrid superconductor–insb nanowire quantum dot devices," *Physical Review B*, vol. 95, no. 1, p. 014515, 2017.

[43] R. Delagrange, D. Luitz, R. Weil, A. Kasumov, V. Meden, H. Bouchiat, and R. Deblock, "Manipulating the magnetic state of a carbon nanotube josephson junction using the superconducting phase," *Physical Review B*, vol. 91, no. 24, p. 241401, 2015.

[44] A. G. Corral, D. van Zanten, K. Franke, H. Courtois, S. Florens, and C. Winkelmann, "Magnetic-field-induced transition in a quantum dot coupled to a superconductor," *Physical Review Research*, vol. 2, no. 1, p. 012065, 2020.

[45] G. Yamahata, S. P. Giblin, M. Kataoka, T. Karasawa, and A. Fujiwara, "Gigahertz single-electron pumping in silicon with an accuracy better than 9.2 parts in 107," *Applied Physics Letters*, vol. 109, no. 1, p. 013101, 2016.

[46] J. P. Pekola, J. J. Vartiainen, M. Möttönen, O.-P. Saira, M. Meschke, and D. V. Averin, "Hybrid single-electron transistor as a source of quantized electric current," *Nature Physics*, vol. 4, no. 2, p. 120, 2008.

[47] A. Kemppinen, M. Meschke, M. Möttönen, D. V. Averin, and J. P. Pekola, "Quantized current of a hybrid single-electron transistor with superconducting leads and a normal-metal island," *The European Physical Journal Special Topics*, vol. 172, no. 1, pp. 311–321, 2009.

[48] D. Van Zanten, D. Basko, I. Khaymovich, J. Pekola, H. Courtois, and C. Winkelmann, "Single quantum level electron turnstile," *Physical review letters*, vol. 116, no. 16, p. 166801, 2016.

[49] N. Ashcroft and N. Mermin, *Solid State Physics*. Philadelphia: Saunders College, 1976.

[50] T. Ouisse, *Electron transport in nanostructures and mesoscopic devices: an introduction*. John Wiley & Sons, 2013.

[51] S. Datta, *Electronic transport in mesoscopic systems*. Cambridge university press, 1997.

[52] M. A. Kastner, "Artificial atoms," *Physics today*, vol. 46, pp. 24–24, 1993.

[53] B. Dutta, J. T. Peltonen, D. S. Antonenko, M. Meschke, M. A. Skvortsov, B. Kubala, J. König, C. B. Winkelmann, H. Courtois, and J. P. Pekola, "Thermal conductance of a single-electron transistor," *Physical review letters*, vol. 119, no. 7, p. 077701, 2017.

[54] E. Osorio, T. Bjørnholm, J. Lehn, M. Ruben, and H. Van der Zant, "Single-molecule transport in three-terminal devices," *Journal of Physics: Condensed Matter*, vol. 20, no. 37, p. 374121, 2008.

[55] K. Moth-Poulsen and T. Bjørnholm, "Molecular electronics with single molecules in solid-state devices," *Nature nanotechnology*, vol. 4, no. 9, p. 551, 2009.

[56] W. Chen, H. Ahmed, and K. Nakazoto, "Coulomb blockade at 77 k in nanoscale metallic islands in a lateral nanostructure," *Applied Physics Letters*, vol. 66, no. 24, pp. 3383–3384, 1995.

[57] Y. A. Pashkin, Y. Nakamura, and J.-S. Tsai, "Room-temperature al single-electron transistor made by electron-beam lithography," *Applied Physics Letters*, vol. 76, no. 16, pp. 2256–2258, 2000.

[58] C. Beenakker, "Theory of coulomb-blockade oscillations in the conductance of a quantum dot," *Physical Review B*, vol. 44, no. 4, p. 1646, 1991.

[59] T. A. Fulton and G. J. Dolan, "Observation of single-electron charging effects in small tunnel junctions," *Physical review letters*, vol. 59, no. 1, p. 109, 1987.

[60] U. Meirav, M. Kastner, and S. Wind, "Single-electron charging and periodic conductance resonances in gaas nanostructures," *Physical review letters*, vol. 65, no. 6, p. 771, 1990.

[61] L. Kouwenhoven, N. Van der Vaart, A. Johnson, W. Kool, C. Harmans, J. Williamson, A. Staring, and C. Foxon, "Single electron charging effects in semiconductor quantum dots," *Zeitschrift für Physik B Condensed Matter*, vol. 85, no. 3, pp. 367–373, 1991.

[62] L. Kouwenhoven, A. Johnson, N. Van der Vaart, A. Van der Enden, C. Harmans, and C. Foxon, "Quantized current in a quantum dot turnstile," *Zeitschrift für Physik B Condensed Matter*, vol. 85, no. 3, pp. 381–388, 1991.

[63] M. A. Kastner, "The single-electron transistor," *Reviews of modern physics*, vol. 64, no. 3, p. 849, 1992.

[64] I. Kulik and R. Shekhter, "Kinetic phenomena and charge-discreteness effects in granulated media," *Zhur. Eksper. Teoret. Fiziki*, vol. 68, no. 2, pp. 623–640, 1975.

[65] D. Averin and K. Likharev, "Coulomb blockade of single-electron tunneling, and coherent oscillations in small tunnel junctions," *Journal of low temperature physics*, vol. 62, no. 3-4, pp. 345–373, 1986.

[66] D. Averin, A. Korotkov, and K. Likharev, "Theory of single-electron charging of quantum wells and dots," *Physical Review B*, vol. 44, no. 12, pp. 6199–6211, 1991.

[67] K. K. Likharev, "Correlated discrete transfer of single electrons in ultrasmall tunnel junctions," *IBM Journal of Research and Development*, vol. 32, no. 1, pp. 144–158, 1988.

[68] A. Hanna and M. Tinkham, "Variation of the coulomb staircase in a two-junction system by fractional electron charge," *Physical review B*, vol. 44, no. 11, p. 5919, 1991.

[69] M. Amman, R. Wilkins, E. Ben-Jacob, P. Maker, and R. Jaklevic, "Analytic solution for the current-voltage characteristic of two mesoscopic tunnel junctions coupled in series," *Physical Review B*, vol. 43, no. 1, p. 1146, 1991.

[70] J. Park, *Electron transport in single molecule transistors*. PhD thesis, University of California, Berkeley, 2003.

[71] J. M. Thijssen and H. S. Van der Zant, "Charge transport and single-electron effects in nanoscale systems," *physica status solidi (b)*, vol. 245, no. 8, pp. 1455–1470, 2008.

[72] M. Reed, J. Randall, R. Aggarwal, R. Matyi, T. Moore, and A. Wetsel, "Observation of discrete electronic states in a zero-dimensional semiconductor nanostructure," *Physical Review Letters*, vol. 60, no. 6, p. 535, 1988.

[73] S. Sapmaz, P. Jarillo-Herrero, J. Kong, C. Dekker, L. Kouwenhoven, and H. van der Zant, "Electronic excitation spectrum of metallic carbon nanotubes," *Physical Review B*, vol. 71, no. 15, p. 153402, 2005.

[74] H. Park, J. Park, A. K. Lim, E. H. Anderson, A. P. Alivisatos, and P. L. McEuen, "Nanomechanical oscillations in a single-c 60 transistor," *Nature*, vol. 407, no. 6800, p. 57, 2000.

[75] E. A. Osorio, K. O'Neill, N. Stuhr-Hansen, O. F. Nielsen, T. Bjørnholm, and H. S. van der Zant, "Addition energies and vibrational fine structure measured in electromigrated single-molecule junctions based on an oligophenylenevinylene derivative," *Advanced Materials*, vol. 19, no. 2, pp. 281–285, 2007.

[76] F. Kuemmeth, K. I. Bolotin, S.-F. Shi, and D. C. Ralph, "Measurement of discrete energy-level spectra in individual chemically synthesized gold nanoparticles," *Nano letters*, vol. 8, no. 12, pp. 4506–4512, 2008.

[77] K. Shibata, K. Seki, P. Luukko, E. Räsänen, K. Cha, I. Horiuchi, and K. Hirakawa, "Electronic structures in single self-assembled inas quantum dashes detected by nanogap metal electrodes," *Applied Physics Letters*, vol. 99, no. 18, p. 182104, 2011.

[78] E. A. Osorio, K. O'Neill, M. Wegewijs, N. Stuhr-Hansen, J. Paaske, T. Bjørnholm, and H. S. Van der Zant, "Electronic excitations of a single molecule contacted in a three-terminal configuration," *Nano letters*, vol. 7, no. 11, pp. 3336–3342, 2007.

[79] N. Roch, S. Florens, V. Bouchiat, W. Wernsdorfer, and F. Balestro, "Out-of-equilibrium singlet-triplet kondo effect in a single c 60 quantum dot," *Journal of Low Temperature Physics*, vol. 153, no. 5-6, pp. 350–358, 2008.

[80] M. L. Perrin, E. Burzurí, and H. S. van der Zant, "Single-molecule transistors," *Chemical Society Reviews*, vol. 44, no. 4, pp. 902–919, 2015.

[81] E. Foxman, U. Meirav, P. McEuen, M. Kastner, O. Klein, P. Belk, D. Abusch, and S. Wind, "Crossover from single-level to multilevel transport in artificial atoms," *Physical Review B*, vol. 50, no. 19, p. 14193, 1994.

[82] D. Averin and A. Korotkov, "Influence of discrete energy spectrum on correlated single-electron tunneling via a mezoscopically small metal granule," *Zh. Eksp. Teor. Fiz*, vol. 97, no. 5, p. 1661, 1990.

[83] E. Bonet, M. M. Deshmukh, and D. Ralph, "Solving rate equations for electron tunneling via discrete quantum states," *Physical Review B*, vol. 65, no. 4, p. 045317, 2002.

[84] M. M. Deshmukh, E. Bonet, A. Pasupathy, and D. Ralph, "Equilibrium and nonequilibrium electron tunneling via discrete quantum states," *Physical Review B*, vol. 65, no. 7, p. 073301, 2002.

[85] S. De Franceschi, S. Sasaki, J. Elzerman, W. Van Der Wiel, S. Tarucha, and L. P. Kouwenhoven, "Electron cotunneling in a semiconductor quantum dot," *Physical review letters*, vol. 86, no. 5, p. 878, 2001.

[86] H. Grabert and M. H. Devoret, *Single charge tunneling: Coulomb blockade phenomena in nanostructures*, vol. 294. Springer Science & Business Media, 2013.

[87] Y. Meir and N. S. Wingreen, "Landauer formula for the current through an interacting electron region," *Physical review letters*, vol. 68, no. 16, p. 2512, 1992.

[88] W. De Haas and G. Van den Berg, "The electrical resistance of gold and silver at low temperatures," *Physica*, vol. 3, no. 6, pp. 440–449, 1936.

[89] J. Kondo, "Resistance minimum in dilute magnetic alloys," *Progress of theoretical physics*, vol. 32, no. 1, pp. 37–49, 1964.

[90] A. Abrikosov, "Physics long island city," 1965.

[91] I. V. Borzenets, J. Shim, J. C. Chen, A. Ludwig, A. D. Wieck, S. Tarucha, H.-S. Sim, and M. Yamamoto, "Observation of the kondo screening cloud," *Nature*, vol. 579, no. 7798, pp. 210–213, 2020.

[92] T. Costi, A. Hewson, and V. Zlatic, "Transport coefficients of the anderson model via the numerical renormalization group," *Journal of Physics: Condensed Matter*, vol. 6, no. 13, p. 2519, 1994.

[93] P. W. Anderson, "Localized magnetic states in metals," *Physical Review*, vol. 124, no. 1, p. 41, 1961.

[94] P. Anderson, "A poor man's derivation of scaling laws for the kondo problem," *Journal of Physics C: Solid State Physics*, vol. 3, no. 12, p. 2436, 1970.

[95] K. G. Wilson, "The renormalization group: Critical phenomena and the kondo problem," *Reviews of modern physics*, vol. 47, no. 4, p. 773, 1975.

[96] N. Andrei, "Diagonalization of the kondo hamiltonian," *Physical Review Letters*, vol. 45, no. 5, p. 379, 1980.

[97] V. Filyov and P. Wiegmann, "A method for solving the kondo problem," *Physics Letters A*, vol. 76, no. 3-4, pp. 283–286, 1980.

[98] M. Pustilnik and L. Glazman, "Kondo effect in quantum dots," *Journal of Physics: Condensed Matter*, vol. 16, no. 16, p. R513, 2004.

[99] M. Grobis, I. G. Rau, R. M. Potok, and D. Goldhaber-Gordon, "The kondo effect in mesoscopic quantum dots," *Handbook of Magnetism and Advanced Magnetic Materials*, 2007.

[100] D. Goldhaber-Gordon, H. Shtrikman, D. Mahalu, D. Abusch-Magder, U. Meirav, and M. Kastner, "Kondo effect in a single-electron transistor," *Nature*, vol. 391, no. 6663, pp. 156–159, 1998.

[101] D. Goldhaber-Gordon, J. Göres, M. Kastner, H. Shtrikman, D. Mahalu, and U. Meirav, "From the kondo regime to the mixed-valence regime in a single-electron transistor," *Physical Review Letters*, vol. 81, no. 23, p. 5225, 1998.

[102] S. M. Cronenwett, T. H. Oosterkamp, and L. P. Kouwenhoven, "A tunable kondo effect in quantum dots," *Science*, vol. 281, no. 5376, pp. 540–544, 1998.

[103] J. Nygård, D. H. Cobden, and P. E. Lindelof, "Kondo physics in carbon nanotubes," *Nature*, vol. 408, no. 6810, pp. 342–346, 2000.

[104] D. Ralph and R. Buhrman, "Kondo-assisted and resonant tunneling via a single charge trap: A realization of the anderson model out of equilibrium," *Physical review letters*, vol. 72, no. 21, p. 3401, 1994.

[105] N. Roch, C. Winkelmann, S. Florens, V. Bouchiat, W. Wernsdorfer, and F. Balestro, "Kondo effects in a c60 single-molecule transistor," *physica status solidi (b)*, vol. 245, no. 10, pp. 1994–1997, 2008.

[106] J. Parks, A. Champagne, G. Hutchison, S. Flores-Torres, H. Abruna, and D. Ralph, "Tuning the kondo effect with a mechanically controllable break junction," *Physical review letters*, vol. 99, no. 2, p. 026601, 2007.

[107] W. Liang, M. P. Shores, M. Bockrath, J. R. Long, and H. Park, "Kondo resonance in a single-molecule transistor," *Nature*, vol. 417, no. 6890, p. 725, 2002.

[108] J. Park, A. N. Pasupathy, J. I. Goldsmith, C. Chang, Y. Yaish, J. R. Petta, M. Rinkoski, J. P. Sethna, H. D. Abruña, P. L. McEuen, *et al.*, "Coulomb blockade and the kondo effect in single-atom transistors," *Nature*, vol. 417, no. 6890, p. 722, 2002.

[109] V. Madhavan, W. Chen, T. Jamneala, M. Crommie, and N. S. Wingreen, "Tunneling into a single magnetic atom: spectroscopic evidence of the kondo resonance," *Science*, vol. 280, no. 5363, pp. 567–569, 1998.

[110] L. Yu, Z. K. Keane, J. W. Ciszek, L. Cheng, M. Stewart, J. Tour, and D. Natelson, "Inelastic electron tunneling via molecular vibrations in single-molecule transistors," *Physical review letters*, vol. 93, no. 26, p. 266802, 2004.

[111] N. Roch, S. Florens, V. Bouchiat, W. Wernsdorfer, and F. Balestro, "Quantum phase transition in a single-molecule quantum dot," *Nature*, vol. 453, no. 7195, pp. 633–637, 2008.

[112] J. R. Schrieffer and P. A. Wolff, "Relation between the anderson and kondo hamiltonians," *Physical Review*, vol. 149, no. 2, p. 491, 1966.

[113] T. Yoshioka and Y. Ohashi, "Numerical renormalization group studies on single impurity anderson model in superconductivity: A unified treatment of magnetic, nonmagnetic impurities, and resonance scattering," *Journal of the Physical Society of Japan*, vol. 69, no. 6, pp. 1812–1823, 2000.

[114] F. Haldane, "Scaling theory of the asymmetric anderson model," *Physical Review Letters*, vol. 40, no. 6, p. 416, 1978.

[115] P. Nozieres, "A "fermi-liquid" description of the kondo problem at low temperatures," *Journal of low température physics*, vol. 17, no. 1-2, pp. 31–42, 1974.

[116] M. Tinkham, *Introduction to superconductivity*. Courier Corporation, 2004.

[117] N. Court, A. Ferguson, and R. Clark, "Energy gap measurement of nanostructured aluminium thin films for single cooper-pair devices," *Superconductor Science and Technology*, vol. 21, no. 1, p. 015013, 2007.

[118] T. Yamamoto, Y. Nakamura, Y. A. Pashkin, O. Astafiev, and J. S. Tsai, "Parity effect in superconducting aluminum single electron transistors with spatial gap profile controlled by film thickness," *Applied physics letters*, vol. 88, no. 21, p. 212509, 2006.

[119] H. Krakauer, M. Posternak, and A. J. Freeman, "Linearized augmented plane-wave method for the electronic band structure of thin films," *Physical Review B*, vol. 19, no. 4, p. 1706, 1979.

[120] M. Croitoru, A. Shanenko, and F. Peeters, "Dependence of superconducting properties on the size and shape of a nanoscale superconductor: From nanowire to film," *Physical Review B*, vol. 76, no. 2, p. 024511, 2007.

[121] P. Wójcik and M. Zegrodnik, "Influence of the electron density on the thickness-dependent energy gap oscillations in superconducting metallic nanofilms," *physica status solidi (b)*, vol. 251, no. 5, pp. 1069–1075, 2014.

[122] S. Nik, P. Krantz, L. Zeng, T. Greibe, H. Pettersson, S. Gustafsson, P. Delsing, and E. Olsson, "Correlation between al grain size, grain boundary grooves and local variations in oxide barrier thickness of al/alo x/al tunnel junctions by transmission electron microscopy," *SpringerPlus*, vol. 5, no. 1, pp. 1–7, 2016.

[123] A. Ghosal, M. Randeria, and N. Trivedi, "Role of spatial amplitude fluctuations in highly disordered s-wave superconductors," *Physical review letters*, vol. 81, no. 18, p. 3940, 1998.

[124] R. Dynes and J. Garno, "Metal-insulator transition in granular aluminum," *Physical Review Letters*, vol. 46, no. 2, p. 137, 1981.

[125] M. Skvortsov and M. Feigel'man, "Superconductivity in disordered thin films: giant mesoscopic fluctuations," *Physical review letters*, vol. 95, no. 5, p. 057002, 2005.

[126] F. Yang, T. Storbeck, T. Gozlinski, L. Gruenhaupt, I. M. Pop, and W. Wulfhekel, "Microscopic charging and in-gap states in superconducting granular aluminum," *arXiv preprint arXiv:1911.02312*, 2019.

[127] F. Levy-Bertrand, T. Klein, T. Grenet, O. Dupré, A. Benoît, A. Bideaud, O. Bourrion, M. Calvo, A. Catalano, A. Gomez, *et al.*, "Electrodynamics of granular aluminum from superconductor to insulator: Observation of collective superconducting modes," *Physical Review B*, vol. 99, no. 9, p. 094506, 2019.

[128] N. Maleeva, L. Grünhaupt, T. Klein, F. Levy-Bertrand, O. Dupre, M. Calvo, F. Valenti, P. Winkel, F. Friedrich, W. Wernsdorfer, *et al.*, "Circuit quantum electrodynamics of granular aluminum resonators," *Nature communications*, vol. 9, no. 1, pp. 1–7, 2018.

[129] T. Fulton, P. Gammel, D. Bishop, L. Dunkleberger, and G. Dolan, "Observation of combined josephson and charging effects in small tunnel junction circuits," *Physical review letters*, vol. 63, no. 12, p. 1307, 1989.

[130] L. Geerligs, V. Anderegg, J. Romijn, and J. Mooij, "Single cooper-pair tunneling in small-capacitance junctions," *Physical review letters*, vol. 65, no. 3, p. 377, 1990.

[131] L. Geerligs, V. Anderegg, P. Holweg, J. Mooij, H. Pothier, D. Esteve, C. Urbina, and M. Devoret, "Frequency-locked turnstile device for single electrons," *Physical review letters*, vol. 64, no. 22, p. 2691, 1990.

[132] D. Gunnarsson, T. Duty, K. Bladh, and P. Delsing, "Tunability of a 2 e periodic single cooper pair box," *Physical Review B*, vol. 70, no. 22, p. 224523, 2004.

[133] V. Maisi, O.-P. Saira, Y. A. Pashkin, J. S. Tsai, D. Averin, and J. P. Pekola, "Real-time observation of discrete andreev tunneling events," *Physical review letters*, vol. 106, no. 21, p. 217003, 2011.

[134] J. P. Nacenta Mendivil, *Direct imaging of electrical fields using a scanning single electron transistor*. Theses, Université Grenoble Alpes, Feb. 2019.

[135] D. Ginsberg, "Upper limit for quasi-particle recombination time in a superconductor," *Physical Review Letters*, vol. 8, no. 5, p. 204, 1962.

[136] J. L. Levine and S. Hsieh, "Recombination time of quasiparticles in superconducting aluminum," *Physical Review Letters*, vol. 20, no. 18, p. 994, 1968.

[137] R. Dynes, J. Garno, G. Hertel, and T. Orlando, "Tunneling study of superconductivity near the metal-insulator transition," *Physical review letters*, vol. 53, no. 25, p. 2437, 1984.

[138] J. P. Pekola, V. Maisi, S. Kafanov, N. Chekurov, A. Kemppinen, Y. A. Pashkin, O.-P. Saira, M. Möttönen, and J. S. Tsai, "Environment-assisted tunneling as an origin of the dynes density of states," *Physical review letters*, vol. 105, no. 2, p. 026803, 2010.

[139] A. Di Marco, V. F. Maisi, F. W. Hekking, and J. P. Pekola, "Effect of photon-assisted andreev reflection in the accuracy of a sinis turnstile," *Physical Review B*, vol. 92, no. 9, p. 094514, 2015.

[140] K. Bolotin, F. Kuemmeth, A. Pasupathy, and D. Ralph, "Metal-nanoparticle single-electron transistors fabricated using electromigration," *Applied Physics Letters*, vol. 84, no. 16, pp. 3154–3156, 2004.

[141] K. I. Bolotin, *Spin-dependent transport in nanoscale structures*. Cornell University, 2007.

[142] F. Kuemmeth, *Spin states and spin-orbit coupling in nanostructures*, vol. 69. 2008.

[143] A. L. Yeyati, J. Cuevas, A. López-Dávalos, and A. Martin-Rodero, "Resonant tunneling through a small quantum dot coupled to superconducting leads," *Physical Review B*, vol. 55, no. 10, p. R6137, 1997.

[144] K. Kang, "Transport through an interacting quantum dot coupled to two superconducting leads," *Physical Review B*, vol. 57, no. 19, p. 11891, 1998.

[145] K. Kang, "Kondo resonance, coulomb blockade, and andreev transport through a quantum dot," *Physical Review B*, vol. 58, no. 15, p. 9641, 1998.

[146] A. V. Balatsky, I. Vekhter, and J.-X. Zhu, "Impurity-induced states in conventional and unconventional superconductors," *Reviews of Modern Physics*, vol. 78, no. 2, p. 373, 2006.

[147] B. W. Heinrich, J. I. Pascual, and K. J. Franke, "Single magnetic adsorbates on s-wave superconductors," *Progress in Surface Science*, vol. 93, no. 1, pp. 1–19, 2018.

[148] L. Yu, "Bound state in superconductors with paramagnetic impurities," *Acta Phys. Sin*, vol. 21, no. 1, pp. 75–91, 1965.

[149] H. Shiba, "Classical spins in superconductors," *Progress of theoretical Physics*, vol. 40, no. 3, pp. 435–451, 1968.

[150] A. Rusinov, "Superconductivity near a paramagnetic impurity," *Soviet Journal of Experimental and Theoretical Physics Letters*, vol. 9, p. 85, 1969.

[151] A. Rusinov, "Theory of gapless superconductivity in alloys containing paramagnetic impurities," *Sov. Phys. JETP*, vol. 29, no. 6, pp. 1101–1106, 1969.

[152] S.-H. Ji, T. Zhang, Y.-S. Fu, X. Chen, X.-C. Ma, J. Li, W.-H. Duan, J.-F. Jia, and Q.-K. Xue, "High-resolution scanning tunneling spectroscopy of magnetic impurity induced bound states in the superconducting gap of pb thin films," *Physical review letters*, vol. 100, no. 22, p. 226801, 2008.

[153] M. Vojta, "Quantum phase transitions," *Reports on Progress in Physics*, vol. 66, no. 12, p. 2069, 2003.

[154] A. Kadlecová, M. Žonda, V. Pokorný, and T. Novotný, "Practical guide to quantum phase transitions in quantum-dot-based tunable josephson junctions," *Physical Review Applied*, vol. 11, no. 4, p. 044094, 2019.

[155] L. P. Kouwenhoven, T. Oosterkamp, M. Danoesastro, M. Eto, D. Austing, T. Honda, and S. Tarucha, "Excitation spectra of circular, few-electron quantum dots," *Science*, vol. 278, no. 5344, pp. 1788–1792, 1997.

[156] T. Matsuura, "The effects of impurities on superconductors with kondo effect," *Progress of Theoretical Physics*, vol. 57, no. 6, pp. 1823–1835, 1977.

[157] V. Meden, "The anderson-josephson quantum dot-a theory perspective," *Journal of Physics: Condensed Matter*, 2019.

[158] M.-S. Choi, M. Lee, K. Kang, and W. Belzig, "Kondo effect and josephson current through a quantum dot between two superconductors," *Physical Review B*, vol. 70, no. 2, p. 020502, 2004.

[159] C. Beenakker and H. Van Houten, "Resonant josephson current through a quantum dot," in *Single-Electron Tunneling and Mesoscopic Devices*, pp. 175–179, Springer, 1992.

[160] E. Vecino, A. Martín-Rodero, and A. L. Yeyati, "Josephson current through a correlated quantum level: Andreev states and π junction behavior," *Physical Review B*, vol. 68, no. 3, p. 035105, 2003.

[161] J. Bauer, A. Oguri, and A. Hewson, "Spectral properties of locally correlated electrons in a bardeen–cooper–schrieffer superconductor," *Journal of Physics: Condensed Matter*, vol. 19, no. 48, p. 486211, 2007.

[162] T. Meng, S. Florens, and P. Simon, "Self-consistent description of andreev bound states in josephson quantum dot devices," *Physical Review B*, vol. 79, no. 22, p. 224521, 2009.

[163] K. Satori, H. Shiba, O. Sakai, and Y. Shimizu, "Numerical renormalization group study of magnetic impurities in superconductors," *Journal of the Physical Society of Japan*, vol. 61, no. 9, pp. 3239–3254, 1992.

[164] O. Sakai, Y. Shimizu, H. Shiba, and K. Satori, "Numerical renormalization group study of magnetic impurities in superconductors. ii. dynamical excitation spectra and spatial variation of the order parameter," *Journal of the Physical Society of Japan*, vol. 62, no. 9, pp. 3181–3197, 1993.

[165] J. Bauer, J. I. Pascual, and K. J. Franke, "Microscopic resolution of the interplay of kondo screening and superconducting pairing: Mn-phthalocyanine molecules adsorbed on superconducting pb (111)," *Physical Review B*, vol. 87, no. 7, p. 075125, 2013.

[166] R. Zitko, "Kondo resonance line-shape of magnetic adatoms on decoupling layers," *arXiv preprint arXiv:1110.4561*, 2011.

[167] A. Aviram, C. Joachim, and M. Pomerantz, "Evidence of switching and rectification by a single molecule effected with a scanning tunneling microscope," *Chemical Physics Letters*, vol. 146, no. 6, pp. 490–495, 1988.

[168] H. He, C. Li, and N. Tao, "Conductance of polymer nanowires fabricated by a combined electrodeposition and mechanical break junction method," *Applied Physics Letters*, vol. 78, no. 6, pp. 811–813, 2001.

[169] B. Xu and N. J. Tao, "Measurement of single-molecule resistance by repeated formation of molecular junctions," *science*, vol. 301, no. 5637, pp. 1221–1223, 2003.

[170] X. Xiao, B. Xu, and N. J. Tao, "Measurement of single molecule conductance: Benzenedithiol and benzenedimethanethiol," *Nano Letters*, vol. 4, no. 2, pp. 267–271, 2004.

[171] M. A. Reed, C. Zhou, C. Muller, T. Burgin, and J. Tour, "Conductance of a molecular junction," *Science*, vol. 278, no. 5336, pp. 252–254, 1997.

[172] L. Wang, L. Wang, L. Zhang, and D. Xiang, "Advance of mechanically controllable break junction for molecular electronics," in *Molecular-Scale Electronics*, pp. 45–86, Springer, 2019.

[173] C. Kergueris, J.-P. Bourgoin, S. Palacin, D. Estève, C. Urbina, M. Magoga, and C. Joachim, "Electron transport through a metal-molecule-metal junction," *Physical Review B*, vol. 59, no. 19, p. 12505, 1999.

[174] J. Reichert, R. Ochs, D. Beckmann, H. Weber, M. Mayor, and H. v. Löhneysen, "Driving current through single organic molecules," *Physical Review Letters*, vol. 88, no. 17, p. 176804, 2002.

[175] C. Li, I. Pobelov, T. Wandlowski, A. Bagrets, A. Arnold, and F. Evers, "Charge transport in single au| alkanedithiol| au junctions: coordination geometries and conformational degrees of freedom," *Journal of the American Chemical Society*, vol. 130, no. 1, pp. 318–326, 2008.

[176] S. Y. Quek, M. Kamenetska, M. L. Steigerwald, H. J. Choi, S. G. Louie, M. S. Hybertsen, J. Neaton, and L. Venkataraman, "Mechanically controlled binary conductance switching of a single-molecule junction," *Nature nanotechnology*, vol. 4, no. 4, p. 230, 2009.

[177] C. Bruot, J. Hihath, and N. Tao, "Mechanically controlled molecular orbital alignment in single molecule junctions," *Nature nanotechnology*, vol. 7, no. 1, p. 35, 2012.

[178] E. Lörtscher, J. W. Ciszek, J. Tour, and H. Riel, "Reversible and controllable switching of a single-molecule junction," *Small*, vol. 2, no. 8-9, pp. 973–977, 2006.

[179] D. Xiang, H. Jeong, D. Kim, T. Lee, Y. Cheng, Q. Wang, and D. Mayer, "Three-terminal single-molecule junctions formed by mechanically controllable break junctions with side gating," *Nano letters*, vol. 13, no. 6, pp. 2809–2813, 2013.

[180] H. Park, A. K. Lim, A. P. Alivisatos, J. Park, and P. L. McEuen, "Fabrication of metallic electrodes with nanometer separation by electromigration," *Applied Physics Letters*, vol. 75, no. 2, pp. 301–303, 1999.

[181] Y. Zhang, Y.-W. Tan, H. L. Stormer, and P. Kim, "Experimental observation of the quantum hall effect and berry's phase in graphene," *nature*, vol. 438, no. 7065, p. 201, 2005.

[182] N. Roch, *Transistors à molécule unique: des effets Kondo exotiques à la spintronique moléculaire*. PhD thesis, 2009.

[183] Y. Hu, H. O. Churchill, D. J. Reilly, J. Xiang, C. M. Lieber, and C. M. Marcus, "A ge/si heterostructure nanowire-based double quantum dot with integrated charge sensor," *Nature nanotechnology*, vol. 2, no. 10, p. 622, 2007.

[184] S. Hermelin, S. Takada, M. Yamamoto, S. Tarucha, A. D. Wieck, L. Saminadayar, C. Bäuerle, and T. Meunier, "Electrons surfing on a sound wave as a platform for quantum optics with flying electrons," *Nature*, vol. 477, no. 7365, p. 435, 2011.

[185] J. Saldaña, A. Vekris, R. Žitko, G. Steffensen, P. Krogstrup, J. Paaske, K. Grove-Rasmussen, and J. Nygård, "Two-impurity yu-shiba-rusinov states in coupled quantum dots," *arXiv preprint arXiv:1812.09303*, 2018.

[186] D. M. van Zanten, D. Sabonis, J. Suter, J. I. Väyrynen, T. Karzig, D. I. Pikulin, E. C. O'Farrell, D. Razmadze, K. D. Petersson, P. Krogstrup, *et al.*, "Photon assisted tunneling of zero modes in a majorana wire," *arXiv preprint arXiv:1902.00797*, 2019.

[187] N. Tao, "Probing potential-tuned resonant tunneling through redox molecules with scanning tunneling microscopy," *Physical Review Letters*, vol. 76, no. 21, p. 4066, 1996.

[188] C. Huang, A. V. Rudnev, W. Hong, and T. Wandlowski, "Break junction under electrochemical gating: testbed for single-molecule electronics," *Chemical Society Reviews*, vol. 44, no. 4, pp. 889–901, 2015.

[189] J. Martínez-Blanco, C. Nacci, S. C. Erwin, K. Kanisawa, E. Locane, M. Thomas, F. Von Oppen, P. W. Brouwer, and S. Fölsch, "Gating a single-molecule transistor with individual atoms," *Nature Physics*, vol. 11, no. 8, pp. 640–644, 2015.

[190] C. A. Martin, R. H. Smit, H. S. van der Zant, and J. M. van Ruitenbeek, "A nanoelectromechanical single-atom switch," *Nano letters*, vol. 9, no. 8, pp. 2940–2945, 2009.

[191] A. R. Champagne, A. N. Pasupathy, and D. C. Ralph, "Mechanically adjustable and electrically gated single-molecule transistors," *Nano letters*, vol. 5, no. 2, pp. 305–308, 2005.

[192] C. A. Martin, J. M. van Ruitenbeek, and H. S. van der Zant, "Sandwich-type gated mechanical break junctions," *Nanotechnology*, vol. 21, no. 26, p. 265201, 2010.

[193] M. L. Perrin, C. J. Verzijl, C. A. Martin, A. J. Shaikh, R. Eelkema, J. H. Van Esch, J. M. Van Ruitenbeek, J. M. Thijssen, H. S. Van Der Zant, and D. Dulić, "Large tunable image-charge effects in single-molecule junctions," *Nature nanotechnology*, vol. 8, no. 4, p. 282, 2013.

[194] M. L. Perrin, E. Galán, R. Eelkema, J. M. Thijssen, F. Grozema, and H. S. van der Zant, "A gate-tunable single-molecule diode," *Nanoscale*, vol. 8, no. 16, pp. 8919–8923, 2016.

[195] S. Ballmann and H. B. Weber, "An electrostatic gate for mechanically controlled single-molecule junctions," *New Journal of Physics*, vol. 14, no. 12, p. 123028, 2012.

[196] Y.-J. Doh, S. D. Franceschi, E. P. Bakkers, and L. P. Kouwenhoven, "Andreev reflection versus coulomb blockade in hybrid semiconductor nanowire devices," *Nano letters*, vol. 8, no. 12, pp. 4098–4102, 2008.

[197] R. M. Barrett, "Microwave printed circuits-a historical survey," *IRE Transactions on microwave theory and techniques*, vol. 3, no. 2, pp. 1–9, 1955.

[198] D. D. Grieg and H. F. Engelmann, "Microwave cable," Oct. 18 1955. US Patent 2,721,312.

[199] C. P. Wen, "Coplanar waveguide: A surface strip transmission line suitable for nonreciprocal gyromagnetic device applications," *IEEE Transactions on Microwave Theory and Techniques*, vol. 17, no. 12, pp. 1087–1090, 1969.

[200] L. Planat, E. Al-Tavil, J. P. Martínez, R. Dassonneville, F. Foroughi, S. Léger, K. Bharadwaj, J. Delaforce, V. Milchakov, C. Naud, *et al.*, "Fabrication and characterization of aluminum squid transmission lines," *Physical Review Applied*, vol. 12, no. 6, p. 064017, 2019.

[201] G. Roussely, E. Arrighi, G. Georgiou, S. Takada, M. Schalk, M. Urdampilleta, A. Ludwig, A. D. Wieck, P. Armagnat, T. Kloss, *et al.*, "Unveiling the bosonic nature of an ultrashort few-electron pulse," *Nature communications*, vol. 9, no. 1, pp. 1–6, 2018.

[202] O.-P. Saira, A. Kemppinen, V. Maisi, and J. P. Pekola, "Vanishing quasiparticle density in a hybrid al/cu/al single-electron transistor," *Physical Review B*, vol. 85, no. 1, p. 012504, 2012.

[203] G. D. Wilk, R. M. Wallace, and J. Anthony, "High-κ gate dielectrics: Current status and materials properties considerations," *Journal of applied physics*, vol. 89, no. 10, pp. 5243–5275, 2001.

[204] J. Robertson, "High dielectric constant oxides," *The European Physical Journal-Applied Physics*, vol. 28, no. 3, pp. 265–291, 2004.

[205] K. Kukli, K. Forsgren, M. Ritala, M. Leskelä, J. Aarik, and A. Haårsta, "Dielectric properties of zirconium oxide grown by atomic layer deposition from iodide precursor," *Journal of The Electrochemical Society*, vol. 148, no. 12, pp. F227–F232, 2001.

[206] K. Kukli, J. Aarik, M. Ritala, T. Uustare, T. Sajavaara, J. Lu, J. Sundqvist, A. Aidla, L. Pung, A. Hårsta, *et al.*, "Effect of selected atomic layer deposition parameters on the structure and dielectric properties of hafnium oxide films," *Journal of applied physics*, vol. 96, no. 9, pp. 5298–5307, 2004.

[207] H. Kim, P. C. McIntyre, and K. C. Saraswat, "Effects of crystallization on the electrical properties of ultrathin hfo 2 dielectrics grown by atomic layer deposition," *Applied physics letters*, vol. 82, no. 1, pp. 106–108, 2003.

[208] V. Miikkulainen, M. Leskelä, M. Ritala, and R. L. Puurunen, "Crystallinity of inorganic films grown by atomic layer deposition: Overview and general trends," *Journal of Applied Physics*, vol. 113, no. 2, p. 2, 2013.

[209] H. Lin, P. Ye, and G. Wilk, "Leakage current and breakdown electric-field studies on ultrathin atomic-layer-deposited al 2 o 3 on gaas," *Applied physics letters*, vol. 87, no. 18, p. 182904, 2005.

[210] S. S. Datta, D. R. Strachan, and A. C. Johnson, "Gate coupling to nanoscale electronics," *Physical Review B*, vol. 79, no. 20, p. 205404, 2009.

[211] J. Chang and Y.-S. Lin, "Dielectric property and conduction mechanism of ultrathin zirconium oxide films," *Applied physics letters*, vol. 79, no. 22, pp. 3666–3668, 2001.

[212] W. Seith and H. Wever, "A new effect in the electrolytic transfer in solid alloys," *Z. Elektrochem*, vol. 57, no. 891, p. 61, 1953.

[213] V. Fiks, "On the mechanism of the mobility of ions in metals," *Soviet Physics-Solid State*, vol. 1, no. 1, pp. 14–28, 1959.

[214] H. Huntington and A. Grone, "Current-induced marker motion in gold wires," *Journal of Physics and Chemistry of Solids*, vol. 20, no. 1-2, pp. 76–87, 1961.

[215] I. Blech and E. Meieran, "Electromigration in thin al films," *Journal of Applied Physics*, vol. 40, no. 2, pp. 485–491, 1969.

[216] J. M. Baik, S. J. Lee, and M. Moskovits, "Polarized surface-enhanced raman spectroscopy from molecules adsorbed in nano-gaps produced by electromigration in silver nanowires," *Nano letters*, vol. 9, no. 2, pp. 672–676, 2009.

[217] K. Luo and Z. Yao, "Fabrication of nanometer-spaced superconducting pb electrodes," *Applied Physics Letters*, vol. 95, no. 11, p. 113115, 2009.

[218] L. Arzubiaga, F. Golmar, R. Llopis, F. Casanova, and L. E. Hueso, "In situ electrical characterization of palladium-based single electron transistors made by electromigration technique," *AIP Advances*, vol. 4, no. 11, p. 117126, 2014.

[219] B. Dutta, D. Majidi, A. García Corral, P. A. Erdman, S. Florens, T. A. Costi, H. Courtois, and C. B. Winkelmann, "Direct probe of the seebeck coefficient in a kondo-correlated single-quantum-dot transistor," *Nano letters*, vol. 19, no. 1, pp. 506–511, 2018.

[220] F. Prins, A. Barreiro, J. W. Ruitenberg, J. S. Seldenthuis, N. Aliaga-Alcalde, L. M. Vandersypen, and H. S. van der Zant, "Room-temperature gating of molecular junctions using few-layer graphene nanogap electrodes," *Nano letters*, vol. 11, no. 11, pp. 4607–4611, 2011.

[221] K. Ullmann, P. B. Coto, S. Leitherer, A. Molina-Ontoria, N. Martín, M. Thoss, and H. B. Weber, "Single-molecule junctions with epitaxial graphene nanoelectrodes," *Nano letters*, vol. 15, no. 5, pp. 3512–3518, 2015.

[222] R. Gaudenzi, J. Island, J. De Bruijckere, E. Burzurí, T. Klapwijk, and H. Van der Zant, "Superconducting molybdenum-rhenium electrodes for single-molecule transport studies," *Applied Physics Letters*, vol. 106, no. 22, p. 222602, 2015.

[223] L. Nguyen, T. Hashimoto, D. N. Zakharov, E. A. Stach, A. P. Rooney, B. Berkels, G. E. Thompson, S. J. Haigh, and T. L. Burnett, "Atomic-scale insights into the oxidation of aluminum," *ACS applied materials & interfaces*, vol. 10, no. 3, pp. 2230–2235, 2018.

[224] I. Giaever and H. Zeller, "Superconductivity of small tin particles measured by tunneling," *Physical Review Letters*, vol. 20, no. 26, p. 1504, 1968.

[225] J. Lambe and R. Jaklevic, "Charge-quantization studies using a tunnel capacitor," *Physical Review Letters*, vol. 22, no. 25, p. 1371, 1969.

[226] H. Zeller and I. Giaever, "Tunneling, zero-bias anomalies, and small superconductors," *Physical Review*, vol. 181, no. 2, p. 789, 1969.

[227] L. Bumm, J. J. Arnold, M. Cygan, T. Dunbar, T. Burgin, L. Jones, D. L. Allara, J. M. Tour, and P. Weiss, "Are single molecular wires conducting?," *Science*, vol. 271, no. 5256, pp. 1705–1707, 1996.

[228] X. Cui, A. Primak, X. Zarate, J. Tomfohr, O. Sankey, A. L. Moore, T. A. Moore, D. Gust, G. Harris, and S. Lindsay, "Reproducible measurement of single-molecule conductivity," *science*, vol. 294, no. 5542, pp. 571–574, 2001.

[229] D. L. Klein, P. L. McEuen, J. E. B. Katari, R. Roth, and A. P. Alivisatos, "An approach to electrical studies of single nanocrystals," *Applied Physics Letters*, vol. 68, no. 18, pp. 2574–2576, 1996.

[230] B. Alperson, I. Rubinstein, G. Hodes, D. Porath, and O. Millo, "Energy level tunneling spectroscopy and single electron charging in individual cdse quantum dots," *Applied physics letters*, vol. 75, no. 12, pp. 1751–1753, 1999.

[231] U. Banin, Y. Cao, D. Katz, and O. Millo, "Identification of atomic-like electronic states in indium arsenide nanocrystal quantum dots," *Nature*, vol. 400, no. 6744, pp. 542–544, 1999.

[232] N. Zhitenev, H. Meng, and Z. Bao, "Conductance of small molecular junctions," *Physical review letters*, vol. 88, no. 22, p. 226801, 2002.

[233] S. I. Khondaker, K. Luo, and Z. Yao, "The fabrication of single-electron transistors using dielectrophoretic trapping of individual gold nanoparticles," *Nanotechnology*, vol. 21, no. 9, p. 095204, 2010.

[234] S. Kubatkin, A. Danilov, M. Hjort, J. Cornil, J.-L. Bredas, N. Stuhr-Hansen, P. Hedegård, and T. Bjørnholm, "Single-electron transistor of a single organic molecule with access to several redox states," *Nature*, vol. 425, no. 6959, pp. 698–701, 2003.

[235] L. Yu, Z. K. Keane, J. W. Ciszek, L. Cheng, J. M. Tour, T. Baruah, M. Pederson, and D. Natelson, "Kondo resonances and anomalous gate dependence in the electrical conductivity of single-molecule transistors," *Physical review letters*, vol. 95, no. 25, p. 256803, 2005.

[236] L. H. Yu and D. Natelson, "The kondo effect in c60 single-molecule transistors," *Nano Letters*, vol. 4, no. 1, pp. 79–83, 2004.

[237] A. N. Pasupathy, R. C. Bialczak, J. Martinek, J. E. Grose, L. A. Donev, P. L. McEuen, and D. C. Ralph, "The kondo effect in the presence of ferromagnetism," *Science*, vol. 306, no. 5693, pp. 86–89, 2004.

[238] L. Rincón-García, A. K. Ismael, C. Evangeli, I. Grace, G. Rubio-Bollinger, K. Porfyrakis, N. Agraït, and C. J. Lambert, "Molecular design and control of fullerene-based bi-thermoelectric materials," *Nature materials*, vol. 15, no. 3, p. 289, 2016.

[239] C. Godfrin, A. Ferhat, R. Ballou, S. Klyatskaya, M. Ruben, W. Wernsdorfer, and F. Balestro, "Operating quantum states in single magnetic molecules: implementation of grover's quantum algorithm," *Physical review letters*, vol. 119, no. 18, p. 187702, 2017.

[240] *https://nanocomposix.com/*.

[241] A. Danilov, S. Kubatkin, S. Kafanov, P. Hedegård, N. Stuhr-Hansen, K. Moth-Poulsen, and T. Bjørnholm, "Electronic transport in single molecule junctions: Control of the molecule-electrode coupling through intramolecular tunneling barriers," *Nano Letters*, vol. 8, no. 1, pp. 1–5, 2008.

[242] C. Joachim, J. K. Gimzewski, R. R. Schlittler, and C. Chavy, "Electronic transparence of a single c 60 molecule," *Physical review letters*, vol. 74, no. 11, p. 2102, 1995.

[243] A. V. Danilov, S. E. Kubatkin, S. G. Kafanov, and T. Bjørnholm, "Strong electronic coupling between single c 60 molecules and gold electrodes prepared by quench condensation at 4 k. a single molecule three terminal device study," *Faraday discussions*, vol. 131, pp. 337–345, 2006.

[244] J. Weippert, L. Hohmann, D. Strelnikov, P. Weis, M. L. Pop, A. Bottcher, and M. M. Kappes, "Desorption of fullerene dimers upon heating non-ipr fullerene films on hopg," *The Journal of Physical Chemistry C*, vol. 123, no. 9, pp. 5721–5730, 2019.

[245] B. Dutta, *Energétique dans les dispositifs à un seul électron basés sur des îlots métalliques et des points quantiques*. PhD thesis, Grenoble Alpes, 2018.

[246] N. Moussy, *Supraconducteurs mésoscopiques étudiés par microscopie tunnel à très basse température*. PhD thesis, 2000.

[247] S. Thiele, *Read-Out and Coherent Manipulation of an Isolated Nuclear Spin: Using a Single-Molecule Magnet Spin-Transistor*. Springer, 2015.

[248] H. Bluhm and K. A. Moler, "Dissipative cryogenic filters with zero dc resistance," *Review of Scientific Instruments*, vol. 79, no. 1, p. 014703, 2008.

[249] A. Zorin, "The thermocoax cable as the microwave frequency filter for single electron circuits," *Review of Scientific Instruments*, vol. 66, no. 8, pp. 4296–4300, 1995.

[250] J. Campbell and R. Knobel, "Feedback-controlled electromigration for the fabrication of point contacts," *Applied Physics Letters*, vol. 102, no. 2, p. 023105, 2013.

[251] *https://assy.micro-coax.com/*.

[252] Z. Keane, J. W. Ciszek, J. Tour, and D. Natelson, "Three-terminal devices to examine single-molecule conductance switching," *Nano letters*, vol. 6, no. 7, pp. 1518–1521, 2006.

[253] M. D. Stewart and N. M. Zimmerman, "Stability of single electron devices: charge offset drift," *Applied Sciences*, vol. 6, no. 7, p. 187, 2016.

[254] A. Aligia, P. Roura-Bas, and S. Florens, "Impact of capacitance and tunneling asymmetries on coulomb blockade edges and kondo peaks in nonequilibrium transport through molecular quantum dots," *Physical Review B*, vol. 92, no. 3, p. 035404, 2015.

[255] A. Anthore, H. Pothier, and D. Esteve, "Density of states in a superconductor carrying a supercurrent," *Physical review letters*, vol. 90, no. 12, p. 127001, 2003.

[256] J. Petta and D. Ralph, "Studies of spin-orbit scattering in noble-metal nanoparticles using energy-level tunneling spectroscopy," *Physical review letters*, vol. 87, no. 26, p. 266801, 2001.

[257] M. Ruby, F. Pientka, Y. Peng, F. von Oppen, B. W. Heinrich, and K. J. Franke, "Tunneling processes into localized subgap states in superconductors," *Physical review letters*, vol. 115, no. 8, p. 087001, 2015.

[258] J. P. Pekola, O.-P. Saira, V. F. Maisi, A. Kemppinen, M. Möttönen, Y. A. Pashkin, and D. V. Averin, "Single-electron current sources: Toward a refined definition of the ampere," *Reviews of Modern Physics*, vol. 85, no. 4, p. 1421, 2013.

[259] H. Knowles, V. Maisi, and J. P. Pekola, "Probing quasiparticle excitations in a hybrid single electron transistor," *Applied Physics Letters*, vol. 100, no. 26, p. 262601, 2012.

[260] D. V. Averin and J. P. Pekola, "Nonadiabatic charge pumping in a hybrid single-electron transistor," *Physical review letters*, vol. 101, no. 6, p. 066801, 2008.

[261] T. Aref, V. Maisi, M. V. Gustafsson, P. Delsing, and J. Pekola, "Andreev tunneling in charge pumping with sinis turnstiles," *EPL (Europhysics Letters)*, vol. 96, no. 3, p. 37008, 2011.

[262] G. Johansson, E. Bratus, V. Shumeiko, and G. Wendin, "Resonant multiple andreev reflections in mesoscopic superconducting junctions," *Physical Review B*, vol. 60, no. 2, p. 1382, 1999.

[263] J. Puertas, *Probing light-matter interaction in the many-body regime of superconducting quantum circuits*. PhD thesis, 2018.

[264] N. N. Rao, *Fundamentals of electromagnetics for electrical and computer engineering*. Pearson Prentice Hall, 2009.

[265] C. R. Paul, *Transmission lines in digital systems for EMC practitioners*. John Wiley & Sons, 2011.

[266] C. A. Mohwinkel, E. F. Johnson, and E. B. Stoneham, "Coplanar waveguide-mounted flip chip," June 18 1996. US Patent 5,528,203.

[267] Y. K. Song and C. C. Lee, "Rf modeling and design of flip-chip configurations of microwave devices on pcbs," in *2004 Proceedings. 54th Electronic Components and Technology Conference (IEEE Cat. No. 04CH37546)*, vol. 2, pp. 1837–1842, IEEE, 2004.

[268] L. Zheng, K. Rodgers, A. Mathewson, B. O'Flynn, M. Hayes, and C. O'Mathuna, "A simulation-based design method to transfer surface mount rf system to flip-chip die implementation," in *3rd Electronics System Integration Technology Conference ESTC*, pp. 1–5, IEEE, 2010.

[269] B. C. Wadell, *Transmission line design handbook*. Artech House, 1991.

[270] D. Cox, S. Behal, M. Disko, S. Gorun, M. Greaney, C. Hsu, E. Kollin, J. Millar, and J. Robbins, "Characterization of c60 and c70 clusters," *Journal of the American Chemical Society*, vol. 113, no. 8, pp. 2940–2944, 1991.

[271] C. Kusch, N. Krawez, R. Tellgmann, B. Winter, and E. Campbell, "Thermal desorption spectroscopy of fullerene films containing endohedral li@ c60," *Applied Physics A*, vol. 66, no. 3, pp. 293–298, 1998.

[272] A. Tokmakoff, D. Haynes, and S. George, "Desorption kinetics of c60 multilayers from al2o3 (0001)," *Chemical physics letters*, vol. 186, no. 4-5, pp. 450–455, 1991.

[273] E. I. Altman and R. J. Colton, "The interaction of c60 with noble metal surfaces," *Surface science*, vol. 295, no. 1-2, pp. 13–33, 1993.

[274] A. O. Pozdnyakov, "Thermal desorption of fullerene c60 from polymer matrices," *Composites science and technology*, vol. 66, no. 16, pp. 3138–3143, 2006.